Air Force Institute of Technology
AFIT Scholar

Theses and Dissertations | Student Graduate Works

3-14-2014

Development of a Detonation Diffuser

Christopher A. Stevens

Follow this and additional works at: https://scholar.afit.edu/etd

Recommended Citation
Stevens, Christopher A., "Development of a Detonation Diffuser" (2014). *Theses and Dissertations*. 578.
https://scholar.afit.edu/etd/578

This Dissertation is brought to you for free and open access by the Student Graduate Works at AFIT Scholar. It has been accepted for inclusion in Theses and Dissertations by an authorized administrator of AFIT Scholar. For more information, please contact richard.mansfield@afit.edu.

FEASIBILITY AND PARAMETER STUDY OF A DETONATION DIFFUSER

DISSERTATION

Christopher A Stevens, CTR

AFIT-DS-ENY-14-M-05

DEPARTMENT OF THE AIR FORCE
AIR UNIVERSITY

AIR FORCE INSTITUTE OF TECHNOLOGY

Wright-Patterson Air Force Base, Ohio

DISTRIBUTION STATEMENT A.
APPROVED FOR PUBLIC RELEASE; DISTRIBUTION IS UNLIMITED

The views expressed in this document are those of the author and do not reflect the official policy or position of the United States Air Force, Department of Defense, or the United States Government.

AFIT-DS-ENY-14-M-05

FEASIBILITY AND PARAMETER STUDY OF A DETONATION DIFFUSER

DISSTERTATION

Presented to the Faculty

Department of Aeronautics and Astronautics

Graduate School of Engineering and Management

Air Force Institute of Technology

Air University

Air Education and Training Command

In Partial Fulfillment of the Requirements for the Degree of

Doctor of Philosophy

Christopher A Stevens BS, MS

Contractor, USAF

Feb 2013

DISTRIBUTION STATEMENT A. APPROVED FOR PUBLIC RELEASE:

DISTRIBUTION IS UNLIMITED

AFIT-DS-ENY-14-M-05

FEASIBILITY AND PARAMETER STUDY OF A DETONATION DIFFUSER

Christopher A Stevens, BS, MS

Contractor, USAF

Approved:

_____//SIGNED//_____ _11Feb2014_

Paul I. King Date

_____//SIGNED//_____ _11Feb2014_

Mark F. Reeder Date

_____//SIGNED//_____ _10Feb2014_

Kevin C. Gross Date

_____//SIGNED//_____ _11Feb2014_

Frederick R. Schauer Date

Accepted:

_____//SIGNED//_____ _28Feb2014_

Adedeji B. Badiru Date

Dean, Graduate School of Engineering and Management

AFIT-DS-ENY-14-M-05

Abstract

This research includes an investigation of the mechanisms of diffraction and reinitiation that enable a detonation diffuser. It describes a set of geometric parameters necessary to design a diffuser for a given detonable mixture and initial channel height. Predetonators with channel height less than the critical height are ineffective because detonations in small channels decouple into separate shock and combustion fronts when the channel height increases. A detonation diffuser allows the channel height to increase by utilizing the decoupled shock wave to reinitiate detonation. In the diffuser, a detonation initially decouples into separate shock and combustion fronts, and then the decoupled shock front reflects from an oblique surface initiating a secondary detonation that survives the expansion. This research investigated the three regions of a detonation diffuser: the initial diffraction, the reflecting surface, and the second diffraction corner. Schlieren video of two-dimensional diffracting detonations recorded the position of the detonation, decoupled shock front and flame front. Observations of the decoupled shocks reflecting from surfaces showed that a 45° reflecting surface must be placed less than 80 mm downstream of the initial diffraction corner to initiate a secondary detonation in more than 91% of repeated trials. Observations of the interaction of diffracting detonations with multiple obstacles revealed that the best performance (smallest separation, and highest Mach number) occurred when the decoupled shock reflected from four separate obstacles at approximately the same time.

Acknowledgements

I would like to thank my Advisor, Dr. Paul King for the opportunity to continue my study at the PhD level. His patient guidance kept me from drifting several times during this rewarding work. Thank you also to my committee members, Dr. Reeder, Dr. Gross, and Dr. Schauer for ensuring the quality of my dissertation.

It was a privilege to work with Dr. Schauer at the Detonation Engine Research Facility through two graduate degrees. I would also like to thank Dr. John Hoke who I rely on as a sounding board and to for the day-to-day oversight that keeps the lab in business and the students out of trouble. Several other people helped me through my research. Curt Rice was invaluable during setup and testing, Justin Goffena fabricated many of the test articles, and Rachel Russo was always willing to look over the data for an outside opinion.

Finally, I want to thanks my parents and sister for their unwavering support and tolerance over the last six years. Whether it was a warm bed, a hot meal, or a sympathetic ear, I have never gone wanting.

Table of Contents

Page

Abstract v

Acknowledgements vi

List of Figures ix

List of Tables xiii

Nomenclature xiv

I. Introduction 1

Motivation 1
Research Objectives 5
Units 10
Organization 10

II. Background 11

Overview 11
Subcritical Detonation Diffraction 11
Detonation Initiation via Shock Reflection 17
Detonation Kernel Development 26

III. Experimental Methodology 31

Overview 31
Experimental Techniques 31
Data Collection Methods 35
Calibration 38
Test Cases 38

IV. Analytical Methodology 52

Overview 52
Shock and Flame Position 52
Separation Distance 56
Shock Mach Number 57
Interpolation Functions 60

V. Results 63

Overview 63
Diverging and Converging Channel Tests 66
Diffraction Angle and Diffraction Corner Radius, Cases D1-D4 70
Reflection angle and obstacle location results, Cases R1-R8 80
Iterative Multiple Obstacle Location Results, Cases M1-M11 99

VI. Discussion 117

Crossover tube studies identify diffraction and reflection parameters. 117
Diverging/Converging experiment establishes feasibility and benefit. 117
Diffraction cases indicate small diffraction angle preferred and corner radius trends mixed. 118
Chance of reinitiation depends strongly on reflection angle and position. 118
Multi-obstacle cases bridged the gap between subcritical and critical diffraction behavior 119

VII. Conclusion and Future Work 120

VIII. Bibliography 122

IX. Appendix A – Schlieren technique, equipment, and uncertainty 125

Technique 125
Equipment 126
Uncertainty 130

Vita 136

List of Figures

Page

1. Diffraction Regimes 2
2. Detonation initiated by non-reacting shock (Thomas, 2002) 3
3. Converging ramp configuration used by Stevens et al. (2011) 4
4. Sequential order and general position of phenomena in a detonation diffuser 6
5. Initial diffraction design parameters 7
6. Reflecting surface design parameters 8
7. Second diffracting corner design parameters 9
8. Construction of a diffracting shock wave (Skews 1967) 11
9. Definition of angle from exit plane (Pintgen, 2004) 13
10. Shock speed decay in subcritical diffraction (Pintgen, 2004) 14
11. Diffraction in channels of decreasing inner radius (Nakayama et al., 2012) 16
12. Surface height for normal and oblique reflecting surfaces 18
13. Detonation initiation by reflecting normal shock (Thomas, 2002) 19
14. Shock initiation in a crossover tube (Nielsen et al., 2011) 20
15. Diffraction and reinitiation in a crossover tube (Nielsen et al., 2011) 22
16. Delayed decoupling due to large corner radius (Nielsen et al., 2011) 23
17. Local explosion due to shock reflection from flat and concave surfaces (Nielsen et al. 2011) 24
18. Detonation initiated by oblique reflection (Stevens et al. 2011) 25
19. DDT observed in hydrogen/oxygen (Urtiew and Oppenheim, 1966). Structures highlighted by the author 28
20. Evolution of cellular structure from a smooth blast wave (Gamezo, 1999) 29
21. PDE as configured for crossover study (Nielsen, 2011a) 32
22. CAD model of optical test section 32

23. Visible strain waves 34

24. Scorch marks (red arrows) on a polycarbonate window.....35

25. Schlieren image of decoupling detonation 36

26. Schlieren (left) and Chemiluminescence (right) of decoupling detonation (Nielsen, 2011b).....37

27. Calibrated pixel dimensions 38

28. Parameters of the diffraction test cases.....39

29. Reflection case parameters 41

30. Case M1 43

31. Case M2 44

32. Case M5 46

33. Case M7 47

34. Diffraction wall location 48

35. Case M9 49

36. Case M11 50

37. Shock and flame fronts 52

38. Initial state of software tool showing diffraction corner and enhanced image 53

39. First point on shock selected, ready to select adjacent pixel. 54

40. Mistakenly pressing 9 instead of 6 results in this state.....55

41. Completed selection of the shock front and the first fifteen coordinate pairs 55

42. Separation distance vectors 56

43. Algorithm for determining shock speed. 59

44. Reinitiation in crossover tubes (Nielsen et al., 2011) 61

45. Schematic of experiment to prove existence of secondary detonations 63

46. Parameters of the D-series and R-series cases 64

47. Diffraction of the secondary detonation causes it to decouple 65

48. Shock and flame propagation in Case M11 (see Fig 32for dimensions) 65

49. Diffraction and reinitiation in a crossover tube (Nielsen et al., 2011)..... 66

50. Decoupling on the diverging ramp (Stevens et al., 2011) 68

51. Local explosion on the converging ramp (Stevens et al., 2001).....69

52. Case D1 ($\theta = 0°$, $r = \infty$) schematic and data fits from 7 runs.....71

53. Case D2 ($\theta = 90°$, r = 2 mm) schematic and data fits from 10 runs 73

54. Case D3 ($\theta = 15°$, r = 2 mm) schematic and data fits from 4 runs 75

55. Case D4 ($\theta = 90°$, r = 25.4 mm) data fitted to 10 runs 77

56. Effect of diffraction angle at a point along the bottom wall 200 mm downstream of the diffraction corner 78

57. Effect of corner radius at two location (200, -51) and (25, 51) 79

58. Case R1 ($\beta = 45°$, $x_0 = 162$ mm, $y_0 = -50.8$ mm) average of 10 runs.....82

59. Case R2 ($\beta = 45°$, $x_0 = 84.7$ mm, $y_0 = -50.8$ mm) average of 10 runs.....84

60. Case R3 ($\beta = 30°$, $x_0 = 80.1$ mm, $y_0 = -50.8$ mm) average of 10 runs.....86

61. Case R4 ($\beta = 15°$, $x_0 = 0$ mm, $y =_0 -50.8$ mm) average of 6 runs.....88

62. Case R5 (r = 25.4 mm, $\beta = 30°$, $x_0 = 80.1$ mm, $y_0 = -50.8$ mm) average of 5 runs 90

63. Case R6 ($\beta = 135°$, $x_0 = 0$ mm, $y_0 = 50.8$ mm) average of 8 runs 92

64. Case R7 ($\beta = 135°$, $x_0 = 43$ mm, $y_0 = 50.8$ mm) average of 8 runs 94

65. Case R8 ($\beta = 135°$, $x_0 = 169$ mm, $y_0 = 50.8$ mm) average of 8 runs 96

66. Trends in the probability of reinitiation. 98

67. Case M1, 13 mm high obstacle with rounded diffraction corner 100

68. Case M2: multiple 6.4 mm high obstacles.....101

69. Case M3: multiple 6.4 mm high obstacles with rounded corners.....102

70. Case M4: multiple 6.4 mm high obstacles in 102 mm tall channel.....103

71. Case M5: 102 mm high channel with obstacles on both walls 104

72. Case M6: 102 mm high channel with rounded obstacles on bottom wall and sharp obstacles on top 105

73. Case M7: Stepped diffraction with obstacles on straight wall 106

74. Case M8: Stepped diffraction with obstacles on offset wall 107

75. Two reflection geometry for diffraction steps 108

76. Case M9: Double reflection with restriction 109

77. Case M10: Double reflection shape without restriction 111

78. Image sequence of case M11: Run 5 $\Delta t = 20$ μs. 113

79. Case M11: Split channel geometry 114

79. Diminishing return of additional obstacles 115

80. Comparison of final separation distance for M-series cases 116

A-1. Z-type schlieren arrangement (Settles, 2001) 125

A-2. Series of schlieren photos of a turbulent gas jet with increasing cut-off. The cut-off degree is a) 0%, b) 20%, c) 40%, d) 60%, e) 80%, f) 90%, g) 95%, and h) 100%. Photos by Rosanna Quiñones (Settles, 2001) 126

A-3. Schlieren arrangement for detonation diffuser study 127

A-4. Previous arrangement 128

A-5. Light source assembly 129

A-6. Focusing mirror with cover 133

A-7. Light emission from detonations 134

A-8. Spectral emission from combustion and camera sensitivity 134

List of Tables

Page

1. Diffraction cases 40

2. Reflection cases 41

3. Multi obstacle cases 42

4. Stoichiometry variable sample values. 58

5. Sample Mach number and constituent values.....59

6. Sample Mach number and constituent variables 60

A-1. High-speed camera comparison.....132

Nomenclature

Acronyms

AIAA	-	American Institute of Aeronautics and Astronautics
AFIT	-	Air Force Institute of Technology
CAD	-	Computer Aided Drafting
CCW	-	Chester-Chisnell-Whitham
CJ	-	Chapman-Jouguet
DDT	-	Deflagration to Detonation Transition
LED	-	Light Emitting Diode
PDE	-	Pulsed Detonation Engine
SI	-	International System of units

Symbols

a	-	Speed of sound
B	-	Bias uncertainty
C_P	-	Constant pressure specific heat
D	-	Detonation velocity
h	-	Surface height
$h_{initial}$	-	Initial channel height
P	-	Pressure or precision uncertainty
M	-	Mach number
MW	-	Molecular weight
N	-	Number of moles
R	-	Specific gas constant
R_u	-	Universal gas constant
R^2	-	Correlation coefficient
r	-	Diffraction corner radius
T	-	Temperature
t	-	Time
u	-	Horizontal gas velocity
U	-	Shock velocity
v	-	Vertical gas velocity
V_{CJ} or U_{CJ}	-	Chapman-Jouguet wave speed
x_0	-	Horizontal leading edge offset
Y	-	Mass fraction
y_0	-	Vertical leading edge offset

Greek

α	-	Expansion wave influence angle
β	-	Reflecting surface angle or angle relative to center line
Δ	-	Discrete difference in a quantity
γ	-	Ratio of specific heats
ε	-	Residual of the least squares fit
η	-	Thomas's Shock initiation parameter
θ	-	Diffraction corner angle
λ	-	Cell size
ϕ	-	Equivalence ratio
τ	-	Induction time
χ	-	Mole fraction

I. Introduction

Motivation

Failure of a detonation front in the transition from a subcritical channel to a supercritical channel is an unaddressed area of concern in the design of pulsed detonation engines. When a predetonator is used to initiate a detonation, the predetonator channel should be as small as possible to minimize the requirements for reactants, but the thrust tube of the PDE should be as large as possible to maximize the thrust per cycle. The detonation in the predetonator channel fails when the shock and combustion fronts decouple due to the area increase. The once decoupled, the combustion is less efficient than a detonation and raises the pressure less than the desired detonation. The benefits of detonation will be maintained if the detonation is reinitiated after decoupling. A detonation diffuser is a device designed to reinitiated detonation during the transition from a subcritical channel, such as the predetonator, to a supercritical channel, such as the thrust tube. The detonation diffuser will utilize the decoupled shock front to reinitiate detonation as the height of the channel increases.

At a sudden area expansion, diffracting detonations decouple or not depending on the initial channel height (Zeldovich, 1956). The critical channel height, which depends on the cell size of the reactant mixture, determines whether decoupling occurs (Mitrofanov, 1965). In supercritical channels, the initial channel height is greater than the critical height, and the detonation diffracts without decoupling (Fig. 1a). In subcritical channels, the detonation decouples into separate shock and deflagration fronts (Fig. 1c). At the critical height, decoupling occurs initially, but naturally occurring, localized explosions reinitiate detonation in the space between the shock and deflagration fronts and restore the detonation mode of combustion (Soloukhin and Ragland, 1969) (Fig. 1b).

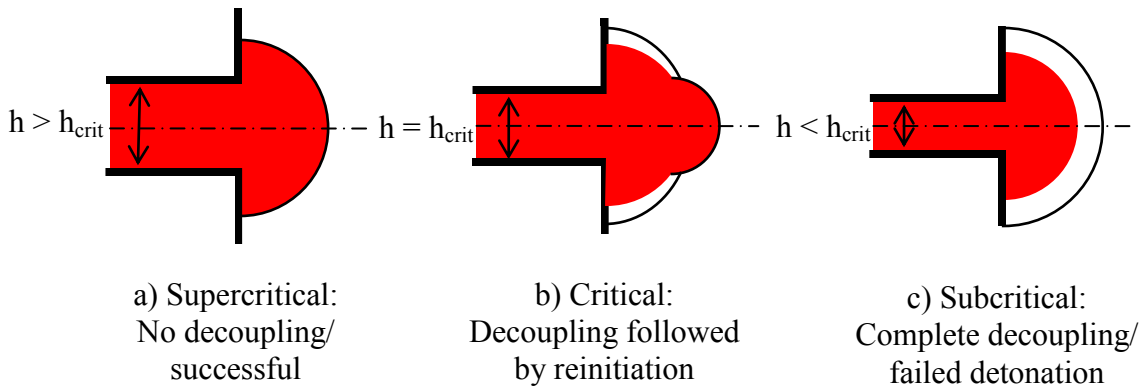

Figure 1. Diffraction regimes in sudden area expansion

Methods will be discussed later that involve using shock reflections to restore a diffracting detonation. Shock reflection causes a local explosion by compressing the reactants so rapidly that chemical reaction begins and remains coupled to the reflected shock wave (Brown and Thomas, 2000). Brown and Thomas (2000) suggested that the presence of a boundary layer is necessary for shock initiation, but Thomas et al. (2002) demonstrated that shock compression alone is sufficient to cause localized explosions and initiate detonation by reflecting a non-reacting shock with the end of a cylinder (Fig. 2). The cylinder experiment eliminated the boundary layer interactions that were present in Brown and Thomas (2000). The minimum shock strength for localized explosion depends on the reflecting surface area, speed of sound in the undisturbed reactants, and ignition delay (Thomas et al., 2002). Thomas et al. defined a criterion for detonation initiation based on these properties that will be discussed in Chapter II.

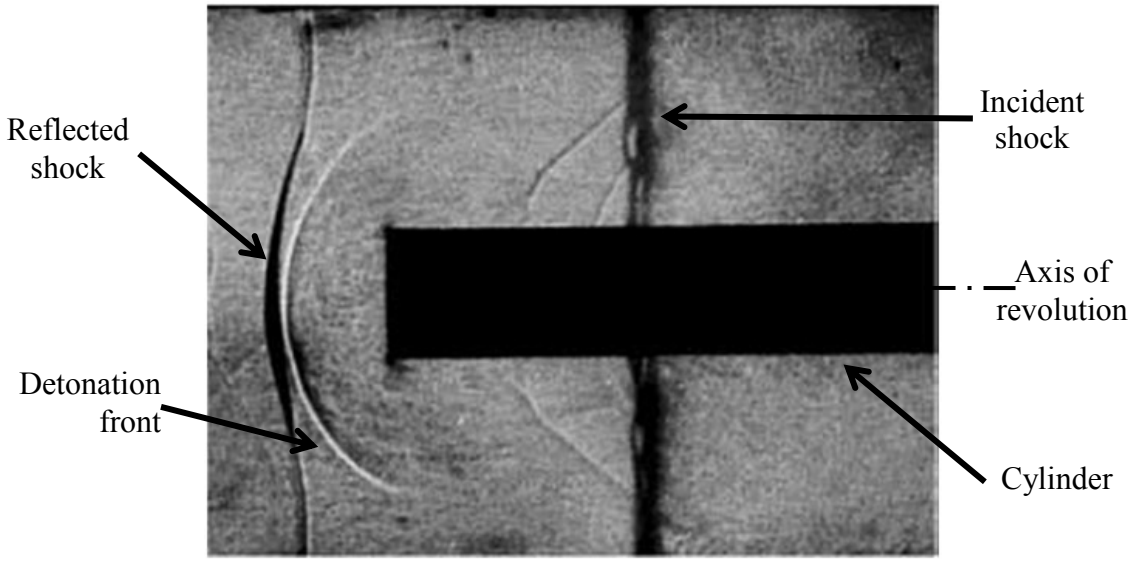

Figure 2. Detonation initiated by non-reacting shock (Thomas et al., 2002)

The minimum incident Mach number for initiation, reported by Thomas et al., is 2.7. The Chapman-Jouguet Mach number is 5.3, and there is sufficient potential in the shockwave from a recently decoupled detonation to initiate a new detonation. Reinitiation can be achieved by reflecting the decoupled shock a done by Thomas et al. did. From this reasoning, it seemed possible to construct a detonation diffuser utilizing reinitiation of the decoupled detonations. Because the diffuser requires only a sufficiently strong shock to initiate detonation it functions even when the initial channel height is subcritical. Unlike the cylinder in Figure 2, a detonation diffuser must reinitiate detonation in the limited time between the passing of the decoupled shock and combustion fronts. Normal reflection of the shock would result in a detonation that runs out of reactants when it encounters the combustion front. Rotating the reflecting surface such that the shock reflection is oblique preserves most of the compression gained by the reflection while giving the newly formed detonation front a route to escape the oncoming combustion front. This research investigates the reflecting angle and position relative to a decoupling detonation of reflecting surfaces. The goal is to induce a planned localized explosion and reinitiate a

detonation that decoupled due to sub-critical diffraction. As will be seen, the initial diffraction decouples the shock and combustion in the primary detonation. The decoupled shock reflects from a reflecting surface causing a localized explosion that evolves into a secondary detonation (see Fig. 3).

The secondary detonation in turn diffracts at a second step and reinitiates at a second reflecting surface. The cycle of diffraction and reinitiation continues until the channel height exceeds the critical height. Stevens et al. (2011) published the first example of a single step detonation diffuser (Fig. 3). The diffuser employed a converging ramp as the reflecting surface. The ramp angle (β) was 14°, with a vertical offset of 13 mm and a rise of 13 mm resulting in zero net expansion. Local explosions occurred near the middle of the converging ramp where the expansion ratio (Eq. 1) was 1.17.

$$Expansion\ ratio = \frac{Channel\ height\ at\ local\ explosion}{Initial\ channel\ height} \quad (1)$$

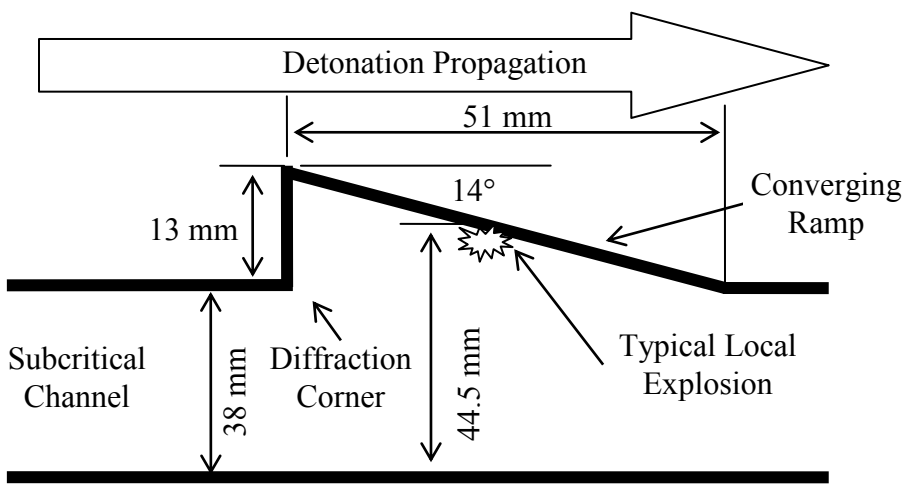

Figure 3. Converging ramp configuration used by Stevens et al. (2011)

A detonation diffuser such as one shown in Fig. 3 is applicable to any situation requiring detonation in a supercritical channel that is supplied by a subcritical channel such as the

transition between predetonator and thrust tube in PDEs. Ideally, the predetonator channel is subcritical to minimize the volume of sensitive mixture, and the thrust tube is as large as possible to maximize the thrust per pulse. The predetonator is a promising initiation means due to small volume and extremely short detonation initiation times and distance, but predetonators see limited use due to sporadic transmission of the pre-detonator detonation to the thrust tubes (Hoke, 2006). A detonation diffuser will remedy the sporadic transmission.

Research Objectives

This research investigates the feasibility of a detonation diffuser. The results demonstrate and parameterize direct initiation of a secondary detonation by the reflection of a shockwave formed when a detonation decouples at the exit of a subcritical channel. The diffuser design is built upon the design studied by Stevens et al. (2012) and shown in Figure 3. This research studies the initial decoupling of the detonation exiting the subcritical channel to determine the locations where the shock propagation Mach number is sufficient for reinitiation and the locations where the decoupled flame front prevents the secondary detonation from propagating to the exit of the diffuser. This research also studies the initiation of secondary detonations to determine the reflecting surface angle and position that result in initiation of a secondary detonation. Finally, this research studies a series of diffuser configurations to determine what effect the number of reflecting surfaces and their arrangement has on the formation and survival of secondary detonations.

This research examines initial diffraction, reinitiation (initiation of secondary detonations), and secondary detonation decoupling in turn to identify and bound the important parameters. Figure 4 shows the regions of interest for initial diffraction, reinitiation, and secondary detonation propagation. In the first phase, the initial diffraction at the first diffraction

corner reveals the decoupled shock strength and distance between the shock and combustion fronts. Knowledge of the shock Mach number ($M_{shock} = V_{shock}/a$) is necessary to position and orient the reflecting surface such the initiation criterion is satisfied.

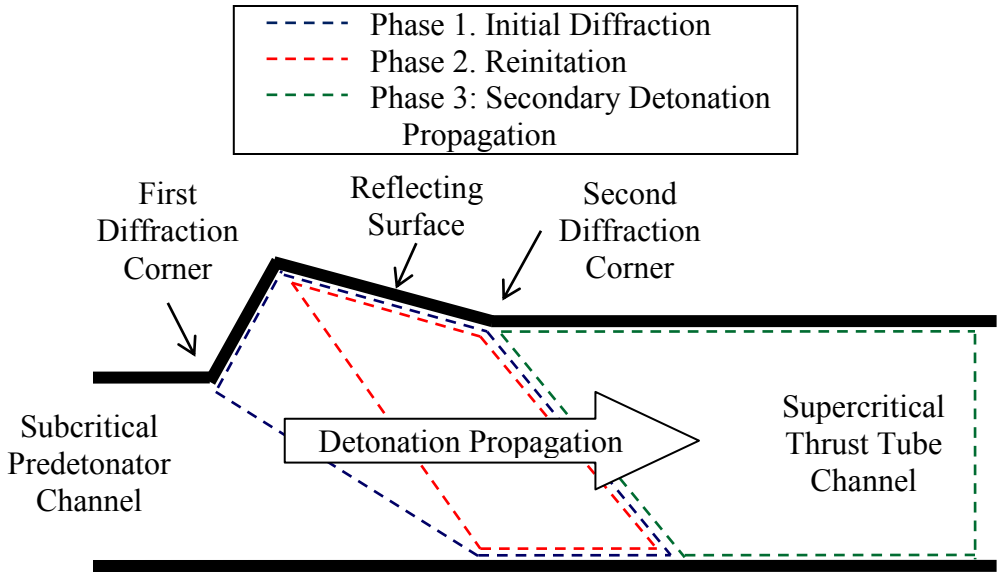

Figure 4. Sequential order and general position of phenomena in a detonation diffuser

Knowledge of the separation distance between shock and combustion or "shock-flame separation" is necessary to avoid trapping the secondary detonation between the first diffraction corner and the reflecting surface.

In phase two, the position of local explosions observed on the reflecting surface determine the range of acceptable angles and offsets for reinitiation. In phase three, the flame separation and shock speed after the second diffraction corner determine the need for additional reflecting surfaces to repeat the process of decoupling and reinitiation until the channel height is greater than the critical channel height.

In the first phase, the experimental objectives include development of maps of the flame separation distance and shock strength downstream of the initial diffraction. The shape of the

first diffraction corner dictates the rate of decrease in shock Mach number and increase in shock-flame separation. To investigate the effect of diffraction angle and corner radius on shock decay, a selection of diffraction angles and corner radii were evaluated (Fig. 5). This experimental sequence was titled "D" as a shorthand for diffraction. The experimental results include contour maps of shock-flame separation distance and shock Mach number as functions of diffraction angle, corner radius.

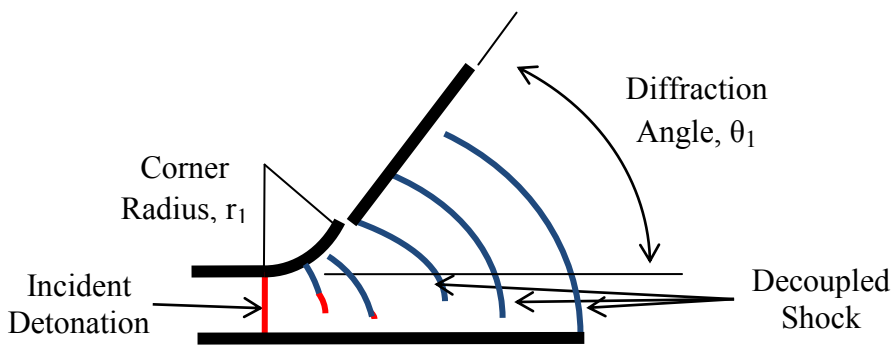

Figure 5. Initial diffraction design parameters

It will be shown that a combination of high shock Mach number and large shock-flame separation distance are preferred for the highest probability of a local explosion without trapping the secondary detonation.

In the second phase, the objective is to obtain the location of local explosions on the converging ramp. A fixed, first diffraction corner geometry will keep the shock Mach number and shock-flame separation profiles constant as the reflecting surface parameters vary. By manipulating reflecting surface angle, and position (horizontal and vertical distance to the diffraction corner) one will systematically vary the strength and turning angle of the incident shock (Fig. 6). The goal of the second phase was to find an optimum location and angle of the reflecting surface. In Ch. III, this test sequence is labeled "R" as a shorthand for reflection. The

occurrence and position of local explosions define the design space for the reflecting surface. Due to the natural statistical variation in the diffracting detonation, the shock–flame separation distance and shock Mach number will be shown to have large, statistical variation. As a result, the occurrence of local explosions requires a statistical treatment. The results in Chapter IV include the probability of local explosion as a function of reflecting surface angle, vertical distance from the diffraction corner, and horizontal distance from the diffraction corner.

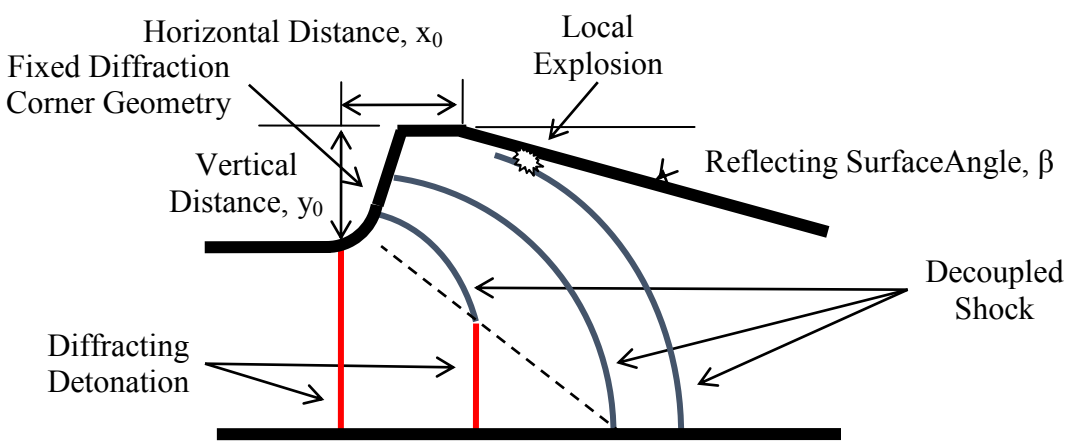

Figure 6. Reflecting surface design parameters

The purpose of the third phase was to complete the transition from the sub critical channel to a super critical channel with minimal decoupling. In the third phase, the objective was a qualitative examination of several multi-reflection geometries. This test series was labeled "M" in CH. III as shorthand for multiple obstacles. Decoupling after the first reinitiation of detonation is to be avoided (Fig 7) because it defeats the purpose of the diffuser; however is was universally observed in the R-series test cases.

The evolution of the M-series test cases was based on the observed decoupling the previous case beginning with the most consistently reinitiating case from the R-series (case R2). In case M1 the obstacle height was shorter and the diffraction corner at the end of the surface had

a larger radius. Later the number of reflecting surfaces was increased (M2-M5), reflecting surfaces were added to the initial diffraction corner (cases M7-M10), and the decoupled shock encountered multiple reflecting surfaces arranged radially (case M11).

The most successful geometry in this research utilized multiple reflection surfaces interacting separately with the initially decoupled shock (see Fig. 33). The separately reinitiated detonations produced local explosions in the region downstream of the reflecting surfaces due to the collision of diffracted shockwaves from the separate, secondary detonations (see Fig. 78). Spontaneous local explosions are the defining characteristic of detonation diffraction from a critical channel (Soloukhin and Ragland, 1969). The occurrence of spontaneous local explosion in a case where the initial channel height is subcritical shows an improvement gained from the addition of reflecting surfaces.

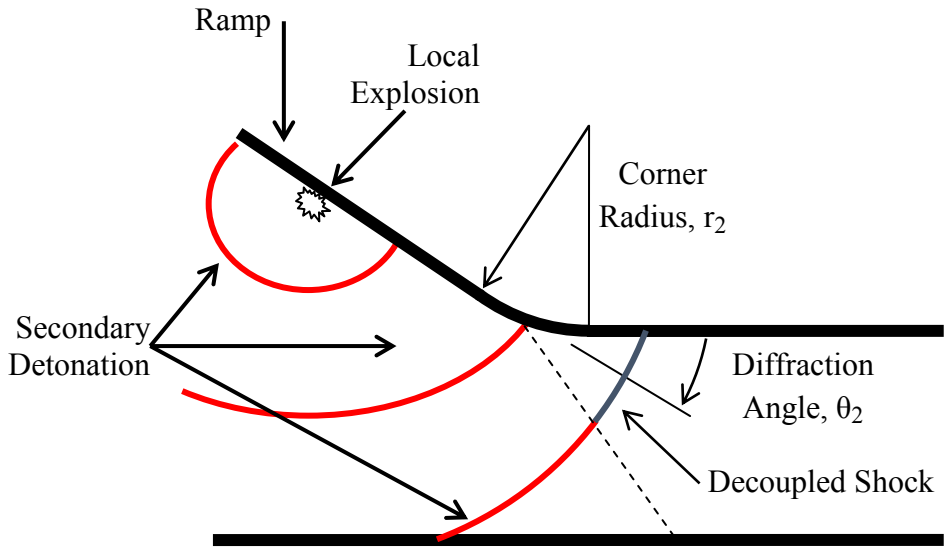

Figure 7. Second diffracting corner design parameters

Units

The detonation for propulsion community works in both the English and SI unit systems. To appeal to a broader audience and reduce the clutter of reporting values in two unit systems, this work reports only the SI units.

Organization

This dissertation begins with a detailed examination of detonation diffraction, shock initiation, and detonation kernel development. The background chapter draws from relevant literature to describe the significant phenomena exploited to develop a detonation diffuser. The experimental methodology chapter describes experimental methods, measurement techniques, equipment requirements, and data acquisition systems. The analytical methods chapter describes the manual and automated data reduction algorithms and the associated uncertainty. The results chapter reports the observations from each of the test cases and describes the limits of the design parameters. A conclusions chapter gathers the wisdom gained from the results to recommend a functional diffuser geometry and additional steps toward an optimized design. Finally, the bibliography lists the literary sources used throughout the paper.

II. Background and Theory

Overview

This chapter details the relevant portions of detonation theory and empirical evidence necessary to understand the reasoning behind the experimental methods used in this research. The first section reviews the literature concerning diffraction of a subcritical detonation. The second section examines prior work on both normal and oblique shock reflections leading to detonation initiation. The final section looks at the development of a detonation kernel.

Subcritical Detonation Diffraction

Skews (1967) constructed a geometric model (Fig. 8) for the head of a disturbance propagating into the fluid behind a normal shock wave during diffraction. The Skews construction is useful for modeling the propagation of the shockwave as it decouples from the combustion front. It lacks any treatment of heat release from combustion and is used only to model the shock propagation after decoupling. Figure 8 shows the state of the diffracting shock at a time, Δt, after the normal shock encounters the corner.

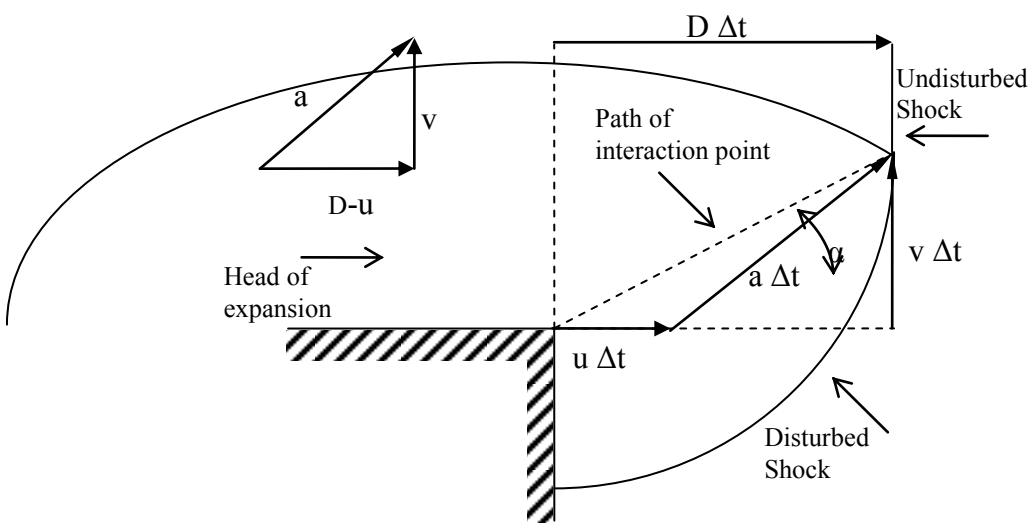

Figure 8. Construction of a diffracting shock wave (Skews 1967)

When the normal shock encounters the diffraction corner, an expansion wave begins at the corner and traverses the normal shock at the post-shock speed of sound (a). Meanwhile, the unaffected portion of the shock continues to propagate at the original velocity (D). The intersection of the expansion wave and the shock traces a straight line out from the corner at an angle α. The angle depends on D, a, and the bulk velocity, u, induced by the shock (Skews, 1967).

$$tan(\alpha) = \frac{v}{D} = \frac{\sqrt{a^2-(D-u)^2}}{D} \quad (2)$$

The portion of the shock disturbed by the expansion wave curves, and the shock velocity decreases. When the initial channel height is subcritical (see Fig. 1), the reduced shock compression causes the shock and combustion fronts to decouple into a leading shock and a trailing flame. When the channel height is greater than the critical height, the loss of compression is insufficient to cause global decoupling of the detonation.

The critical channel height is a function of the cross-section of the channel, and the stability of the detonation wave (Lee 2007). Lee (2007) deemed as "unstable" any detonable mixture that resulted in a detonation with cellular structure. For the 2D entrance channel used in this work, Lee found that the critical channel height was six times the cell size defined as λ.

Pintgen (2004) examined the decoupled shock speed and shock-flame separation distance for reactant mixtures of hydrogen/oxygen/argon and hydrogen/N_2O in detonations diffracting from subcritical channels. Reported were the shock velocity and shock-flame separation distance as functions of time and angle measured from the exit plane of the initial channel, (labeled β in Fig. 9), but not as a function of position. Pintgen used four methods to calculate distance traveled by a shock between photographic frames. The first used the measurement from a point on one shock to the closest point on the shock in the following frame, the "forward

closest" method (see Fig. 9). The second was a measurement from an arbitrary point to the closest point on the shock in the preceding frame in a "backward closest" method. The third and fourth were measurements along a vector normal to the shock front. Measuring to the following frame was "forward normal" and measuring to the preceding frame was "backward normal."

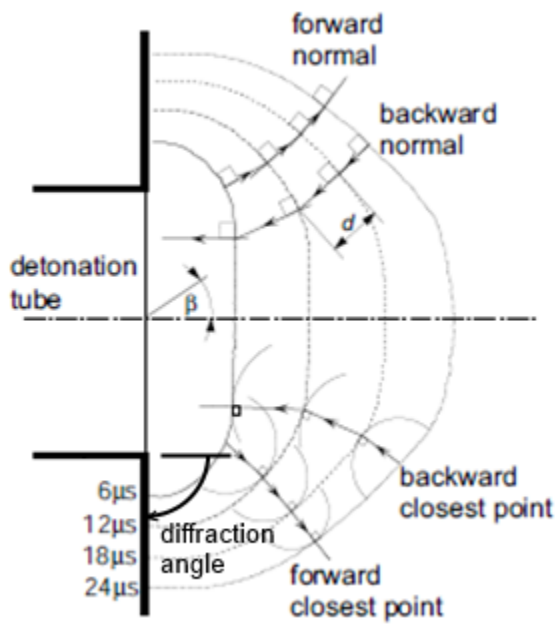

Figure 9. Measurement methods used to obtain lead shock velocity (Pintgen, 2004)

The velocity profiles obtained from these measurements indicate where the shock Mach number decreases most slowly giving the best probability of reinitiation when the shock reflects.

Pintgen found that the shock speed was highest near the centerline of the channel and decreased as β increased (Fig. 10). The shock speed also decreased rapidly in time dropping over 50% in the first 50 µs of diffraction. Unfortunately, Fig. 10 is unsuited for the purposes of this research because Pintgen (2004) considered only one combination of diffraction angle and corner radius (90° diffraction angle, 0 mm radius). This research uses a configuration with the same diffraction angle and slightly larger diffraction angle (2.0 mm) extensively as a baseline for comparison to different diffraction angle and corner radii.

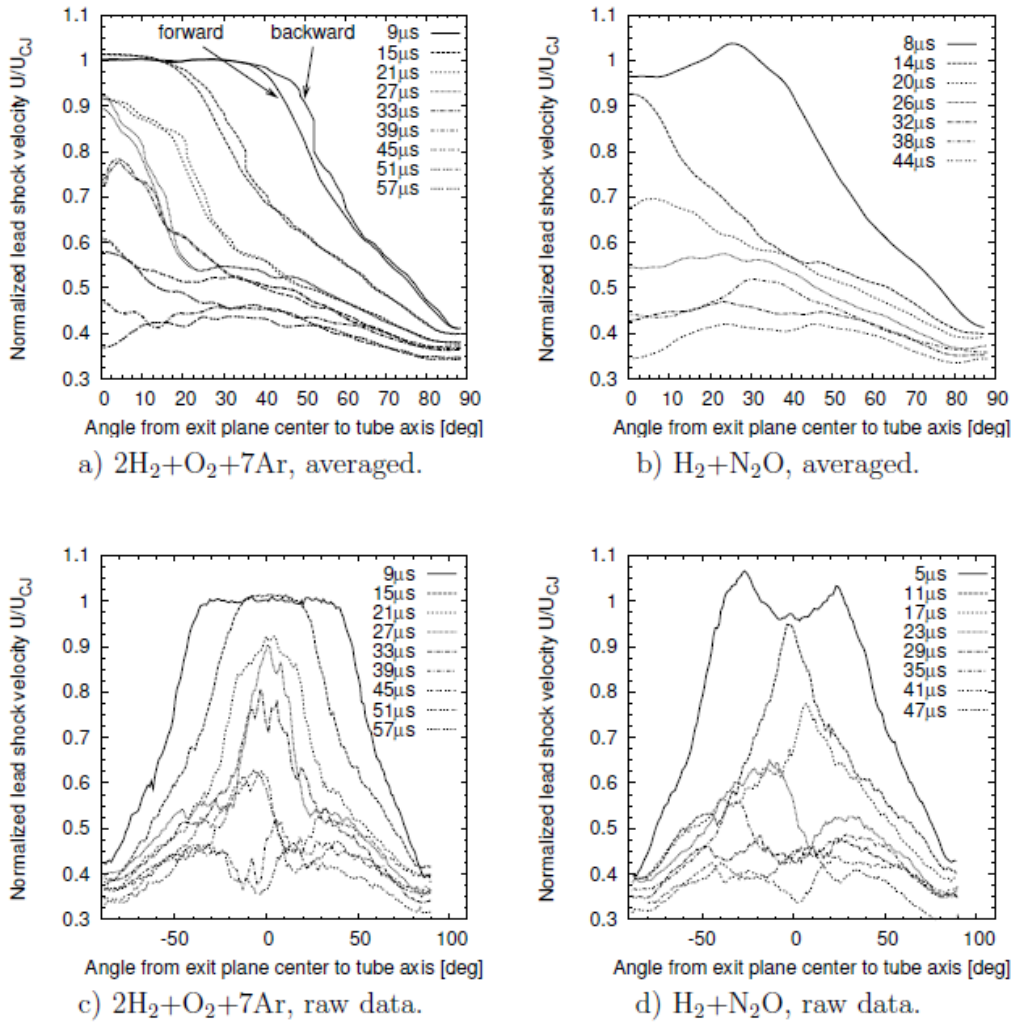

Figure 10. a) Averaged velocity profiles assuming axis symmetry for forward and backward closest point method, 2H2+O2+7Ar, P_0 = 1 bar. Legend gives point in time after detonation exited the tube. b) Averaged velocity profiles assuming axis symmetry for forward and backward closest point method, H2+N2O P_0 = 0.4 bar. Legend gives point in time after detonation exited the tube. c) Normalized velocity obtained with forward closest point technique for 2H2+O2+7Ar, P_0 = 1 bar. d) Normalized velocity obtained with forward closest point technique for H2+N2O P_0 = 0.4 bar (Pintgen, 2004).

A lower diffraction angle alone can prevent decoupling (Nettleton 1987). In Fig. 10, the diffraction angle was 90°. Nettleton (1987) predicted a maximum diffraction angle below which the rate of expansion is small enough to prevent decoupling of the detonation. For a reactant mixture with γ = 1.4, Nettleton (1987) predicts no decoupling at diffraction angles below 14.5°. Nettleton (1987) derived the minimum angle from a combination of the Chester-Chisnell-

Whitham shock diffraction theory and the Chapman-Jouguet detonation wave-speed theory. According to Nettleton's analysis, the minimum angle maintains a sufficient shock velocity along the diverging wall for detonation. Nettleton (1987) did not incorporate triple point interactions that aid in sustaining detonations, and experimental work by the author shows that some decoupling occurs for angles as small as 14° (Stevens at al., 2011(a)) and at 15° a detonation does not fully decouple (see Fig. 53).

The impetus to vary the diffraction corner radius in the current work was prompted by observations in crossover tubes by Nielsen et al. (2011) who varied the crossover tube geometry and found a delay in decoupling when the diffraction corner radius was increased. A 25.4 mm in comparison to a 2.0 mm radius indicated a qualitative delay in decoupling of the incident detonation front. Nakayama et al. (2012) also reported increased wave speed as the inner radius increased in a curved, square cross-section channel. In Fig. 11, Nakayama et al. show the onset and increase of decoupling as the inner wall radius decreases. The minimum ratio of radius to cell size was 21 for prevention of the unstable mode where decoupling occurs. For a stoichiometric mixture of hydrogen and air, the cell size is 8.19 mm (Ciccarelli et al., 1994), and thus the minimum radius to prevent decoupling according to Nakayama et al. would be 172.2 mm. The current work differs because there is no outer wall to reflect triple points and restore detonation in the unstable mode. It is unknown what the minimum radius would be without the outer wall, and Nakayama is the best available prediction. Because decoupling is desirable to separate the shock and flame prior to reinitiation, the diffraction corner radius was always less than the predicted 172.2 mm in the current work. Two diffraction corner radii were studied to determine the sensitivity of decoupling to the radius. The next section explains why decoupling is necessary to make the transition from a subcritical channel to a supercritical channel.

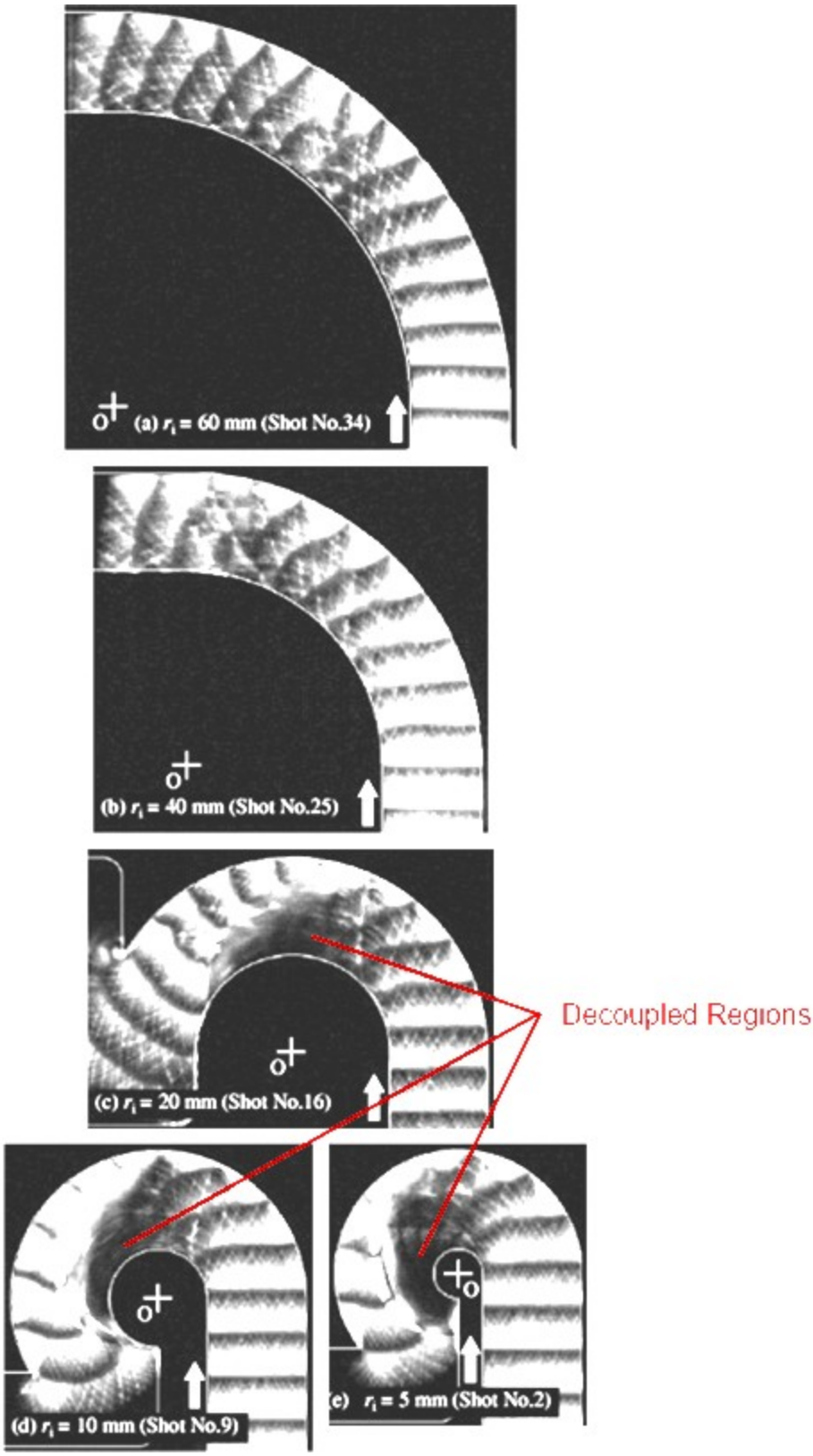

Figure 11. Diffraction in channels of decreasing inner radius. Stoichiometric mixture of ethylene and oxygen. Decoupling is visible when r_i < 40 mm in panels c, d, and e. (Nakayama et al., 2012)

Detonation Initiation via Shock Reflection

Localized explosions are the precursor to stable, cellular detonation. Local explosions occur in both DDT (Urtiew and Oppenheim, 1966) and diffracting detonations exiting critical height channels (Soloukhin and Ragland, 1965). In DDT, local explosions occur in the space between the leading normal shock and the accelerating combustion front (Urtiew and Oppenheim, 1966). In critically diffracting detonations, local explosions occur near the in the space between the decoupled shock and combustion front (Soloukhin and Ragland, 1965). In both situations, the local explosion results in a detonation kernel that grows, develops cellular structure, and stabilizes in a channel to become a planar detonation front.

Localized explosions also occur when high Mach number shocks reflect from surfaces (Brown and Thomas, 2000 and Thomas et al., 2002). Early detonation experiments found that detonation could also be initiated by normal shock reflection at the end wall of a shock tube (Saitsev and Soloukhin, 1958 and Strehlow and Cohen, 1962). In either case, the formation of a detonation depends on local speed of sound, reflecting surface area, and induction delay of the detonable mixture (Thomas et al., 2002). A critical condition below which detonation initiation is improbable is $\eta < 1$, where η is the ratio of surface height (h) to the product of post-shock speed of sound (a) and induction delay (τ) shown in Eq. 3.

$$\frac{h}{\mathrm{a}\,\tau} = \eta \qquad (3)$$

Induction delay is the time that passes between the shock reflection and the onset of heat release by chemical reaction of the reactants. Thomas et al. defined surface height for a normal shock reflection. In the current work the definition has been generalized for oblique reflections as the perpendicular distance from the channel wall to the end of the obstruction (Fig. 12.).

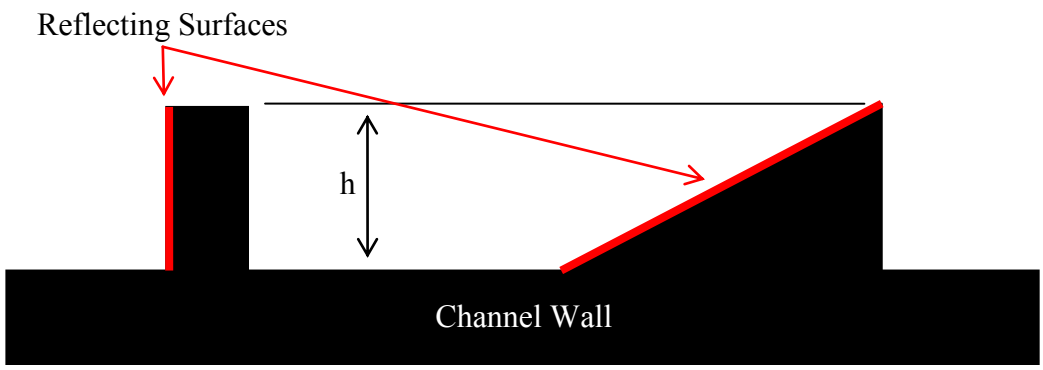

Figure 12. Surface height for normal and oblique reflecting surfaces

To address the suggestion by Brown and Thomas that a shock/boundary layer interaction might be necessary to initiate detonation, Thomas et al. (2002) utilized a normal shock reflection from the end of a cylinder to quantify the critical conditions (Fig. 13). Prior to the shown frames, a right traveling shock impacted the circular face of the cylinder causing a reflected shock and a flame front to form. For the cylinder, Thomas et al. substituted the cylinder radius for the surface height to adapt Eq. to the new configuration. In the experimental frames on the left, η was 0.93 and the mixture ignited after the reflection, but did not detonate. In the simulated frames on the right, η was 1.00 and the shock reflection initiated detonation. Taken together, the experimental and simulation results validate the substitution of radius for height in the critical condition for detonation initiation and remove the boundary layer requirement suggested by Brown and Thomas. The current work relies on this finding first when extending the definition of surface height to oblique reflecting surfaces and later when using multiple reflecting surfaces to initiate multiple, separate detonations from the same decoupled shock.

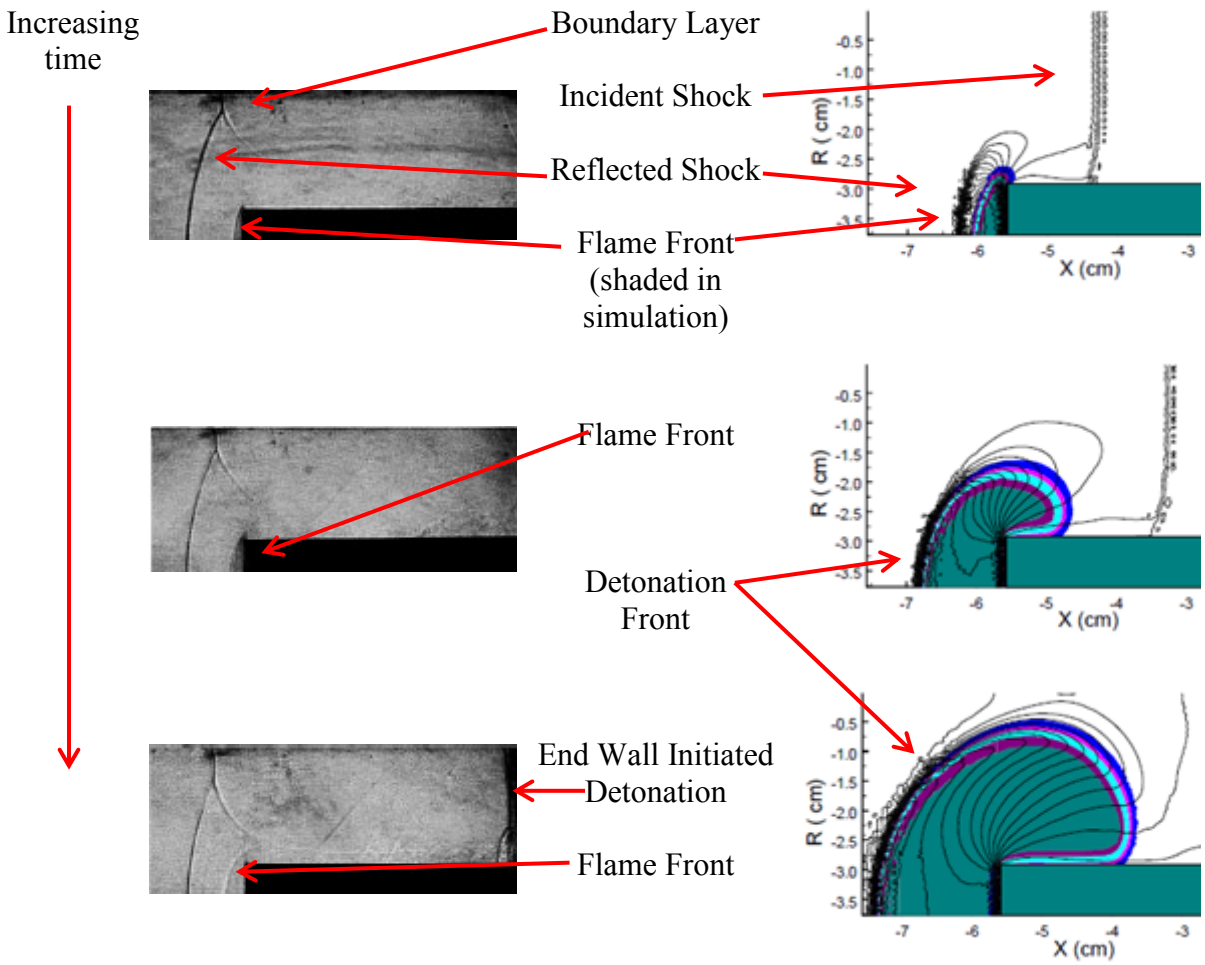

(a) Experiment, η = 0.93 (b) Simulation, η = 1.0

Figure 13. Detonation initiation by reflecting normal shock (Thomas et al., 2002)

The earliest evidence of reinitiation by oblique shock reflection came from crossover tube studies (Nielsen et al., 2011). A crossover tube also causes diffraction of the detonation, and reinitiation can occur when the decoupled shock reflects from the reflecting surface (Fig. 14).

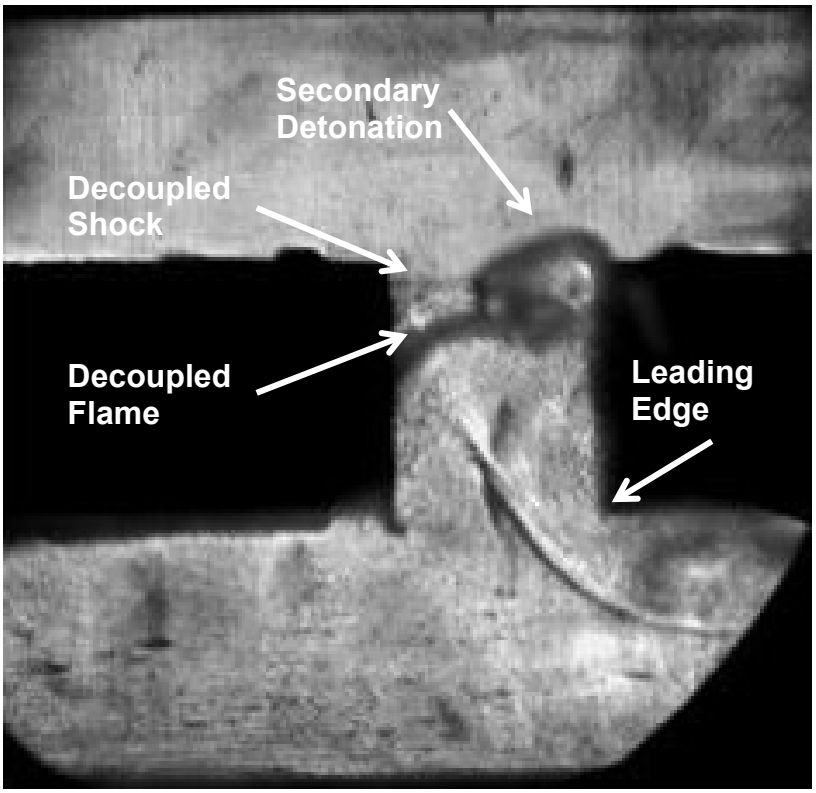

Figure 14. Shock initiation in a crossover tube (Nielsen et al., 2011)

The decoupled shock was nearly normal to the reflecting surface on impact and the secondary detonation formed in the crossover tube did not propagate back to the primary tube because the combustion front consumed the reactants before the detonation arrived. Diffraction at the exit of the crossover tube caused the secondary detonation to decouple and it was necessary to add DDT obstacles to the secondary tube to transition to detonation (Nielsen, 2011).

The crossover geometry in Fig. 14 has an identical diffraction corner, but the reflection surface is perpendicular to the channel wall and not attached. The result is a secondary detonation that is isolated or from the remaining reactants by combustion products or "trapped" (Fig. 16). The diffraction angle is 90° and the corner radius is 2.0 mm. The reflection angle is 90° and the leading edge of the reflecting surface is 38.1 mm downstream of the diffraction corner. The vertical offset is 0 mm. Local explosions occur after the decoupled flame front

reaches the reflecting surface preventing the secondary detonation from propagating downstream. Trapped detonations are undesirable in a detonation diffuser because a trapped detonation cannot propagate downstream. The key to preventing a trapped secondary detonation is minimizing the delay between shock reflection and reinitiation known as the induction delay (τ) while maximizing the separation distance between the decoupled shock and flame to allow the secondary detonation time to propagate downstream before the decouple combustion front arrives.

The crossover tubes used in detonation branching configurations (Nielsen, 2011 and Camardo, 2012) share phenomena with the detonation diffuser. The decoupling and reinitiation processes are identical. Stable detonation waves undergo diffraction at the crossover and decouple (Fig. 15b). Shock reflection on the opposite wall of the crossover tube reinitiates detonation (Fig. 15c), and diffraction occurs again at the end of the crossover tube (Fig. 15d). Because of the similarities, crossover tube studies were a good starting point for the current diffuser.

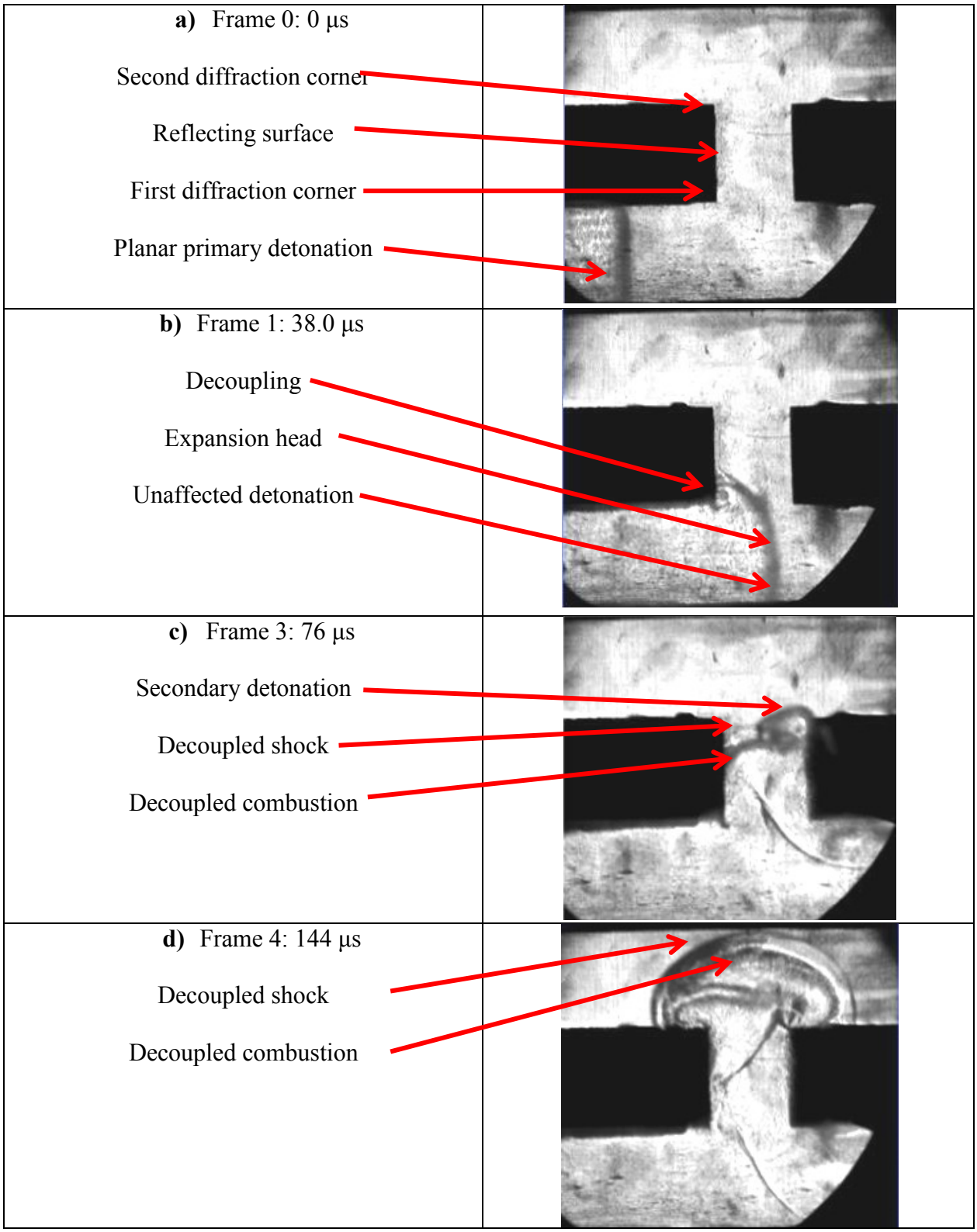

Figure 15. Diffraction and reinitiation in a crossover tube (Nielsen et al., 2011)

The most significant difference between a crossover tube and a diffuser is the orientation of the reflecting surface. The reflecting surface is typically parallel to the initial detonation front in a crossover tube to reduce the volume of the crossover tube. Flow loss considerations are secondary to minimizing the volume of fuel/air mixture needed to fill the crossover, as the crossover tube produces little thrust. In a detonation diffuser, the diffuser volume contributes to thrust and the flow losses are more prevalent than in a crossover configuration. As a result, the desired reflection angle is as small as reliable reinitiation allows. The crossover tube studies suggested that increasing the radius of the initial diffraction corner delays decoupling within the crossover tube (Fig. 16). In the second frame of Fig. 16a, the separation distance is 4.89 ± 0.98 mm, and in Fig. 16b, the separation distance is 4.03 ± 0.98 mm. The difference was small and the uncertainties were large enough that a better experiment was needed to draw a statistically significant conclusion, but the trend is encouraging so diffraction corner radius was included as a parameter in the D-series test cases. Unlike the separation distance difference, shock reflection induced detonations were obvious in the crossover tube videos.

a)

b)

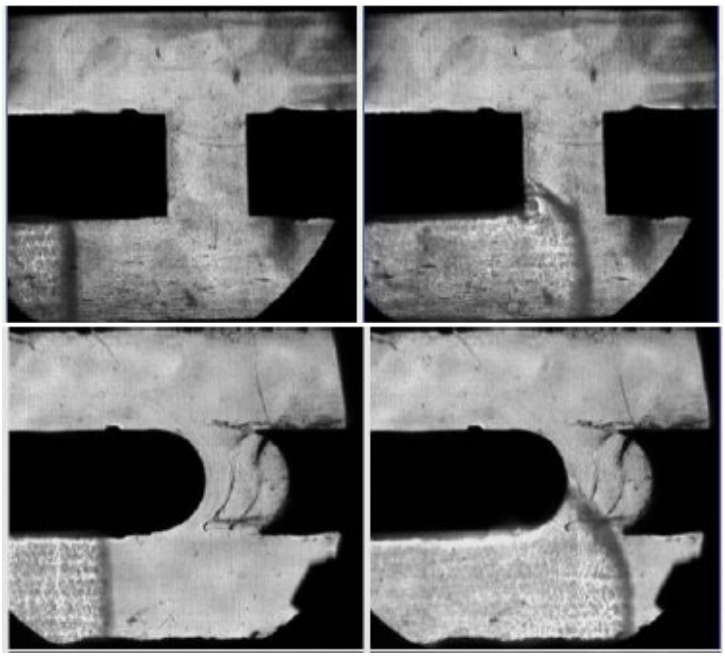

Figure 16. Delayed decoupling due to large corner radius (Nielsen et al., 2011)

Reinitiation was observed on both flat and concave reflecting surfaces (Fig. 17). The increased diffraction angle due to the concavity ensured decoupling in the second detonation tube. The remaining test cases avoided concave reflecting surfaces to reduce diffraction at the end of the reflecting surfaces.

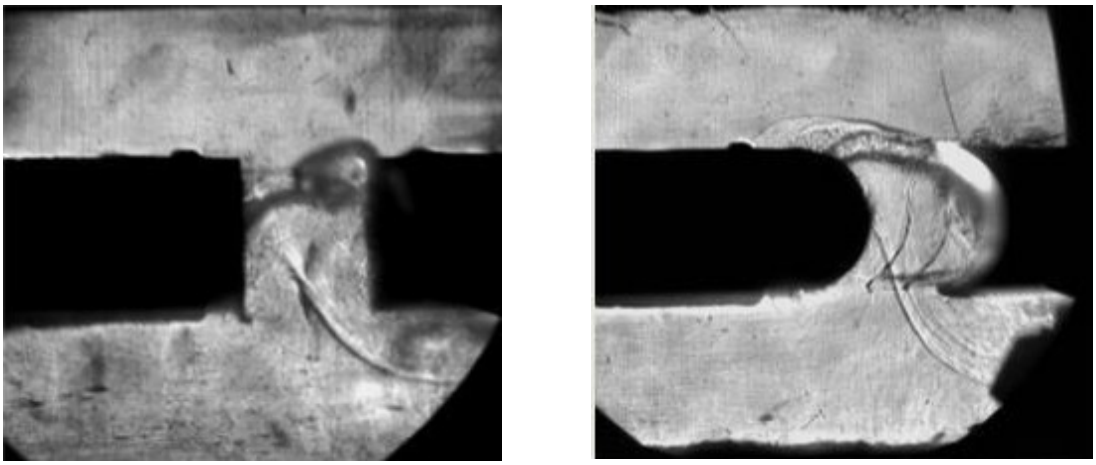

a) Flat wall b) 25 mm concave radius

Figure 17. Local explosion due to shock reflection from flat and concave surfaces (Nielsen et al. 2011)

Oblique reflections also initiate detonation provided the compression is sufficient. Detonation initiation after an unsteady oblique shock reflection was observed by Stevens et al. (2011). In Fig. 18, Stevens et al. compare a 2D simulation of diffraction and reinitiation to experimental frames from a 38 cm high, 50 cm deep channel. In the first frame of the simulation, diffraction begins, but it is not yet visible in the experiment. In the second frame of both series, separation is visible. In the simulation, the separation region is a light blue region between the shock and the flame. In the experiment, the separation region is a subtle dark band following the shock front. In the last frame of each series, detonation has reinitiated along the reflecting surface.

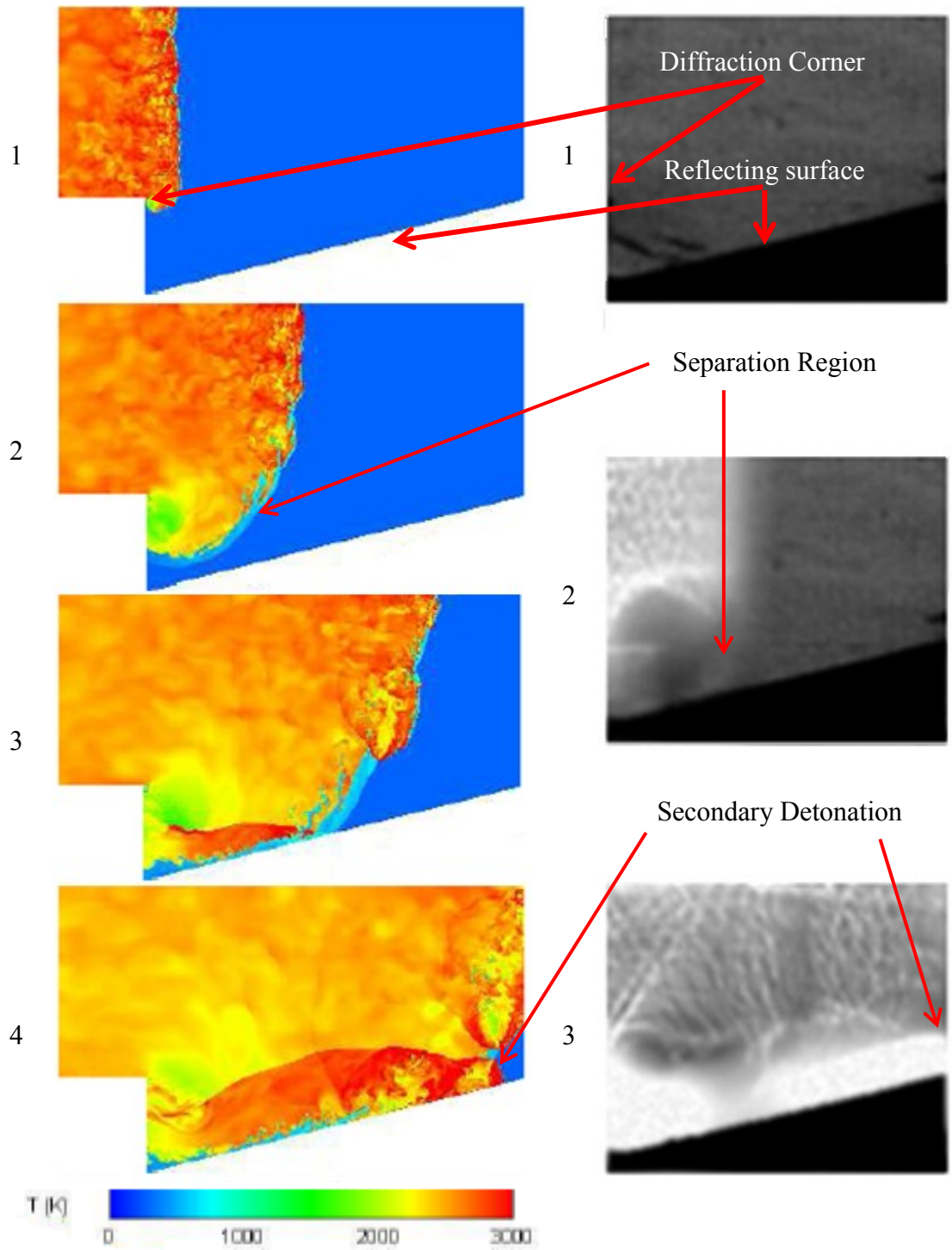

Figure 18. Detonation initiated by oblique reflection (Stevens et al. 2011)

The geometry in Fig. 18 contains most but not all of the parts of a detonation diffuser. The configuration has a diffraction angle of 90°, a corner radius of 0.0 in the simulation (2.0 mm in

the experiment), a reflection angle of 14° and a vertical offset of -12.7 mm. There is no visible diffraction at the end of the reflection surface because the end is not visible.

Detonation Kernel Development

In Figure 15, the local explosion occurs near the midpoint of the reflecting surface. Since there is significant shot-to-shot variation expected in the decoupled shockwave, an excess of reflecting surface will be necessary to improve the probability of a local explosion, thus the detonations begun by local explosions in a detonation diffuser need to propagate along the remainder of the reflecting surface and past the second diffraction corner at the end for the diffuser to be effective. The natural evolution the local explosion into a detonation wave determines the speed and shape of the detonation front as it encounters the diffraction corner at the end of the surface. The secondary detonation will initially be overdriven (Schauer et al., 2005), and the excess wave-speed will be important to overcome the loss due to diffraction at the second diffraction corner. To determine the maximum angle of diffraction that the detonation can tolerate without decoupling, it is necessary to characterize the evolution of the detonation from local explosion to the quasi-stable cellular mode exhibited by detonations in channels (Urtiew and Oppenheim 1966). In the cellular mode, the local detonation Mach number varies in a repeating pattern dependent on the propagation of transverse shock waves that intersect the detonation front. The cellular mode is quasi-stable because the local wave speed varies, but the average speed of advance does not.

Experimental studies of DDT show initial detonation kernel propagation dominated by the local speed of sound and shock induced velocity. Urtiew and Oppenheim (1966) captured the propagation in a 25 mm x 38 mm rectangular cross-section channel with framing schlieren

images (Fig. 19). In the first frame of Fig. 19, the local explosion has occurred in the boundary layer along the top wall of the channel sometime between 30 and 35 μs (between consecutive frames). The detonation convected with the bulk motion behind the normal shock, and expanded until the detonation front caught up with the normal shock at approximately the 40 μs mark. Part of the wave front continued to propagate through the post shock region and encountered the deflagration front at the same time. The detonation front reached the bottom wall of the channel consuming the reactants before the deflagration arrived just after the 45 μs mark. Without reactants, the deflagration perished by 50 μs. The part of the detonation that passed the normal shock slowed because of the lower pressure and temperature ahead of the shock. The detonation front picked up velocity instabilities from interaction with normal shock. The instabilities grow in size from 40 μs to 50 μs as the detonation front continues downstream and will eventually stabilize as cellular structure (Urtiew and Oppenheim, 1966).

Detonation front encounters normal shock then flame front

Detonation passes normal shock as it propagates across channel

Detonation speed governed by reactant pressure and temperature is lower after passing normal shock

Post shock reactants completely consumed, deflagration ceases, and detonation begins to stabilize.

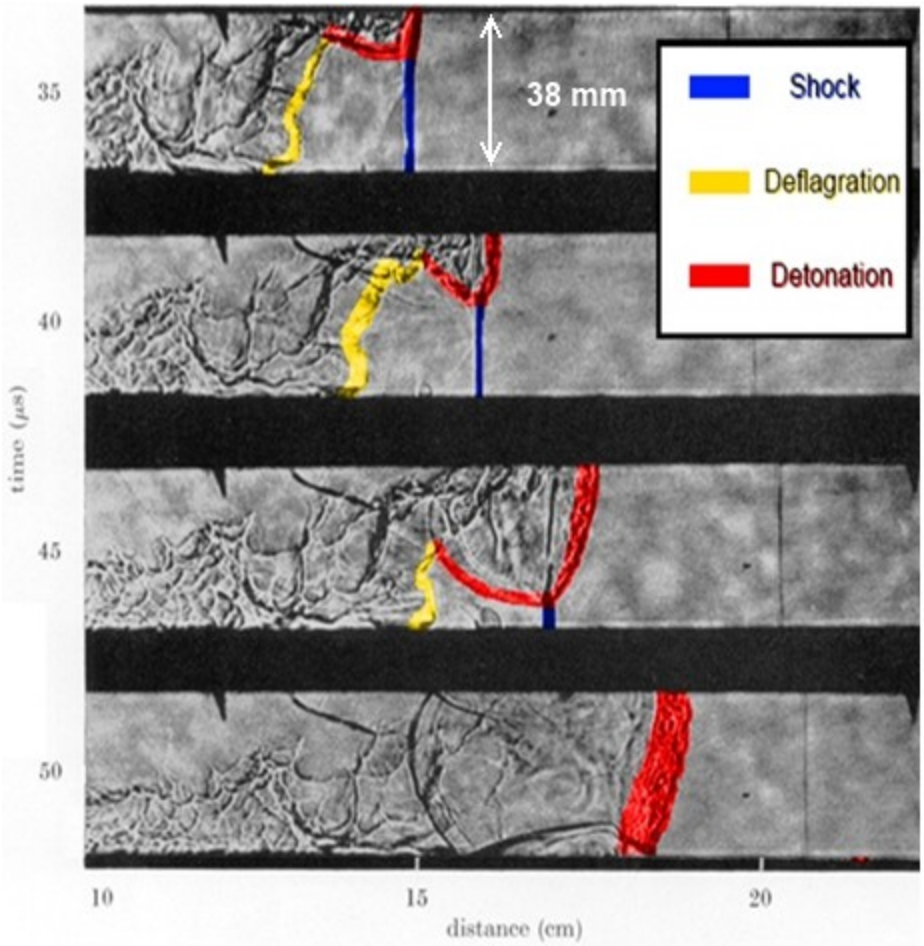

Figure 19. DDT observed in hydrogen/oxygen (Urtiew and Oppenheim, 1966). Structures highlighted by the author

Local explosions produce a smooth spherical blast wave that evolves cellular structure after developing instability (Gamezo et al., 1999). Numerical simulation of blast waves (Fig. 16) expands the time scale of the onset of instability showing the transition from a smooth blast wave to quasi-stable cellular detonation that happens too quickly to capture with the imaging technique used by Urtiew and Oppenheim in Fig. 19.

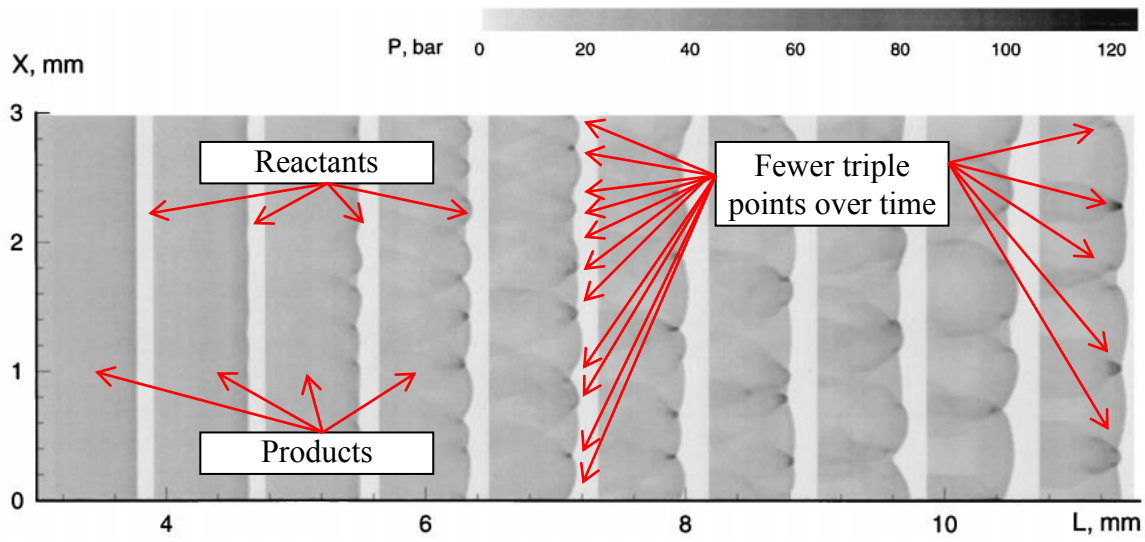

Figure 20. Evolution of cellular structure from a smooth blast wave (Gamezo, 1999)

Gamezo et al. (1999) found that triple points form as the result of instability in the blast wave and weak turbulence in the reactants. The perturbations cause wrinkling in the smooth wave, and transverse waves form. At L = 6 mm in Fig. 20, the cell size is small because there are many perturbations of the blast wave. As the detonation wave slows, some triple points disappear and the cell size increases. Over time, the cellular detonation wave slows asymptotically to the CJ speed and the cell size becomes constant.

In the detonation diffuser, secondary detonations that form along the reflecting surface do not encounter the far wall of the channel before the end of the reflecting surface, and the collected data will show whether the secondary detonation or the decoupled shock will reach the end of the second diffraction corner first. How the secondary detonation reacts to the diffraction corner at the end of the surface will depend on the shock speed and number of triple points present at that moment. Since no published data describes that interaction, this research reports the speed of secondary detonations before and after encountering the second diffraction corner and the shock Mach number and shock-flame separation distance when the secondary detonation decoupled.

The literature concerning detonation diffraction, shock initiation of detonation, and evolution of a detonation front from local explosions suggests three sets of measurements necessary to enable analysis of a detonation diffuser. The first measurements are the shock Mach number and shock-flame separation distance as functions of diffraction angle (θ_i) and corner radius (r_i). The second measurements are location and probability of local explosions as functions of reflecting surface angle and position. The final set of measurements are shock speed and separation distance after diffraction of a secondary detonation. This research reports all three sets experimentally as any numerical solution would require experimental validation. The next section describes the experimental methods employed. A successful detonation diffuser initiates one or more secondary detonations that do not decouple when the final channel height is greater than the critical channel height.

III. Experimental Methodology

Overview

The experimental methods in this research fall under one of two headings: experimental techniques or data collection methods. Experimental techniques describe the equipment and procedures for initiating detonation and subjecting detonations to test articles. Data collection methods describe the apparatus and procedures that collect information from the detonation as it interacts with test articles. Chapter IV will discuss data reduction and uncertainty. The techniques and collection methods depend on each other and on the characteristics of a detonation wave. As a result, a combination of careful planning and mid-course adjustments ensured relevant, accurate measurements.

Experimental Techniques

Investigating detonation diffraction and shock initiation requires a source of repeatable detonations. The research PDE at the Detonation Engine Research Facility is one such source. Schauer et al. (2001) first published the details of the engine. Nielsen (2011) included a description of the configuration used for schlieren visualization of crossover geometries (Fig. 21). The PDE head and Tube 2 were kept and a new section consisting of a narrow channel with a large, instantaneous increase in channel height (Fig. 22) replaced Nielson's "test rig" and "manifold" sections. Hence, an expansion section was introduced in the upward direction, which is physically much like Fig. 4 except that the expansion is in the opposite direction.

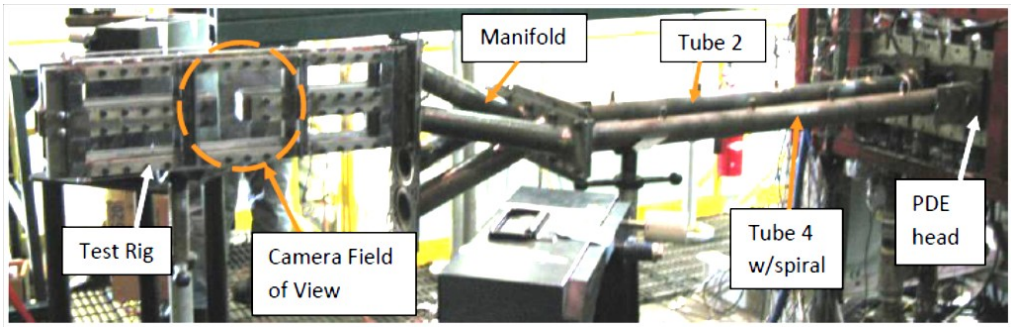

Figure 21. PDE as configured for crossover study (Nielsen et al., 2011)

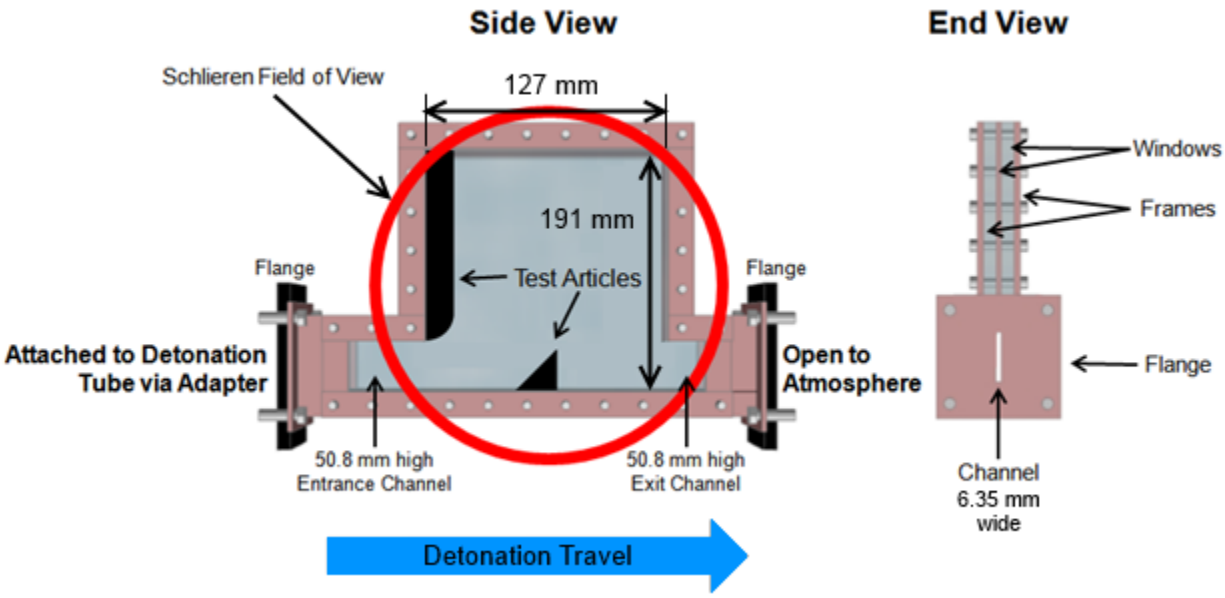

Figure 22. CAD model of optical test section

The PDE operates on a wide variety of gaseous and liquid fuels offering a wide range of cell sizes. The detonation frequency is adjustable from 8 Hz to 40 Hz, and the ignition can be set to operate in "burst mode" firing for a predetermined number of cycles. Adjusting the equivalence ratio of the mixture gives control of cell size for a specific fuel/air mixture (Ciccarelli et al., 2004).

The design of the research PDE presents some undesired effects. The detonation tube pressure at ignition is not explicitly controlled, and the dynamics of filling cause variations of pressure throughout the detonation tube (Helfrich, 2006). Applying an ignition delay of 4 ms

after the close of the fill valves mitigated the variations. The periodic fill process also contributes to local variations in equivalence ratio. Fuel flows into the airstream constantly as the air flow varies resulting in locally rich and lean conditions. Use of a second detonation tube 180° out of phase with the test section (Tube 4 in Fig. 21) halved the time that the fill valves were closed and reduced the variations so that they were less than 5%. With the mitigation of its undesired characteristics, the research PDE served as the source of reactants and detonations for all test cases.

After fill, ignition, and DDT, detonations passed into an optical test section containing the various test articles (Fig. 22). An adapter gradually transitioned from the circular detonation tube cross-section to the narrow channel in the test section. The channel was 6.35 mm wide (from window to window) or 77% of the 8.19 mm cell width for stoichiometric H2/Air at atmospheric pressure and temperature (Ciccarelli et al., 1994). The small width of the channel suppressed cellular structure in that dimension. The optical section begins with a section of subcritical, rectangular channel ($h/\lambda = 6.2$) and opens into a taller section containing the geometry under study (Fig. 22). A stoichiometric mixture of H2/Air was used in all test cases for a consistent ratio of initial channel height to cell size.

After the adapter, the channel size was constant for 127 mm allowing the wave speed to stabilize. The entrance channel height was 50.8 mm opening up to a maximum height of 191 mm. The test section had optical access for schlieren visualization via two polycarbonate windows. The windows were each 12.7 mm thick and tolerated the impulsive detonation loading without any evidence of fatigue after hundreds of detonations.

An unexpected phenomenon encountered early in testing was the propagation of strain waves through the polycarbonate windows. The strain caused a small change in the refraction of

light through the window. The resulting distortion of the light was on the order of the refraction caused by density gradients within the channel, and appeared as light and dark bands in the recorded images (Fig. 23). A strain gage, attached to an expended window, verified that the waves were due to the bending of the windows and not due to density gradients within the test section. Initially, a software filter attempted to remove the waves from the recorded images, but proved unable to discern the strain waves from flames. Reducing the sensitivity of the schlieren system reduced the visibility of the strain waves with acceptable results, and the affected cases were repeated.

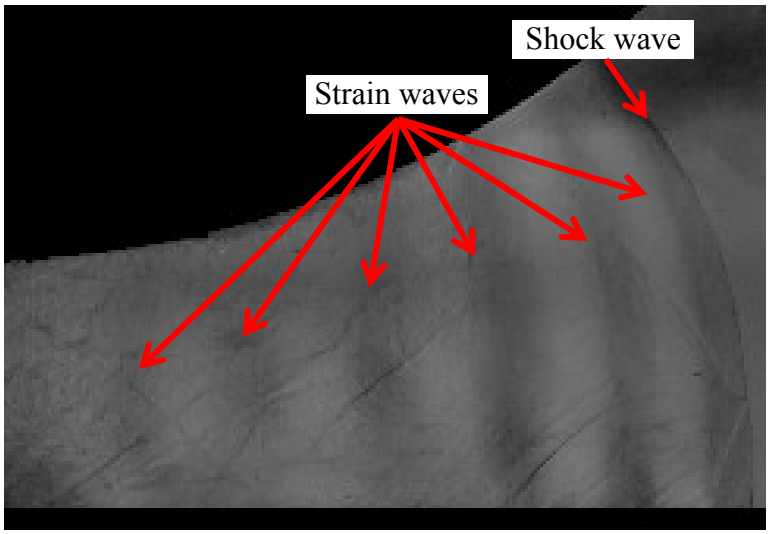

Figure 23. Visible strain waves

The test section survived the intense pressures and temperatures associated with detonation. Peak pressures in excess of 3 MPa and peak temperatures near 3000 K are typical of a detonation front (Zeldovich, 1956), but the maximum values are short lived, and 12.7 mm thick polycarbonate was an acceptable material for windows. Brittle surface coatings intended to improve scratch resistance were tried, but the strain on the windows caused the coating to fracture. Without a scratch-resistant coating, the windows regularly suffered abrasion from the

test articles. The heat from local explosions did burn away a small amount of the window surface after several cycles (Fig. 24), but the damage from abrasion was far more significant. The windows were replaced whenever the damage obscured the shock and flame within the channel.

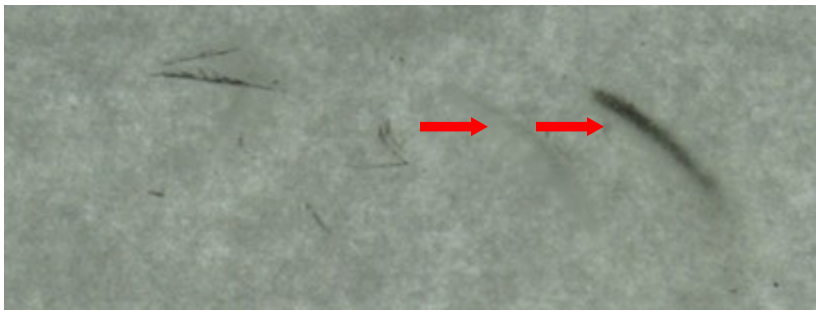

Figure 24. Scorch marks (red arrows) on a polycarbonate window.

The test section allowed for simple exchange of test articles. Quick changeover was important, as testing time is limited at the DERF. Two studs permitted the removal of one window at a time. The test article rested on the remaining window until secured. Safety wire secured the test article to the side of the test section until the bolts holding the windows were tight, preventing movement of the test article.

Data Collection Methods

Schlieren visualization was the preferred measurement technique for detailed study of diffraction and local explosions. Schlieren visualization depicts density gradients making both shock and combustion fronts visible (Fig. 25). A minimal schlieren visualization system is composed of a light source, two focusing mirrors, a knife-edge, and a screen on which to project the image. A camera usually replaces the screen to capture video of unsteady flows. Appendix A describes the system in full. Because of its ability to visualize both shock and combustion and to record at high frame rates, schlieren visualization saw extensive use throughout the diffuser development.

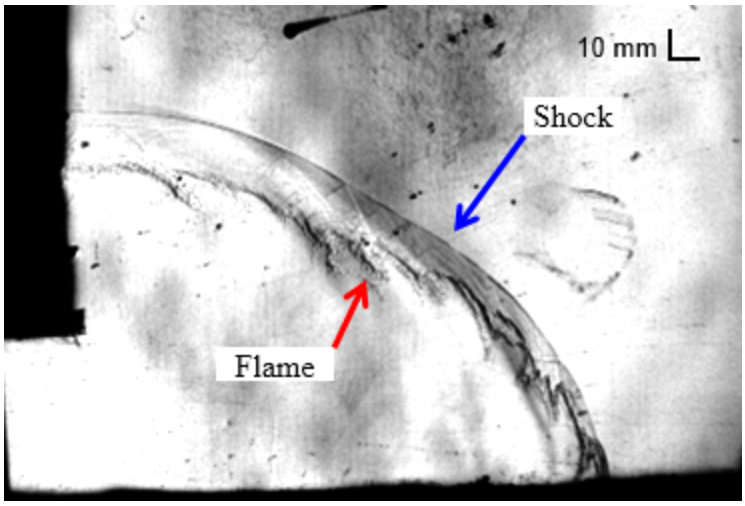

Figure 25. Schlieren image of decoupling detonation

The schlieren technique is analog, and only the camera limits frame rate and resolution. Cellular structure and wave speed dictate the resolution and frame rate requirements. The minimum resolution (measured in mm/pixel) necessary to image cellular structure is half the cell width per pixel according to the Nyquist-Shannon sampling theorem, and the maximum temporal resolution was 240,000 frames per second. All images had a spatial resolution of 0.650 mm/pixel. The temporal restriction relaxes for diffracting detonations, as it is unnecessary to capture the transverse wave collisions. Instead, the temporal resolution depends on the dimensions of the test article. Resolutions in this work ranged from 4.76 μs (210000 frame/s) to 25.0 μs (40000 frame/s) often with data from multiple frame rates combined into one data set. The exposure of each image was 293 ns, and the resulting motion blur at Chapman Jouguet speed (~1971 m/s) was 0.578 mm. The RMS uncertainty due to motion and spatial resolution was 0.871 mm.

Chemiluminescence is a verification tool for identifying combustion separately from other structures in the flow. A camera recorded images of the chemiluminescent emissions from chemical reactions for a crossover tube geometry in experiments carried out in prior research (Fig. 26) (Nielsen, 2011). Because the same camera was used to record the schlieren and

chemiluminescence images, the same resolution and uncertainty considerations apply to both. No equipment beyond a zoom lens, a high frame rate camera, and optical access to the detonation are needed, making setup faster than schlieren visualization. The weakness of chemiluminescence is its inability to detect non-emitting phenomena, and thus the decoupled shock that initiates a secondary detonation is invisible. Because it added no new information, chemiluminescence was only as a verification tool for flame from propagation and local explosion detection.

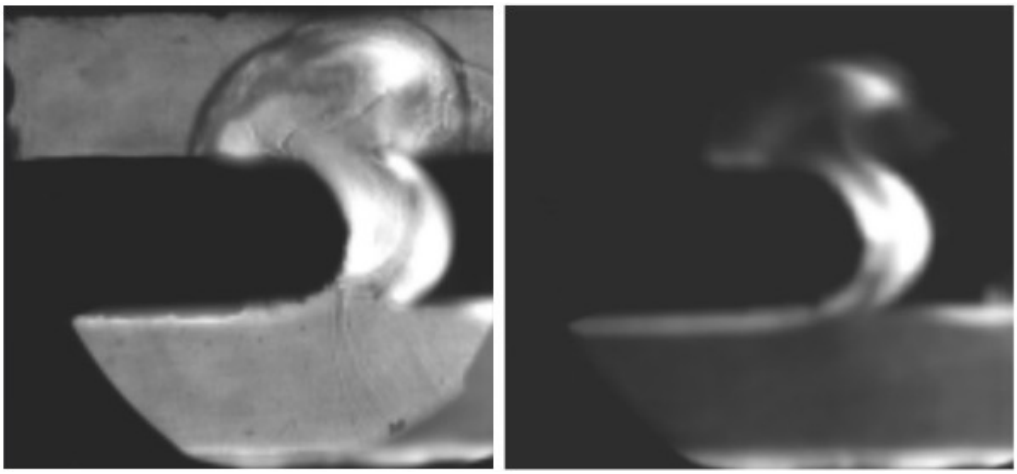

Figure 26. Schlieren (left) and Chemiluminescence (right) of decoupling detonation (Nielsen, 2011)

Ion probes are a simple solution for measuring wave speed when optical access is not available. Ion probes are essentially capacitors that close a circuit when combustion ions are present. Wave speed is computed as linearly proportional to the time of flight between two probes. Two pairs of probes measured wave speed upstream of the optical section to verify detonation prior to entering the optical test section. Low difference between the wave speeds at each location confirmed that the detonation was propagating at the CJ speed. The uncertainty in wave speed measured by ion probes is a function of the distance between the probes, the sampling frequency, and interpretation of the capacitor-like waveform. The sample rate for ion

probes in this work was a constant 1 MHz, and the distance between adjacent ion probes was always 150 mm. The uncertainty in distance between the probes was 0.8 mm, the uncertainty in time is 0.5 μs, and the uncertainty in the waveform was 12.8 m/s. The total uncertainty in wave-speed was 30.0 m/s.

Calibration

Shock speed and shock-combustion separation distance derive from the position of the shock and flames in each image. To measure the position of these structures, image calibration was necessary. The position was a function of the optical magnification, pixel size, and distance from the camera to the test section. To bypass deconvolving the effects of all three variables, pixel positions were calibrated using the initial channel height. The initial channel was always visible, and it had a known height of 50.8 mm. The calibrated size and center-to-center distance of the square pixels averaged 0.647 mm (Fig. 27), and the uncertainty in position across all cases was 0.324 mm.

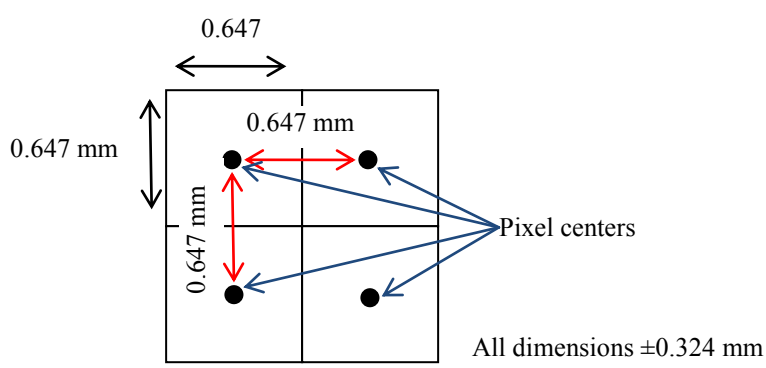

Figure 27. Calibrated pixel dimensions

Test Cases

This research set out to accomplish three phases of study. The first phase will quantify the shock Mach number and separation distance after a detonation encounters a diffraction corner (D-series). The second will determine the reflecting surface angle and position that offer

the best chance of reinitiation (R-series). The third phase will investigate multiple obstacle geometries to narrow the field of possible configurations (M-series). The test cases mirror the phases of the research.

There were three sets of test cases (diffraction "D", reflection "R", and multiple obstacles "M") as well as a single control case. This section contains dimensioned drawings of each. The control case was a straight channel the same height as the entrance of the test section (50.8 mm) and 300 mm in length (Fig. 28).

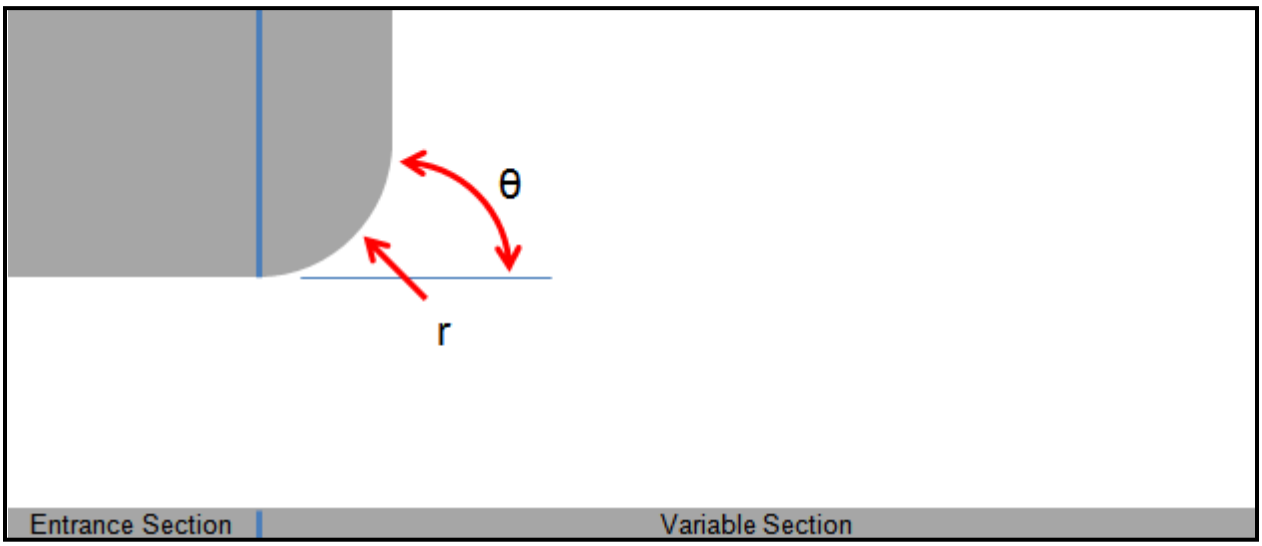

Figure 28. Parameters of the diffraction test cases.

Because each case included a unique, handmade test article, the test matrix was kept coarse while still bounding the limits of decoupling or reinitiation, except in the multiple obstacle cases. Those latter tests included a series of incremental changes intended to approach successful transition to a super-critical channel.

In the diffraction cases, two parameters were examined: diffraction angle (θ) and corner radius (r) (Fig. 28). Table 1 lists the four configurations tested. Case D1 was a control with no diffraction. Data from the control established the CJ speed for the remaining cases. Cases D2

and D3 compared diffraction angles while keeping corner radius constant. Decoupling was expected and occurred in Case D2, but in Case D3 the diffraction angle was 0.5° greater than the theoretical limit proposed by Nettleton (1983). The presence of transverse shockwaves not included in the Nettleton's analysis made it unclear if decoupling would occur. The result was partial decoupling which will be discussed in Chapter IV. Cases D2 and D4 varied the diffraction corner radius while keeping the angle constant. In Case D2, the radius was small enough for the expansion to be considered instantaneous. In Case D4, the radius was the same as in the Nielsen et al. (2011) crossover study. The configuration in Case D2 was selected for use in the next test series investigating the shock-reflecting surface because the instantaneous expansion required the least downstream distance to implement and will be shown to have the largest separation between decoupled shock and flame fronts believed to be important to prevent trapping secondary detonations between the reflecting surface and the flame front.

Table 1. Diffraction cases

Case #	Diffraction angle (°)	Corner radius (mm)
D1	0	∞
D2	90	2.0
D3	15	2.0
D4	90	25.4

A second set of eight test cases examined the limits of detonation reinitiation caused by oblique shock reflection. The parameters of the set were primarily reflection angle (β), downstream distance from the diffraction corner (x_0) and vertical distance from the diffraction corner (y_0) (Fig. 29). Case R5 revisited diffraction corner radius (r) to rule out any effect on reinitiation not inferable from the diffraction cases. Table 2 lists the configurations tested.

Cases R1 and R2 bounded the downstream limit for placement of a reflecting surface. Cases R2, R3, and R4 found a minimum limit for the reflecting surface angle. Cases R3 and R5 looked for any relationship between diffraction corner radius and reinitiation. Cases R6, R7, and R8 bounded two limits on reinitiation for a reflecting surface offset 50.8 mm vertically from diffraction corner. The reflection cases did not include investigation of the diffraction of secondary detonations that form due to shock reflection.

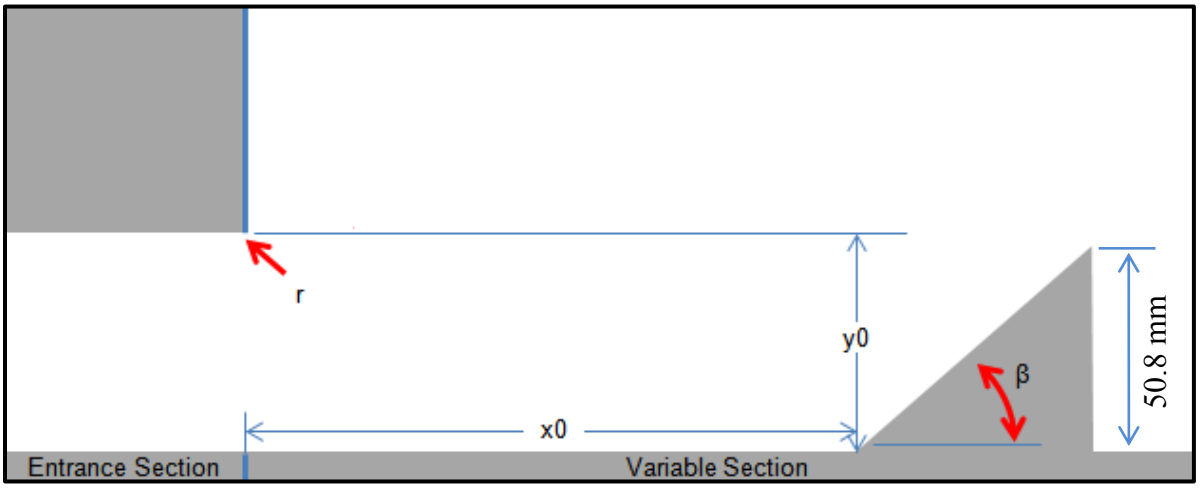

Figure 29. Reflection case parameters

Table 2. Reflection cases

Case	r (mm)	β (°)	x0 (mm)	y0 (mm)
R1	2.0	45	162.2	-50.8
R2	2.0	45	84.7	-50.8
R3	2.0	30	80.1	-50.8
R4	2.0	15	0.0	-50.8
R5	25.4	30	80.1	-50.8
R6	2.0	-45	0	50.8
R7	2.0	-45	43.0	50.8
R8	2.0	-45	169.3	50.8

A third set of 11 cases used the information on angle and position to investigate configurations for a detonation diffuser. The third set of cases followed an iterative path starting from Case R2 with each step improving the chances of reinitiation and reducing the chance of

decoupling. Table 3 lists the configurations and their design parameters. The first diffraction angle and corner radius were constant for all cases at 90° and 2.0 mm respectively. Case M1 began by attempting to reduce or eliminate decoupling after a secondary detonation formed by reducing the height of the obstacle (h) and increasing the radius of the secondary diffraction corner (r_2). As the tests cases progressed, others design variables were included such as the number of reflecting surfaces, their position, and the number steps in the initial diffraction. In Table 3, the design parameters are highlighted when they change to emphasize the design choices.

Table 3. Multi-obstacle test cases

Case	Obstacle Height (mm)	r_2 (mm)	Obstacle Count	Final Channel Height (mm)	Top or Bottom	Diffraction Steps	Number of Trials
R2	50.8	0.3	1	241	Bottom	1	
M1	12.7	6.4	1	241	Bottom	1	4
M2	6.21	0.3	14	241	Bottom	1	22
M3	5.43	3.2	14	241	Bottom	1	7
M4	6.21	0.3	14	102	Bottom	1	8
M5	5.43 (top) / 6.21 (bottom)	3.2 / 0.3	28	102	Both	1	16
M6	5.43	3.2	28	102	Both	1	7
M7	6.35	0.3	12	102	Top	8	10
M8	6.35	0.3	12	102	Bottom	8	5
M9	6.15	0.3	5	241	Both	3	9
M10	6.15	0.3	4	241	Both	3	5
M11	N/A	0.3	4	241	N/A	1	8

Due to the number of variables considered in the M-series cases and the iterative development of each, it is useful to describe the cases in turn. Case M1 (Fig. 30) reduced the height of the obstacle (h_1) in Case R2 from 50.8 mm to 12.7 mm to verify that a smaller obstacle also reinitiates detonation, and increased the diffraction corner radius (r_2) at the end of the reflecting surface.

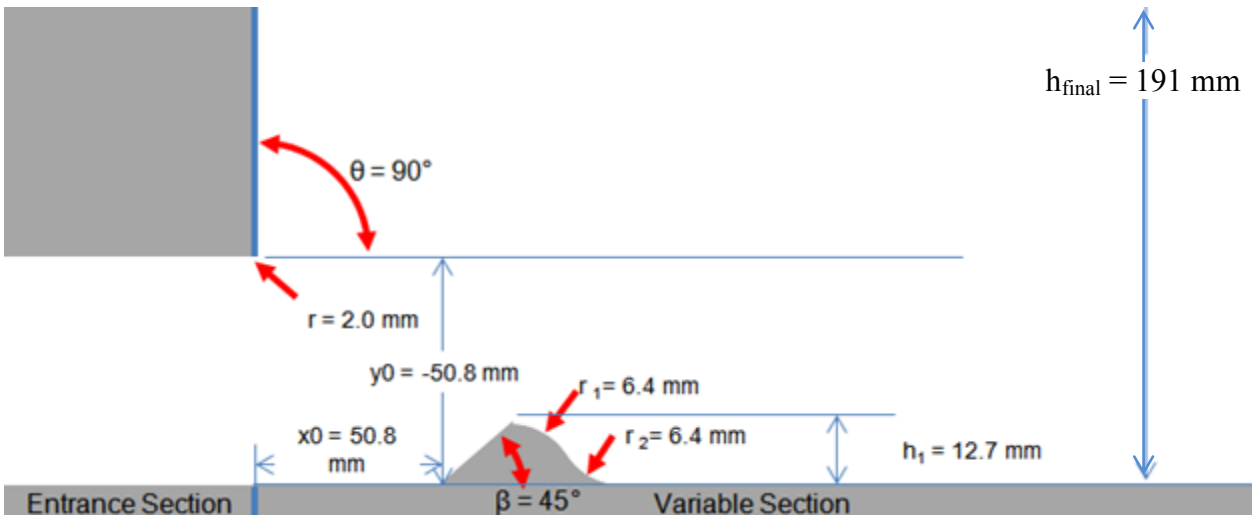

Figure 30. Case M1

The decision to change two design variables in parallel would seem to prevent independent analysis of each variable, however; the diffraction corner radius had no bearing on the chances for reinitiation since the leading shock encountered it after the reflecting surface. Decoupling of the secondary detonation was only applicable once reinitiation occurred, and the only prerequisite for comparing secondary diffraction corners was a coupled detonation front. As a result, the secondary diffractions are comparable between cases where the obstacle height differed. After successful reinitiation in Case M1, the secondary detonation decoupled both at the secondary diffraction corner and in the region above the obstacle. Case M2 continued to reduce the height of the obstacle, and included more obstacles in an attempt to increase the chances of a secondary detonation surviving (Fig. 31).

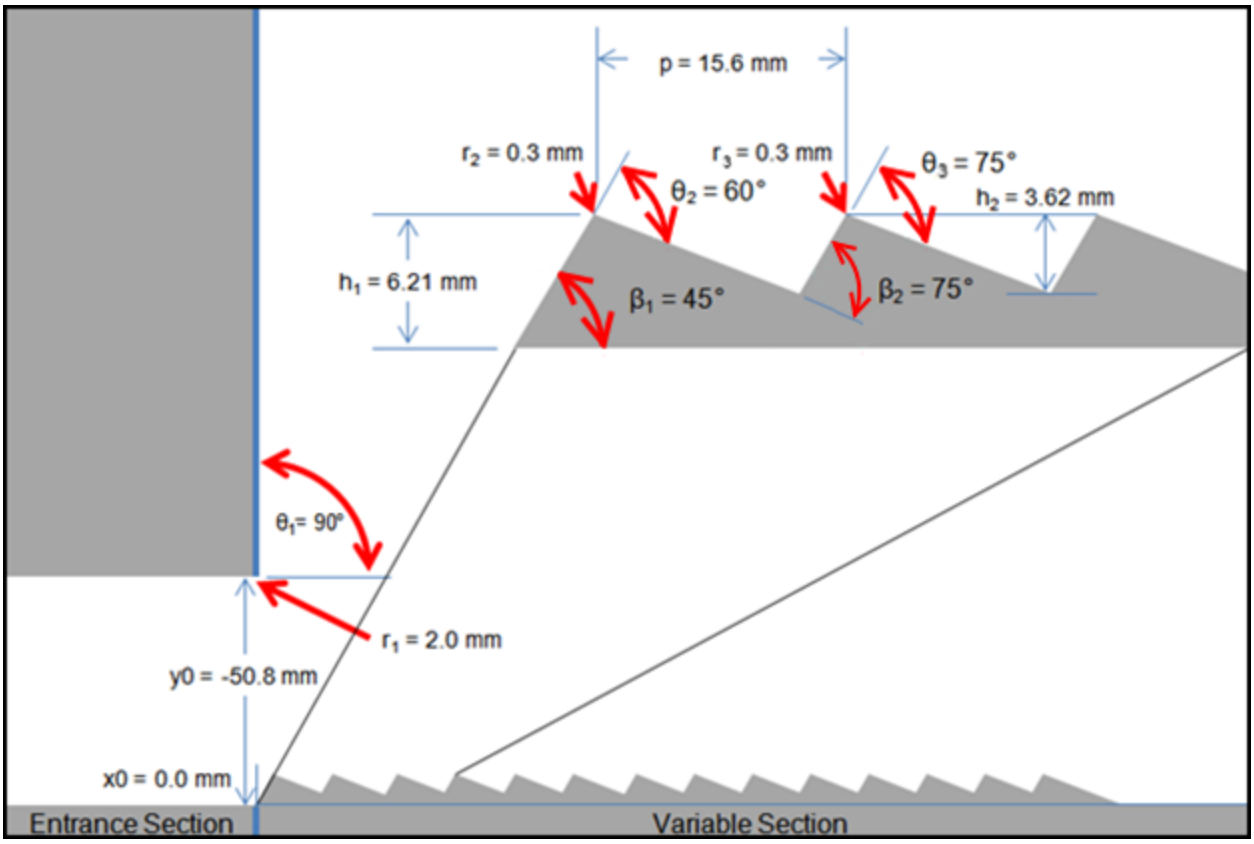

Figure 31. Case M2

There were 14 separate reflecting surfaces in Case M2. This configuration was expected to cause a reinitiation event at every reflection surface. Then the secondary detonations would each partially decouple before the next reinitiation. Each detonation then followed a series of decoupled shocks as they traversed the lead shock front. Once a sufficient number of transverse shocks were present, their combined compression would allow a secondary detonation to propagate completely across the lead shock front completing the transition from subcritical to supercritical channel height.

In testing, reinitiation occurred for an average of 11 obstacles before the lead shock lost too much strength. The compression of the shocks resulting from the preceding secondary detonations was insufficient for the last one to remain coupled, and detonation did not propagate

downstream. To mitigate some of the decay of the secondary detonations the tops of the obstacles were rounded to increase the secondary diffraction radii in case M3.

For M3, increasing the secondary diffraction corner radii from 0.3 mm to 3.2 mm increased the mean number of reinitiations from 10 to 11. While the r_2 change was a move in the right direction, it was far from enough improvement for detonation to survive. Because the lead shock reached the end of the obstacles before the first transverse shock reached the top of the channel, the author hypothesized that reducing the channel height (M4) would allow the later transverse shocks to interact with the reflections of the preceding shocks before the end of the test section. Further, reducing the final channel height (M4) decreased the decay of the transverse shocks since the shocks traversed the lead shock in less time. It was hypothesized that the shock collisions and reduced traverse time would cause local explosions along the top of the channel, and that the secondary detonations from the top and bottom of the channel would merge into a single, fully coupled detonation front. Testing in Case M4 did not confirm the hypothesis because no local explosions were observed at the top of the channel likely because the shock decay was still sufficient to reduce the probability of reinitiation to zero. Another iteration was necessary and Case M5 added obstacles to the top of the channel.

For M5, because obstacles reliably reinitiated detonation from a decoupled shock at the bottom of the channel when the first obstacle was 85 mm downstream of the diffraction corner, it was reasonable to assume the same was true of the top of the channel when the first obstacle was closer to the diffraction corner. A new set of obstacles identical to that of case M3 were placed at the top of the channel without changing the final channel height from M4 (Fig. 32). This configuration was the first multi-obstacle configuration to exhibit shock initiated combustion along the top of the channel.

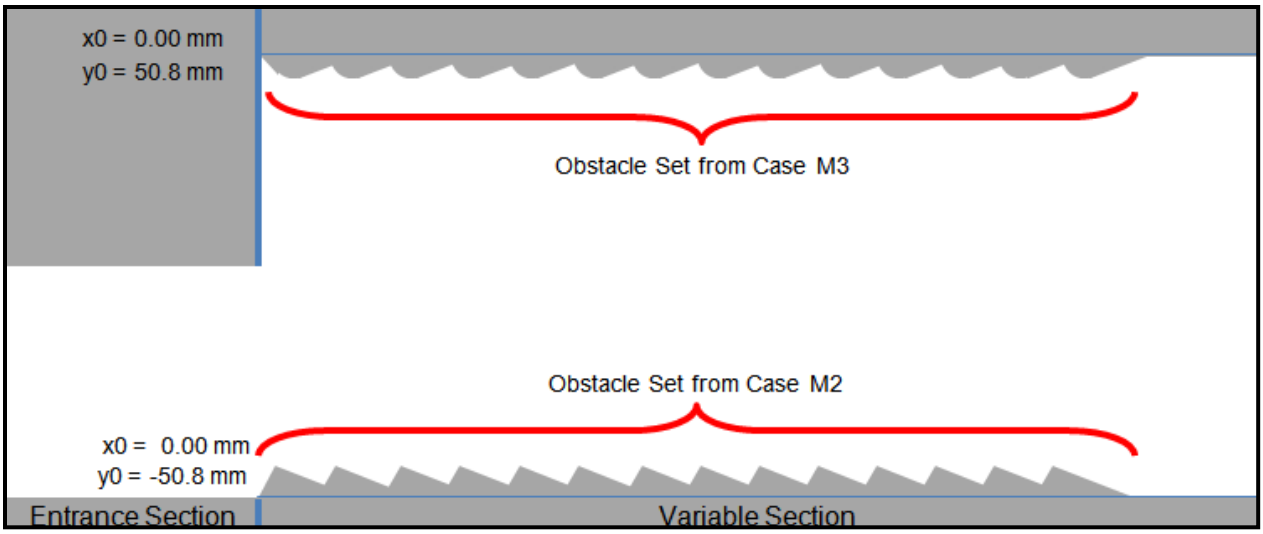

Figure 32. Case M5

In one of the eight repeat trials of the M5 configuration, the 11th obstacle reinitiated a detonation that failed to reach the end of the test section. The results in Case M5 were promising, and it seemed reasonable to round the diffraction corners of the obstacles at the bottom of the channel again for Case M6.

As in Case M3, increasing the diffraction radii did not cause enough improvement for successful fully coupled detonation at the end of the test section. One of the 16 repeat trials for M6 resulted in a secondary detonation at the top of the channel. Unlike in case M5, the detonation remained partially coupled through the end of the test section. At this point, it seemed unlikely that obstacles set so far vertically from the initial diffraction corner would be sufficient to reinitiate detonation by the end of the test section. Case M7 began to modify the diffraction corner by dividing the change in channel height into eight discrete segments (Fig. 33).

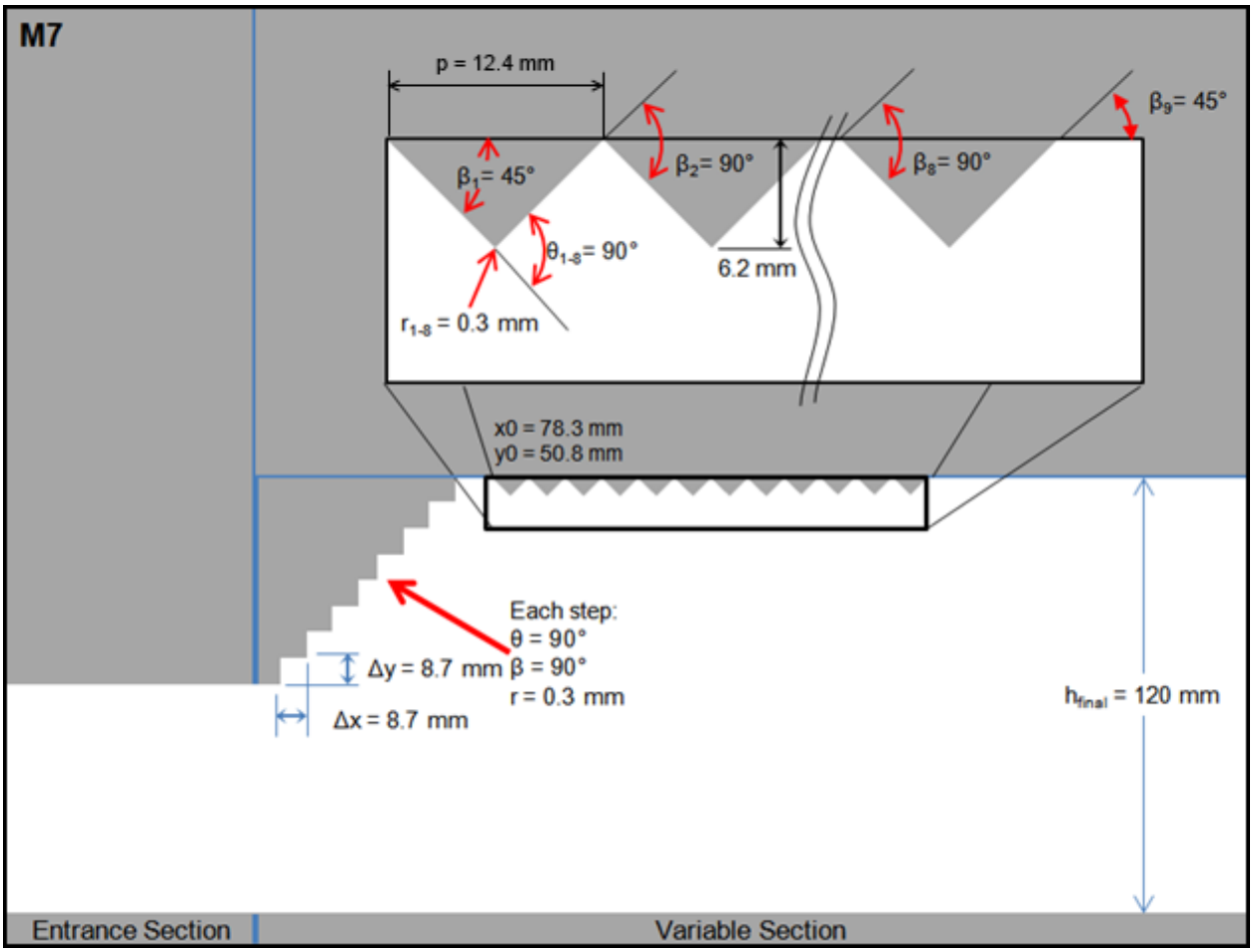

Figure 33. Case M7

For M7, the eight steps in the diffraction were each 8.7 mm in height, slightly larger than the 8.19 mm cell size of stoichiometric hydrogen/air at 1 atm initial pressure (Ciccarelli, 1994). Setting the step height equal to the cell width allowed an average of one triple point to interact at each step. The reflected triple points were expected to maintain detonation unlike in previous cases. A new set of 12 obstacles followed the diffraction steps along the top of the channel. The obstacles had a shorter pitch of 12.4 mm to increase the rate of diffraction and reinitiation. In testing, the primary detonation decoupled after the first diffraction step and shock reflections from the obstacles failed to reinitiate detonation. Since the obstacles were unable to reinitiate detonation at the top of the channel, they were moved to the bottom of the channel in Case M8 where it was known that reinitiation would occur.

The obstacles reinitiate detonation in Case M8; however, the secondary detonations again decoupled before reaching the top of the channel. The decoupling along the diffraction steps contradicted the hypothesis that the short, cell-sized steps would partially mitigate decoupling of the primary detonation front. Instead of mitigating the decoupling, it was reasoned that a new diffraction wall (Fig. 34) could be redesigned to reflect the decoupled lead shock twice for each diffraction corner as shown by the outline in Figure 30. Case M9 implemented a double reflection both on the diffraction wall and on the bottom of the channel (Fig. 35).

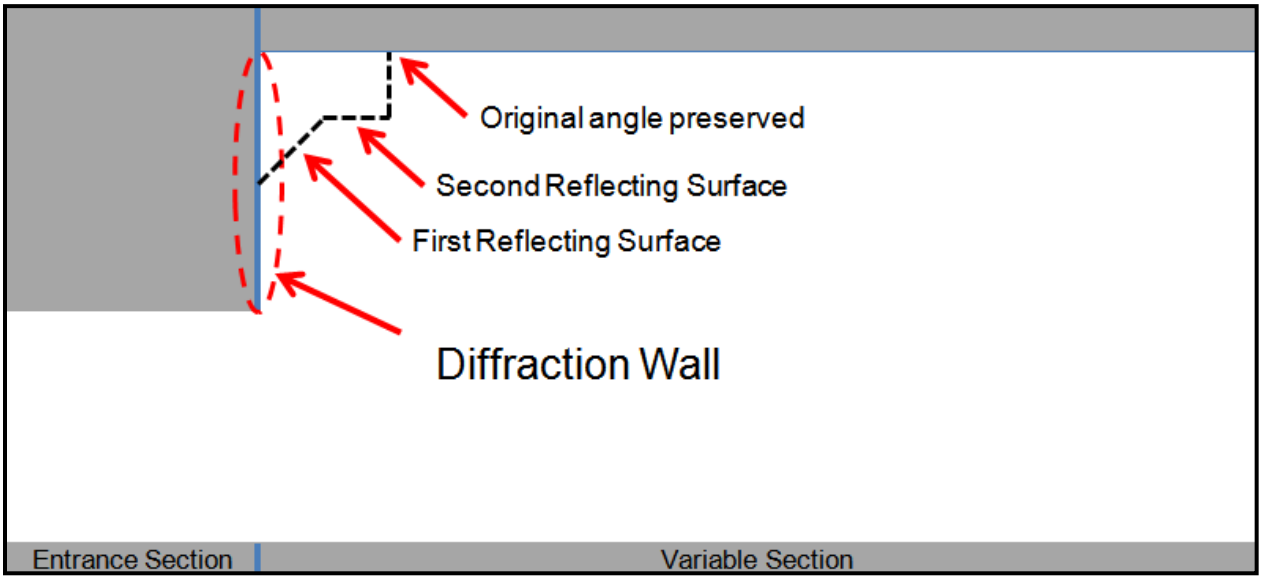

Figure 34. Diffraction wall location

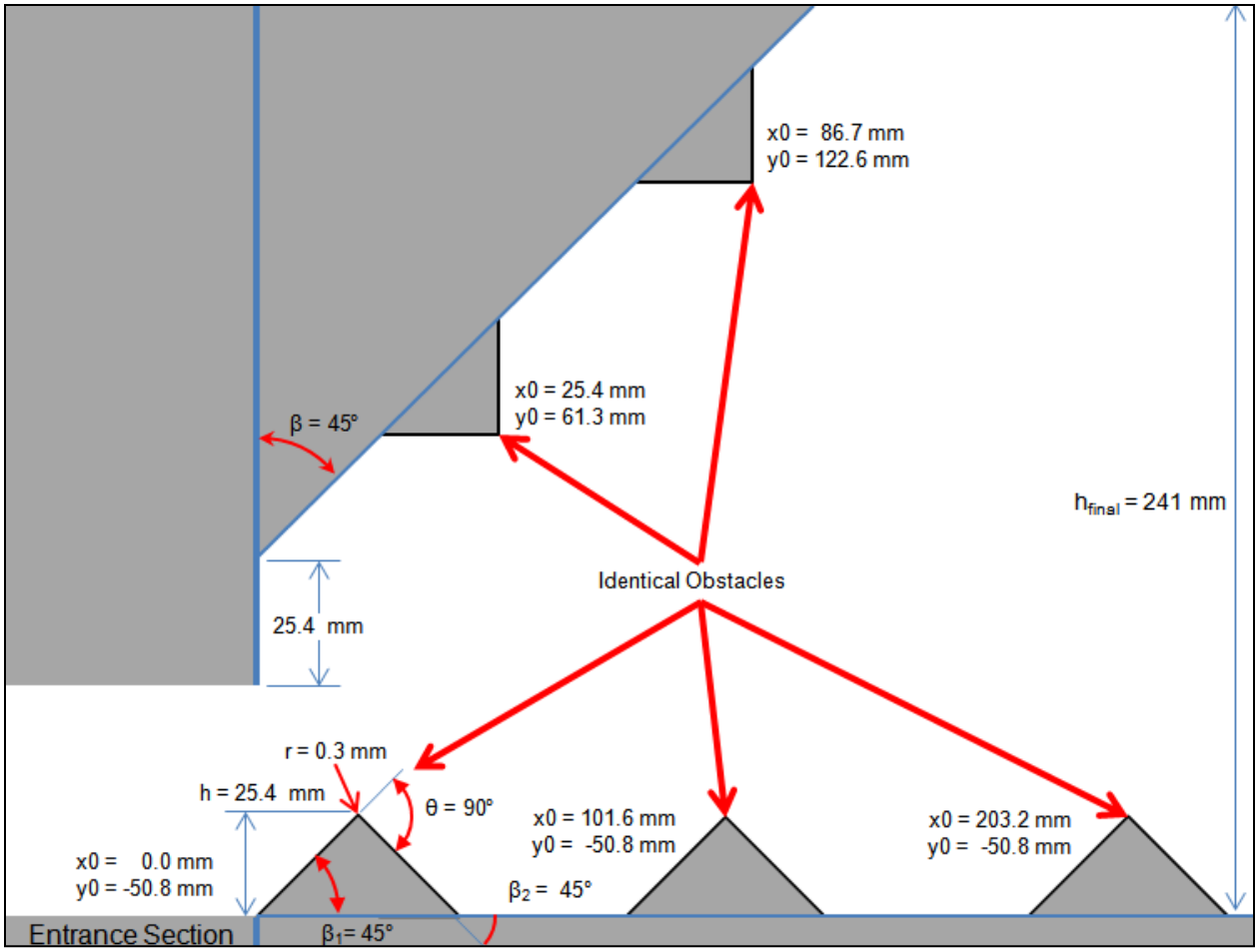

Figure 35. Case M9

Early in the testing of Case M9, it became apparent that the first obstacle on the bottom of the channel was restricting the flow of reactants in to the test section. As a result, the initial detonation decoupled before reaching the test section. To reduce the restriction, the first obstacle on the bottom of the channel was removed for Case M10. Removing the obstacle reduced the restriction enough that the initial detonation no longer decoupled before the test section.

In testing M10 detonation reinitiation occurred at the first bottom obstacle in each of five repeat trials, but nowhere else. There was some infrequent shock ignition along the upper obstacles. At this point lining the upper and lower walls of the channel with obstacles had failed to do more than reinitiate one secondary detonation at a time none of which were sufficiently strong to complete a transition to detonation in the final channel. The next logical step was to

reinitiate several detonations at roughly the same time and then let them merge into a single detonation front.

In Case M11 (Fig. 36), four obstacles were attached to the windows of the test section so that the channel split into five channels. The obstacles were arranged using the shock Mach number map from case D2 so that reinitiation would occur on one wall of each of the five channels. Then the secondary detonations would travel down the five channels expanding gradually before emerging at the same time to merge into a single detonation front.

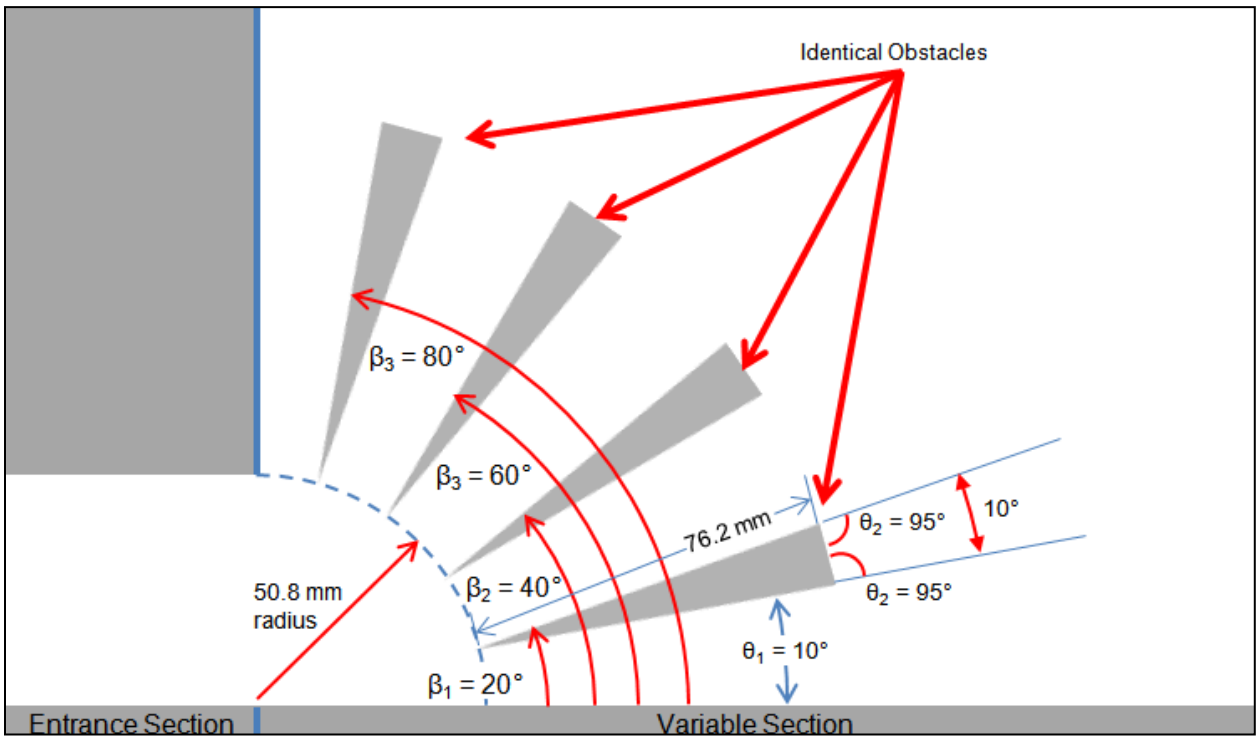

Figure 36. Case M11

This arrangement resulted in the first local explosions to occur as the result of collisions of two diffracting shockwaves (see Fig. 78). The behavior appears identical to that of detonations diffracting after emerging from critical channels (Soloukhin and Ragland, 1965). The M11 configuration bridged the gap between the subcritical and critical cases of detonation diffraction.

In Chapter III, the experimental hardware was discussed at some length. The focus was on the methods for obtaining a repeatable experiment and providing complete descriptions of the test cases and the reasoning behind the design choices in each case. In Chapter IV the focus shifts to the collection and analysis of data collected. The image analysis, data reduction, and uncertainty calculations give quantitative meaning to the results presented in Chapter V.

IV. Analysis Methodology

Overview

Schlieren images of shocks and flames were used to construct a clear picture of the diffraction and reinitiation processes. Tedious hand selection of points along the shock and flame fronts gave a basis for analysis of the motion of those structures. The distance between the flame and shock were derived from a forward, closest-point measurement (see Fig. 9) from the flame to the shock. The velocity of the shock front was derived from an interpolation of the shock position in two adjacent frames. These two measurements were sufficient to construct accurate interpolation functions that enabled the prediction of reinitiation.

Shock and Flame Position

The first step in the analysis was hand selection of the shock and flame position. Shocks were identifiable by a thin, smooth wave front at a position ahead of any flames (Fig. 37).

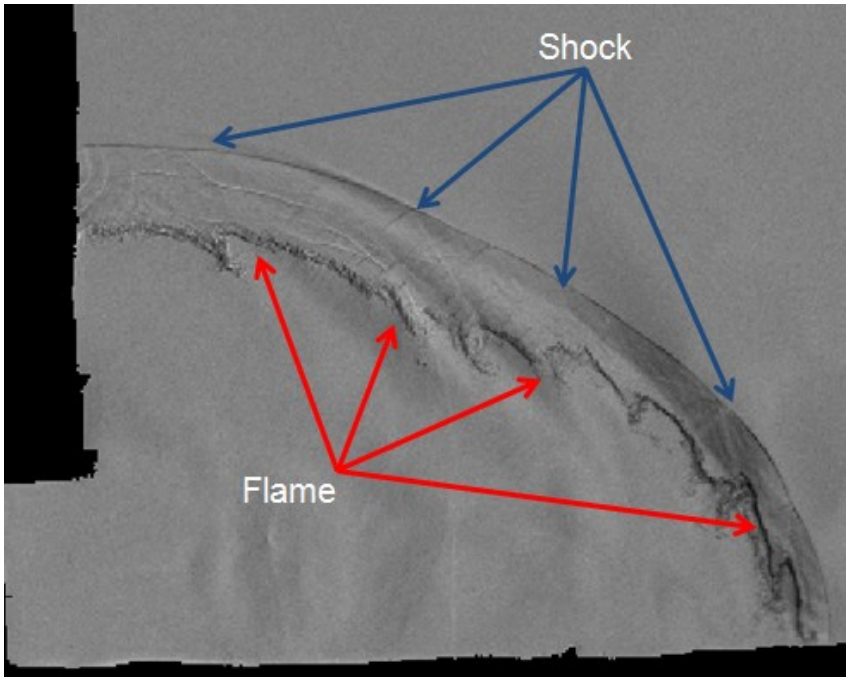

Figure 37. Shock and flame fronts

Flames were much thicker than shocks and usually included protrusions resulting from local variations in flame speed. Efforts to automate the identification of shocks and flames in the schlieren images were thwarted by the presence of reflected shocks, detonation fronts and multiple flame fronts, and the author resorted to hand processing of the schlieren images. An author-built software tool, included in Appendix C greatly aided the process. The tool loaded the desired frame from a video and modified it for display. The modification process subtracts a background image of window defects, adjusts the contrast, and shades the visible walls and obstacles blue. The tool then displays the modified frame (Fig. 38) and prompts the user to select the first point on either a shock or flame. Before making a selection, the user has the option to change the magnification and position of the window in relation to the image for ease of visibility.

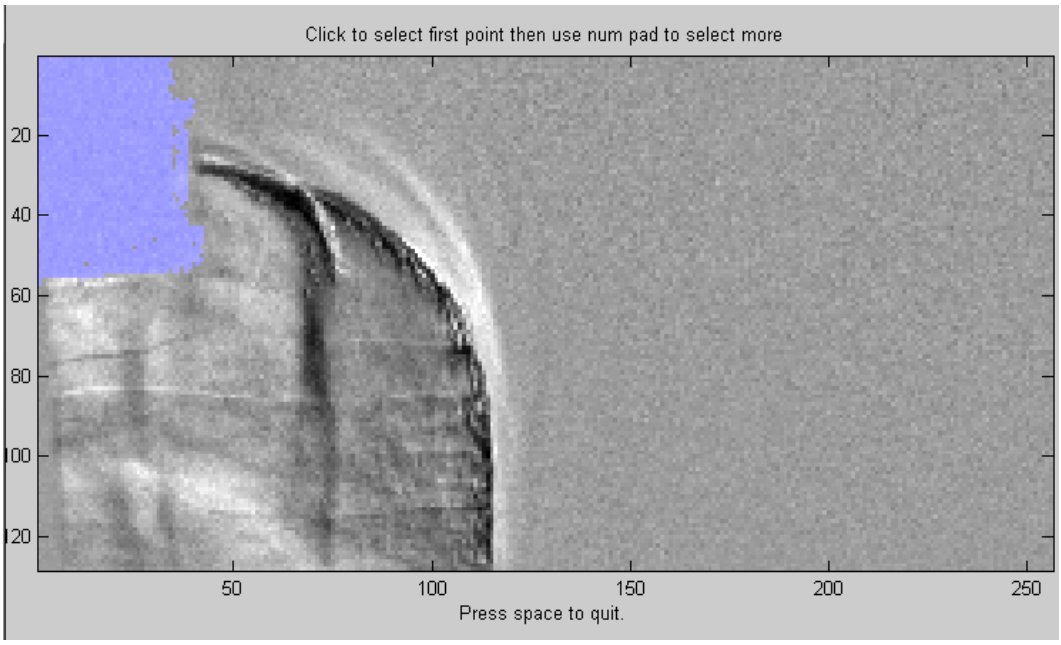

Figure 38. Initial state of software tool interface showing diffraction corner and enhanced image

Once satisfied with the window size and position, the user selects the first pixel on one end of the shock or flame. The software colors that pixel red (Fig. 39). Then, it records the coordinates, and changes the input mode from mouse to keypad.

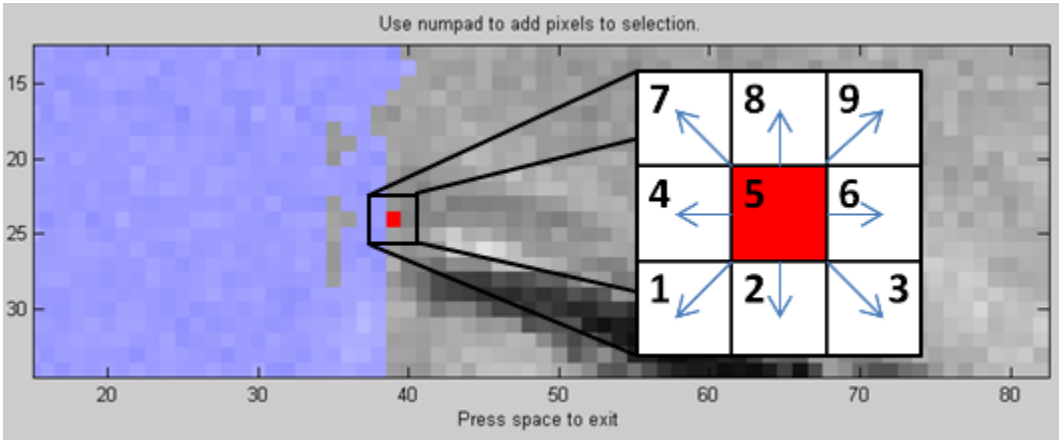

Figure 39. First point on shock selected, ready to select adjacent pixel.

In keypad mode, pressing a key adds the coordinates of the adjacent pixel in that direction to the list of coordinates describing the shock or flame. Pressing "4" adds the pixel directly to the left and pressing "6" adds the pixel to the right.

Pixel selection continues as the user selects the next pixel along the structure. With each selection, the software marks the new pixel, updates the list of coordinates, and, when necessary, re-centers the view. Mistakes due to typos (Fig. 40) were corrected via an undo feature that rewinds the selection one pixel at a time by pressing the 5 key.

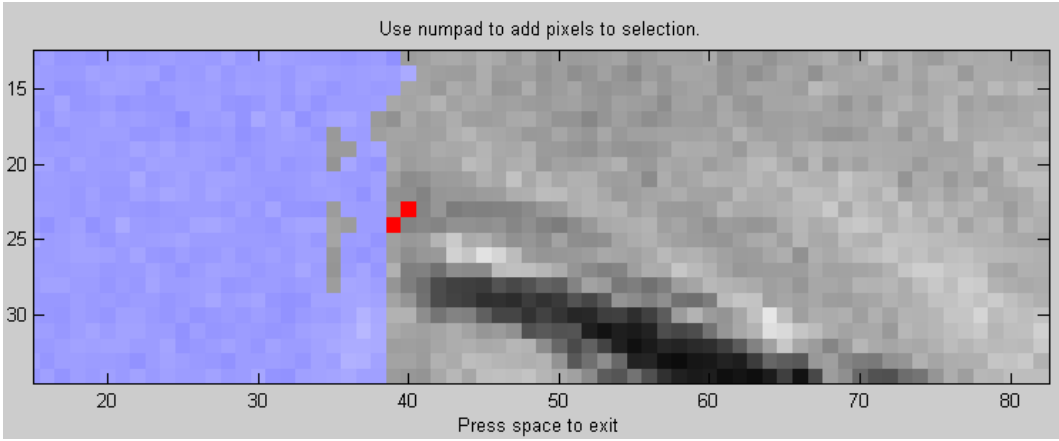

Figure 40. Mistakenly pressing 9 instead of 6 results in this state.

The result is a path of red pixels on screen and an ordered list of the coordinates of the pixels (Fig 41). When the user completes the selection, the software returns the list of coordinates and exits. Flames were handled in the same manner, by following the leading edge of the combustion front including any protrusions and recesses. Runtime per frame is around 2 minutes, and the 2002 frames processed in this manner yielded about 509,000 coordinate pairs. The tool took about 10 hours to code, and the total time to hand process the shock and flame positions was approximately 180 man-hours.

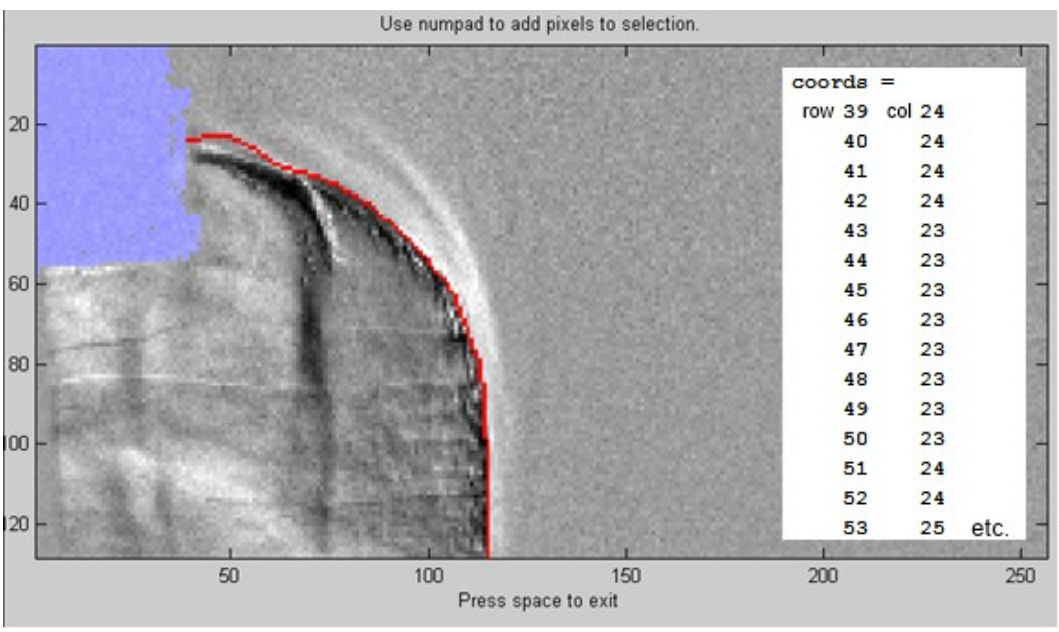

Figure 41. Completed selection of the shock front and the first fifteen coordinate pairs

Separation Distance

A forward, closest-point method calculated the separation distance for each point on the flame front. The algorithm first applied a calibration (Eq. 4) to the shock and flame pixel coordinates to convert from pixels to millimeters.

$$x_{mm} = \frac{h_{initial,\ mm}}{h_{initial,\ pix}} x_{pix} \tag{4}$$

The algorithm then calculated the distance from each point on the flame to all of the points on the shock using Eq. 5.

$$distance = \sqrt{\Delta x^2 + \Delta y^2} \tag{5}$$

The algorithm then assumes that the minimum distance best represents the separation distance at that location on the flame (Fig. 42).

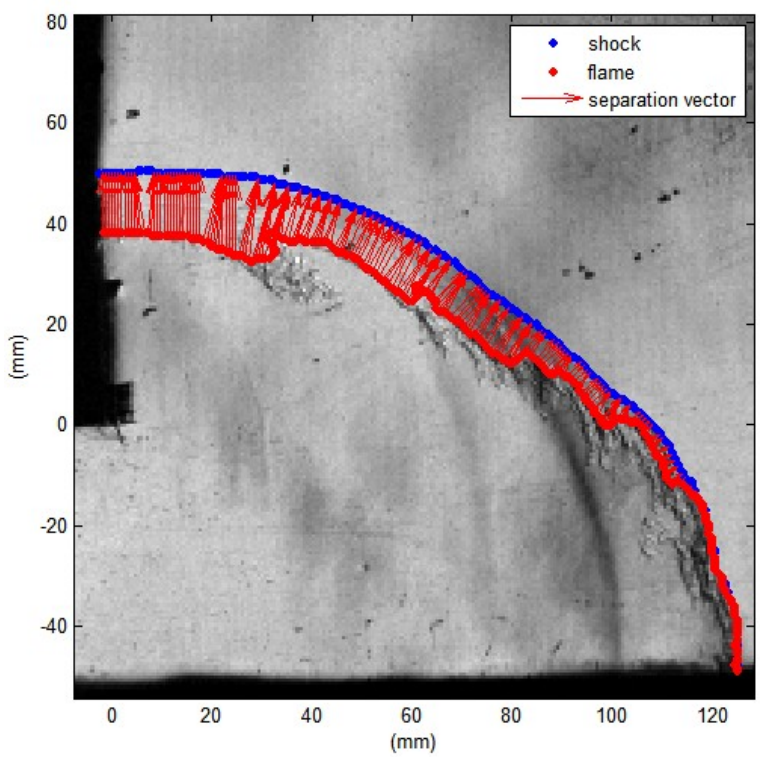

Figure 42. Separation distance vectors

The bias uncertainty in Δx and Δy is half the pixel width (0.324 mm) and the bias uncertainty in distance is given in Eq. 6.

$$B_{distance} = \left(\left(B_{\Delta x} \cdot \Delta x/\sqrt{\Delta x^2 + \Delta y^2}\right)^2 + \left(B_{\Delta y} \cdot \Delta y/\sqrt{\Delta x^2 + \Delta y^2}\right)^2\right)^{1/2} \quad (6)$$

for a sample where Δx = 3 pix and Δy = 4 pix, the separation distance is 5.00 ± 0.324 mm.

Shock Mach Number

The post-shock flow field (pressure, temperature, density, and velocity) depends solely on the Mach number at which the wave travels. Mach number was calculated from the temperature of the reactants, the equivalence ratio, stoichiometry, and the frame-to-frame shock displacement as shown below. The post-shock conditions were calculated from the shock jump equations (Anderson, 1982).

The sole mixture used in experiments was stoichiometric hydrogen and air. At stoichiometric conditions, the equivalence ratio (ϕ) is unity. For each mole of hydrogen combusted, the equivalence ratio dictates the number of moles of oxygen and nitrogen present (Eq. 7) (Turns, 2000).

$$N_{O2} = (x + y/4)/\phi \quad (7)$$

where x is the number of carbon atoms (0) and y is the number of hydrogen atoms (2) per molecule of fuel. The number of moles of nitrogen is determined by the natural ratio of nitrogen to oxygen in air (Eq. 8).

$$N_{N2} = 3.76 * N_{O2} \quad (8)$$

The mole fractions of the various reactants are equal to the number of moles of that species divided by the total number of moles (Eq. 9).

$$\chi_i = N_i/\sum_i N_i \quad (9)$$

The bias uncertainties in the N_i and χ_i were calculated using Eq. 10 (Coleman and Steele, 1989).

$$B_N = \left(\sum_{m=1}^{n}\left(B_m \frac{\partial N}{\partial x_m}\right)^2\right)^{1/2} \tag{10}$$

Table 4 gives values for N_i and χ_i and their respective uncertainties.

Table 4. Stoichiometry variable sample values

Variable	value	uncertainty
N_{H2}	1.0	0 (exact)
ϕ	1.000	0.001
N_{O2}	0.5	0.001
N_{N2}	1.88	0.00188
ΣN_i	3.38	0.00195
χ_{H2}	0.2959	1.604E-4
χ_{O2}	0.1479	1.539E-4
χ_{N2}	0.5562	5.788E-4

The specific heat at constant pressure of the mixture is a function of the mole fractions and the specific heats of the component species (Eq. 11).

$$C_{p,mix} = \sum_i C_{p,i}\chi_i \tag{11}$$

The specific gas constant for the mixture is a function of the universal gas constant, the mole fractions, and the molecular weights of the components (Eq. 12).

$$R = R_u / \sum_i MW_i \cdot \chi_i \tag{12}$$

The ratio of specific heats is a function of C_p and R (Eq. 13)

$$\gamma = C_p / \left(C_p - R\right) \tag{13}$$

The speed of sound in the test section (a) is a function of the ratio of specific heats (γ), temperature (T), and the mixture specific gas constant (R) (Eq. 14). The speed of sound was constant throughout the test cases. Table 5 gives the values and uncertainties for C_p, R, γ, and a in addition to the MW_i and $C_{p,i}$ values used in Eqs. 11 and 12.

$$a = \sqrt{\gamma \cdot R \cdot T} \tag{14}$$

Table 5. Sample Mach number and constituent values

Variable	Value	Bias Uncertainty	Units
$C_{p,H2}$	28.877	0.001	kJ/kmol-K
$C_{p,O2}$	29.331	0.001	kJ/kmol-K
$C_{p,N2}$	29.075	0.001	kJ/kmol-K
MW_{H2}	2.016	0.001	g/mol
MW_{O2}	31.999	0.001	g/mol
MW_{N2}	28.013	0.001	g/mol
Cp	1.3811	0.0156	kJ/kg-K
R	0.3976	0.00357	kJ/kg-K
γ	1.4043	0.0384	-
a	**409.3**	**0.144**	**m/s**

The Mach number of the shock was found by dividing the distance traveled between frames by the time interval and the speed of sound (Eq. 15).

$$M = \sqrt{\Delta x^2 + \Delta y^2}/(\Delta t \cdot a) \tag{15}$$

The distance traveled by the shock was found using the central finite difference method described in Figure 43.

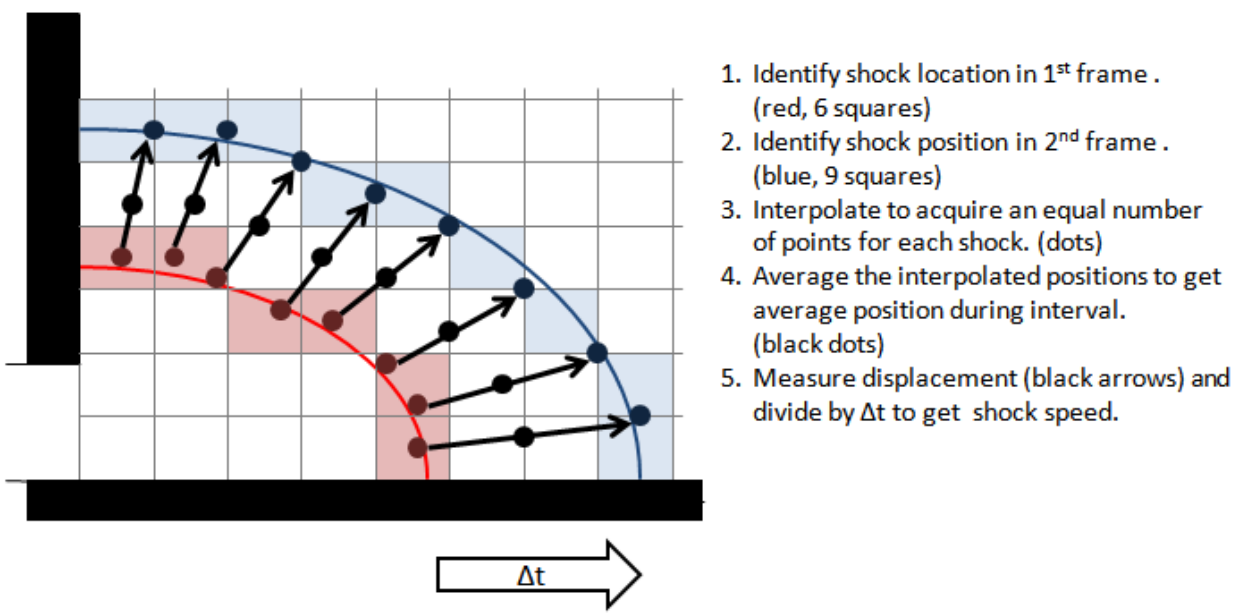

Figure 43. Algorithm for determining shock speed.

The central difference method reports speeds half way between the two shocks and requires an equal number of starting and ending points. Unlike flames, shocks have a relatively slowly varying curvature, and it was appropriate to interpolate points along the shocks so that there were an equal number of points on each shock front. Averaging the locations of the two shocks yielded the midpoints where the Mach number was reported. The bias uncertainty in the horizontal and vertical distances was the width of a pixel, and the manufacturer-reported uncertainty in frame interval (Δt) was 20 ns. Table 6 reports sample values and bias uncertainties of Δx, Δy, Δt and M.

Table 6. Sample Mach number and constituent variables

Variable	Value	Bias Uncertainty	Units
a	409.3	0.144	m/s
Δx	$7.958*10^{-3}$	$0.647*10^{-3}$	m
Δy	$6.580*10^{-3}$	$0.647*10^{-3}$	m
Δt	$4.75*10^{-6}$	$20*10^{-9}$	s
M	**5.312**	**0.334**	

Interpolation Functions

Measurements of flame separation and shock Mach number could not be collected for a regularly spaced grid of positions due to the frame rate limit for the Phantom v711 camera. The time interval between frames resulted in discrete spatial measurements, As a result, there were spatial gaps in the data (Fig. 44), and very few locations had the repeated measurements needed to calculate precision error. To reconcile the statistical variation and fill in the voids, a fitting function was devised. The fitting function had to be continuous in x and y and be a linear combination of terms such that a linear least squares fit could be applied to find the coefficients for each term. A two-dimensional power series (Eq. 16) met the requirements, and linear least

squares fitting was used to obtain coefficients ($a_{n,m}$) from the measured separation distance and Mach number data in each test case.

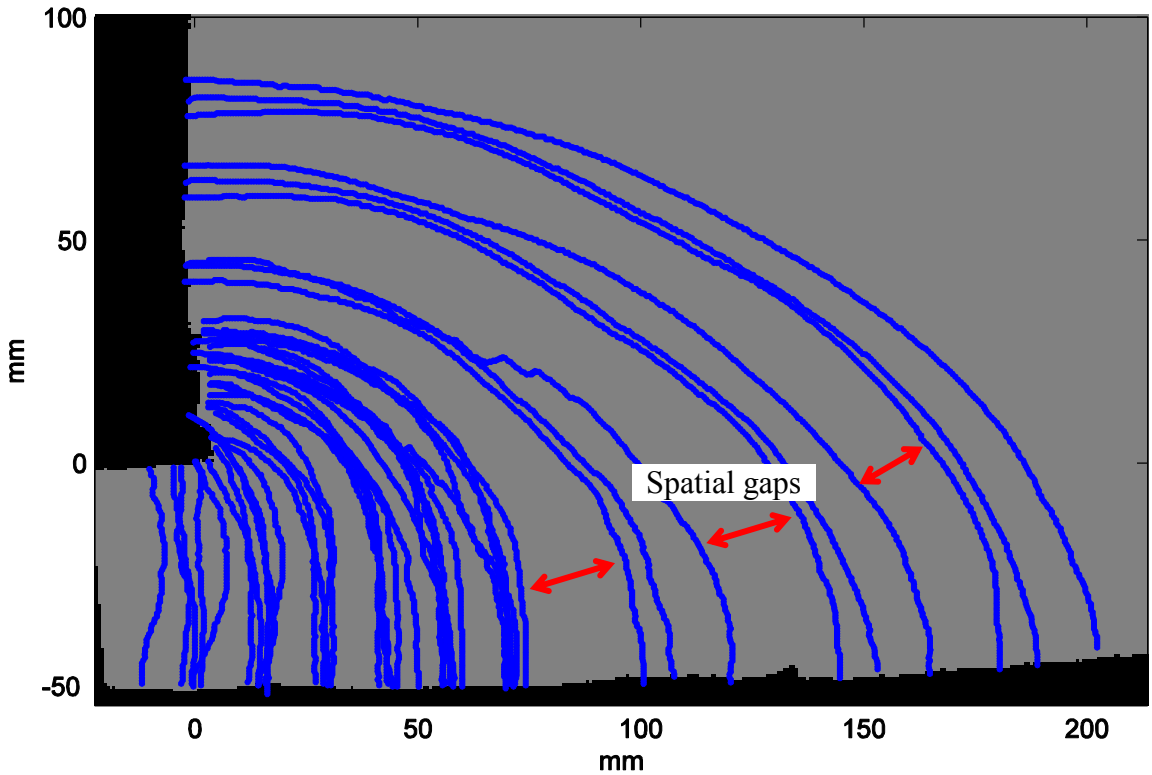

Figure 44. Consolidated shock position measurements from all runs of Case D2. Note spatial gaps in measurements due to 40 kfps frame rate used to increase image size.

$$f(x,y) = \sum_{n=0}^{\infty} \sum_{m=0}^{\infty} a_{n,m} x^n y^m \tag{16}$$

In practice, the series must be truncated to a maximum power (p). The choice of p is a tradeoff between minimizing the error of the function at the measured points and limiting the effect of outliers on the function. In each test case, the series was truncated to the power that produced the least mean absolute error.

The coefficients were calculated using the linear least squares regression. The regression seeks to minimize the difference between the fitting function and the measured data. It takes the form of Eq. 17

$$\boldsymbol{y} = [X]\boldsymbol{a} + \boldsymbol{\varepsilon} \tag{17}$$

where the elements of **y** are the measured separation distances or Mach numbers, **a** is a vector of the coefficients, and **ε** is the error. For a data set with n measurements and a fitting function of power p, [X] is:

$$[X] = \begin{bmatrix} 1 & x_1 & \cdots & y_1^p \\ 1 & x_2 & & y_2^p \\ \vdots & & \ddots & \vdots \\ 1 & x_n & \cdots & y_n^p \end{bmatrix} \tag{18}$$

Equation 19 gives the coefficients that minimize the root sum square of the elements of **ε**.

$$\boldsymbol{a} = [X]^{-1} * \boldsymbol{y} \tag{19}$$

The full code of the fitting function is included in Appendix C.

The fitting functions allowed the calculation of precision errors based on the entire data set for each test case. When calculating the precision error, the fitted data, X_{fit}, was substituted for the mean, $\bar{X}$, in Coleman and Steele to give Equation 20 (Coleman and Steele, 1989). The value of t in Eq. 20 was 1.96 for 95% a confidence interval because all of the data sets had sufficient samples to use the normal distribution in place of the student's t-distribution.

$$P_X = t * \left[\frac{1}{n-1}\sum_{i=1}^{n}\left(X_i - X_{fit,i}\right)^2\right]^{1/2} / \sqrt{n} \tag{20}$$

The maximum precision error in separation distance was $6.64\text{x}10^{-2}$ mm and the maximum precision error in Mach number was 0.0124. Both of the precision errors were an order of magnitude smaller than the bias errors; therefore, the bias dominates the total error. Combining the bias and precision errors gives maximum uncertainties of 0.650 mm (4.34%) for separation distance and 0.334 (6.29%) for Mach number.

V. Results

Overview

A proof of concept experiment was designed by the author to prove the existence of secondary detonations caused by oblique reflection of a diffraction detonation (Fig. 45). An increase in the chemiluminescence along the reflecting surface indicated detonation in the test section, and wave speed measurements downstream of the reflecting surface also indicated a detonation, but the integration time of the images in this initial look was too long to quantify the conditions leading to reinitiation.

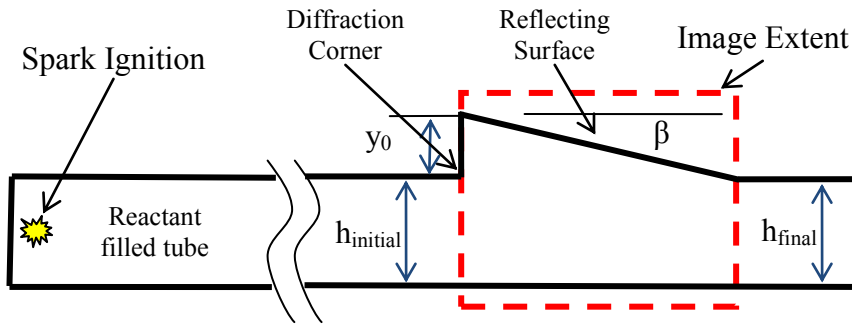

Figure 45. Schematic of experiment to prove existence of secondary detonations

After the proof of concept experiment, the author began an organized exploration of diffraction parameters with the D-series test cases. Study of the diffraction angle, θ, and the corner radius, r (Fig. 46) revealed that radius had little effect on the separation distance or shock Mach number while there was no need for reinitiation hardware when the diffraction angle was less than 15° because the detonation did not fully decouple.

In the R-series cases, it was observed that reinitiation occurred within a bounded set of the reflection ramp parameters. The maximum downstream distance (x_0) for reinitiation from a 45° surface was between 1.67 and 3.19 times the initial channel height, h_{intial}, when $y_0 = 0$.

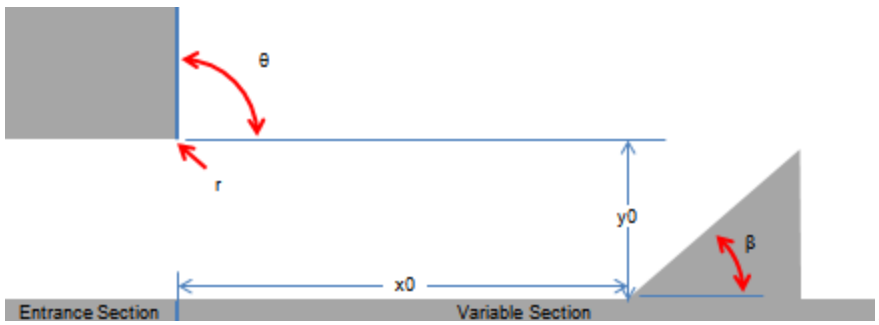

Figure 46. Parameters of the D-series and R-series cases

The minimum reflecting angle (β) for reinitiation at the plane of the diffraction corner was 15°. At a vertical offset (y_0) of h_{intial}, a 45° reflecting surface caused reinitiation only at downstream distances between $0.846 \cdot h_{intial}$ and $3.33 \cdot h_{intial}$. Variation in the diffraction corner radius had no significant effect on diffraction or reinitiation contrary to the qualitative evidence in Nielsen et al. (2011).

Diffraction of the secondary detonations prevented any of eleven M-series cases from successfully propagating detonation into the final channel height (Fig. 47). All of the M-series cases were analyzed qualitatively foregoing a time consuming quantitative analysis until a successful geometry was observed. The Cases M1 and M2 showed that reinitiation occurred for reflecting obstacle heights as small as 0.77λ, but rounding the diffraction corner at the end (M1) did not prevent decoupling. Cases M2 through M10 added more reflecting surfaces along the walls of the channel and those suffered from a combination of repeated diffraction of the reinitiated detonation waves. In some, more than one reinitiation occurred but the detonation never survived into the supercritical channel. Interestingly, case M11 displayed a second round of reinitiation after diffraction of the secondary detonations (Fig. 48). In this case, reinitiation was caused by the collision of two decoupled shocks from two secondary detonations in adjacent radial channels.

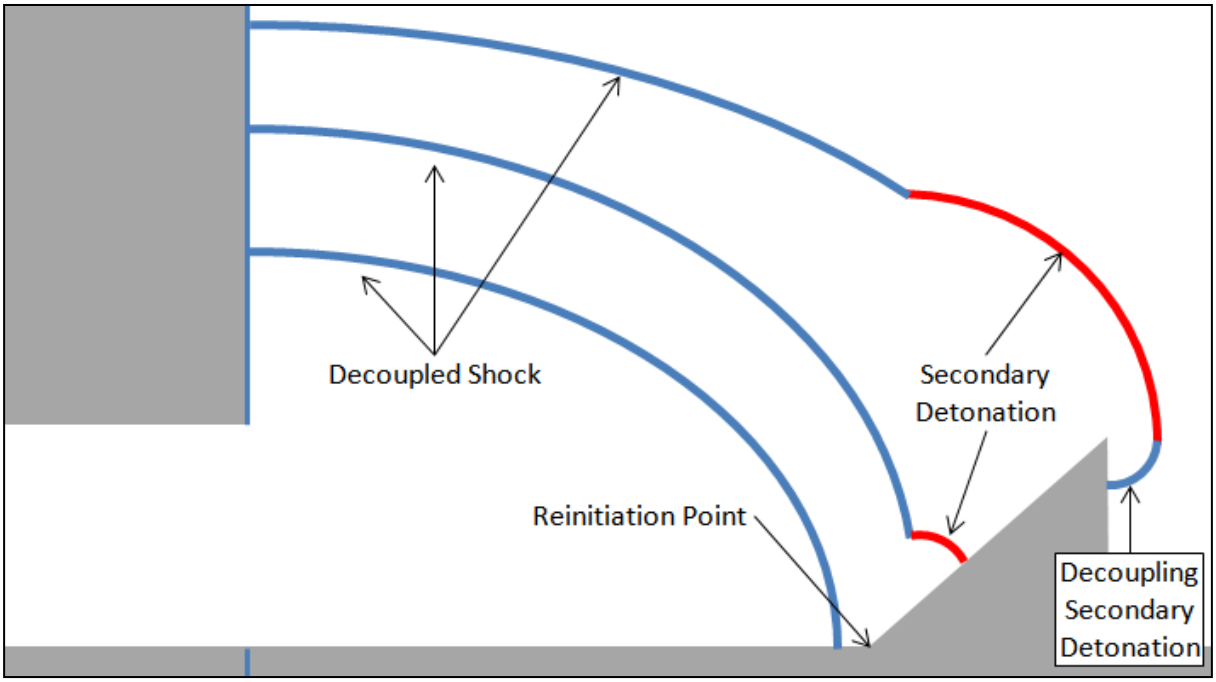

Figure 47. Diffraction of the secondary detonation causes it to decouple

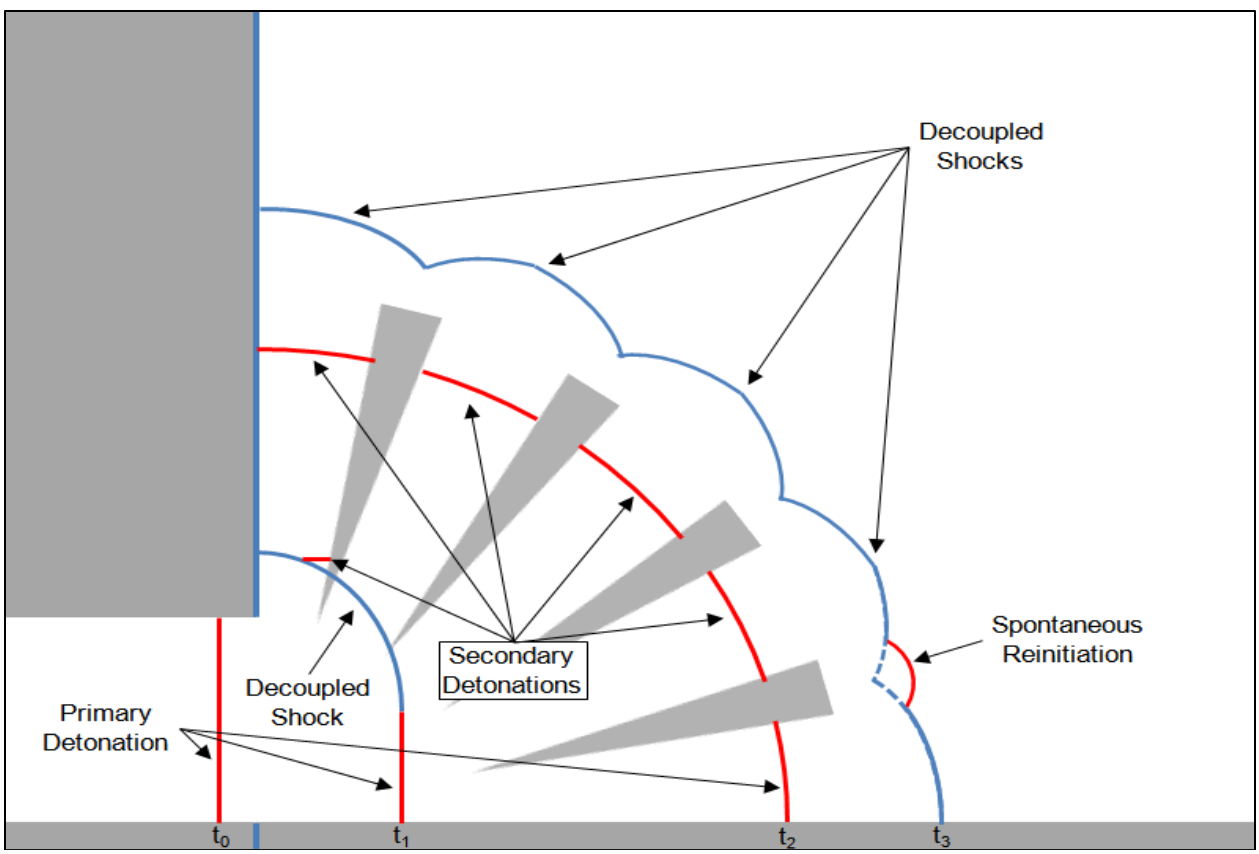

Figure 48. Shock and flame propagation in Case M11 (see Fig 36 for dimensions)

Diverging and Converging Channel Tests

Stevens et al. (2011) contains the first experimental data collected specifically for the development of a detonation diffuser. Two geometric test cases were considered, a 14° diverging ramp and a step expansion followed by a 14° converging ramp (Fig. 49). The two geometries utilize different approaches to a diffuser. The diverging case seeks to limit the diffraction angle such that the initial detonation never decouples, and the converging case allows decoupling to occur so that detonation will reinitiate due to the shock reflection from the converging wall.

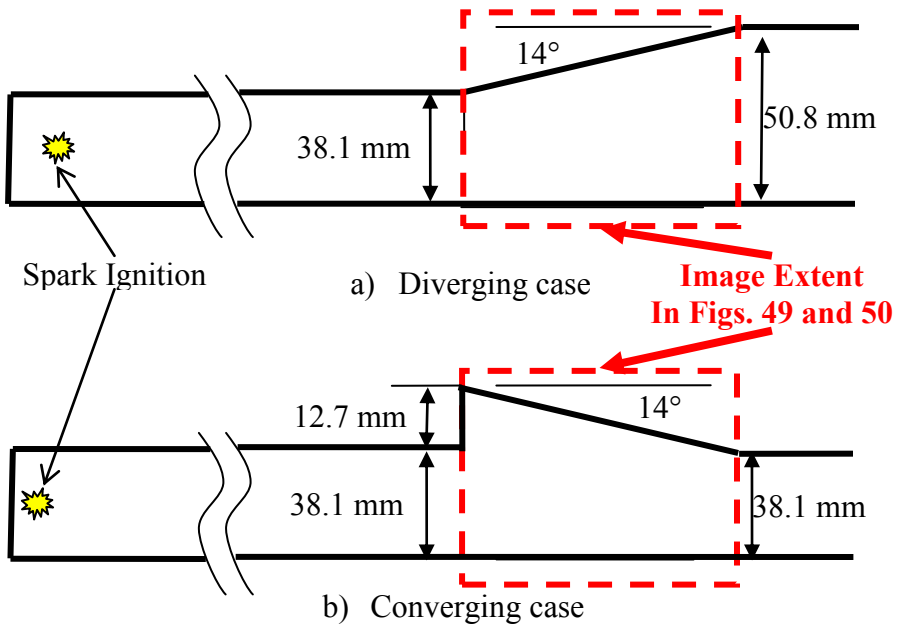

Figure 49. Diverging and converging test configurations (Stevens et al. 2011)

Since the cell size was 8.19 mm, the initial channel height of 38.1 mm was subcritical ($h/\lambda = 4.7$) in both cases. The diffraction angle in the diverging case (14°) was 0.5° less than the predicted limit of 14.5° (Nettleton 1987). The final channel height of 50.8 mm was barely supercritical ($h/\lambda = 6.20$) according to Lee's (1995) definition of the critical height, but it was as large as the test section allowed at the time. The length of the transition to a supercritical channel would be 176 mm.

Schlieren imaging of the diverging case indicated decoupling despite the small ramp angle (Fig. 50). To avoid decoupling, the diffraction angle has to be smaller, but other angles were not tested. For a benchmark to compare to the converging case, it was assumed that a 13.5° diffraction angle was sufficient to avoid decoupling in the diverging case since 14° was not sufficient. The target transition length was 182 mm corresponding to the 13.5° diffraction angle. It was hypothesized that a diffract, decouple, and reinitiate approach would complete the transition in less distance due to the shorter distance needed for a 90° diffraction. This reasoning lead to the exclusive use of diffraction and reinitiation rather than diffraction alone in the remainder of this work.

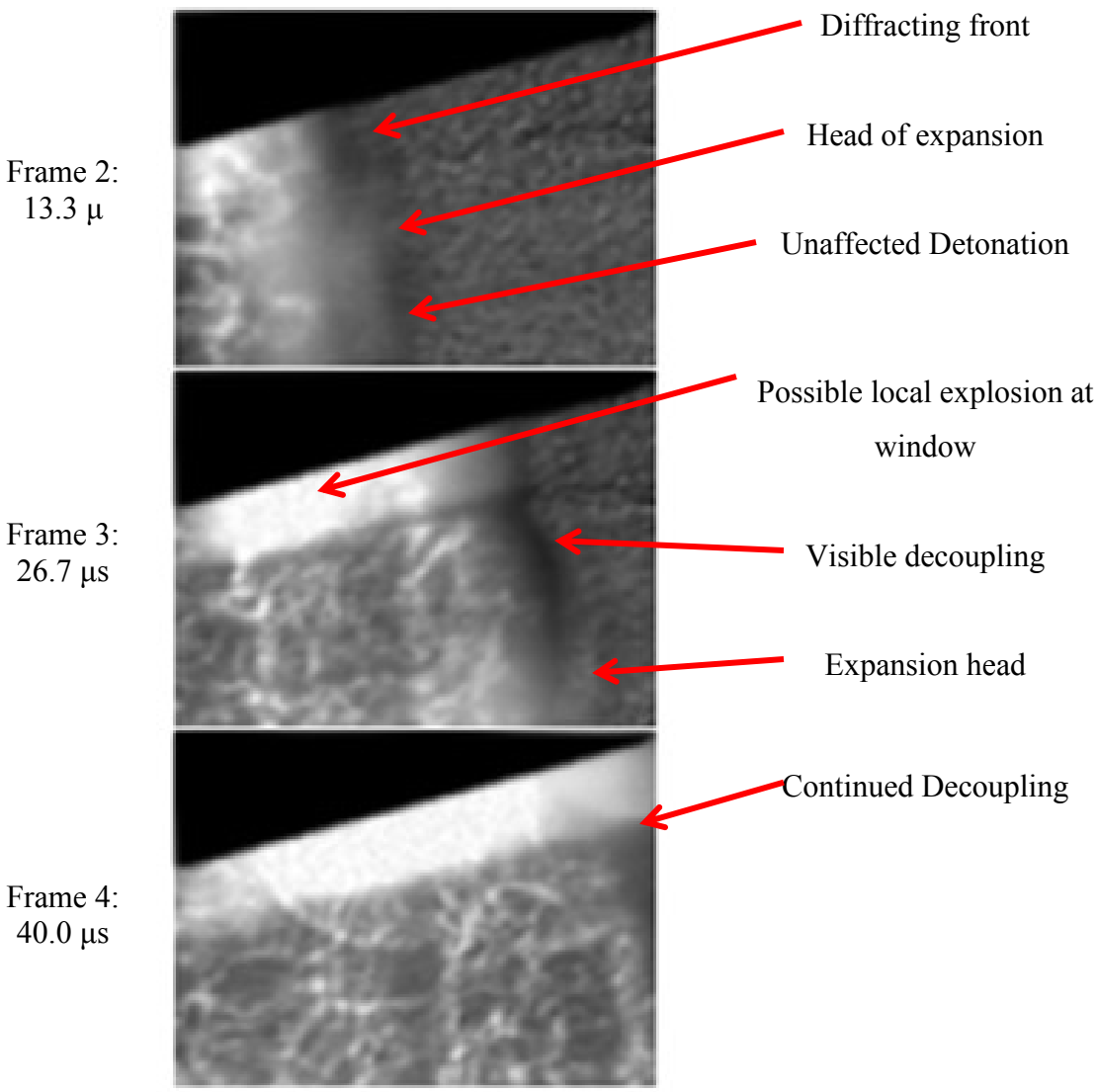

Figure 50. Decoupling on the diverging ramp (Stevens et al., 2011)

In the converging case, the initial channel height was also 38.1 mm. The step widened the channel by 12.7 mm to its maximum (50.8 mm). Then the converging wall reduced the channel height back down to 38.1 mm with a reflecting angle of 14°. It was unknown if, or where, detonation would reinitiate, but any observed reinitiations had to occur at a location where the channel height was greater than the initial height.

Schlieren images indicated reinitiation at the midpoint of the converging wall (Fig. 51). The first frame of the video shows decoupling of the primary detonation after the 12.7 mm step. The second frame shows two bright regions where reinitiation occurred. The first is in the corner where the converging ramp meets the top of the test section. The second begins at the midpoint of the converging wall and continues off to the right side of the frame. The channel height at the point of reinitiation was 44.5 mm. The successful reinitiation lead to some speculation on the result of adding more obstacles to the geometry. Had the converging wall ended at the point of reinitiation and been followed by another 12.7 mm step and converging wall the pattern of diffract, decouple, and reinitiate could have repeated as many times as needed to reach the critical channel height. The total length of such a transition is 178 mm, a 2.3% reduction in length. Due to the length reduction, diverging geometries were abandoned for the rest of the test cases.

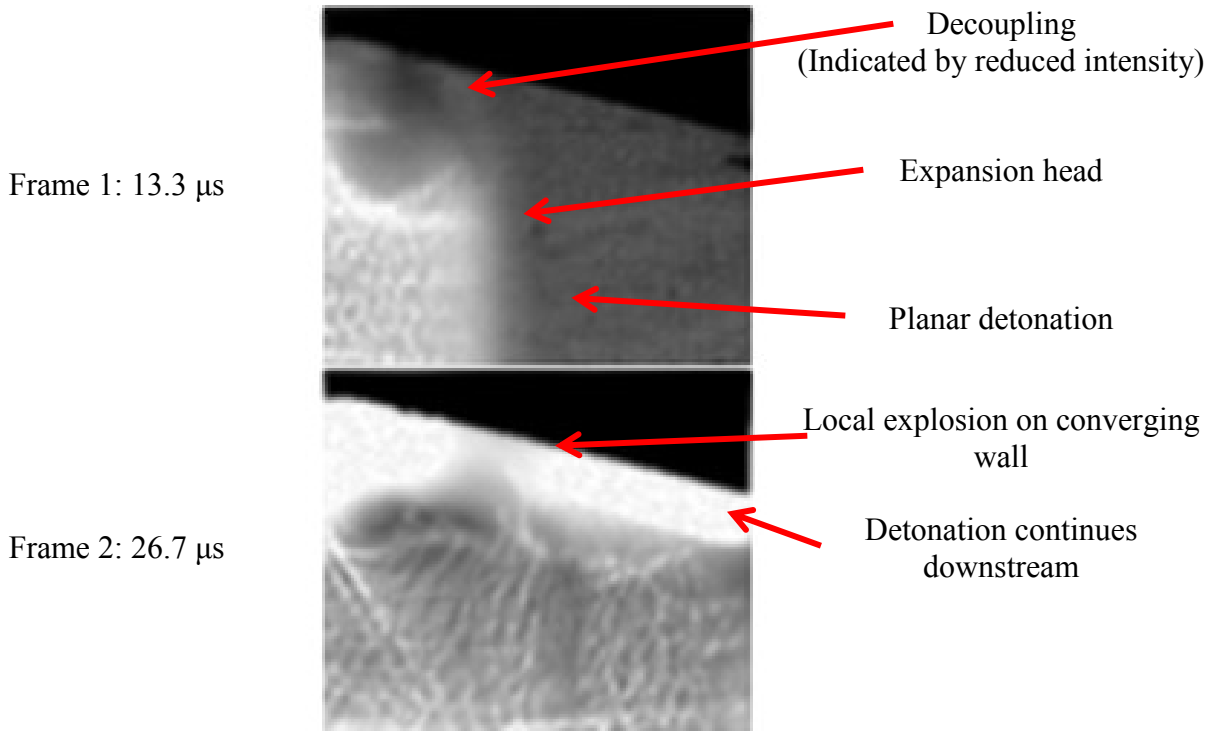

Figure 51. Local explosion on the converging ramp (Stevens et al., 2001)

The diverging and converging cases were useful for deciding to further study diverging or converging geometries, but the frame rate was too low and the exposure too long to accurately measure the position of shocks, flames, and detonations. Beginning with the diffraction series, the exposure of the schlieren images was short enough and the spatial resolution (mm/pixel) large enough that the images could be analyzed quantitatively with uncertainties sufficiently small for statistical significance. Due to the quantity of data, the raw images of the D, R, and M series runs are included in Appendix B.

Diffraction angle and diffraction corner radius, cases D1-D4

The D-series of high precision, quantitative test cases studied two geometric parameters of the diffraction corner, the diffraction angle and corner radius. Diffraction angle was included because it can unilaterally determine if decoupling occurs. Corner radius was included because it influenced the separation distance in crossover tubes. These two parameters were studied first because they do not require a reflecting surface in the test section.

Case D1

Case D1 was the control for the quantitative test cases, a straight channel (Fig. 52a). A straight channel should not exhibit diffraction or decoupling of the detonation front, and the wave speed through the section is the Chapman-Jouguet speed for the mixture. A declining wave speed or any separation indicates a poor transition from the upstream detonation tube to the test section. Figure 52b shows the separation distance profile for a combination of four runs. One run had a small region where the upper part of the wave was initially decoupled, visible in the upper left of the figure. In the black regions of the figure, excess sealant or the walls of the channel blocked the schlieren light path. The gray regions were visible, but fell outside of the region bounded by measured data points. Outside the boundary, the fitting function discussed in

Chapter IV would rely on extrapolation instead of interpolation removing the bounds on precision error. The wave quickly recoupled, but it increased the fitted separation and lowered the fitted Mach number in the upper left corner of the fitted data (Figs. 52b and 52c). The mean Mach number in Fig. 52c was 5.36 ± .334.

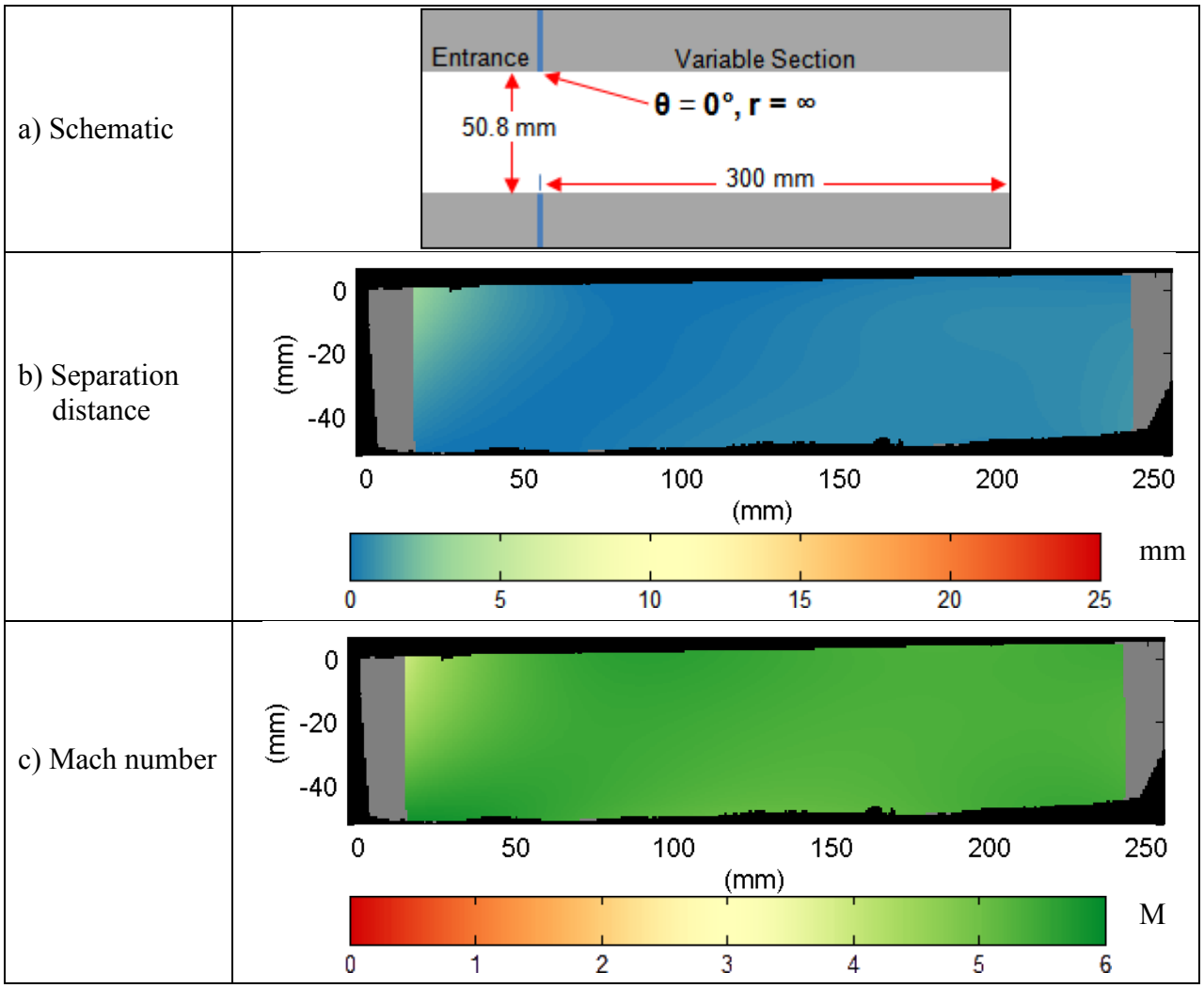

Figure 52. Case D1 (θ = 0°, r = ∞) schematic and data fits from 7 runs.

Case D2

Case D2 had a diffraction angle of 90.0° and a corner radius of 2.00 mm (Fig. 53a). This is a frequent geometry in diffraction studies (Mitrofanov 1965, Moen et al. 1982, Shepherd and Akbar 1999, Pintgen 2004, Arienti and Shepherd 2005, Nielsen 2011, Camardo 2012), but this is the first study to record the separation distance in addition to Mach number.

The detonation quickly began to decouple after the diffraction corner (Fig. 53b) and the entire front decoupled within 30 mm along the vertical wall. Coupled combustion endured longer on the horizontal, straight wall owing to the sonic propagation of the expansion across the detonation front, but full decoupling still occurred by the time the wave traveled 180 mm downstream.

Mach number degraded quickly along the diffraction wall as the separation increased (Fig 53c). This configuration favors placing a reflecting surface directly in the path of the emerging detonation front for reinitiation. The Mach number is higher along the bottom wall and a surface attached to the bottom of the channel cannot trap reactants. Along the diffraction wall, the shock weakens more quickly, and an offset surface above the diffraction corner is prone to trapping reactants due to the nearly vertical propagation of the shock. Trapped secondary detonations appear in two of the R-series test cases both of which had their reflecting surfaces attached to the top wall of the channel.

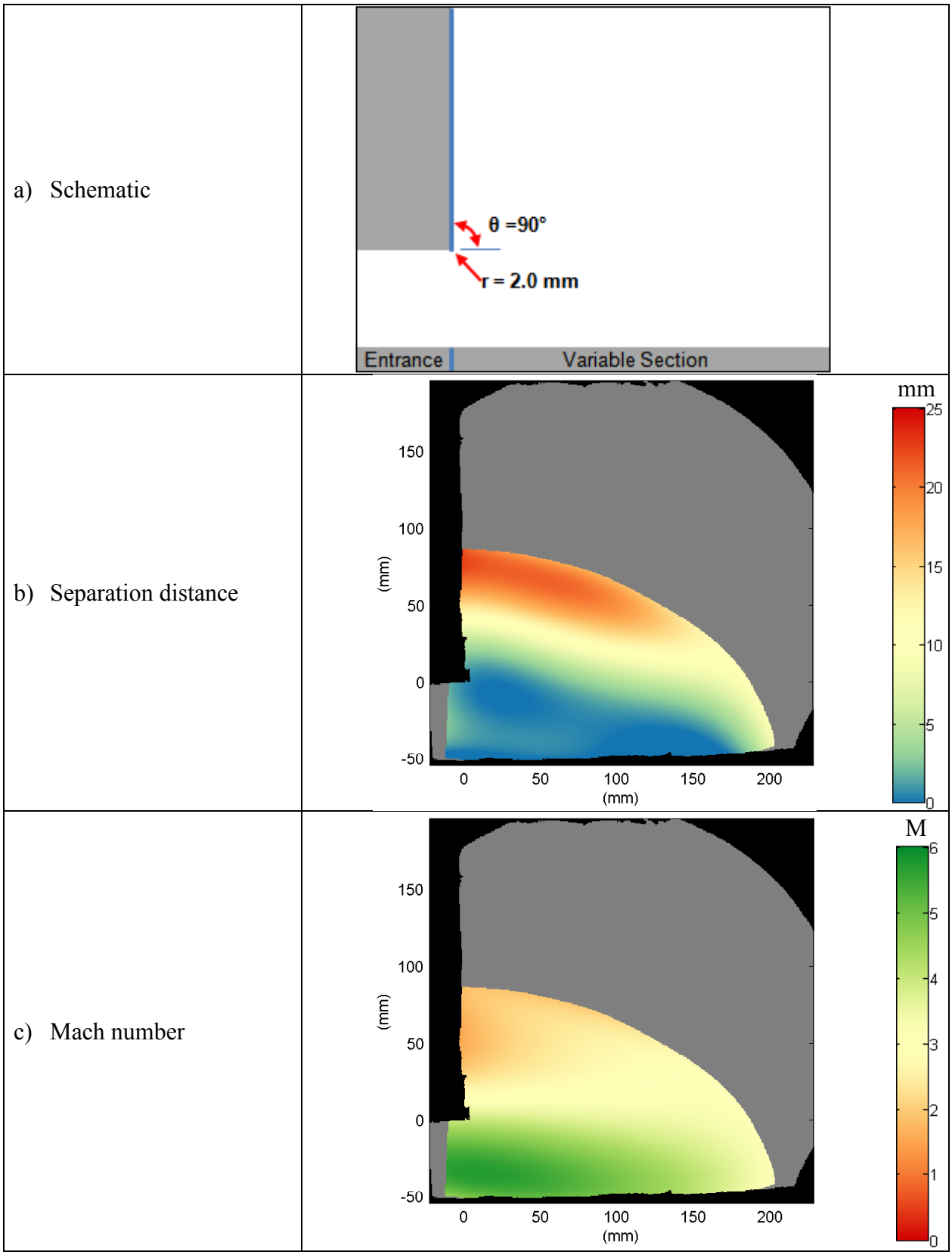

Figure 53. Case D2 (θ = 90°, r = 2 mm) schematic and data fits from 10 runs

In case D3, the diffraction angle was 15°, and the corner radius was 2 mm (Fig. 54a). As shown in Figure 54b, the detonation never fully decouples. Figure 54b shows that some decoupling occurs because the separation distance is greater than zero in much of Figure 54b, but the shock and flame never completely separate. The mean separation remains low, but is higher than in the straight channel. Since detonation never fully decouples, the Mach number remains high on average (Fig. 54c) with a slow region just downstream of the diffraction corner and a gradual decrease as the channel height increases. The gradual decrease in Mach number suggests that, given enough length, full decoupling will occur. Obviously, this arrangement is ideal for the survival of the detonation; however, the increase in area is very gradual and the mixture must remain constant through the transition. Shock reinitiation has neither of these constraints.

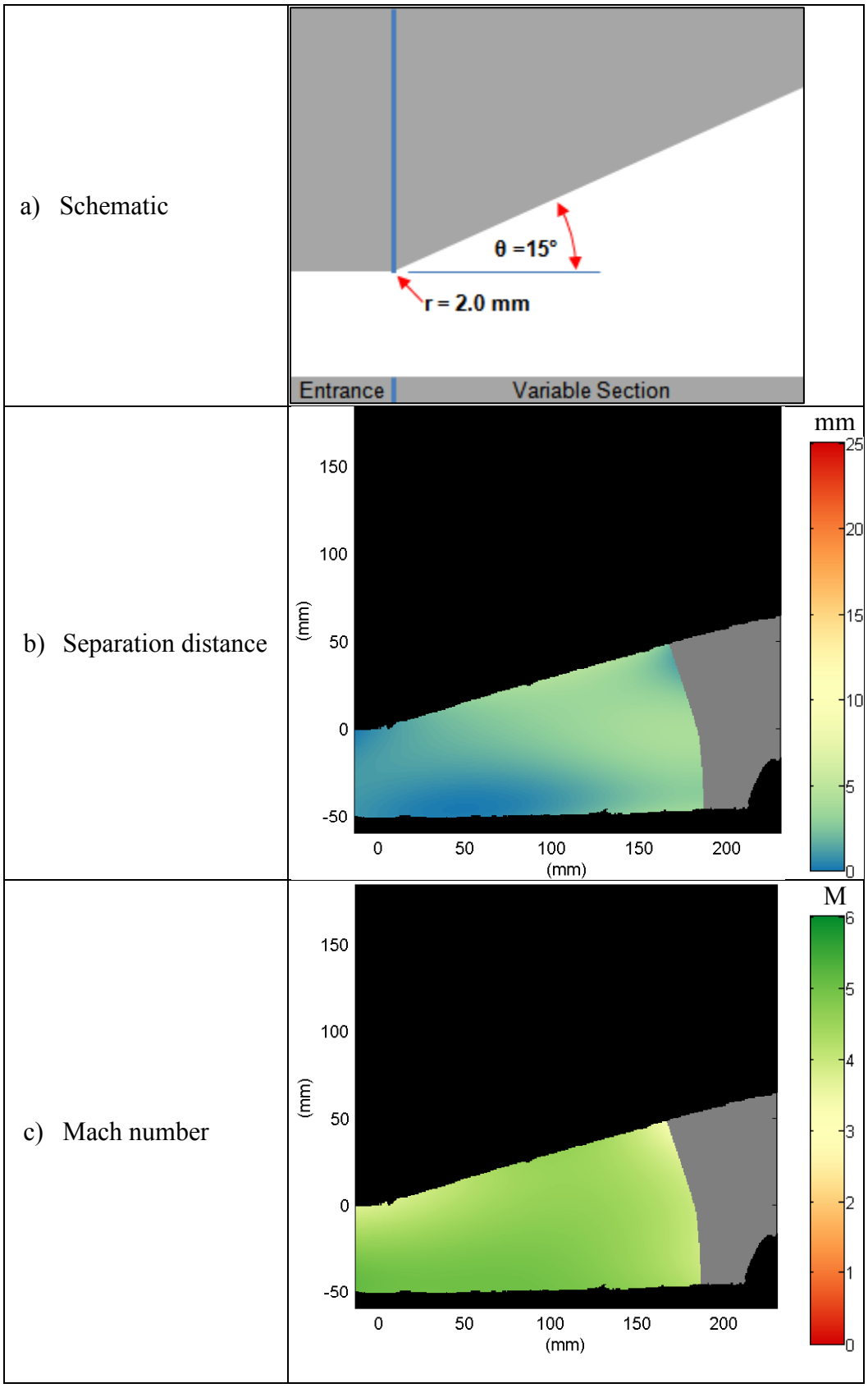

Figure 54. Case D3 (θ = 15°, r = 2 mm) schematic and data fits from 4 runs

Case D4

Case D4 was similar to case D2 except that the diffraction corner radius was 25.4 mm instead of 2 mm (Fig. 55a). The increased corner radius resulted in some reduction in the separation until the end of the curved section of wall (Fig. 55b). Overall, there was no significant reduction in separation. The Mach number of the lead shock was slightly higher than that of D2 near the diffraction corner, but the increase was less than the uncertainty (Fig. 55c). It is possible that further increase of the corner radius could lead to significant improvement in the separation or the Mach number, but a large corner radius also requires more fuel to fill the volume. For this reason, corner radius should not drive the design of a detonation diffuser.

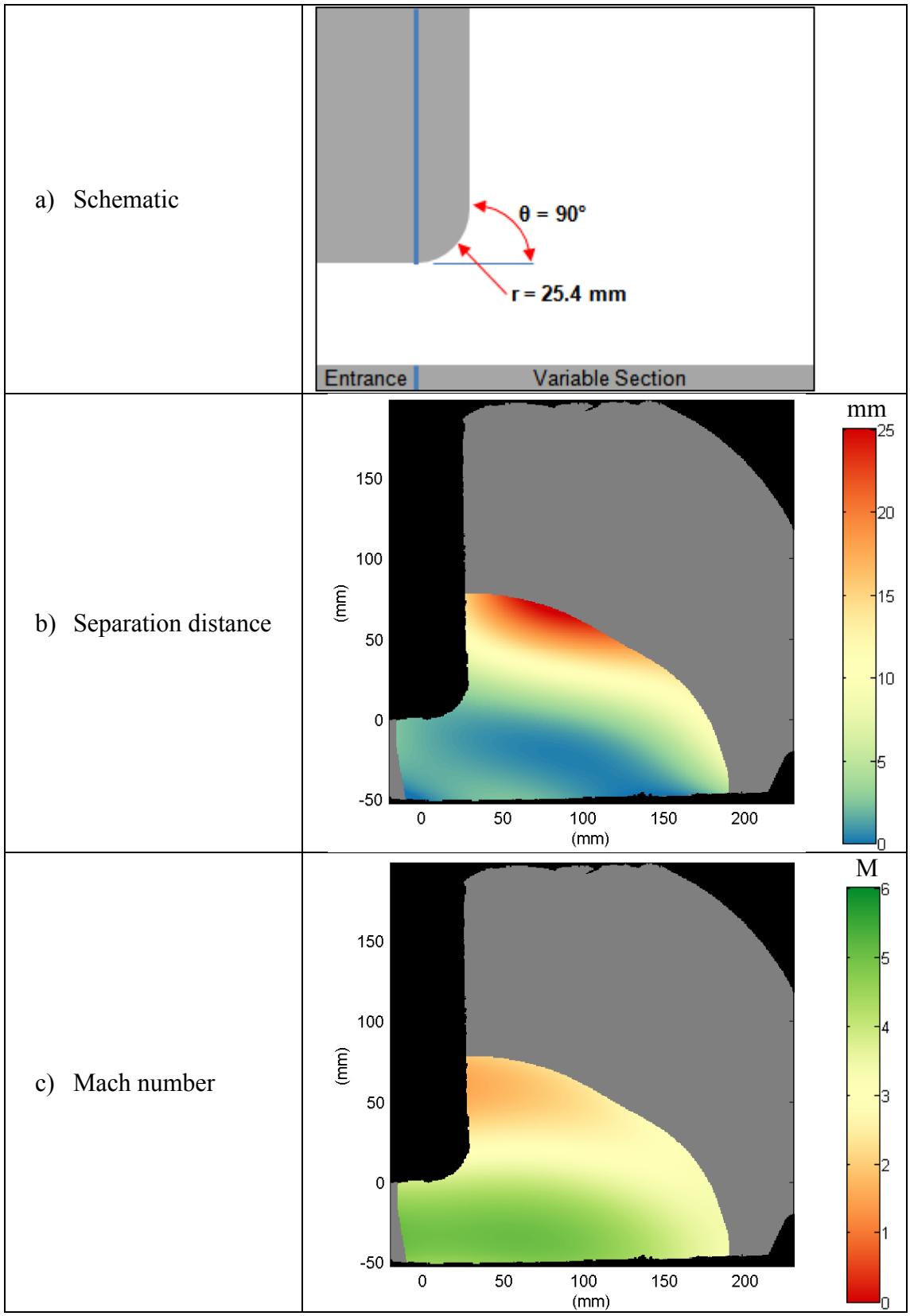

Figure 55. Case D4 (θ = 90°, r = 25.4 mm) data fitted to 10 runs.

Composite results of the D-series

In the diffraction test cases, the shock-flame separation distance and the shock Mach number varied separately. In cases D1, D2, and D3 diffraction angle was the sole independent variable. Figure 56 shows the effect of diffraction angle on separation distance (Fig. 56a) and Mach number (Fig. 56b) at a single spatial point along the bottom wall of the test section 200 mm downstream of the diffraction corner. The separation distance increases linearly with diffraction angle at a rate of 0.1075 mm/deg. The correlation coefficient (R^2) of the separation data is unity to the second decimal place, which indicates that the trend is likely linear. The Mach number declines with increasing diffraction angle, but with an R^2 of 0.83, the trend is non-linear, and linear trend-line passes outside the error bars of two of the three points in Fig. 56b. The decline in Mach number is about the same in the first 15° as in the reaming 75°.

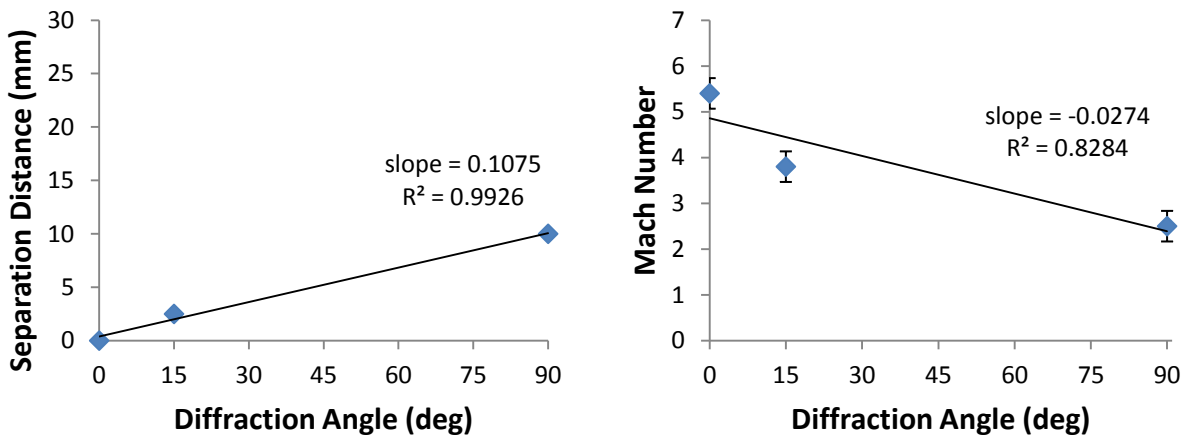

a) Separation distance b) Mach number

Figure 56. Effect of diffraction angle at a point along the bottom wall 200 mm downstream of the diffraction corner

In cases D2 and D4, the corner radius varied independently. The increase in corner radius from 2.00 mm to 25.4 mm had a small, mixed effect on the separation distance and Mach number (Fig. 57). At a point close to the diffraction wall (x =25 mm, y = 50 mm relative to the diffraction corner), the separation increased with corner radius (Fig. 57a), and the Mach number decreased (Fig. 57b). At a point further downstream and closer to the bottom wall of the channel (x = 200 mm, y = -50 mm), separation decreased, and Mach number increased as the corner radius increased. From Figure 56, any choice of corner radius will need to consider the location of the reflecting surface (top or bottom wall) when striving to optimize separation distance and Mach number.

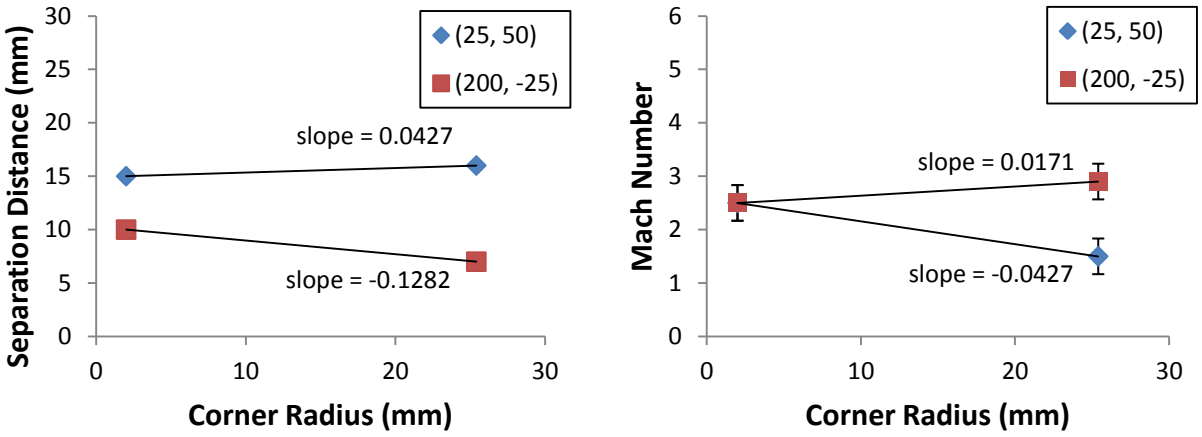

a) Separation distance b) Mach number

Figure 57. Effect of corner radius at two location (200, -51) and (25, 51)

Reflection angle and obstacle location results, cases R1-R8

The results of the cases D1 through D4 promote the use of geometry from case D2 to investigate the placement and angle of a reflecting surface. Corner radius had no significant effect on the diffraction, and the 90° diffraction angle minimizes the transition length and fuel requirements. In cases R1-R8, the diffraction angle was 90° and the corner radius was 2 mm with one exception, Case R5. Case R5 revisited the 25.4 mm corner radius to determine any unforeseen effect the radius might have on the combination of diffraction corner and reflecting surface. Improvement is signified by a reduction in separation and increase in Mach number in the R and M series test cases. A secondary detonation will have zero separation and a Mach number in excess of the CJ Mach number (5.3).

Case R1

In case R1, a 45° reflecting surface began on the straight wall 162.2 mm downstream ($x_0 = 3.19 \cdot h_{initial}$) of the plane of the diffraction corner (Fig. 58a). Detonations began to diffract at the corner and completely decoupled by the time the shock reached the reflecting surface (Fig. 58b) as evidenced by the non-zero separation distance. In three of the ten duplicate runs, reinitiation occurred at the intersection of the ramp and the bottom wall. In every case where reinitiation occurred, the secondary diffraction at the end of the ramp caused decoupling of the secondary detonation. In the cases where reinitiation did not occur, ignition of the reactants occurred and a secondary flame followed the reflected shock along the surface.

In Fig. 58b, the low probability of reinitiation and quick decoupling of the resulting secondary detonations resulted in a small decrease in the fitted separation distance near the reflecting surface compared to case D2. Likewise, the Mach number (Fig. 58c) is greater near the reflecting surface than in case D2. The geometry in case R1 had a 30% chance to produce a secondary detonation where all of the D-series cases had a 0% chance.

a) Schematic	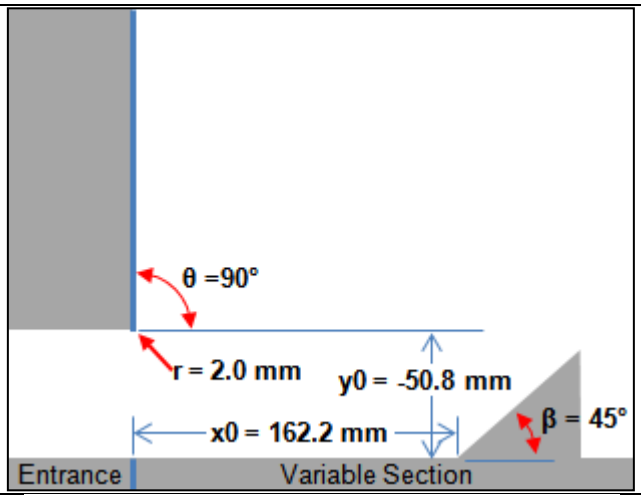
b) Separation distance	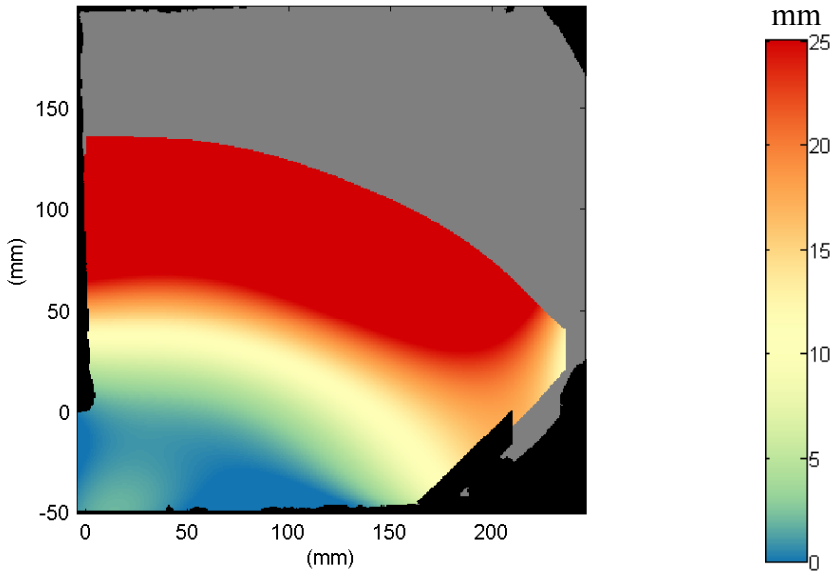
c) Mach number	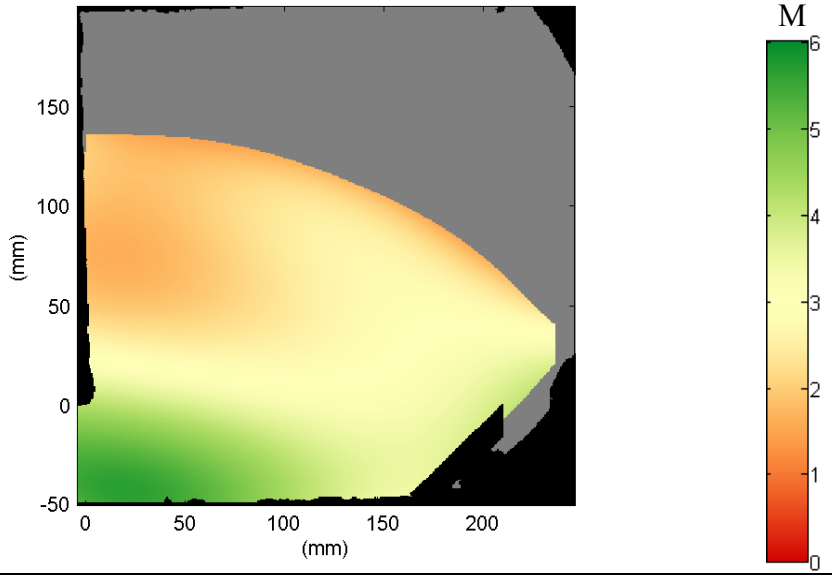

Figure 58. Case R1 (β = 45°, x0 = 162 mm, y0 = -50.8 mm) average of 10 runs

Case R2

In case R2, a 45° reflecting surface began on the straight wall 84.7 mm ($1.67 \cdot h_{initial}$) downstream of the diffraction corner (Fig. 59a). In this arrangement, the detonations did not fully decouple before reaching the reflecting surface as evidences by the separation distance at the beginning of the reflecting surface. Reinitiation occurred in all of the ten duplicate runs (100% probability) and the resulting region of small separation centered at x = 150 mm, y = 25 mm is apparent in Figure 59b. None of the secondary detonation waves survived the second diffraction and the fit predicts decoupling within 50 mm of the end of the reflecting surface (x = 135 mm). The Mach number exceeded 5.0 in the region of secondary detonation (Fig. 59c). The peak, fitted Mach number was lower than the CJ Mach number observed in Case D1 (5.3) because of run-to-run variation of the size of the secondary detonation. Case R2 had the highest chance of reinitiation with 100% of the duplicate trials resulting in a secondary detonation and the most preferable Mach number and separation distance among the R-series cases.

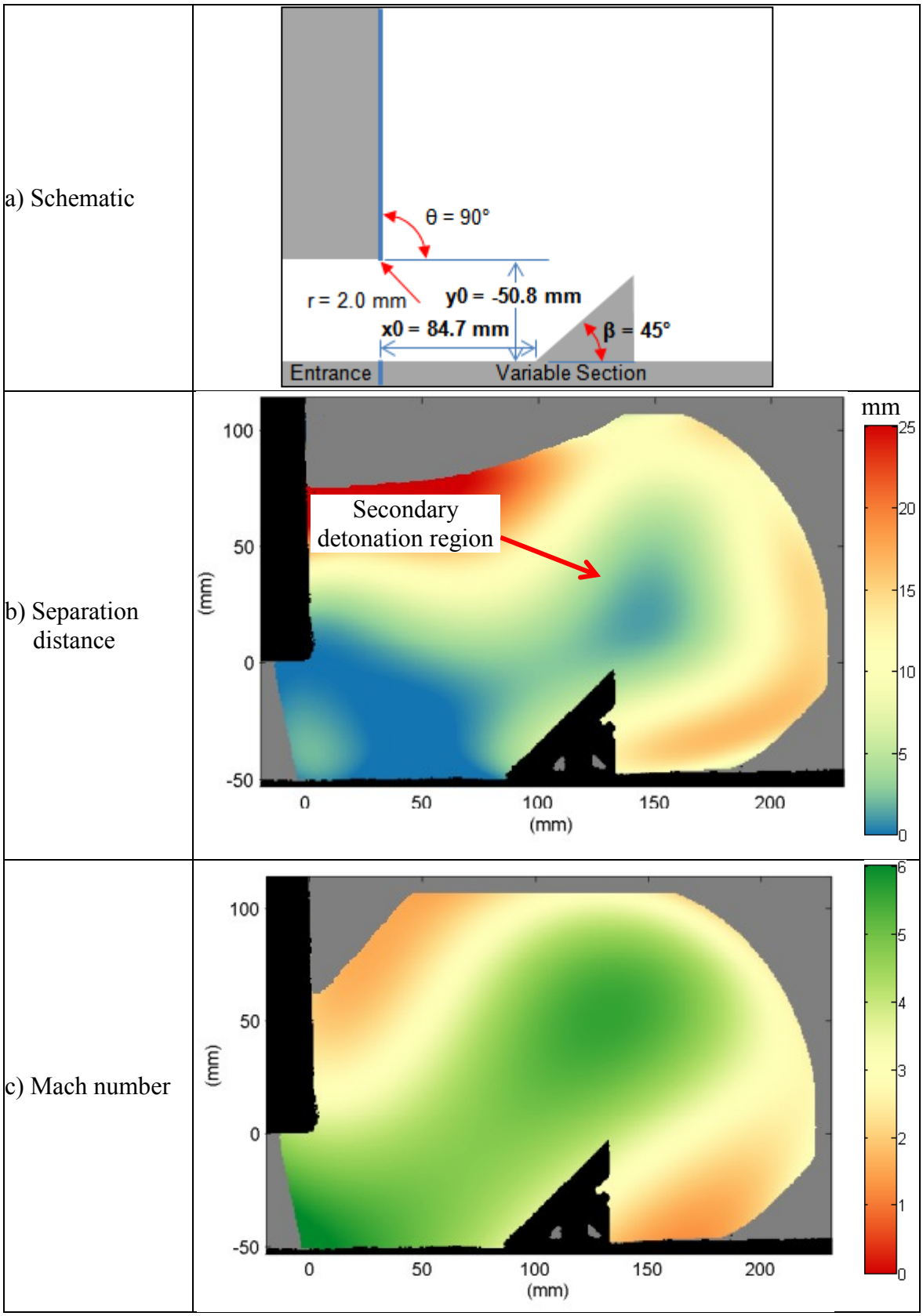

Figure 59. Case R2 (β = 45°, x_0 = 84.7 mm, y_0 = -50.8 mm) average of 10 runs

Case R3

In case R3, the placement of the reflecting surface was approximately the same as in case R2, but the reflecting angle was 30° rather than 45° (Fig. 60a). The reduced angle reduced the compression of the reflected shock, and reduced the size of the region of zero-separation associated with reinitiated detonation (Fig. 60a). The probability of reinitiation was lower than in Case R2 because seven of the ten duplicate runs successfully reinitiated (70% probability). The decreased probability of reinitiation increased the mean separation in Figure 60b. As in cases R1 and R2, all of the secondary detonations decoupled fully after the second diffraction corner. Full separation occurs within 25 mm of the second diffraction corner. Mach number (Fig. 60c) better indicates the region of detonation above the reflecting surface though the peak Mach number was further reduced by the lower probability of reinitiation compared to case R2. Case R3 had the second highest chance of reinitiation among the R-series test cases. Only R2 had higher.

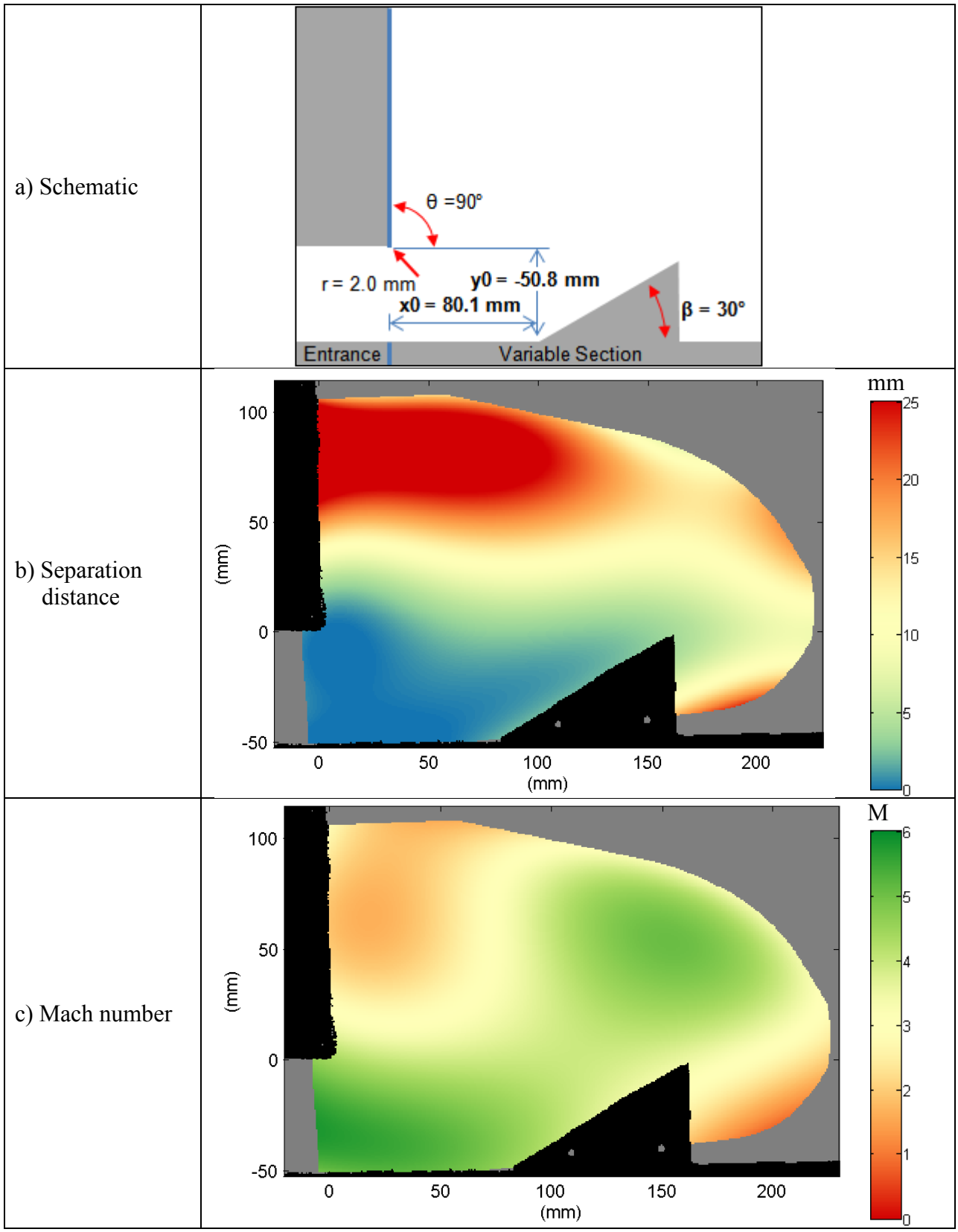

Figure 60. Case R3 (β = 30°, x_0 = 80.1 mm, y_0 = -50.8 mm) average of 10 runs.

Case R4

Case R4 continued the trend of decreasing reflection angle (45° - 30° - 15°) (Fig. 61a). Due the length of the obstacle needed for the surface height to equal that of cases R2 and R3, the reflection surface began directly opposite the diffraction corner so that it would fit in the test section. Unlike the higher reflection angles, the probability of reinitiation was very low with one instance of reinitiation in six duplicate trials (17 % probability). The fitted separation between the shock and flame continued to grow over time despite the reflection, and there was no region of low separation (Fig. 61b) and high Mach number (Fig. 61c) typical of reinitiation. The lack of reinitiation when x_0 = 0 mm suggests that the ramp angle was too shallow for reinitiation at any position downstream of the diffraction corner. With a 17% chance of reinitiation, case R4 ranked sixth of the R-series, better than only R8 and R7.

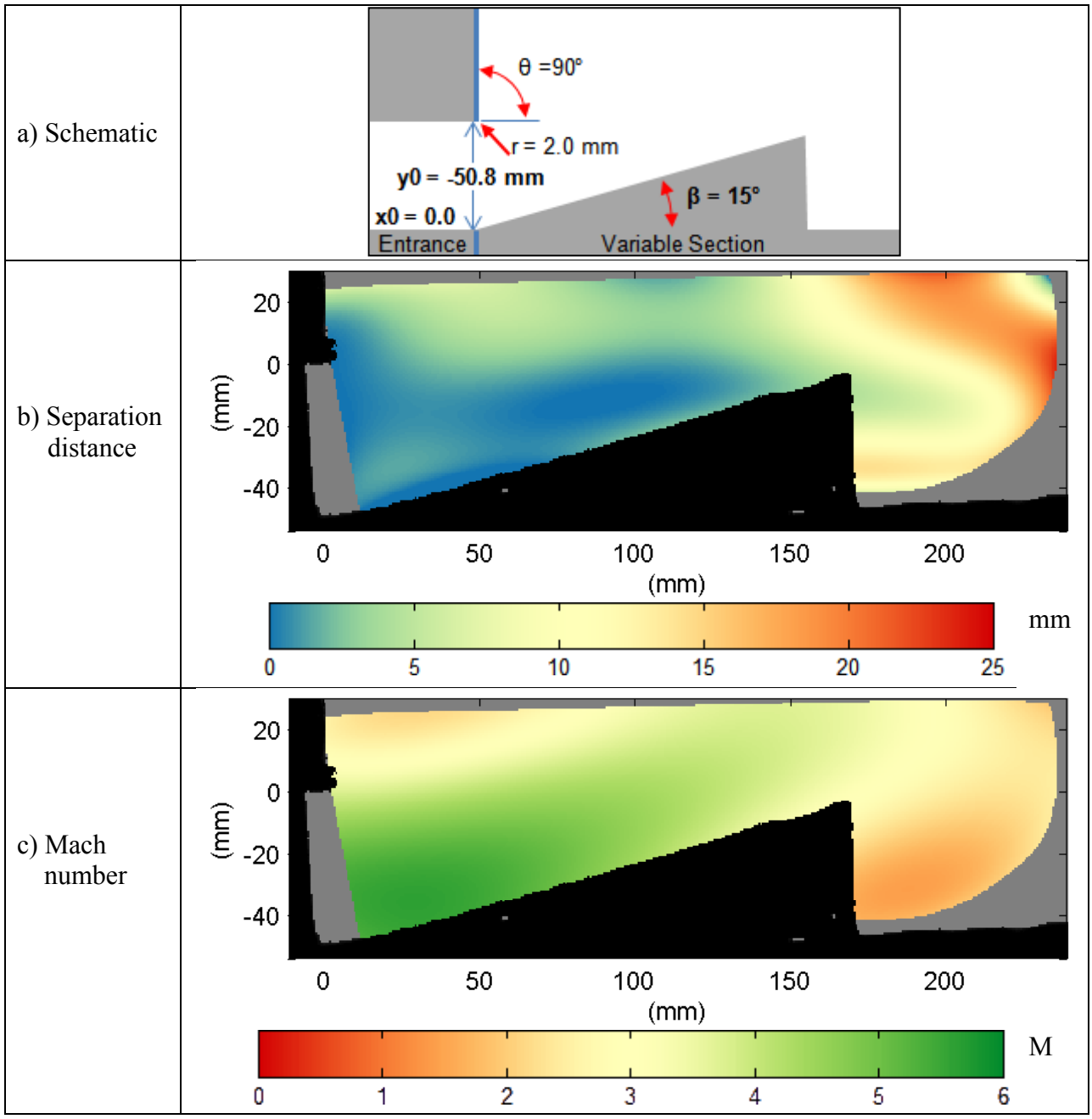

Figure 61. Case R4 (β = 15°, x_0 = 0 mm, y_0 = -50.8 mm) average of 6 runs

Case R5

Case R5 revisited the larger diffraction corner radius (r = 25.4 mm) from case D3 (Fig. 62a). No change relative to case R3 in the probability of reinitiation, the fitted separation distance (Fig. 62b), or the fitted Mach number (Fig. 62c) was expected, and the results confirm that expectation. Comparing case R3 to case R5, there was the same small increase in Mach number and small reduction in separation distance near the diffraction corner as reported in Case D3 relative to case D2. Reinitiation occurred in five of the six duplicate trials (83% probability), which is the same as case three within the margin of error (±17%). There appears to be no significant advantage to increased diffraction corner radius. Case R5 tied case R3 for second highest chance of reinitiation among the R-series cases and demonstrates no advantage or disadvantage to a larger diffraction corner radius within the range of 0.2 to 25 mm.

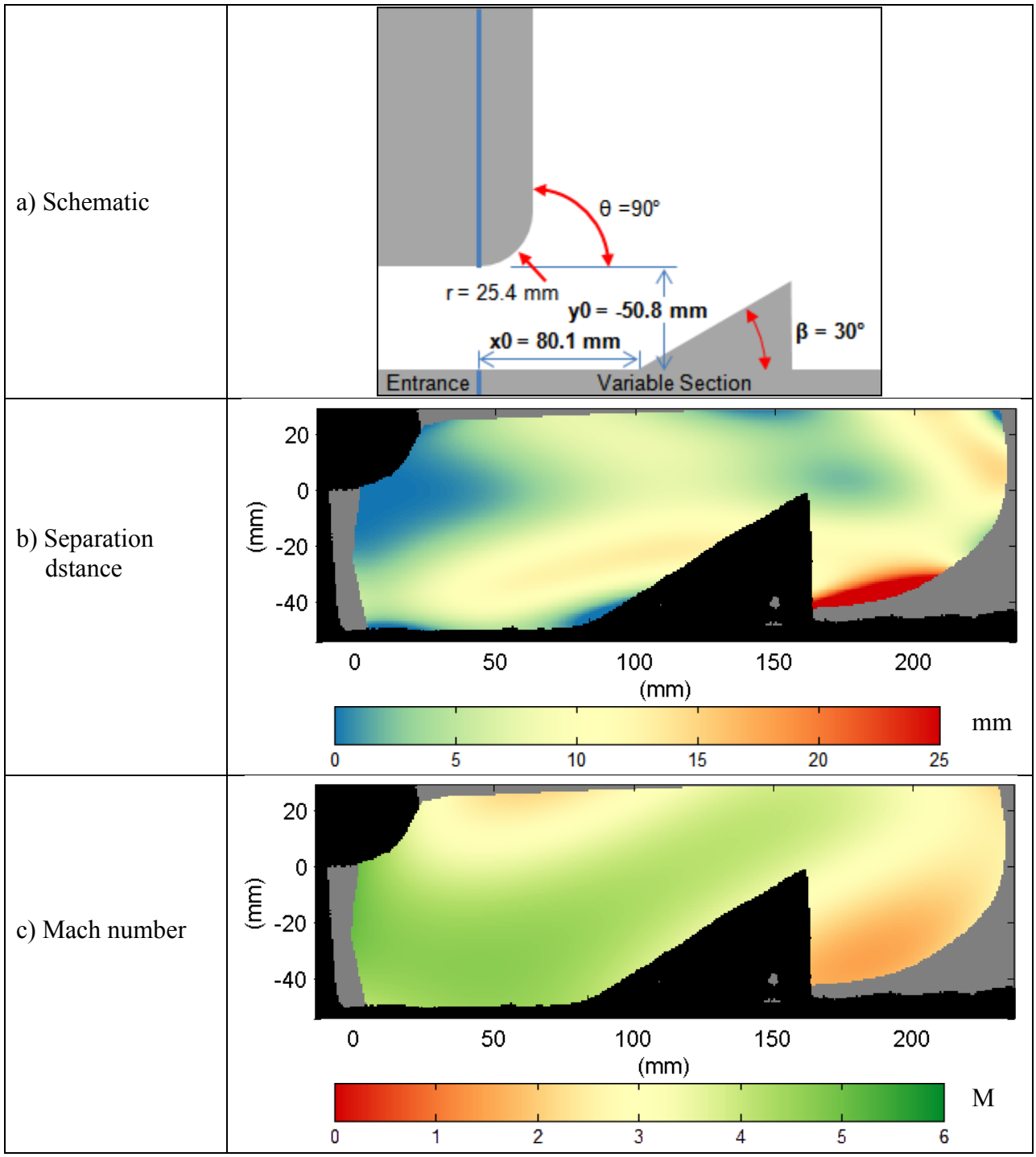

Figure 62. Case R5 (r = 25.4 mm, β = 30°, x_0 = 80.1 mm, y_0 = -50.8 mm) average of 5 runs

Case R6

Beginning with case R6, the reflecting surface began one initial channel height (50.8 mm) above the diffraction corner on the same side of the channel (Fig. 63a). In this configuration, the Mach number before reflection was lower than in cases R1-R5. Case R6 was the first case to exhibit trapping of a secondary detonation between the vertical wall and the reflecting surface. The beginning of the reflecting surface was the point where diffraction wall and the obstacle met ($x_0 = 0$). In all of the eight duplicate runs, the decoupled shock encountered the obstacle near the end of the reflecting surface ($x_0 = 50$ mm), and the separation distance was too small to allow a secondary detonation to propagate downstream (Fig. 63b). In two of the runs reinitiation occurred (25% probability), but the secondary detonation waves were trapped between the vertical wall, the reflecting surface, and the decoupled combustion front. Neither the separation distance in Figure 64b nor the Mach number in Figure 64c indicated any improvement (reduced separation distance) over case D2 due to the presence of the reflecting surface. Case R6 demonstrated a low chance of reinitiation (25%) ranking fifth out of the R-series cases, but the geometry was completely ineffective because the secondary detonations formed in a region of reactants bounded by the reflecting surface and the decoupled combustion front. The infrequent, secondary detonations quenched once the reactants in that region were consumed.

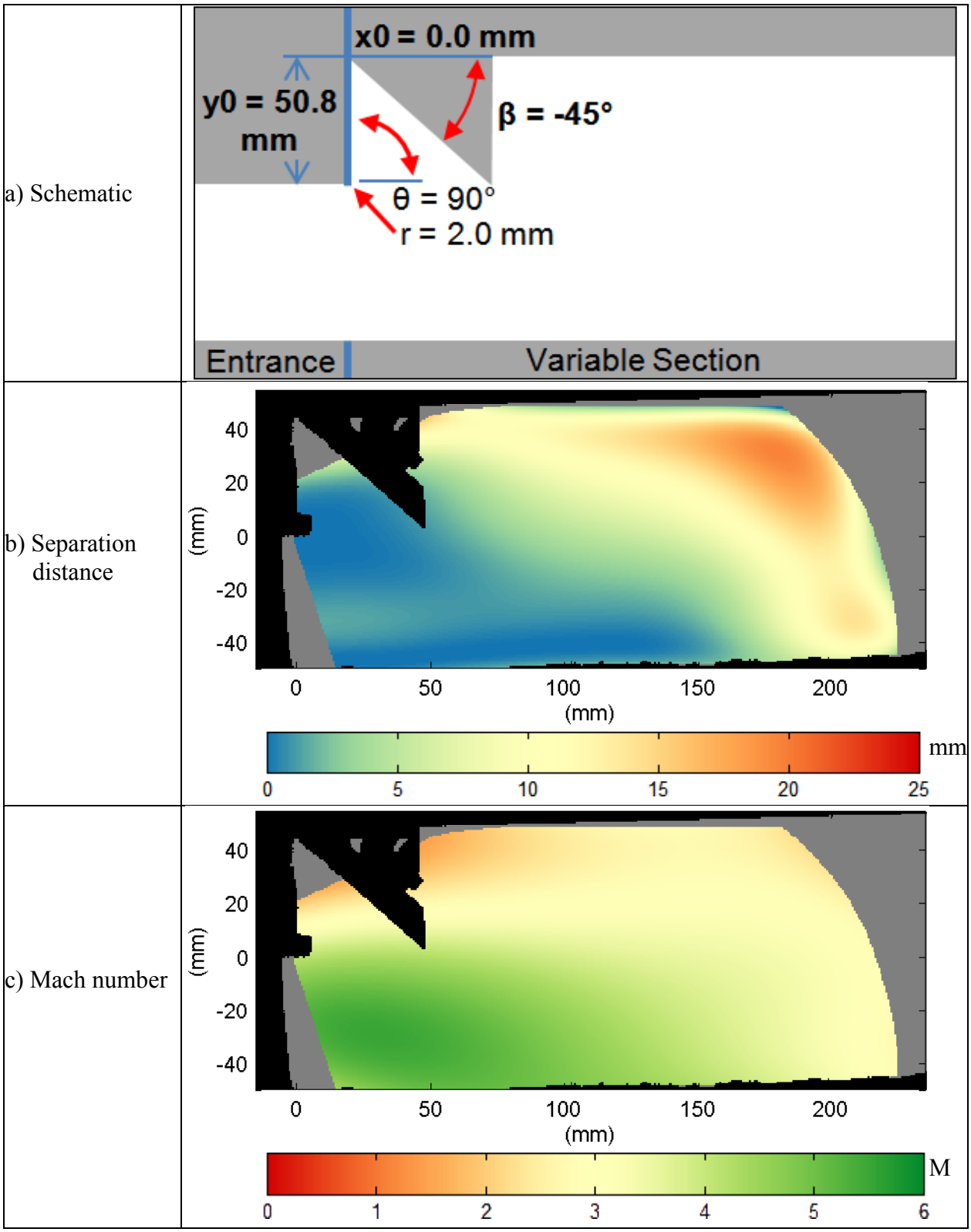

Figure 63. Case R6 (β = 135°, x_0 = 0 mm, y_0 = 50.8 mm) average of 8 runs.

Case R7

In case R7, the reflecting surface was moved to x_0 = 43 mm ($0.85 \cdot h_{initial}$) on the upper wall of the channel (Fig. 64a). At this location, the first contact between the decoupled shock and the reflecting surface occurred near the midpoint of the reflecting surface. The incident Mach number at the reflecting surface was the lowest of any case yet and the resulting shock reflection was insufficient for reinitiation. Reinitiation occurred in none of the eight duplicate runs (0% probability). The separation distance (Fig 64b) and Mach number (Fig. 64c) exhibit no significant difference from case R6 or from case D2. As in case R6, a pocket of reactants became isolated between the top wall of the channel, the reflecting surface and the combustion front, but unlike case R6 there was no secondary detonation to trap in case R7. Case R7 performed the worst of the R-series cases with no chance of reinitiation due to low shock Mach number at the reflecting surface.

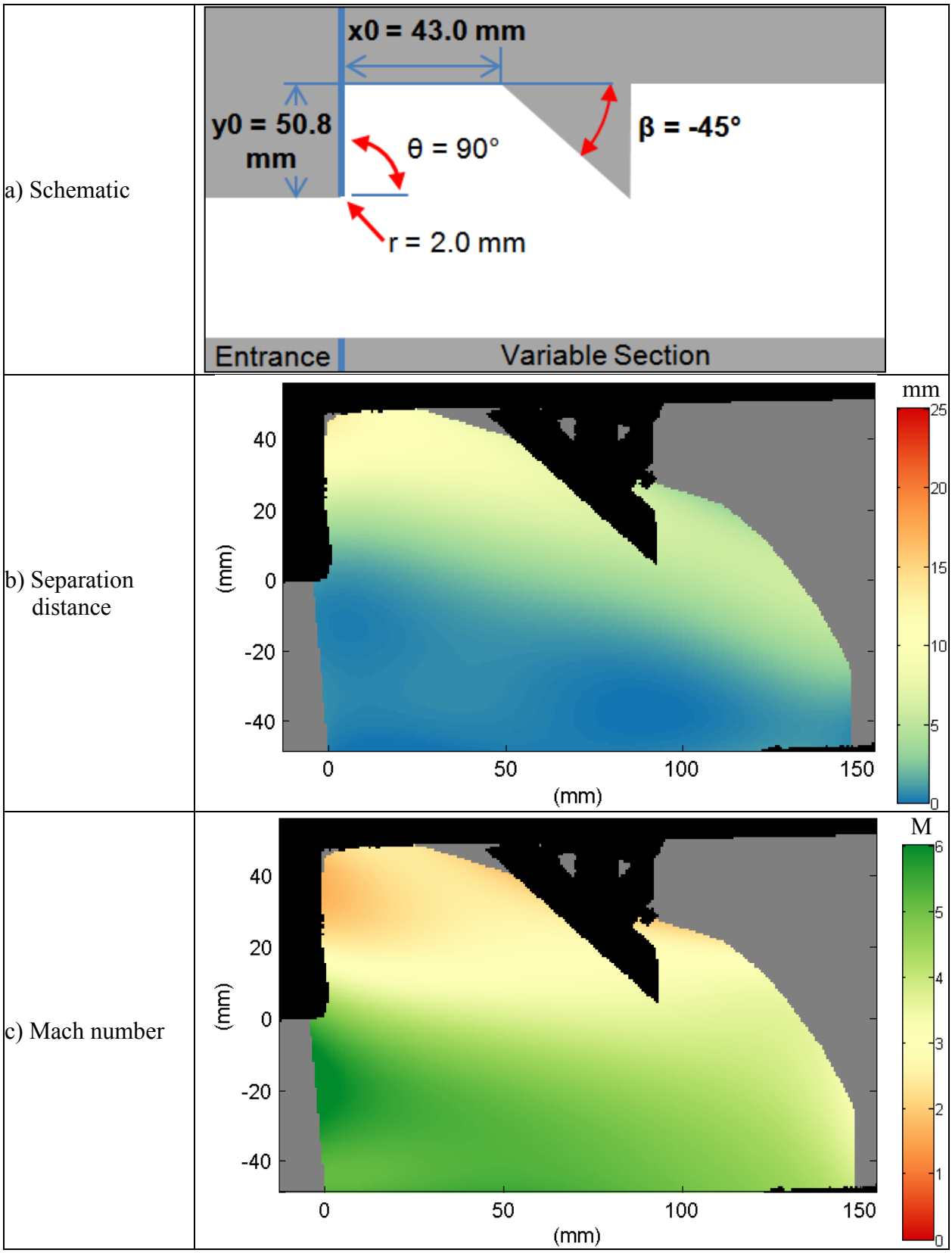

Figure 64. Case R7 (β = 135°, x_0 = 43 mm, y_0 = 50.8 mm) average of 8 runs.

Case R8

In the final reflection case, the reflecting surface was located at x_0 = 169 mm ($3.33 \cdot h_{initial}$) on the top wall of the channel (Fig. 65a). The main difference between this and case R7 was the reflection of the decoupled shock wave from the upper wall of the channel before encountering the reflecting surface. The combination of two reflections, one from the top of the channel and one from the reflecting surface, was sufficient for reinitiation to occur in four of the nine duplicate runs (44% probability). Along the reflecting surface, the separation distance decreased (Fig. 65b), and the Mach number increased (Fig. 65c) compared to case D2. In every case, the secondary detonation decoupled after the second diffraction corner. How far the secondary detonation traveled before fully decoupling is unknown because the secondary detonations were still partially coupled when they reached the end of the image frame. This configuration had the best probability of reinitiation among the geometries with a positive vertical offset ($y_0 = h_{initial}$), but there was no configuration tested wherein reinitiation occurred 100% of the time. Case R8 had the second lowest change of reinitiation of the R-series cases and performed better than case R7 only because of the additional shock reflection from the top of the channel. Based on cases R6-R8, vertical offset should be minimized in the design of a detonation diffuser.

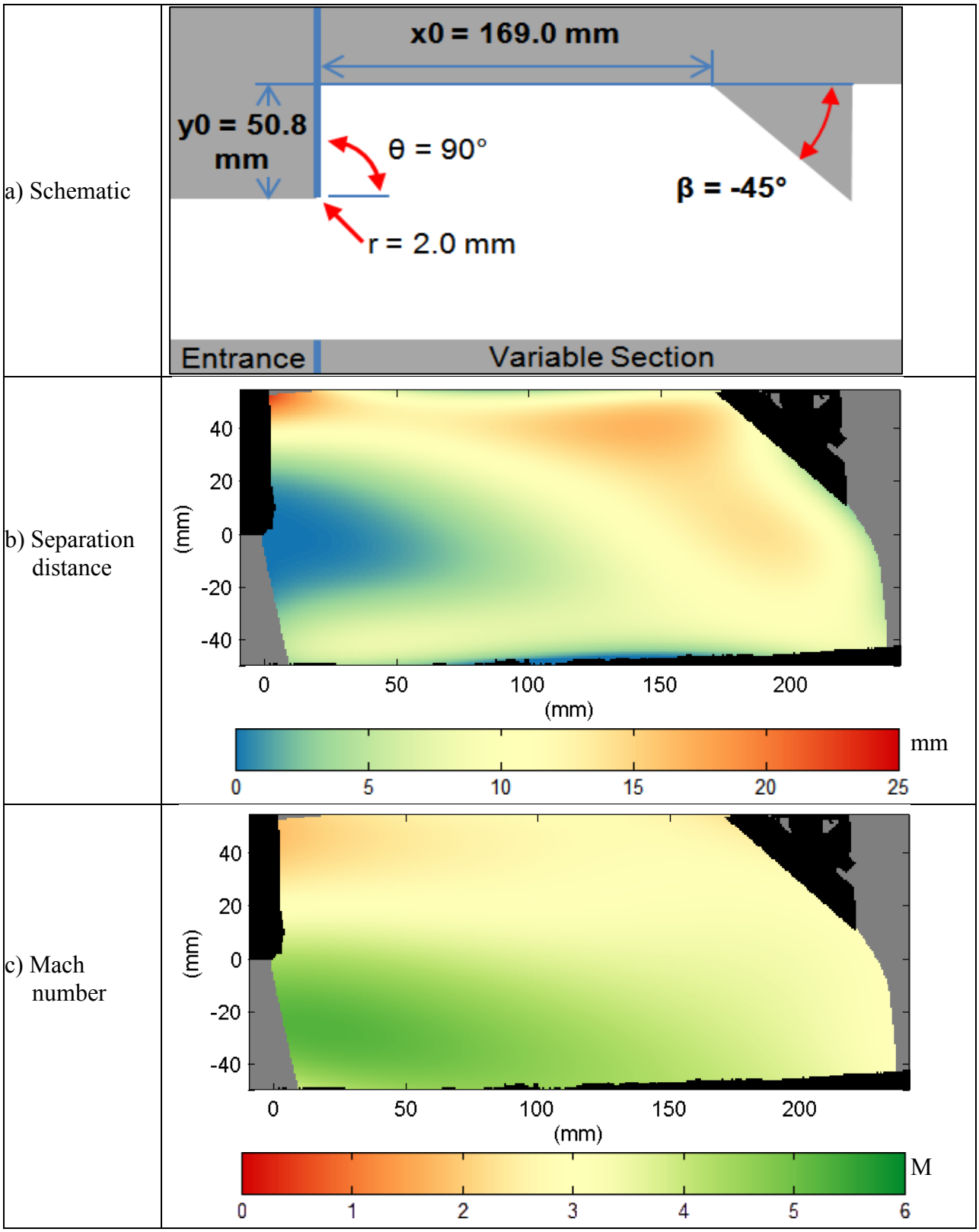

Figure 65. Case R8 (β = 135°, x_0 = 169 mm, y_0 = 50.8 mm) average of 9 runs.

The cases in the R-series explored a parameter space consisting of reflecting angle and location to determine where reinitiation was likely to occur. Figure 66 shows how the probability of reinitiation depends on the reflecting surface angle and location. Reinitiation was certain in case R2, and reinitiation occurred intermittently in cases R1, R3-R5, and R8. Figure 66a shows that the probability of reinitiation increases with reflection angle (β). As β increases, the component of the shock velocity normal to the surface increases resulting in higher compression and higher probability of reinitiation. The probability of reinitiation as a function of x_0 in Fig. 66b depended greatly on the vertical offset, y_0. As the vertical offset increased from $-h_{initial}$ to $h_{initial}$, the minimum x_0 for reinitiation increased quickly, beginning at 0.0 and increasing to $1.67 \cdot h_{initial}$ at a vertical offset of $y_0 = h_{initial}$. The minimum limit of x_0 for reinitiation occurred because secondary detonations were trapped by the decoupled combustion fronts. As x_0 increased, larger separation distances allowed secondary detonations to escape the combustion fronts, but a single shock reflection was insufficient to reinitiate detonation. Two reflections of the decoupled shock (once from the top wall of the channel and once from the reflecting surface) were sufficient to increase the probability of reinitiation to 17% at $x_0 = 3.33 \cdot h_{initial}$. Once x_0 was sufficiently large ($x_0 > 1.67 \cdot h_{initial}$), reinitiation was no longer certain (100% probability) on the bottom of the channel ($y_0 = -h_{initial}$) because the decoupled shock decayed too much before encountering the reflecting surface.

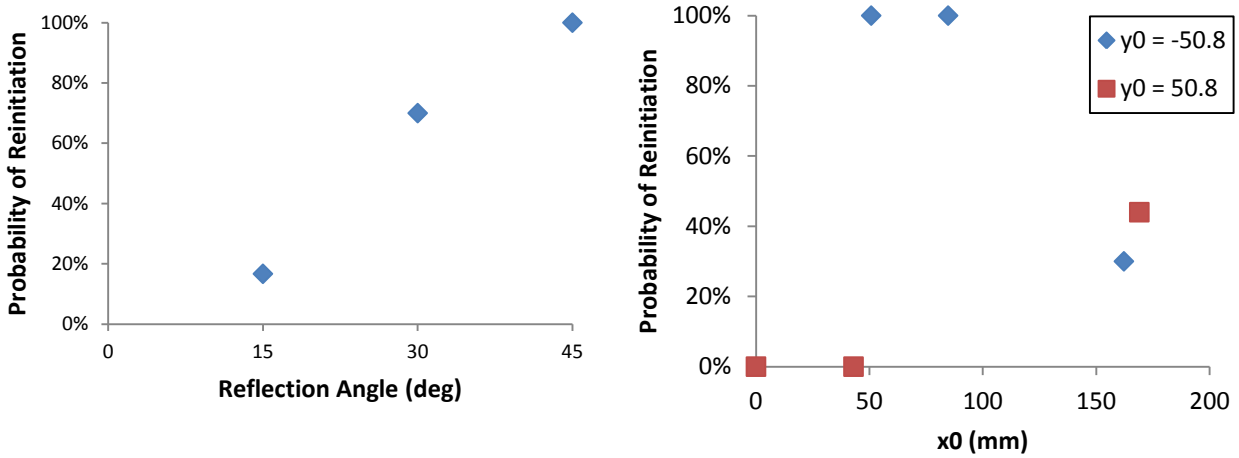

a) Trend in β (x_0 = ~80 mm, y_0 = -50.8 mm)

b) Trends in x_0 and y_0 (β = 45°)

Figure 66. Trends in the probability of reinitiation

Iterative multiple obstacle case results, cases M1-M11

The final set of test cases expands upon the quantitative data from the reflection cases. The number of different test cases in the multiple obstacle set made quantitative analysis impractical, and it was unnecessary for any case without successful transmission of a secondary detonation. Of the twelve cases, none resulted in detonation in the supercritical channel, but each contributed to understanding of the secondary detonation and the second diffraction corner. The second diffraction corner remains the obstacle to a successful detonation diffuser.

Case M1

In case M1, the second diffraction corner had a radius of 13 mm in an attempt to prevent decoupling (Fid. 67a). Since the data analyses from the two previous cases with large diffraction corner radii were incomplete at the time, this was considered a useful test case. In each of four trials, diffraction occurred after the obstacle and the secondary detonation failed (Fig. 67b). Figure 66b is a composite of frames from a single video highlighting the reinitiation and subsequent diffraction. The shock and flame in each frame was shaded in a different color to distinguish that frame from its neighbors. The chronological order of shading colors is blue, green, red, and black. After four frames, the cycle repeats.

a) Schematic

b) Composite frame
$\Delta t = 20.4\ \mu s$

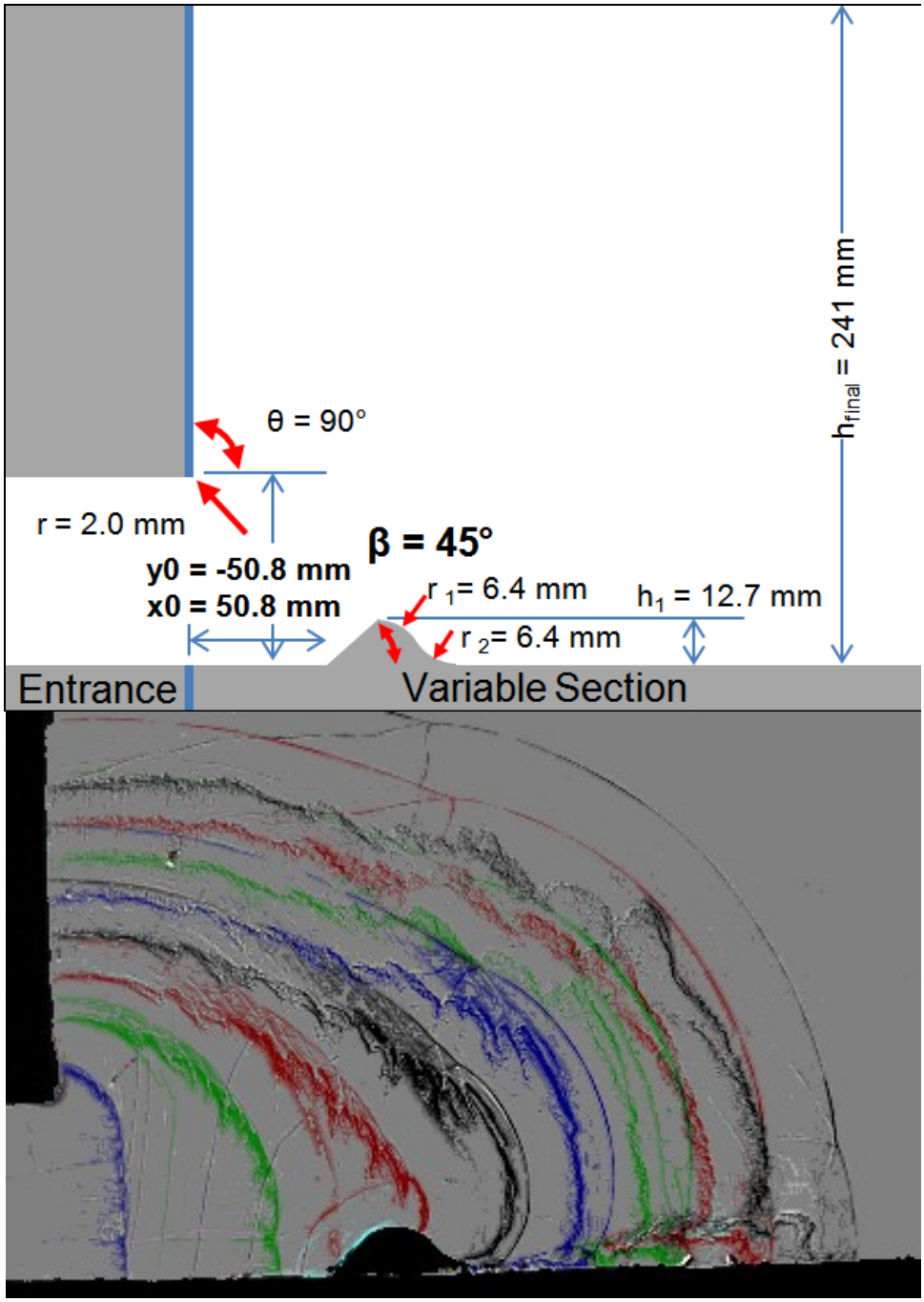

Figure 67. Case M1, 13 mm high obstacle with rounded diffraction corner

Case M2

In case two, reinitiation began in two places (Fig. 68b). The first was either the third or fourth obstacle and the second was one of the last three obstacles. Neither secondary detonation traveled across the shock front without decoupling. After this case, the sharp diffraction angle at the top of each ramp was rounded to reduce the severity of the diffraction. The reduced height of the obstacles continued to have no effect on reinitiation.

a) Schematic

b) Composite Frame
$\Delta t = 20.4\ \mu s$

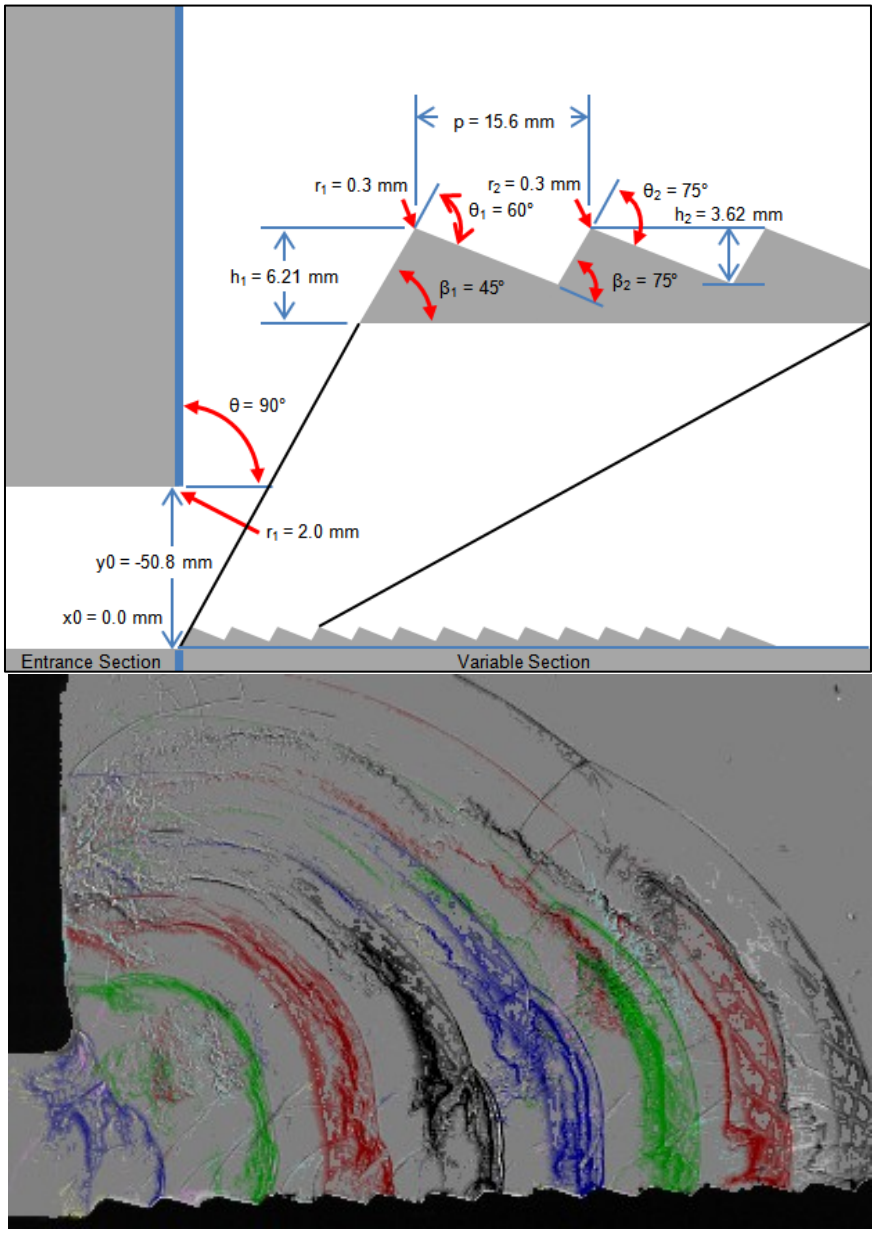

Figure 68. Case M2: multiple 6.4 mm high obstacles

Case M3

The rounded diffraction corners increased the number of reinitiation events in case three from two to three (Fig. 69b). Again, the secondary detonations decoupled before reaching the upper wall of the channel. After case M3, the channel height was reduced to 102 mm to decrease the distance the secondary detonation waves and their associated decoupled shocks had to travel before encountering a solid surface.

a) Schematic

b) Composite Frame: $\Delta t = 20.4\ \mu s$

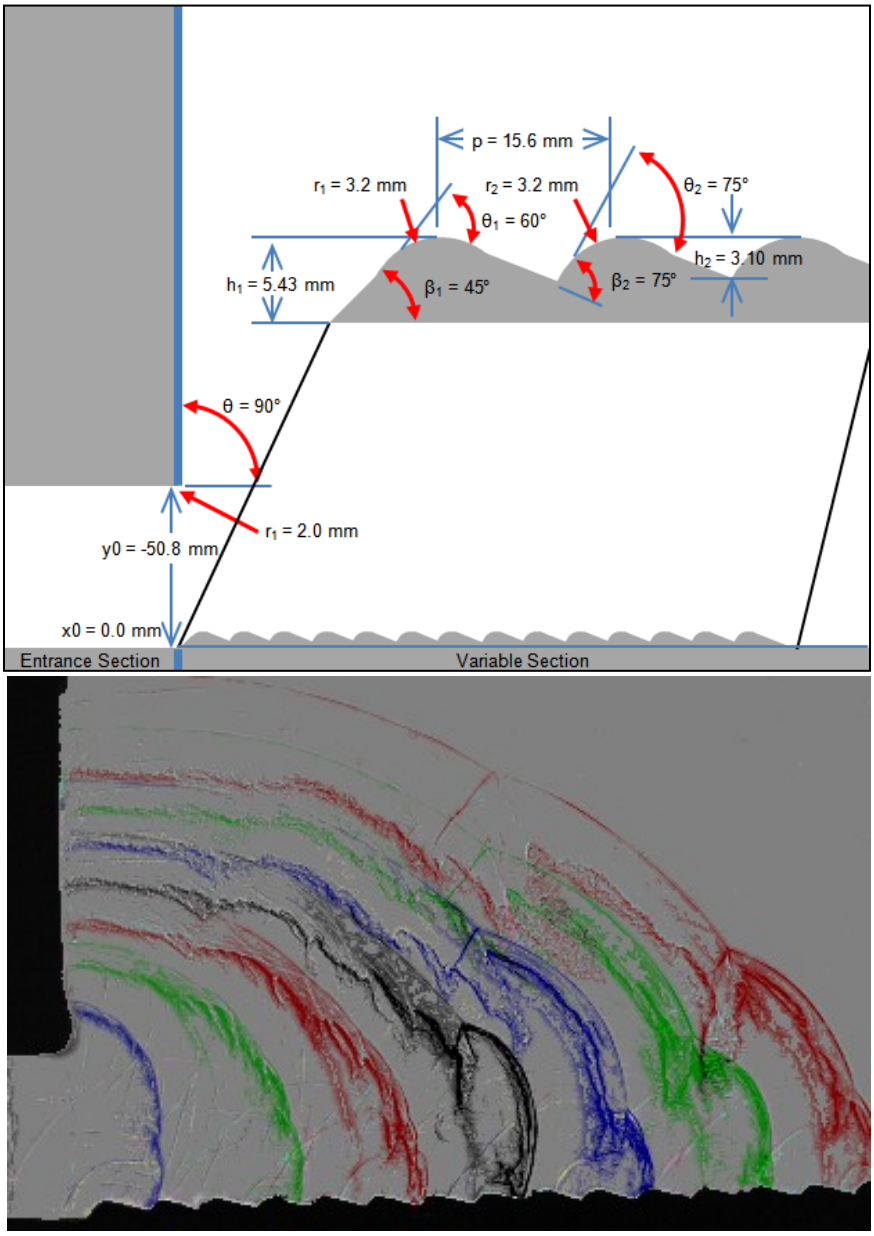

Figure 69. Case M3: multiple 6.4 mm high obstacles with rounded corners

Case M4

The smooth upper wall of the shortened channel in Case M4 (Fig. 70a) reflected the decoupled shocks, but the reflections were too weak for reinitiation (Fig. 70b). The transverse shocks from the second and third secondary detonations did not reach the upper wall before the leading shock reached the end of the test section. In the next iteration, a second set of obstacles was added to the top of the channel to form more transverse waves in order to foster more secondary detonations.

a) Schematic

b) Composite Frame: $\Delta t = 20.4\ \mu s$

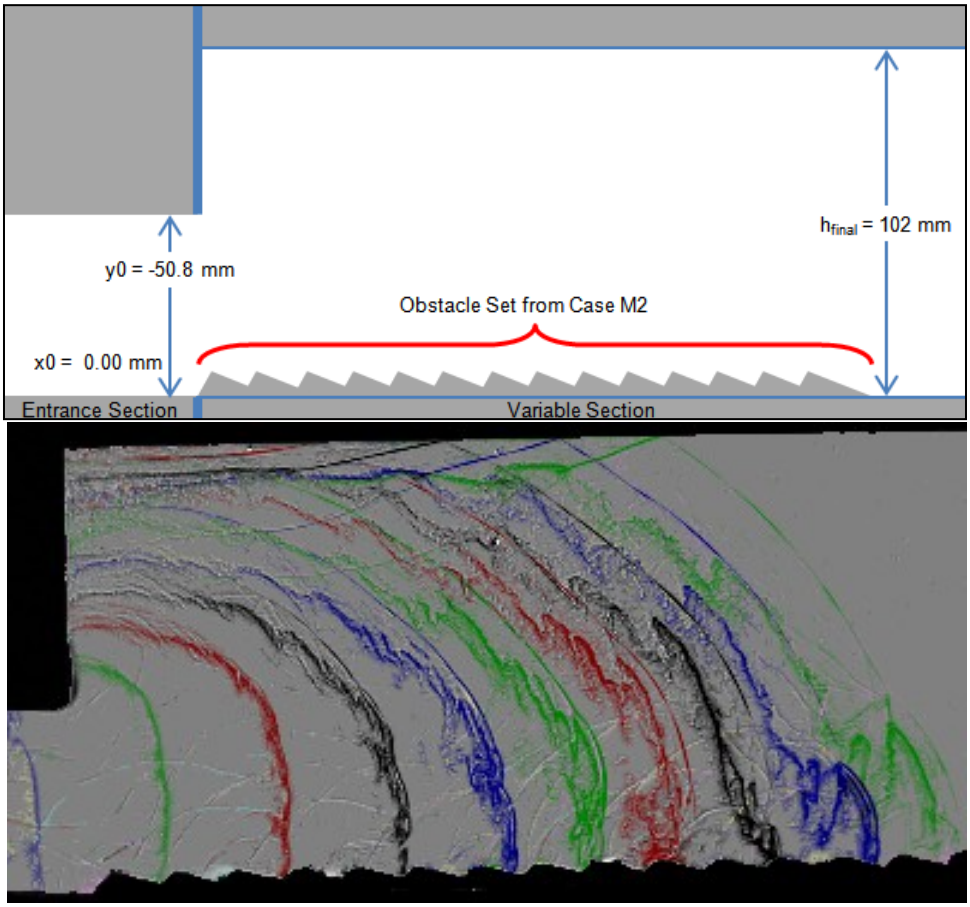

Figure 70. Case M4: multiple 6.4 mm high obstacles in 102 mm tall channel

Case M5

With two sets of obstacles (Fig. 71a), the picture became muddled with several sets of transverse waves overlapping the lead shock in previous frames (Fig. 71b). Two or three secondary detonations formed on the bottom of the channel, but none formed on the top. This was due to the low Mach number of the lead shock at the top of the channel. The separation distance in the final frame was the smallest of the cases so far. In the run shown in figure 71b part of the wave front remained coupled, but that was not consistent across multiple duplicate trials.

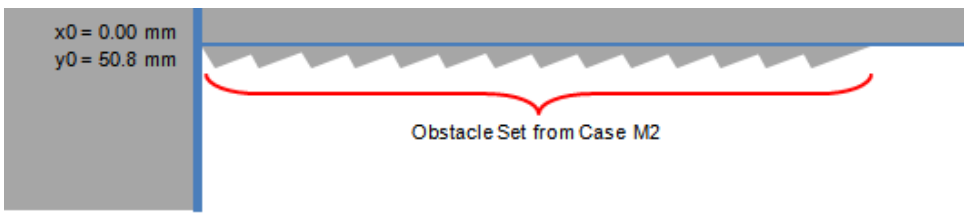

a) Schematic

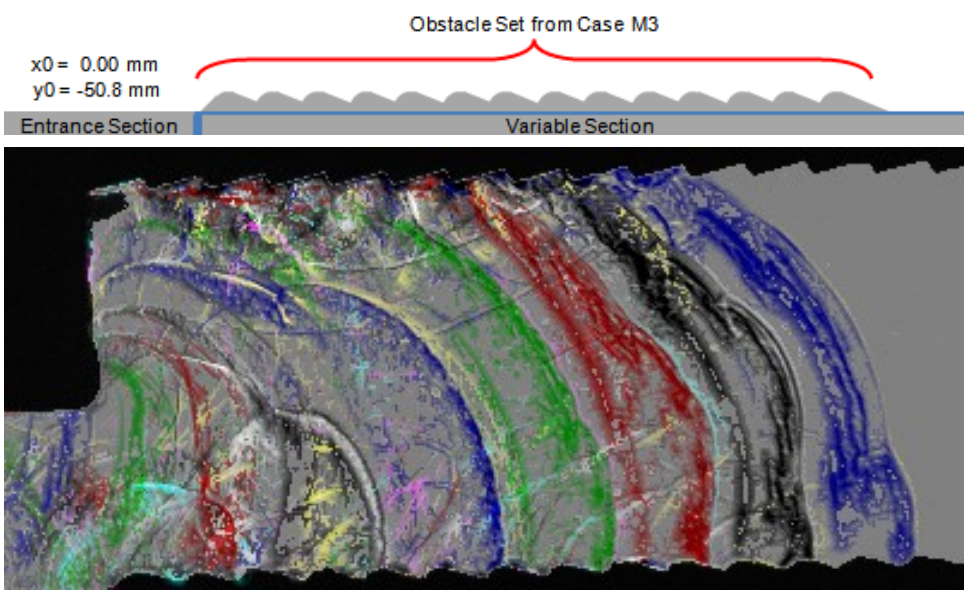

b) Composite Frame: $\Delta t = 20.4\ \mu s$

Figure 71. Case M5: 102 mm high channel with obstacles on both walls

Case M6

To better foster secondary detonation at the top of the channel, the obstacles at the top had their diffraction radius increased in Case M6 (Fig. 72a). Partially coupled wave fronts at the end of the test section were rare and no more likely than in Case M4. Multiple transverse shocks continued to muddle the composite though there were no more secondary detonations. There was no significant difference in the behavior in the two cases. At this point, the test cases changes to a different avenue, modifying the diffraction corner in conjunction with a series of reflection obstacles.

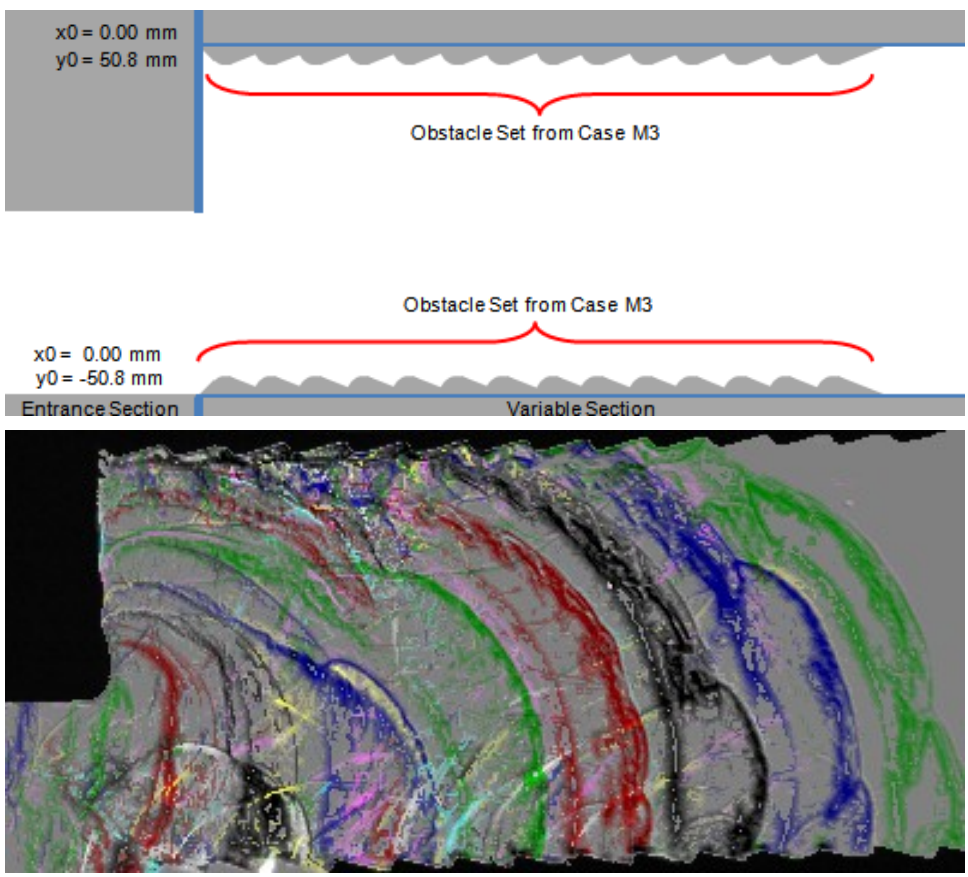

a) Schematic

b) Composite Frame: $\Delta t = 20.4\ \mu s$

Figure 72. Case M6: rounded obstacles on top and bottom walls

Case M7

In case M7 (Fig. 73a), the stepped diffraction corner caused one secondary detonation, and the obstacles on the top of the channel caused none in any of the repeat trials. This configuration performed poorly compared to the case M6, and the separation distance was clearly larger in the final frame (Fig. 73b). This case was the first to exclude obstacles on the bottom of the channel. In the next case, the obstacle set was placed on the bottom of the channel.

a) Schematic

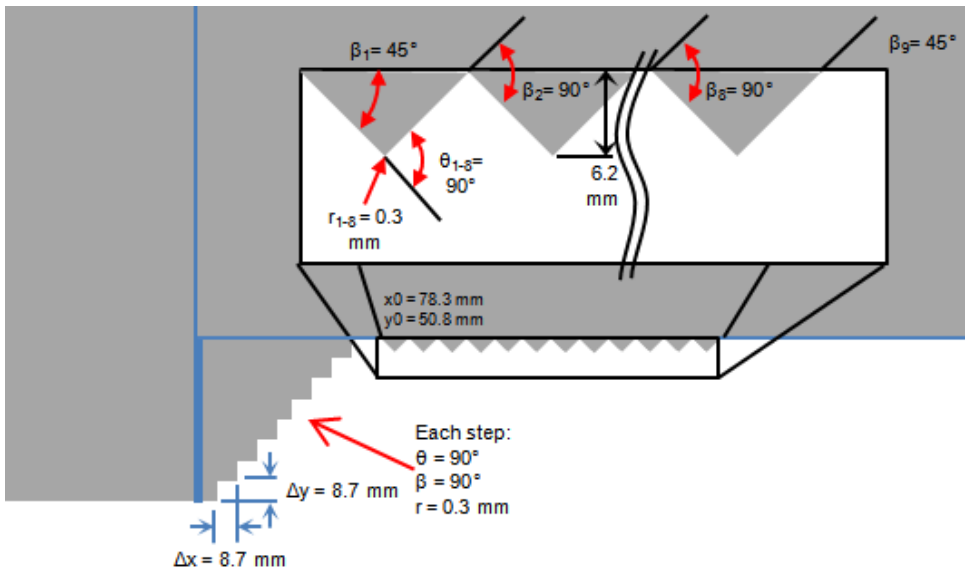

b) Composite Frame: $\Delta t = 20.4\ \mu s$

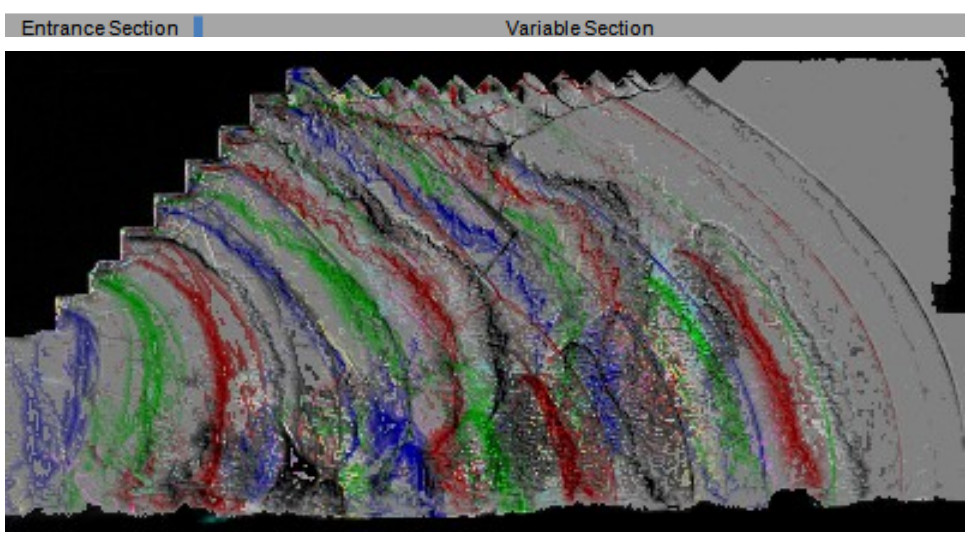

Figure 73. Case M7: Stepped diffraction with obstacles on top wall

Case M8

Moving the set of reflecting obstacles to the bottom of the channel was an improvement (Fig. 74a) because reinitiation occurred at least once. There was at least one reinitiation on the stepped diffraction (Fig. 74b), and none among the obstacle set. At this point, it was clear that the stepped diffraction corner performed worse than previous cases and the next case increased the size of the steps and put some space between the obstacles in order to create two reflections per diffraction.

a) Schematic

b) Composite Frame: $\Delta t = 20.4\ \mu s$

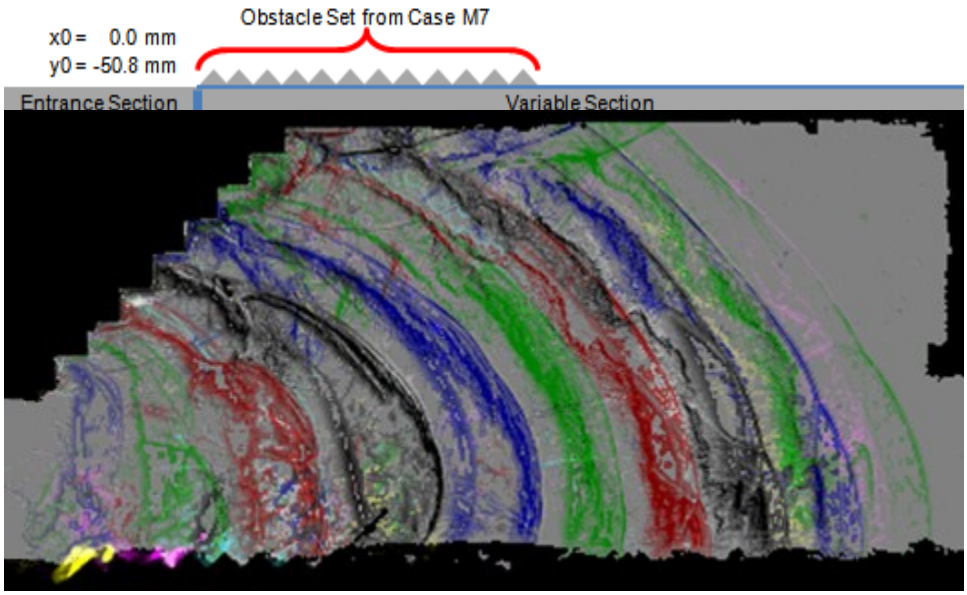

Figure 74. Case M8: Stepped diffraction with obstacles on bottom wall

Case M9

Because decoupling occurred despite the stepped diffraction corner, it seemed possible to reinitiate detonation using the decoupled shock. In case M9, the steps were redesigned to promote reinitiation by splitting the single 90° turn in the wall into two 45° reflections (Fig. 75). The size of the steps was increased to reduce the number of diffractions that a secondary detonation would encounter, and a similar set of obstacles was placed on the bottom of the channel (Fig. 76a). In this configuration, reinitiation always occurred at the first and second obstacles on the bottom of the channel but never at the third obstacle (Fig. 76b). The first obstacle along the diffracting wall caused reinitiation in every case, but the second never did. The first bottom obstacle constricted the channel height in such a way that the combined diffraction of the initial diffraction corner and the diffraction corner at the top of the obstacle reduced the shock strength too much for any further secondary detonations. This was unexpected at the second obstacle on the bottom of the channel should also cause a reinitiation based on reflection case two. The obstacle also restricted flow during filling of the test section forcing increased fill pressure an undesired side effect.

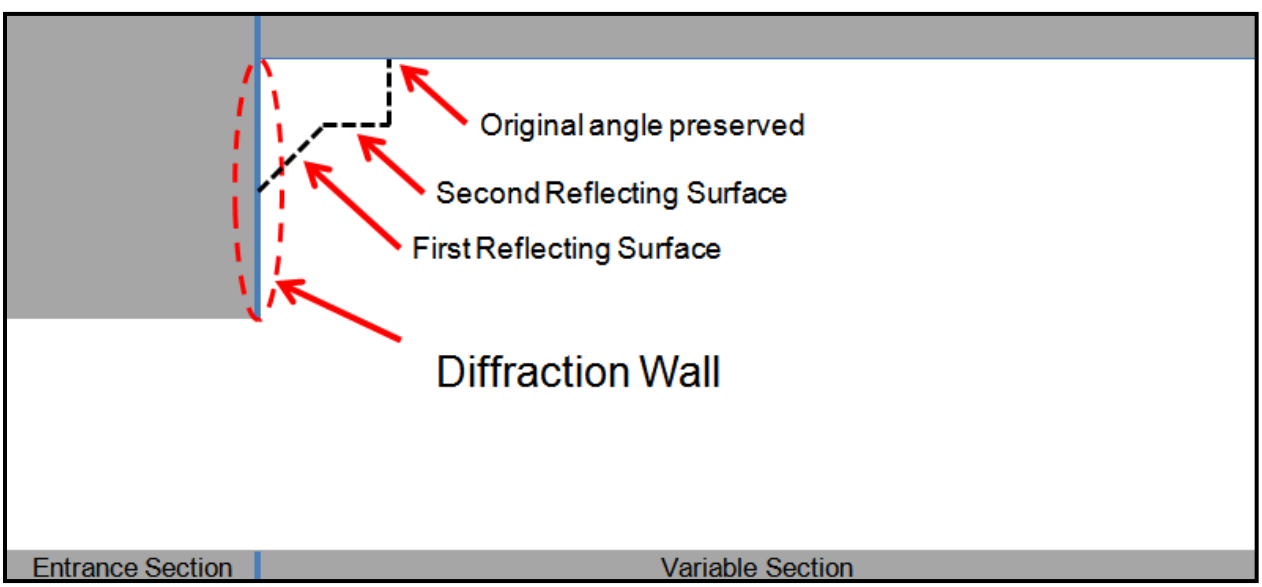

Figure 75. Two-reflection geometry for diffraction step

a) Schematic

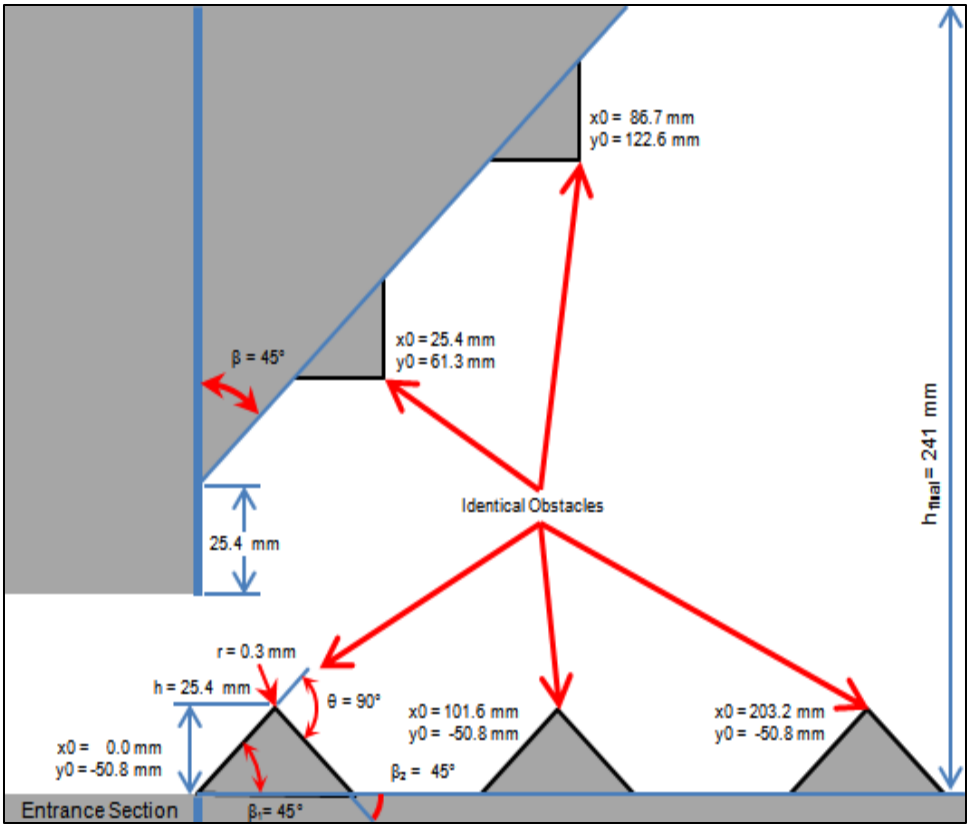

b) Composite Frame:
$\Delta t = 48.8\ \mu s$

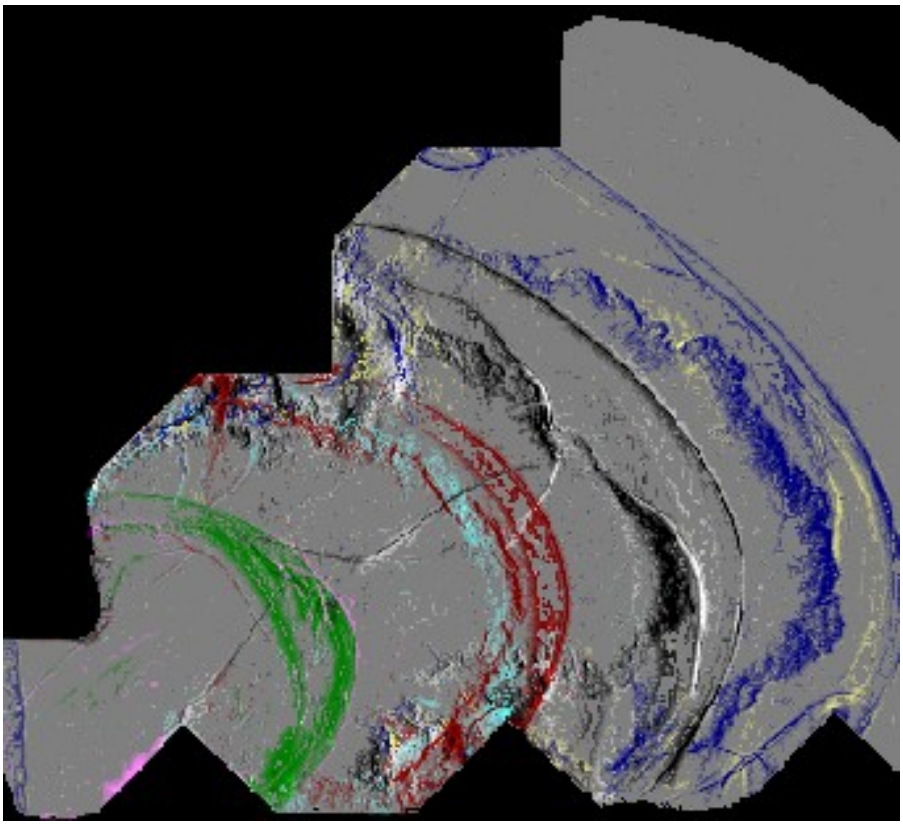

Figure76. Case M9: Double reflection with restriction

Case M10

To relieve the flow restriction caused by the first obstacle, and stagger the diffraction of the initial corner and the obstacles, the first obstacle was removed for case M10 (Fig. 77a). The first, bottom obstacle caused secondary detonation in all five duplicate trials (Fig. 77b). The secondary wave decoupled before traversing the channel in each case, and none of the other obstacles cause reinitiation. Unlike case M9, some of the trials saw shock ignition on the top two obstacles and on the second bottom obstacle. Elevated fill pressures were unnecessary with the first obstacle removed.

a) Schematic

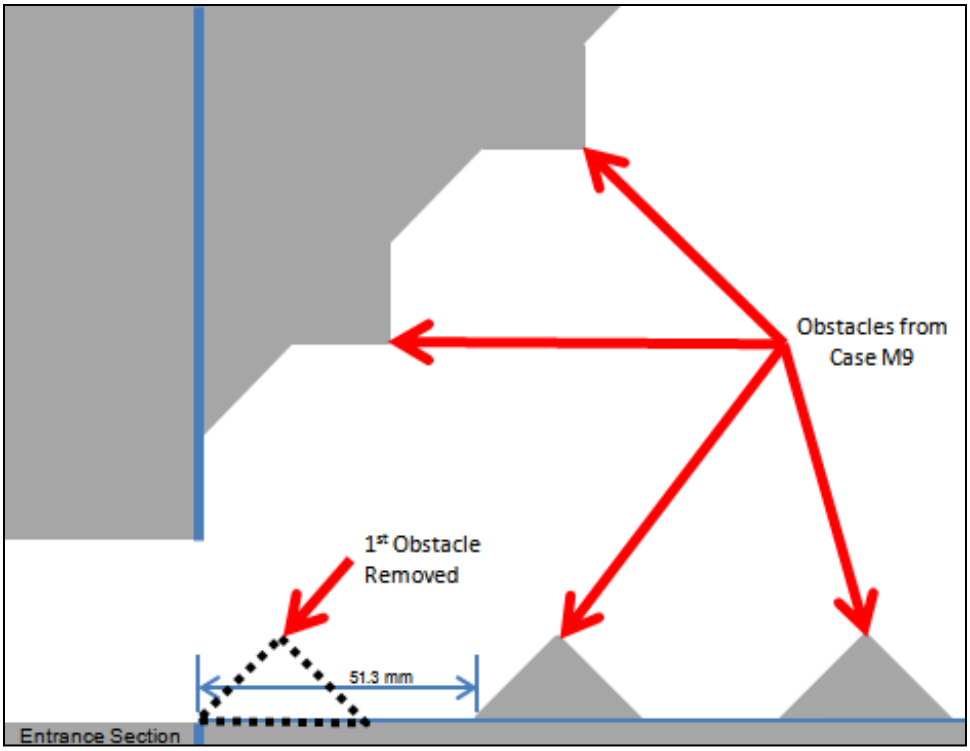

b) Composite Frame:
$\Delta t = 48.8\ \mu s$

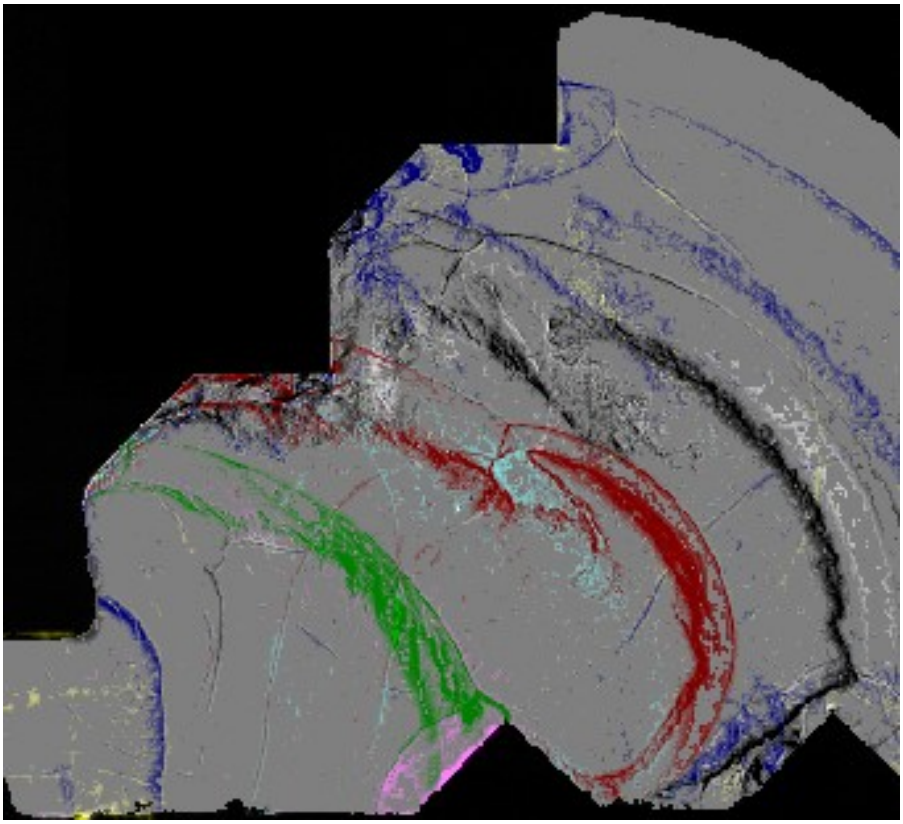

Figure 77. Case M10: Double reflection shape without restriction

Case M11

The final case arranged four obstacles so that the lead shock encountered all of them within 20μs (Fig78). The obstacles were placed with the leading edges on a circle of radius 50.8 mm centered opposite the initial diffraction corner (Fig 79a). The reflection angle of each obstacle exceeded 45° relative to the incident, decoupled shock wave, and the incident shock Mach number exceeded necessary for reinitiation obtained from the R-series test cases. Case M11 was the first configuration to utilize the shock Mach number data from case D2 and the reinitiation requirements obtained in the R-series test cases. This critical information was not available earlier because of the long data processing times required obtain the shock Mach number in case D2.

The result of the informed design of case M11 was four secondary detonation waves, and no decoupling of the initial detonation (Fig. 79b). The five detonation waves traveled down the expanding channels ($\theta_1 = 10°$) between the obstacles. Often, partial decoupling occurred, but all of the waves reached the ends of the obstacles at about the same time. The secondary diffraction corners completely decoupled the secondary detonations, but the collision of decoupled shocks leaving two adjacent channels sometimes caused another secondary detonation. This was the best result of the multiple obstacle cases because it exhibited the spontaneous reinitiation that defines detonation diffraction from critical channels.

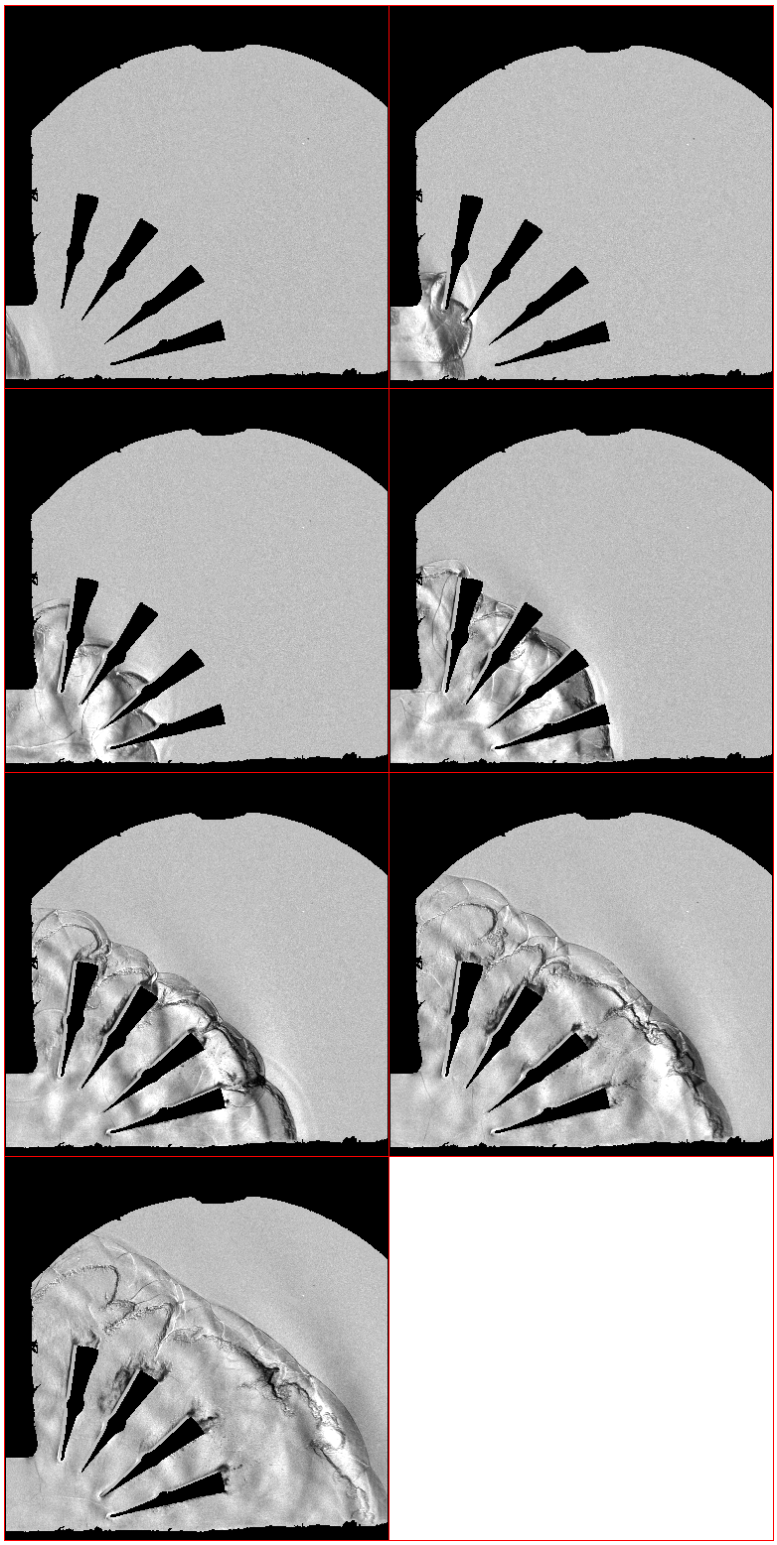

Figure 78 Image sequence of case M11: Run 5 Δt = 20 μs.

a) Schematic

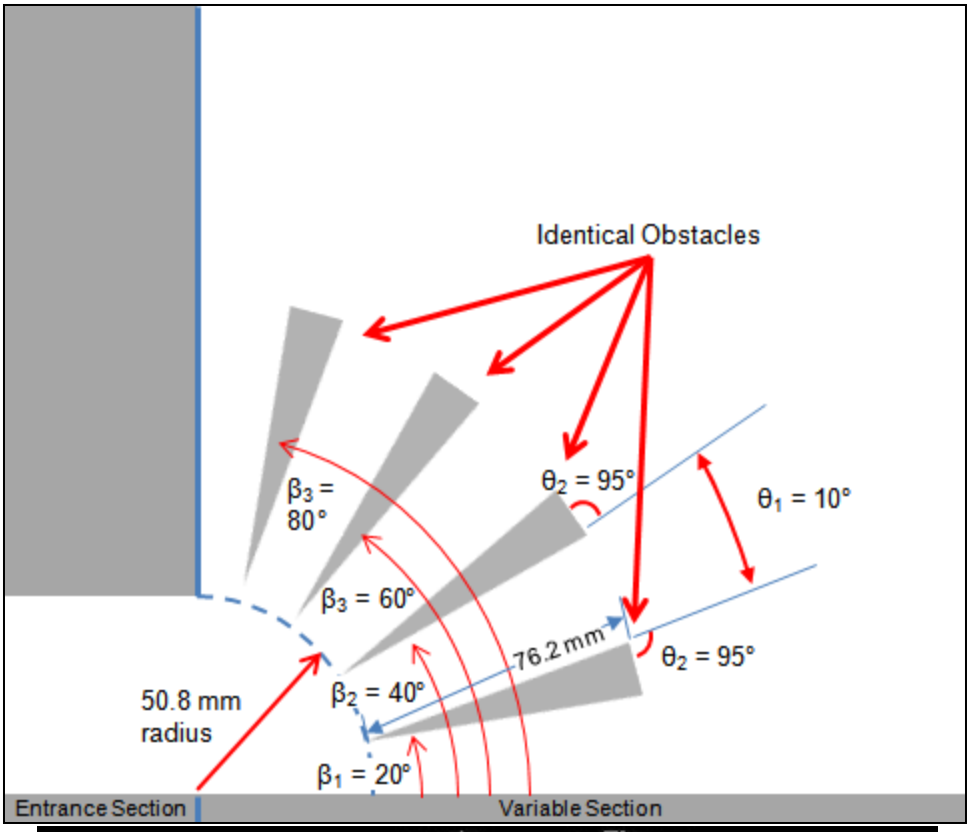

b) Composite Frame: $\Delta t = 48.8\ \mu s$

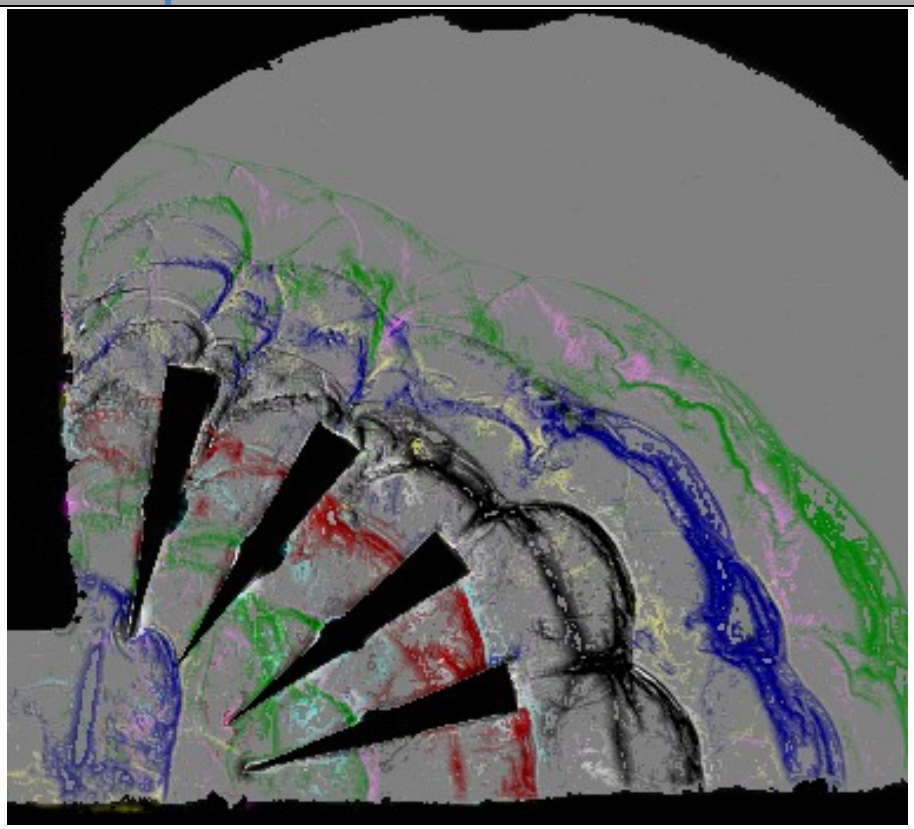

Figure 79. Case M11: Split channel geometry

Overall trends in reinitiation for the M series cases

The multi-obstacle cases utilized different numbers of obstacles, and in general, the cases with more obstacles had more reinitiations. The added obstacles come at the cost of higher flow loss. Figure 78 shows that each additional obstacle has a reduced maximum chance of causing a reinitiation. For 14 or more obstacles, the chance of reinitiation is at most 86%. Based on Figure 79, no more than 12 obstacles should be used for the current channel height and fuel because there is no additional benefit from the added obstacles.

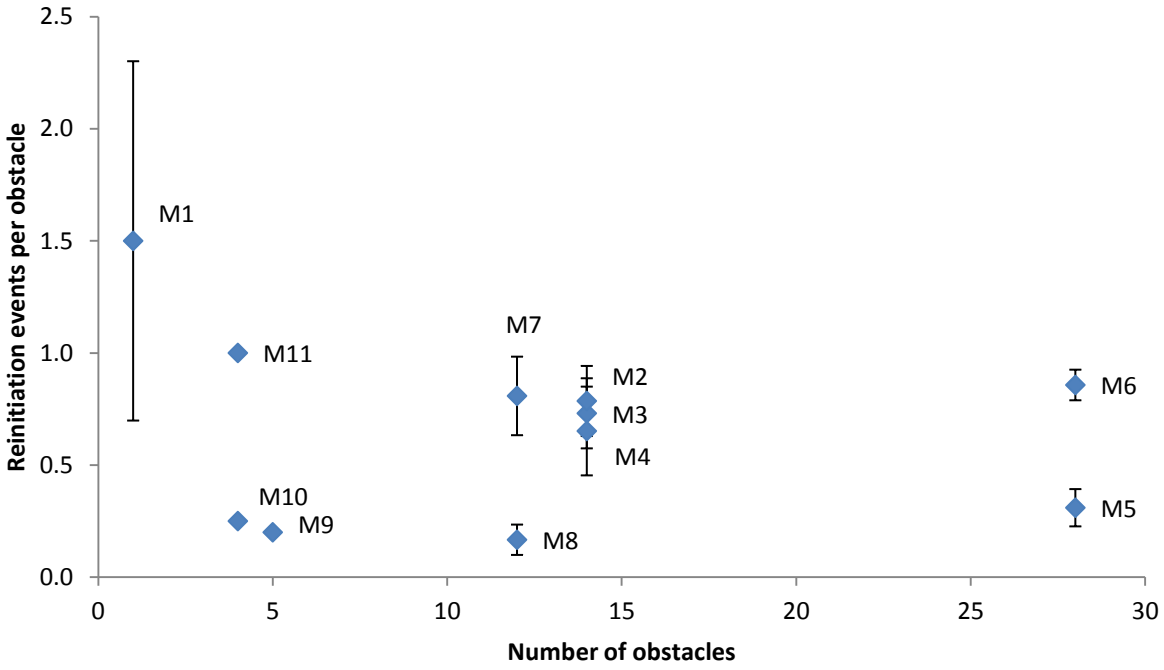

Figure 80. Diminishing return of additional obstacles

For a simple quantitative comparison of the different configurations, the separation distance was measured at two points in each case. One point was at the bottom of the channel in the last frame where the leading shock was visible, and the other was along the diffraction wall in the frame before the lead shock encountered the top of the channel. These measurements provided a basic indicator of the performance in each case. Smaller separations were preferred since they indicated the least time after decoupling. Figure 80 shows how the separation distances evolved through the series. In the early cases (M1-M3), low separation at the bottom of the channel came with high separation at the. Starting with case M4, separation at the top began to match the bottom, and at the end of the series, both are at their lowest.

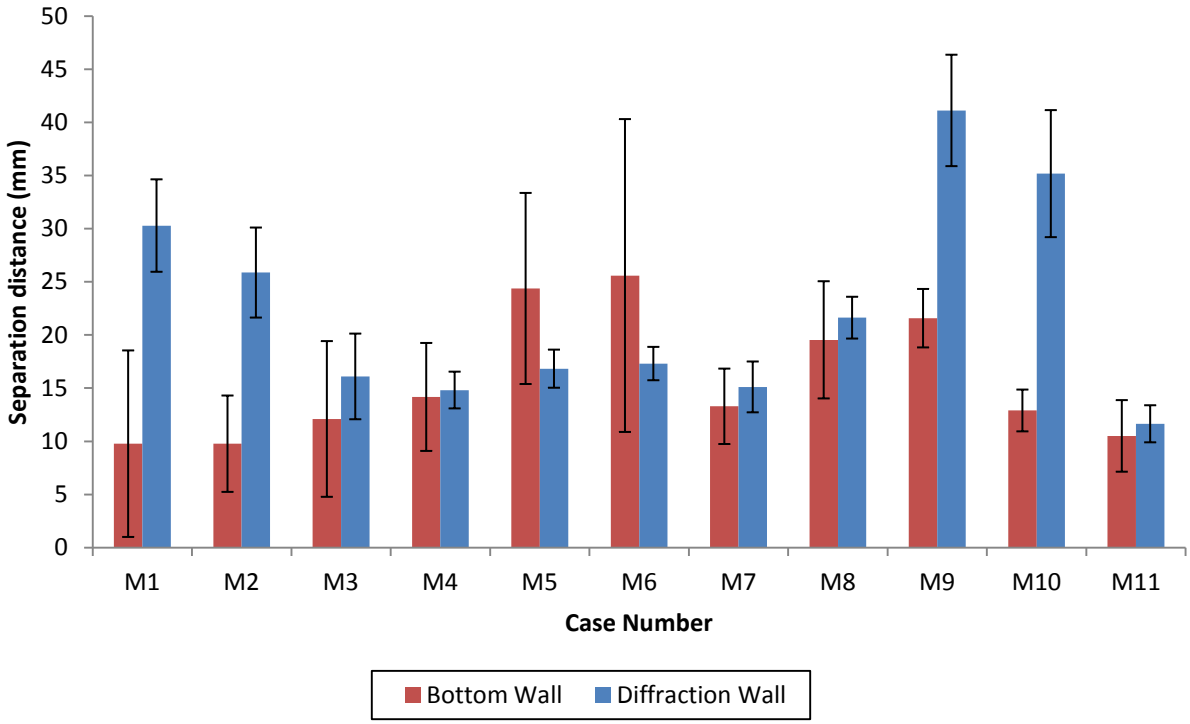

Figure 81. Comparison of final separation distance for M-series cases

VI. Discussion

Crossover tube studies identify diffraction and reflection parameters.

In a crossover tube, the incoming detonation first diffracts when it encounters the entrance of the crossover tube (Fig. 15). Then the decoupled shock reflects from the reflecting surface reinitiating detonation. Shock reflection and subsequent reinitiation of detonation inspired the concept of a detonation diffuser that used a combination of diffraction and reinitiation to transmit a detonation from a subcritical channel to a supercritical channel without going through DDT.

Crossover tube experiments were useful for identifying some of the important parameters in a detonation diffuser (Figs. 16 and 17). The diffraction angle, diffraction corner radius, and the reflecting surface angle were the three parameters that influenced the diffraction and reinitiation in crossover tubes. Each parameter was studied in depth to determine the effect on reinitiation.

Diverging/Converging experiment establishes feasibility and benefit.

To determine whether a detonation diffuser utilizing decoupling and reinitiation was feasible and beneficial, an experiment was carried out to compare a diverging geometry to a step expansion followed by a converging wall (Figs. 50 and 51). The divergence angle in the diverging case was less than the theoretical maximum for a detonation to remain coupled, but in disagreement with theory decoupling was observed in schlieren video. In the converging case, the primary detonation decoupled before it encountered the converging wall. Then a large increase in chemiluminescence near the midpoint of the converging section signaled reinitiation. Analysis of the two cases indicated that the converging configuration would result in a 2.3% shorter transition to a supercritical channel height than a diverging channel.

Diffraction cases indicate small diffraction angle preferred and corner radius trends mixed.

Following the Diverging/Converging experiment, the results aim to satisfy the research objective defined in Chapter I. The diffraction test cases (D-series) provide the required maps of shock Mach number and separation distance (Figs. 53–55). In the D-series of test cases, measurements of the separation distance and shock Mach number indicated that detonations partly decouple at a diffraction angle of 15° and fully decouple at larger angles (Figs. 53 and 54). Partial, temporary decoupling explains the decoupling that was observed at diffraction angles less than the theoretical limit in the previously discussed diverging/converging experiment. The separation distance increases linearly with diffraction angle at a point 200 mm ($3.94 \cdot h_{initial}$) downstream of the diffraction corner (Fig. 56a). The Mach number also decreased with increasing diffraction angle, but the trend was nonlinear with larger rate of decline between 0° and 15° than between 15° and 90° (Fig. 56b). Increasing the corner radius had mixed results depending on location. Near the bottom of the channel, the separation distance decreased and the Mach number increased (both of which are preferred) (Fig. 57a). At a point along the vertical wall ($y_0 = h_{initial}$), the separation increased and the Mach number decreased at rates similar to the improvements along the bottom of the channel (Fig. 57). Later, in case R5 the corner radius was shown to have no statistically significant effect on reinitiation (Fig. 62). The combination of mixed and insignificant effects suggests that an arbitrary choice of corner radius is acceptable in the range of 2-25 mm.

Chance of reinitiation depends strongly on reflection angle and position.

The R-series test cases found the range in each of three parameters (β, x_0, and y_0) were reinitiation occurred and the probability of reinitiation within those ranges. Reinitiation of detonation via oblique shock reflection had two operational regions. In the first region,

reinitiation was certain due to ample compression of reactants and sufficient separation between the shock and combustion fronts (Fig. 66a). Reinitiation was certain for the operating space where $\beta = 45°$, $y_0 = -h_{initial}$, and $x0 \leq 1.67 \cdot h_{initial}$ (Fig. 66a). In the second region, reinitiation occurred in some fraction of the repeated trials (Fig. 66a). The probability of reinitiation increased with increasing β, decreased with increasing x_0 and decreased with increasing y_0 (Fig. 66). When $y_0 = h_{initial}$, reinitiation only occurred for $x_0 = 3.33 \cdot h_{initial}$ and only 44% of the time (Fig. 66b). There was a tradeoff between shock strength and separation distance when $y_0 = h_{intial}$. At lower x_0 secondary detonations became trapped by the decoupled combustion front, and at high x_0 the lead shock decayed too much for a secondary detonation to form (Fig.66b).

Multi-obstacle cases bridged the gap between subcritical and critical diffraction behavior

The multi-obstacle test cases satisfied the phase 3 research objectives by quickly iterating on the size, number and position of obstacles using a qualitative evaluation of each geometry. The M-series cases utilized the information gained from the D and R series to bridge the gap between subcritical and critical diffractions. Two cases (M6 and M11) maintained partial coupling when the wave reached the end of the test section (Figs. 72 and 78). One of the two (M11) also exhibited spontaneous reinitiation after the obstacles (Fig. 78b). In case M11, the spontaneous reinitiation of detonation indicated critical diffraction behavior. The results indicate that a fully successful detonation diffuser should initiate multiple secondary detonations that combine to form a fully coupled detonation front. The first two steps for improving the geometry in following design iterations are to eliminate the expansion in the channels between obstacles and to reduce the diffraction angle at the end of the obstacles.

VII. Conclusion and Future Work

A detonation wave in a subcritical channel decouples when diffracted. Decoupling is undesired in the transition between a predetonator and the thrust tube in PDEs where the smallest possible predetonator minimizes weight and fuel requirements. A detonation diffuser of the type studied in this research reinitiates detonation after the decoupling by reflecting the decoupled shock wave back into itself. The initial diffraction angle, θ, should be as small as space considerations allow, and the corner radius, r, can be anywhere between 2 and 25 mm with no adverse effect. An oblique shock reflection is sufficient to reinitiate detonation with sufficient shock strength and mixture sensitivity. The reflection angle must be 45° or greater for certain reinitiation. The lead obstacle if placed on the wall of the channel opposite the diffraction corner (bottom wall) should be no more than $1.67 \cdot h_{initial}$ downstream. Moving the lead obstacle away from the bottom wall reduced the minimum downstream distance and the minimum distance was 0 when the lead obstacle was $h_{initial}$ above the diffraction corner. Multiple obstacles in series caused multiple reinitiations, but there was a diminishing return associated with each additional obstacle. No more than 12 obstacles should be used in series. A better design reinitiated detonation in four separate sub channels, and exhibited the spontaneous reinitiation that defines a critical diffraction.

Future research in detonation diffraction and reinitiation should concentrate on separate reinitiation of several secondary detonations from the initially decoupled shock. The first two steps of further investigation are to reduce the diffraction angle at the ends of the obstacles in case M11 and to eliminate the expansion in the channels between obstacles. The ultimate goal is to achieve fully coupled detonation at a super-critical channel height at the exit of the diffuser.

Once the channel height exceeds the critical height, no special geometry is necessary to expand into arbitrarily large thrust tubes.

VIII. Bibliography

Anderson, J. D., *Modern Compressible Flow: with Historical Perspective*, 3rd Ed., McGraw-Hill, New York, 1982

Arienti, M. and Shepherd, J.E. "A Numerical Study of Detonation Diffraction", *Journal of Fluid Mechanics*, Vol. 529, pp. 117-146, 2005.

Brown, C. J. and Thomas, G. O. "Experimental Studies of Ignition and Transition to detonation induced by the Reflection and Diffraction of Shock Waves," S*hock Waves,* Vol. 10, pp-23-32, 2000.

Bartlma, F. "The Propagation of Detonation Waves in Channels of Varying Cross-Section," *Journal of Fluid Mechanics*, Vol. 218, pp. 225-238, 1990.

Camardo II, L. A., "Determination of Effective Crossover Location and Dimensions for Branched Detonation in a Pulsed Detonation Engine" M. S. Thesis, *Air Force Institute of Technology,* Wright-Patterson AFB, Ohio, March 2012.

Ciccarelli, G., Ginsberg, T., Boccio J. L., Finfrock, C., Gerlach, L., "Detonation Cell Size Measurements in High-Temperature Hydrogen-Air-Steam Mixtures at the BNL High Temperature combustion Facility", NUREG/CR-6391, United States Nuclear Regulatory Commission, 1994

Coleman, H. W. and Steele, W. G., *Experimentation and Uncertainty Analysis for Engineers,* John Wiley & Sons, New York, 1989.

Gamezo, V. N., Desbordes, D., and Oran, E. S. "Formation and Evolution of Two-dimensional Cellular Detonations," *Combustion and Flame,* Vol. 116, pp. 154-165, 1999

Hoke, J., Bradley, R., Gallia J., and Schauer, F. "The Impact of Detonation Initiation Techniques on Thrust in a Pulsed Detonation Engine," AIAA-2006-1023, *44th AIAA Aerospace Sciences Meeting and Exhibit*, Reno, NV, 2006.

Kaneshige M. and Shepherd, J. E. *Detonation Database*. Technical Report FM97-8, GALCIT, July 1997.

Knox, B. W., Forliti. D. J., Stevens, C. A., Hoke, J. L., and Schauer, F. R., "Unsteady Flame speed control and Deflagration-to-Detonation Transition enhancement using fluidic Obstacles" AIAA Paper 2010-151, *48th AIAA Aerospace Sciences Meeting Including the New Horizons Forum and Aerospace Exposition,* Orlando FL, January 2010

Knox, B. W., Forliti, D, J., Stevens, C. A., Hoke, J. L., and Schauer, F. R., "A Comparison of Fluidic and Physical Obstacles for Deflagration-to-Detonation Transition", AIAA Paper 2011-587, *49th AIAA Aerospace Sciences Meeting Including the New Horizons Forum and Aerospace Exposition,* Orlando FL, January 2011

Lee, John H. S. *The Detonation Phenomenon*. 1st ed., Cambridge University Press, Cambridge, 2007

Mitrofanov, V. V., "The Diffraction of Multifront Detonation Waves," *Soviet Physics Doklady,* Vol. 9, pp.1055, 1965

Moen, I. O., Murray, S. B., Bjerketvedt, D., Rinnan, A., and Knystautas, R. "Diffraction of Detonation from Tubes into a Large Fuel-Air Cloud," *Symposium International on Combustion*, Vol. 19, Issue 1, pp 635-644, 1982

Nettleton, M. A., *Gaseous Detonations: their nature, effects, and control*, Chapman and Hall, New York, 1987

Nielsen, J. M., King, P. I., Schauer, F. R., Stevens, C. A., and Hoke, J. L., "Detonation Propagation through Ducts in a Pulsed Detonation Engine", AIAA Paper 2011-585, *49th AIAA Aerospace Sciences Meeting Including the New Horizons Forum and Aerospace Exposition,* Orlando FL, 2011

Nielsen, J. M. "Detonation Propagation through Ducts in a Pulsed Detonation Engine," M. S. Thesis, *Air Force Institute of Technology,* Wright-Patterson AFB, OH, 2011

Nakayama, H., Takahiro M., Kasahara, J., Matsuo, A., and Sasamoto, Y. "Stable Detonation wave propagation in Rectangular-Cross-Section Curved Channels" *Combustion and Flame* Vol. 159, Issue 2, pp 859-869, February 2012.

Pintgen, F., "Detonation Diffraction in Mixtures with Various Degrees of Instability," Ph.D. Thesis, *California Institute of Technology,* Pasadena CA, 2004

Saitsev, S. G. and Soloukhin, R. I., *Proc. Ac. Sc. U.S.S.R. Phys. Chem. Sec.* (1958) pp 122

Schauer, F., Stutrud, J., and Bradley, R. "Detonation Initiation Studies and Performance results for Pulsed Detonation Engines," AIAA paper 200-1129, *39th AIAA Aerospace Sciences Meeting and Exhibit,* Reno NV, 8-11 January 2001

Schultz, E., and Shepherd, J. "Validation of Detailed Reaction Mechanisms for Detonation Simulation," *Explosion Dynamics Laboratory Report FM99-5*, Pasadena, CA, 2000.

Settles, G. S., Schlieren and shadowgraph techniques: visualizing phenomena in transparent media, Springer-Verlag, New York, 2001

Shepherd, J. E. and Akbar, R. "Detonation Diffraction," 22nd International Symposium on Shock Waves, London, July 18-23 1999

Skews, B. W. "The Shape of a Diffracting Shock Wave," *Journal of Fluid Mechanics,* Vol. 29, pp-297-304, 1967

Soloukhin, R. I. and Ragland, K. W. "Ignition Processes in Expanding Detonations," *Combustion and Flame,* Vol. 13, Issue 3, pp 295-302, June 1969

Stevens, C. A., Gamezo, V. N., King, P. I., Schauer, F. R., and Hoke, J. L., "Interaction of Detonations with Ramps" *49th AIAA Aerospace Sciences Meeting Including the Nnew Horizons Forum and Aerospace Exposition,* Orlando FL, January 2011, AIAA Paper 2011-324

Stevens, C.A., Gamezo, V. N., King, P. I., Schauer, F. R., and Hoke, J. L., "Interaction of Detonations with Ramps" 36th Dayton Cincinnati Aerospace Science Symposium, Dayton OH, March 2011.

Stevens, C. A., King, P.I., Schauer, F.R., and Hoke, J.L., "Detonation Reinitiation by Oblique Shock Reflection", 50th AIAA Aerospace Sciences Meeting, Nashville, TN, January 2012, AIAA Paper 2012-0978.

Stevens, C.A., King, P.I., Schauer, F.R., and Hoke, J.L., "An Experimental Study of Detonation Diffraction and Reinitiation" 51st AIAA Aerospace Sciences Meeting, Dallas TX, January 2013, AIAA Paper 2012-1027.

Strehlow, R. A. and Cohen, A. "Initiation of Detonation," *Phys. Fluids,* Vol. 5, Issue 1, pp 97, 1962

Thomas, G. O., Ward, S. M., Williams, R. L., and Brambrey, R. J., "On critical conditions for detonation initiation by shock reflection from obstacles," *Shock Waves,* Vol. 12, pp. 111-119, 2002

Turns, Stephen R., *An Introduction to Combustion: Concepts and Applications*, 2nd Ed. McGraw-Hill, Boston, 2000.

Urtiew P.A., Oppenheim A. K., "Experimental Observations of the Transition to Detonation in an Explosive Gas," *Proceedings of the Royal Society of London. Series A, Mathematical and Physical Sciences*, Vol. 295, No. 1440 (Nov. 8, 1966), pp. 13-28.

Vision Research Inc. *1Mpx v-Series Spectral Response,* Support document for the Phantom v12.1 camera, *http://www.visionresearch.com/uploads/Docs/SpectralResponse/1Mpx_vSeries_Spectral_Response.pdf,* accessed 25 April 2011

Zeldovich, Y. B. "An Experimental Investigation of Spherical Detonation of Gases," *Sov. Phys. Tech. Phys.* 1956

IX. Appendix A – Schlieren technique, equipment, and uncertainty

Technique

Schlieren visualization takes advantage of the coupling between density and refractive index to make structures visible in transparent media (Settles, 2001).

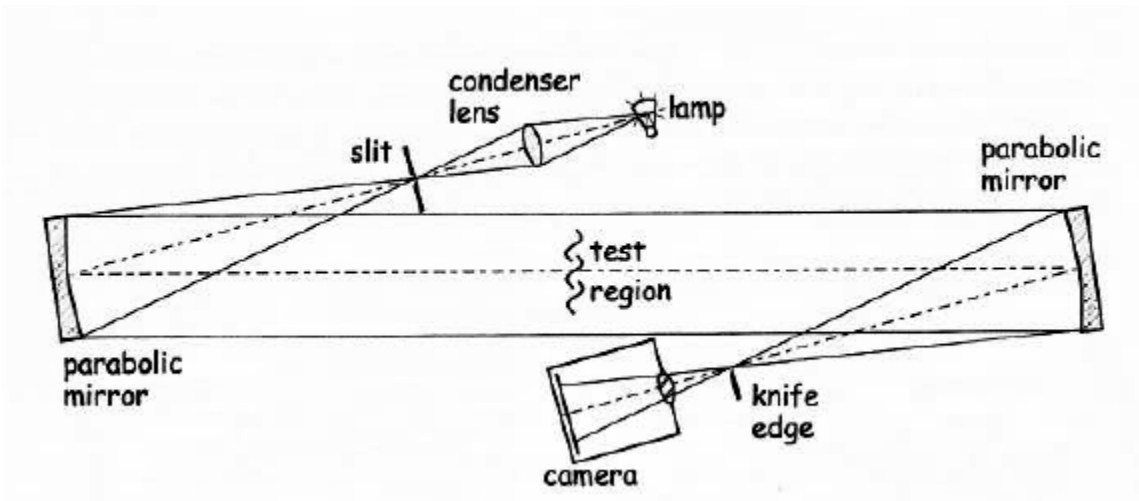

Figure A-1. Z-type schlieren arrangement (Settles, 2001)

In Fig. A-1, the primary mirror collimates light from a point source (the slit). The parallel light passes through the test region where density gradients diffract some of the rays. The secondary mirror focuses the remaining parallel beam to an image of the source. The diffracted rays focus to points away from the image of the source. The direction a ray is displaced depends on the sign of the density gradient, and the distance depends on the magnitude of the gradient. Beyond the source image, an image of the test region forms. Without further interference, structures in the flow are visible as shadows with adjacent bright areas on either side (Fig. A-2a). Adding a knife-edge at the source image blocks some of the rays eliminating the bright band on one side of a structure and revealing the direction of gradients.

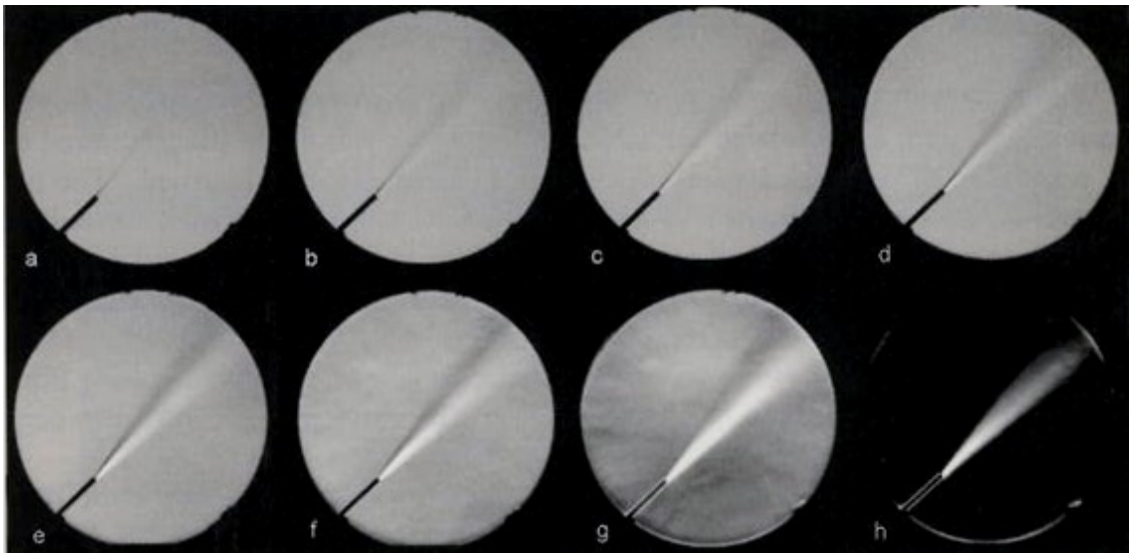

Figure A-2. Series of schlieren photos of a turbulent gas jet with increasing cut-off. The cut-off degree is a) 0%, b) 20%, c) 40%, d) 60%, e) 80%, f) 90%, g) 95%, and h) 100%. Photos by Rosanna Quiñones (Settles, 2001)

The selection of a camera determines the spatial and temporal characteristics of the recorded images. The schlieren technique is analog and the magnification, resolution, exposure, and frame rate of the camera determine the sampling and uncertainty of the image. Magnification and pixel count set the spatial resolution. Frame rate and exposure set the temporal resolution.

Equipment

The schlieren system used in this research is an adaptation of the z-type configuration (Fig. A-3). The layout changed significantly after Nielsen's crossover study (Fig. A-4) because the camera was too far from the test section to bring objects into sharp focus, and to decrease distortion of the parallel beam due to the large turning angles at the fold mirrors. The drawback of the current layout is that all four mirrors, the light source, and the camera table must be moved to image a different section of the thrust tube.

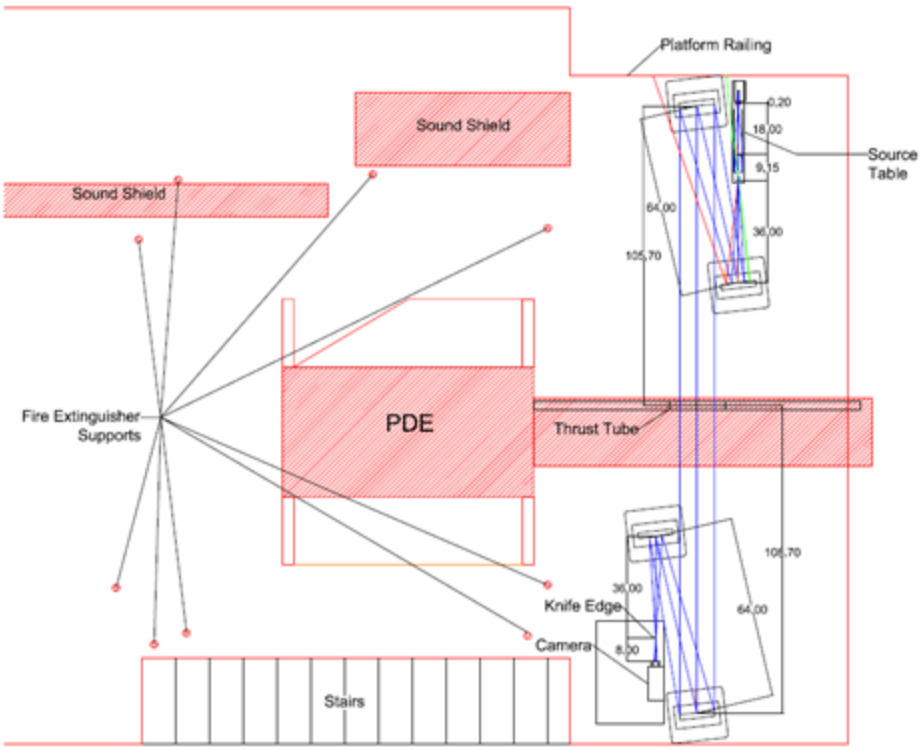

Figure A-3. Schlieren arrangement for detonation diffuser study

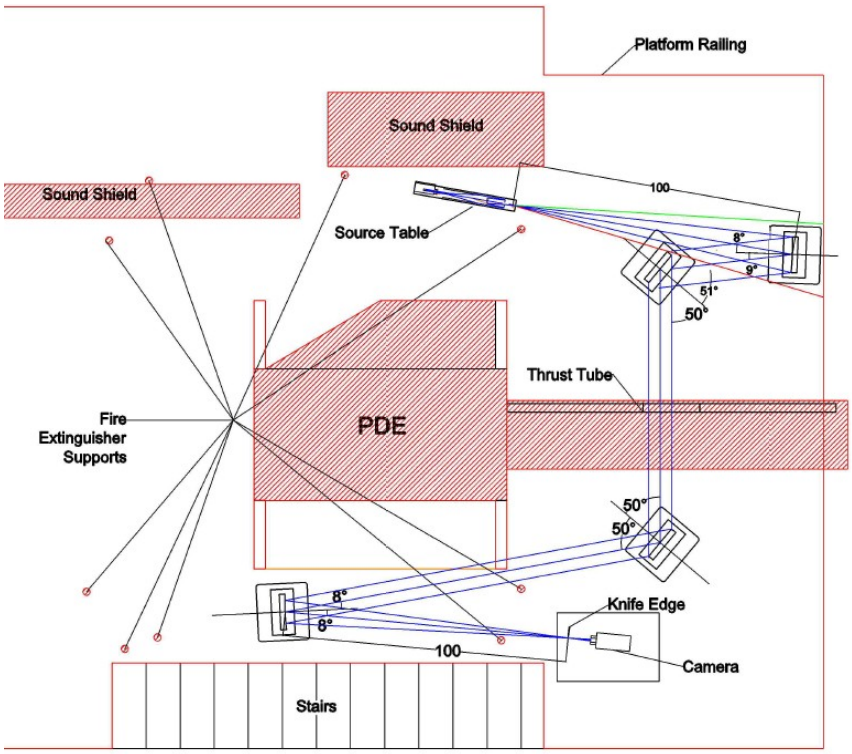

Figure A-4. Previous arrangement

The system is composed of a custom light source, two 318 mm diameter, focusing mirrors, two 318 mm diameter flat mirrors, a knife edge, and a camera.

The light source consists of a 9000lm LED, two lenses, a pinhole, and a blackout tube all mounted to an optical breadboard (Fig. A-5). The lenses condense the light from the aperture diameter of the lamp to the diameter of the adjustable slit. The slit was useful for alignments since it produces a small image at the focal plane, but no aperture was used for imaging. The pinhole sharpens the focus. A blackout tube blocks stray light preventing interference with the parallel beam. The entire apparatus attaches to a breadboard to preserve the alignment between uses.

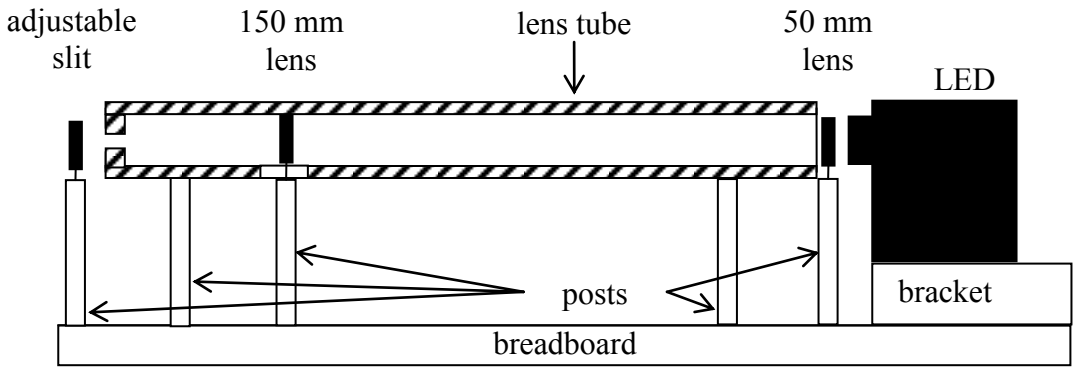

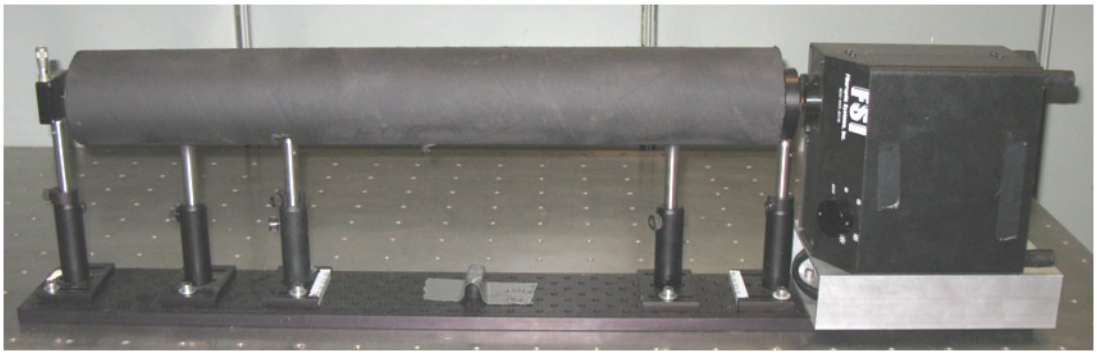

Figure A-5. Light source assembly

The focusing mirrors are aluminum first surface mirrors with 2.54 m local length (Fig. A-6). The mirror substrate is Pyrex ® ground to a parabolic curvature with focal length accuracy of ±1.5%. The surface accuracy is 1/8th of the median wavelength. For the visible spectrum, the accuracy is 70 nm. The reflective coating is a thin layer of pure aluminum. A 275 nm thick SiO layer prevents oxidation and protects the aluminum. The adjustable mounts hold the mirrors and sheet metal covers prevent damage between uses. The mounts bolt to heavy stands with adjustable legs for leveling. The flat mirrors are also high quality first surface mirrors. The construction of the flat mirrors is identical to the focusing mirrors. They also have 1/8th wavelength surface accuracy. The mounts and stands used for the flat mirrors are the same as for the focusing mirrors.

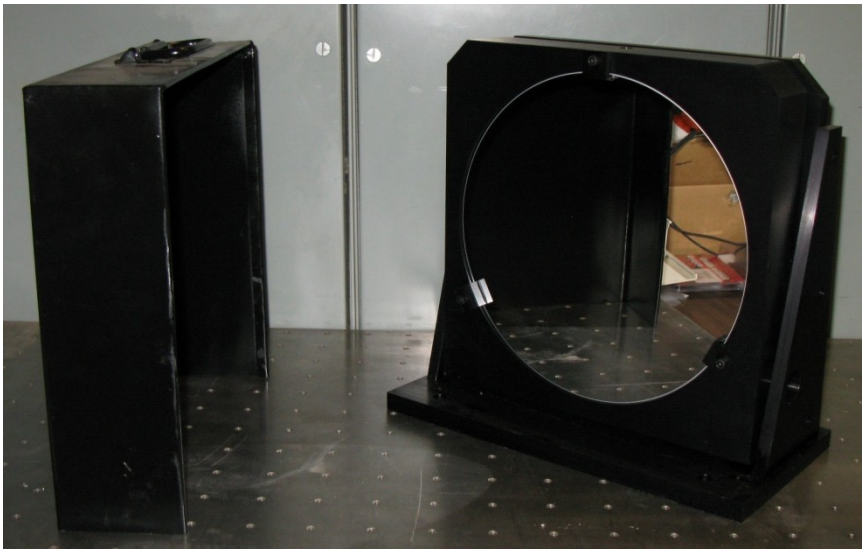

Figure A-6. Focusing mirror with cover

The knife-edge is an ordinary razor blade mounted on a translation stage. An optical filter mount that bolts to the translation stage holds the razor blade. A filter mount holds the blade vertically or horizontally to image horizontal or vertical gradients respectively. The stage

allows 25 mm of overall travel, and has a fine threaded screw for fine placement. Daily inspection of the edge ensured that there were no nicks or corrosion that could affect the cut-off.

The camera used for detonation diffuser study was a Phantom v710. The V710 has a 1280 by 800 pixel array and full resolution frame rate of 7530 frame/s. At reduced resolution, the maximum frame rate increases 1.4 million times per second. The exposure is adjustable from 296 ns to 1 ms. An external trigger starts recording within 100 ms of the first detonation in a burst. A laptop equipped with control software adjusts the camera settings and saves images over a network connection.

Uncertainty

The selection of a camera determines the spatial and temporal uncertainty in schlieren images. The schlieren technique is analog, and the camera governs magnification, pixel count, exposure, and frame rate. Magnification and pixel count set the spatial resolution while frame rate and exposure set the temporal resolution.

As an example, consider detonation of stoichiometric hydrogen/air at standard temperature and pressure. Hydrogen is widely used in detonation study due to high sensitivity and small cell size. High sensitivity makes detonation easy to achieve, and small cell size reduces the size of experiments. Stoichiometric hydrogen/air has a theoretical CJ velocity of 1971 m/s (Schultz, 1999), and cell size of 8.19mm (Ciccarelli et al., 1994). In the proposed optical test section, the initial channel height is 50.8 mm or 6.20 λ significantly less than the critical channel height. Assuming a cell of equal width and length, triple point collisions take place every 4.16 μs. In order to satisfy the Nyquist Sampling Theorem for cell size, the temporal resolution must be shorter than 2.08 μs, and the spatial resolution must be smaller than 4.09 mm.

Converting to frame rate, the minimum allowable frame rate is 481000 frame/s. The minimum number of pixels needed to resolve a cell in the 203 mm wide viewing section is 50.

The frame rate and pixel count requirements vary depending on cell size and CJ velocity. The minimum cell size for subcritical diffraction in the optical section is 5.08mm ($H = 10\ \lambda$), and the maximum is 50.8 mm ($H = \lambda$). The corresponding spatial resolutions are 80 pixels and 4 pixels respectively. CJ velocities range from 1100 m/s to 2200 m/s for hydrogen/air depending on equivalence ratio. The corresponding minimum frame rates are 43000 frame/s and 874000 frame/s respectively. The stoichiometric example falls roughly half way between the limits. The Phantom v7.0 camera used in Stevens et al. (2011) ran at 265 pixels by 64-pixel resolution and 75000 frame/s. As a result, the temporal resolution was insufficient to capture the cellular structure.

Four commercially available cameras meet the frame rate requirement for stoichiometric hydrogen/air detonation. They are the Phantom v12.1 and Phantom v710 by vision research, the Fastcam SA-5 by Photronics, and the HPV-2 by Shimadzu. The HPV-2 has memory for only 100 frames making it inappropriate for observing the entire process of diffraction and reinitiation in a detonation diffuser. The remaining cameras force a trade-off between frame rate and image resolution. Table 1 compares the resolution and frame rate settings of each camera. The Phantom v7.1 is included for reference. The Phantom v710 has the highest sample rate of the four cameras and the shortest available exposure at 296 ns. Recent purchase of a Phantom v710 for the DERF ensures its availability for testing.

Table A-1. High-speed camera comparison

Phantom v7.0				Phantom v12.1			
resolution		Frame rate	Sample rate	Resolution		Frame rate	Sample rate
X (pix)	Y (pix)	(frame/s)	(pix/s)	X (pix)	Y (pix)	(frame/s)	(pix/s)
800	600	4796	2.30E+09	1280	800	6242	6.39E+09
640	480	7207	2.21E+09	1280	720	6933	6.39E+09
512	512	8213	2.15E+09	512	512	20978	5.50E+09
256	256	26143	1.71E+09	256	256	66997	4.39E+09
128	128	67796	1.11E+09	128	128	183250	3.00E+09
64	64	121212	4.96E+08	128	64	330469	2.71E+09
32	32	160000	1.64E+08	128	8	1000000	1.02E+09
Phantom v710				Fastcam SA-5			
Resolution		Frame rate	Sample rate	resolution		frame rate	sample rate
X (pix)	Y (pix)	(frame/s)	(pix/s)	X (pix)	Y (pix)	frame/s	pix/s
1280	800	7530	7.71E+09	1024	1024	1000	1.05E+09
512	512	25000	6.55E+09	832	444	20000	7.39E+09
256	256	79000	5.18E+09	512	373	50000	9.55E+09
128	128	215600	3.53E+09	256	64	300000	4.92E+09
128	32	685800	2.81E+09	128	64	420000	3.44E+09
128	16	1077500	2.21E+09	128	24	775000	2.38E+09
128	8	1400000	1.43E+09	64	16	1000000	1.02E+09

An undesired effect of detonation is the light generated by combustion. Hydrogen/air emits mostly in the UV band, and the effect on imaging is small (Fig. A-7a). Hydrocarbon fuels emit much more light in the visible range (Fig. A-7b), and the light obscures the cell structure of a detonation.

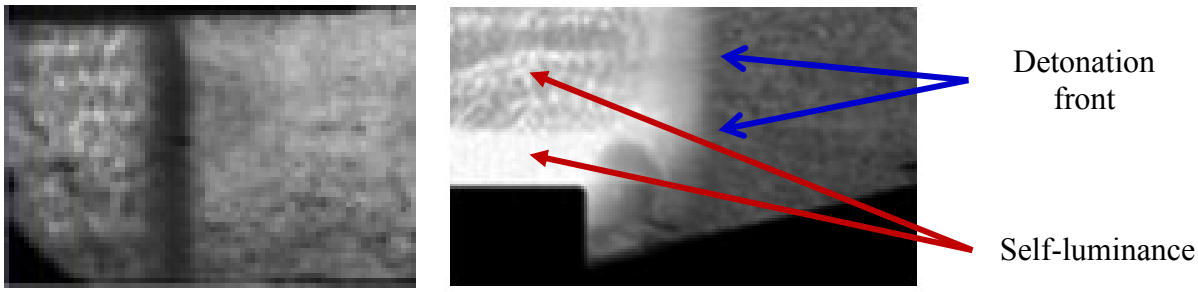

Weak emission from H2-Air Detonation

Strong emission from HC-Air detonation

Figure A-7. Light emission from detonations

Because the emission depends on wavelength, a spectral filter can block the light from detonation while passing light from another source. Figure 35 shows the emission spectra of hydrogen/air and acetylene/air detonations. Both detonations have weak emission from 650 nm to 700 nm. Meanwhile, the CMOS sensors employed by all of the cameras considered are near peak sensitivity at 700 nm (Fig. A-8c). Filtering for such a narrow band of wavelengths will reduce the intensity of light reaching the camera. A brighter source may be necessary for sufficient illumination.

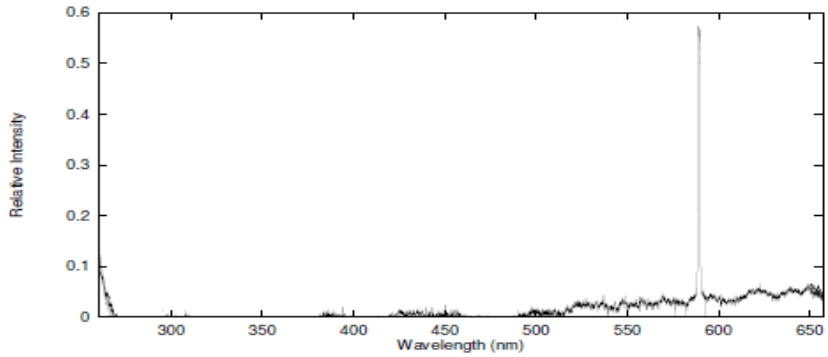

H2+0.5O2+1.88N2 detonation at 101kPa

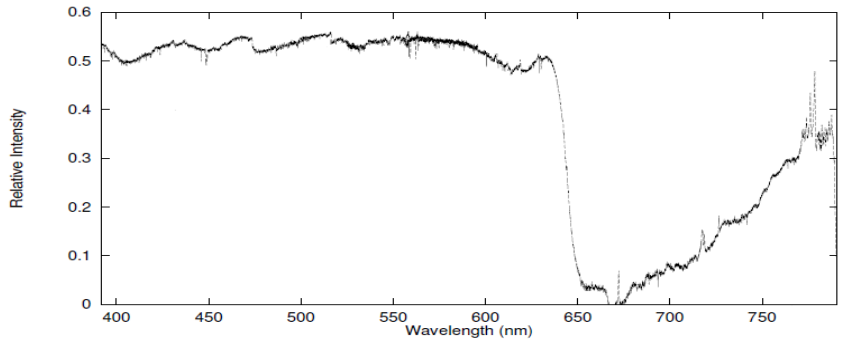

C2H2+Air flame at 101kPa

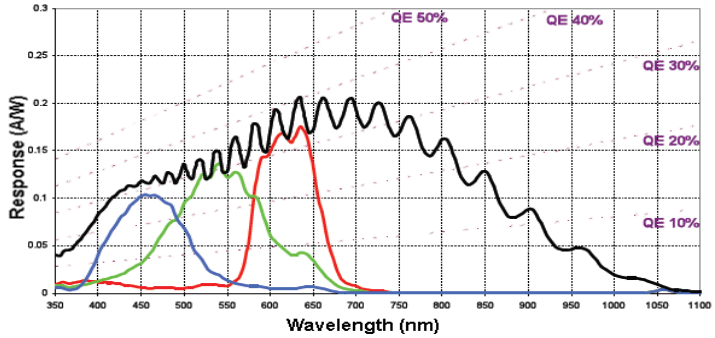

Phantom v12.1 spectral response: black line denotes monochrome model.

Figure A-8. Spectral emission from combustion and camera sensitivity

The Phantom v710 measures position, time, and speed with low uncertainty. The bias uncertainty in position is a function of the image resolution and exposure time. Again, consider the theoretical stoichiometric hydrogen/air detonation this time combined with the Phantom v710 camera. The wave speed is 1971 m/s and the cell size is 8.19 mm. The camera settings are 64 by 64 pixel resolution, 685800 frame/s, and 296 ns exposure. Uncertainty in the position of an object is the root sum squared of the uncertainties due to pixel size and the distance traveled

during exposure. The uncertainty due to pixel size varies from 0.200 mm to 0.0139 mm depending on the selected resolution (32 pixels and 128 pixels respectively over the 200 mm wide test section). The total uncertainty ranges from 0.0443 mm to 0.204 mm. The pixel size was the most important factor when setting up high frame rate imaging and should be as small as allowable for sufficient frame rate. The bias uncertainty in velocity calculated for the example is 15.5 m/s. For the 1100 m/s to 2200 m/s range the uncertainty varies from 7.48 m/s to 18.1 m/s.

X. Appendix B Test Article Drawings

D-Series Cases

Case D1

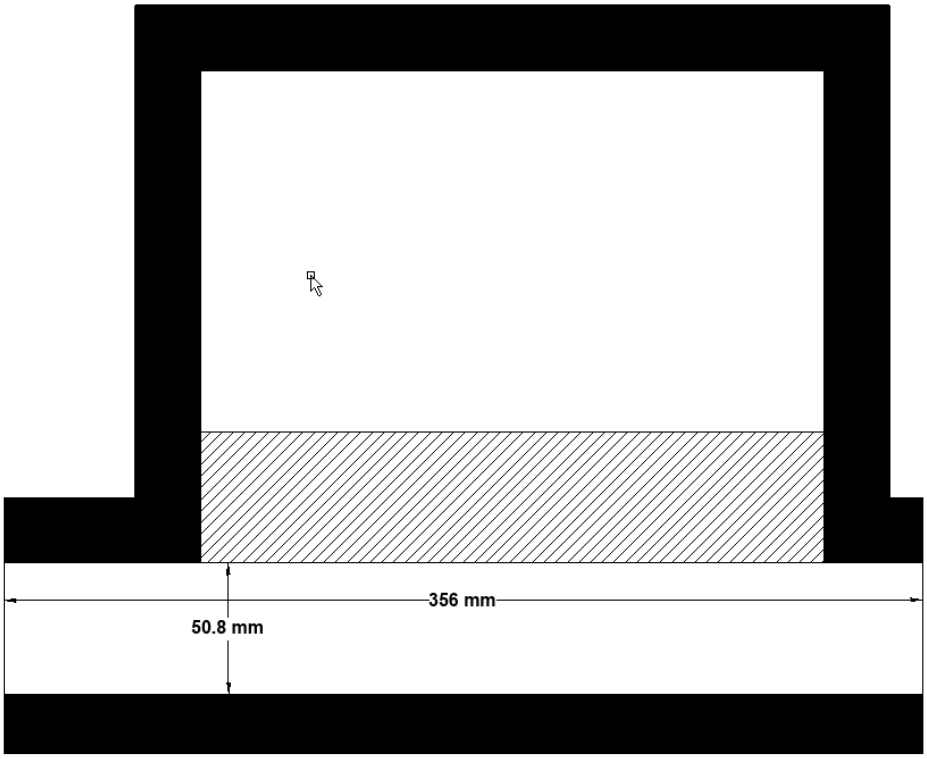

Case D2

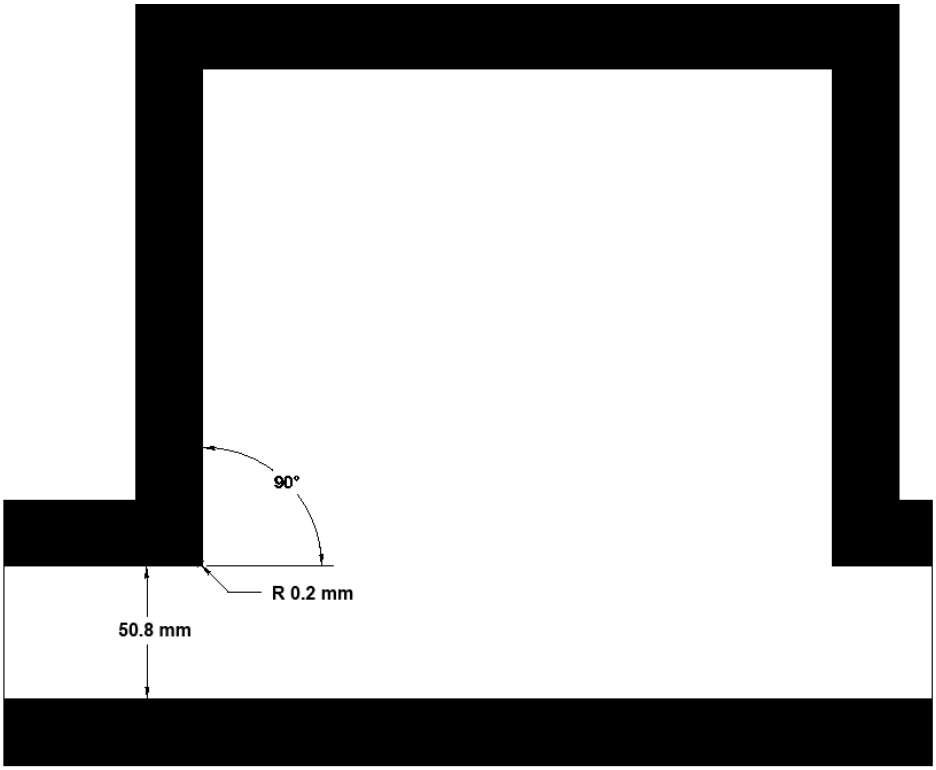

Case D3

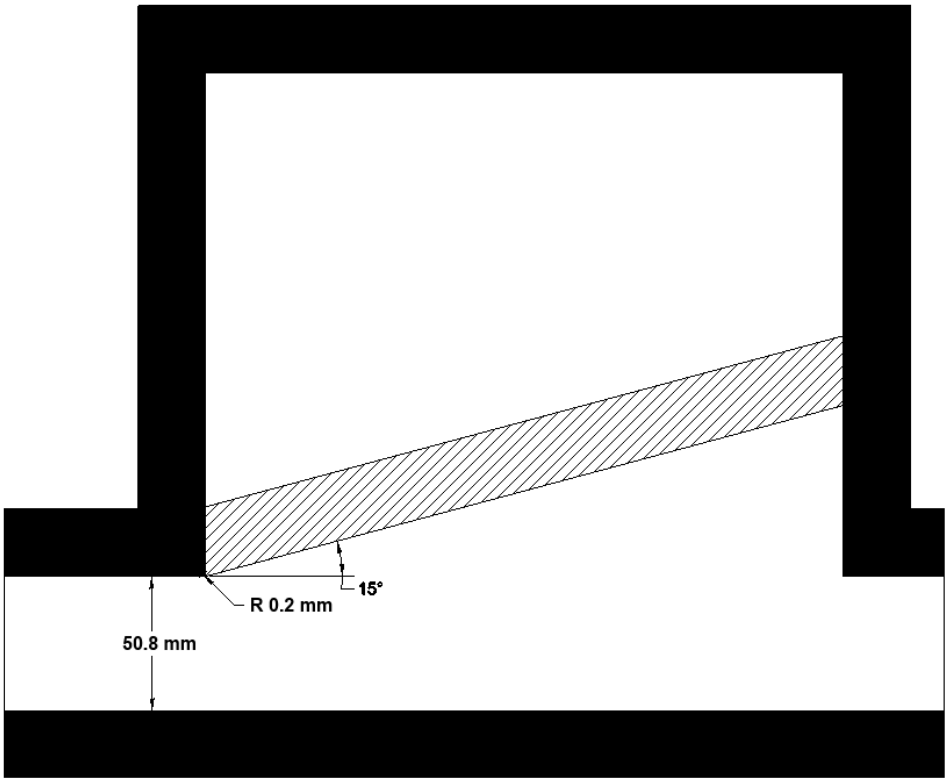

Case D4

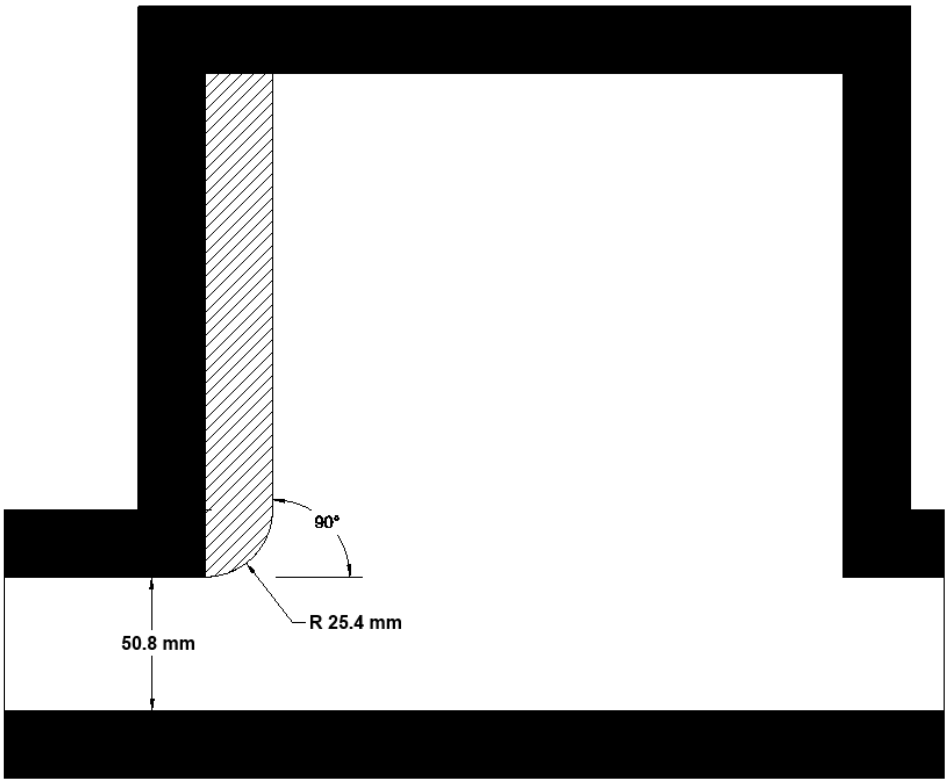

R-series Cases

Case R1

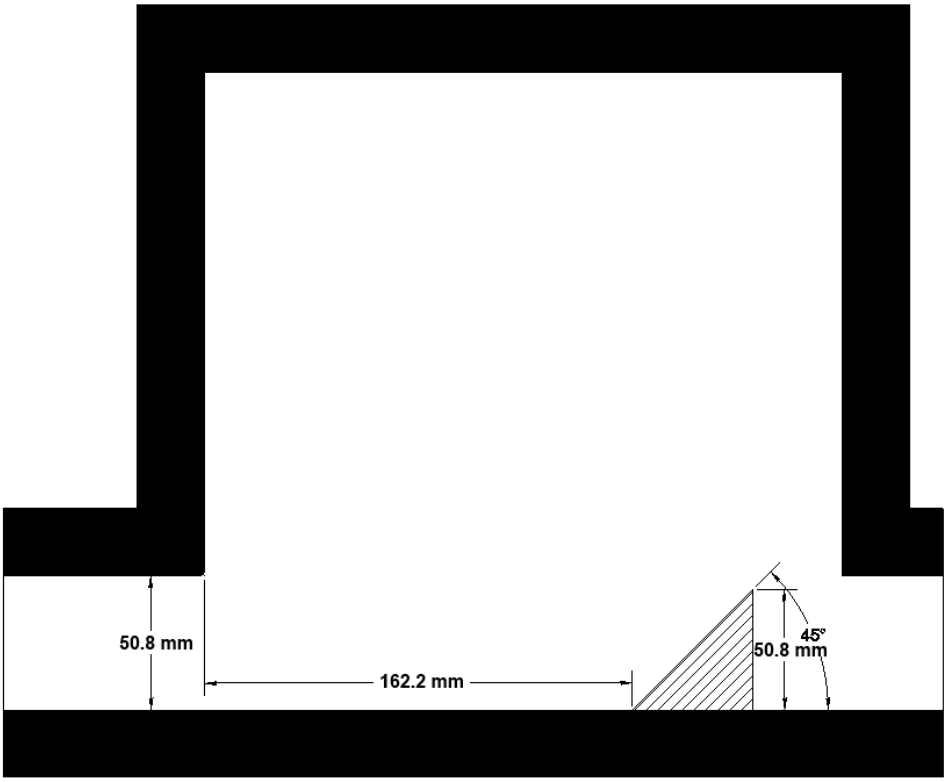

Case R2

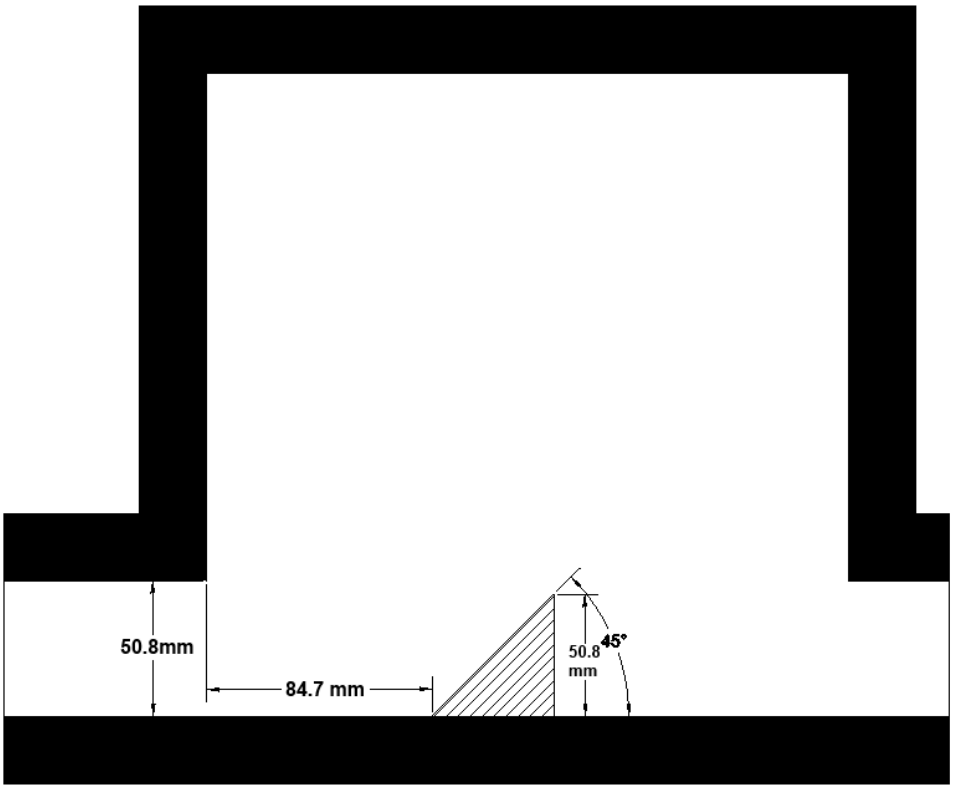

Case R3

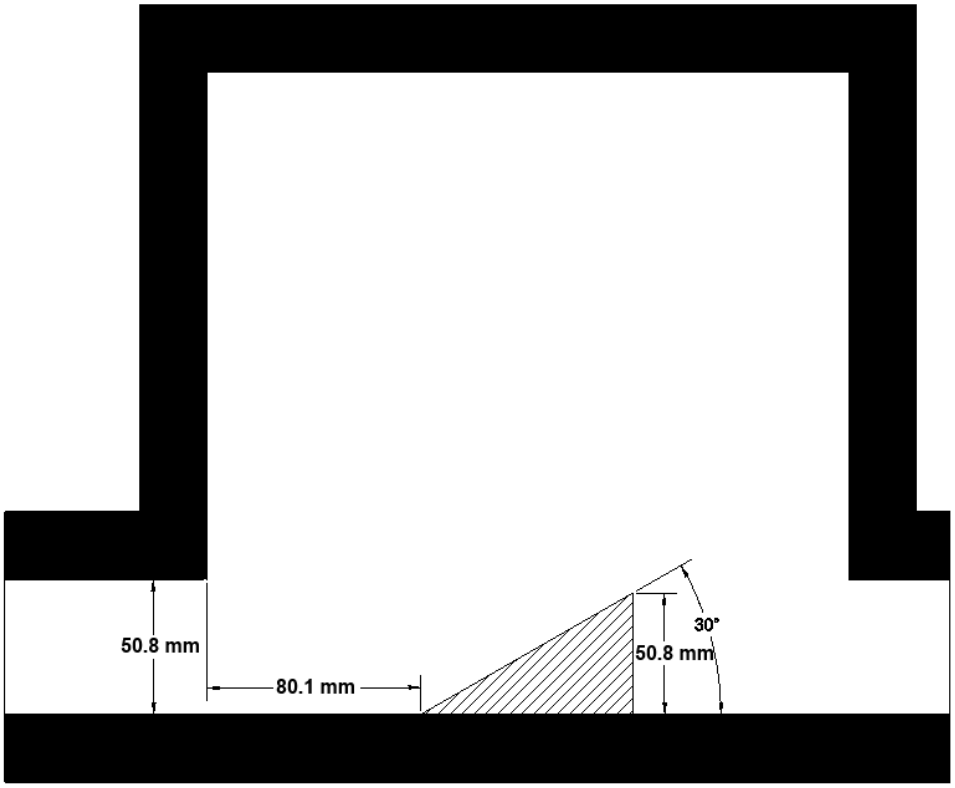

Case R4

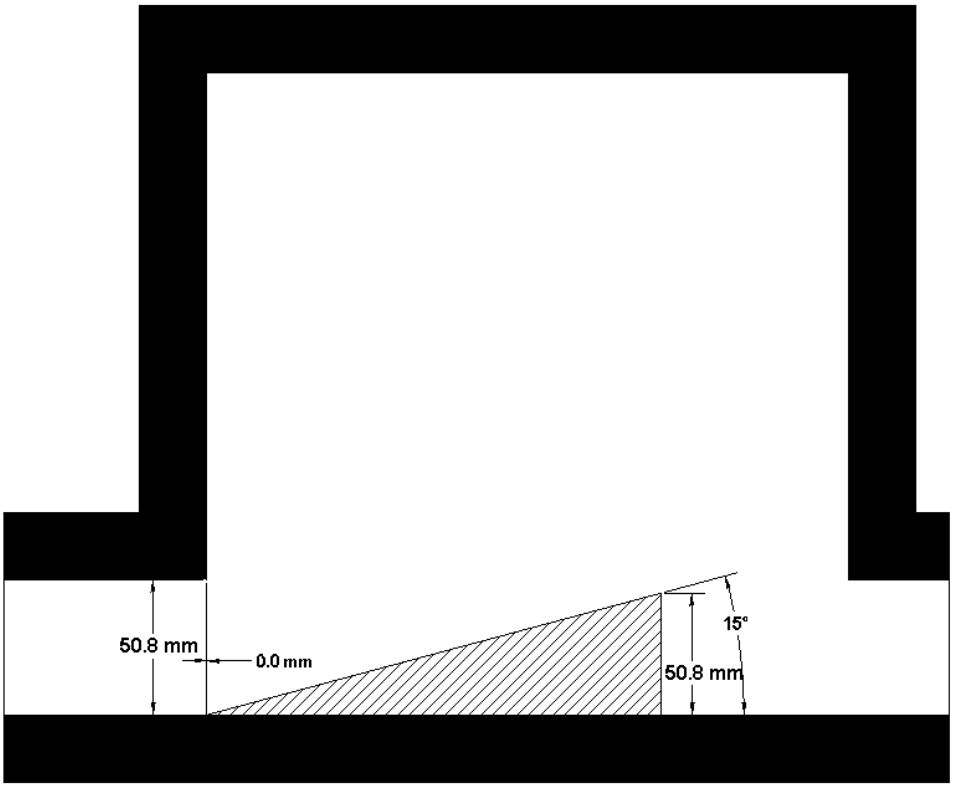

Case R5

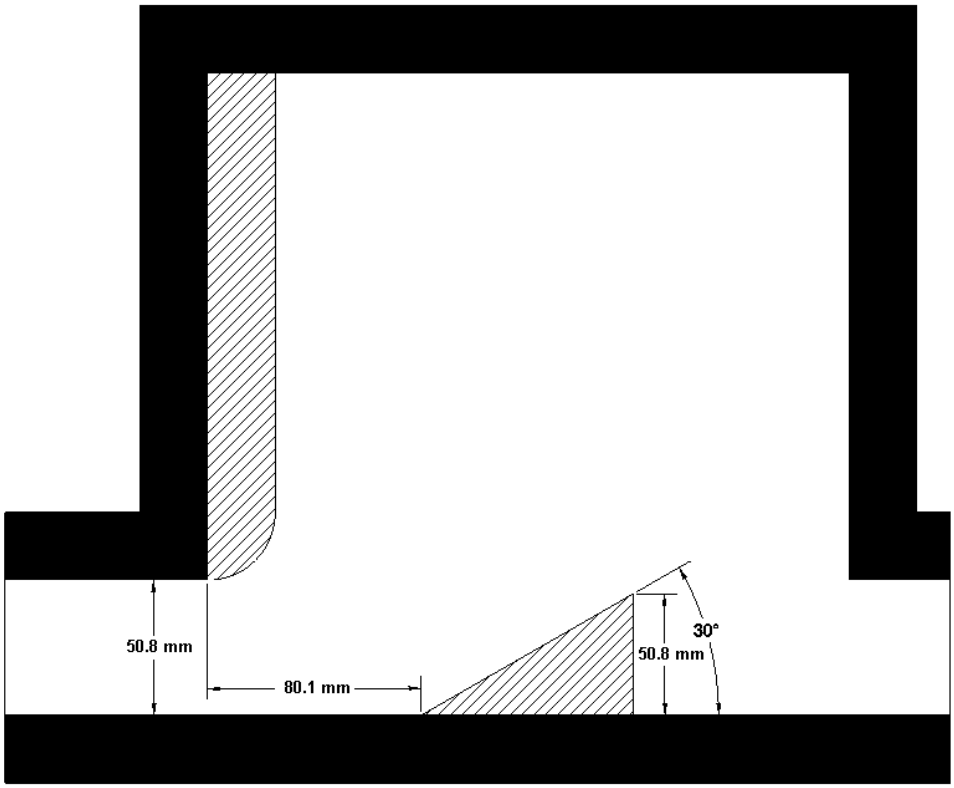

Case R6

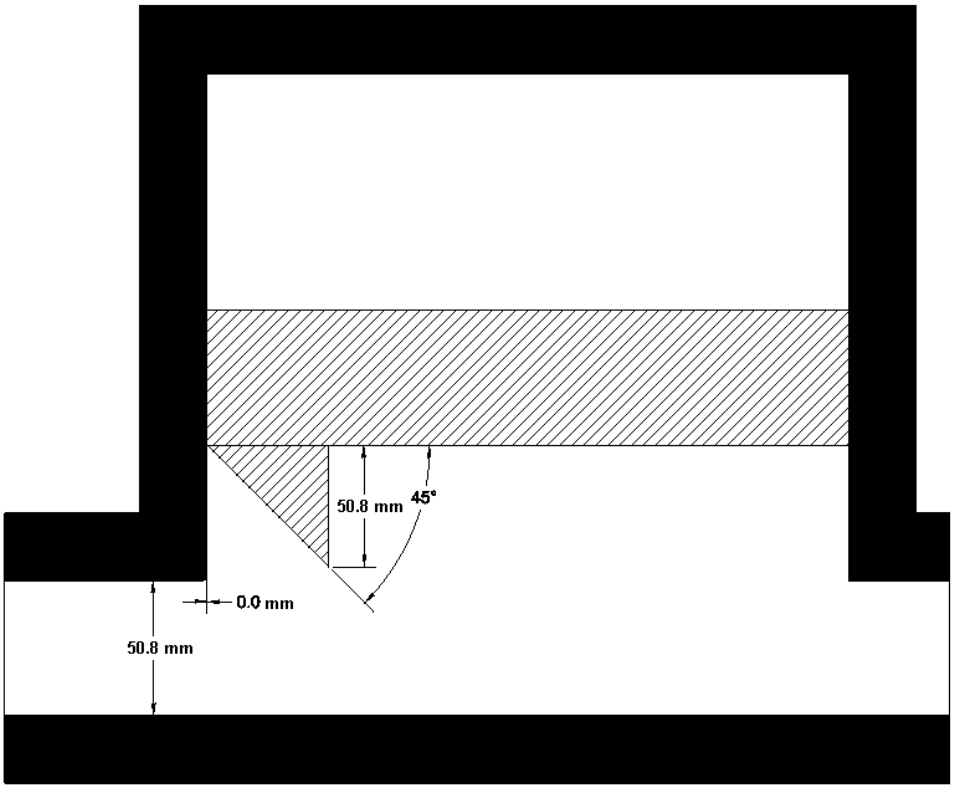

Case R7

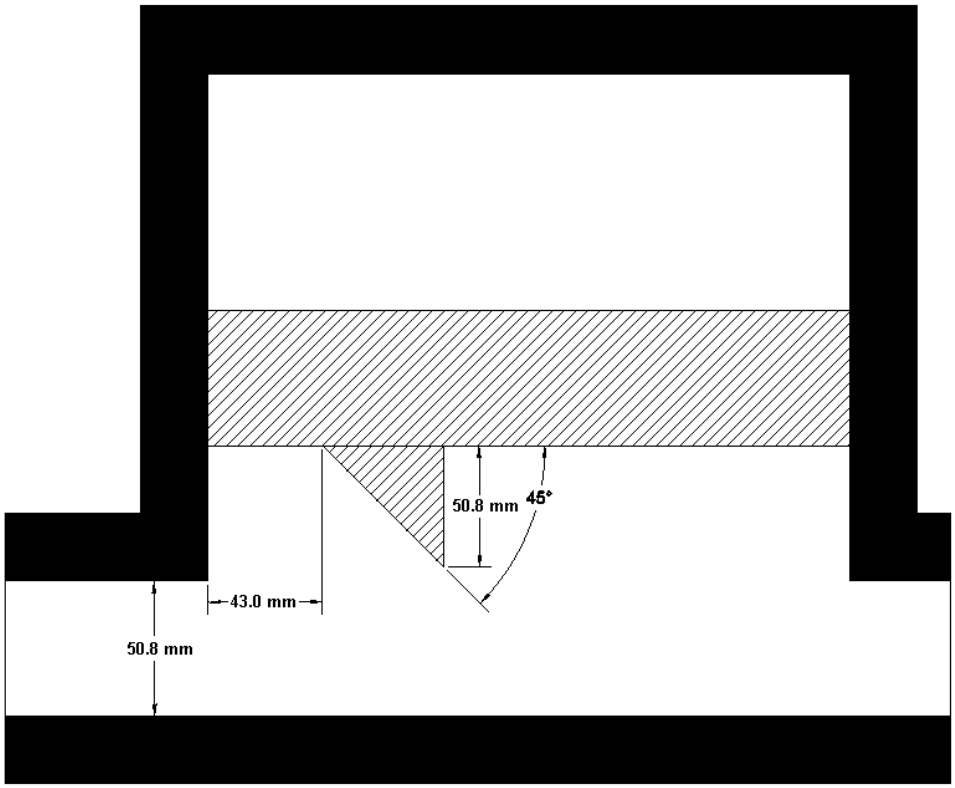

Case R8

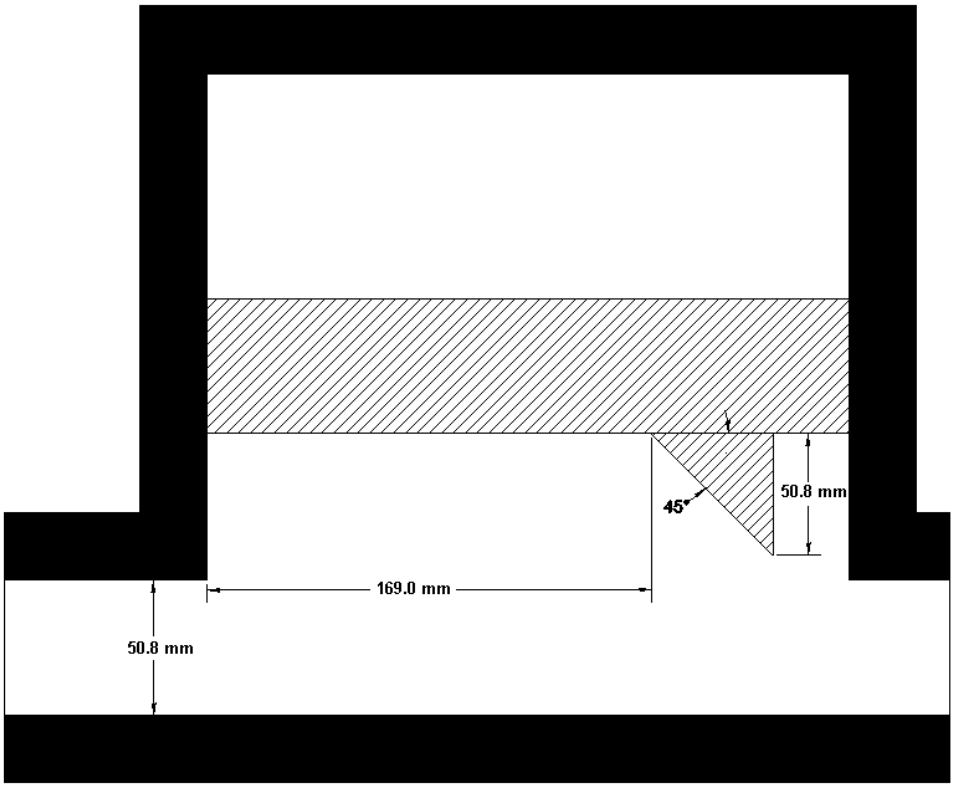

M-series Cases

Case M1

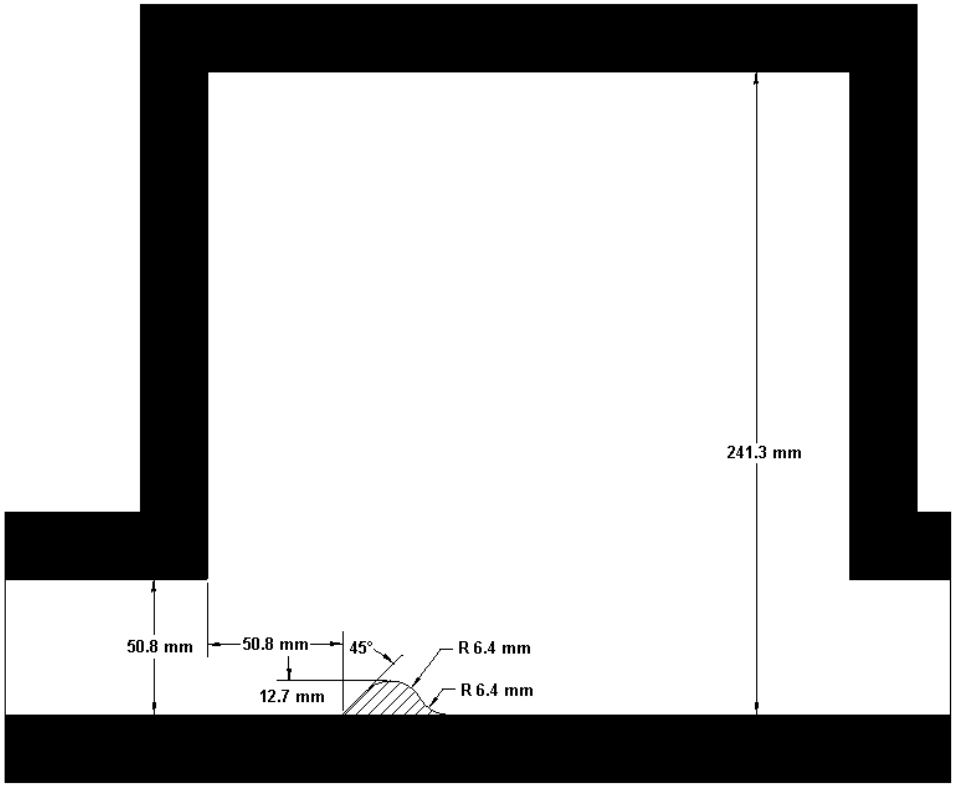

Case M2

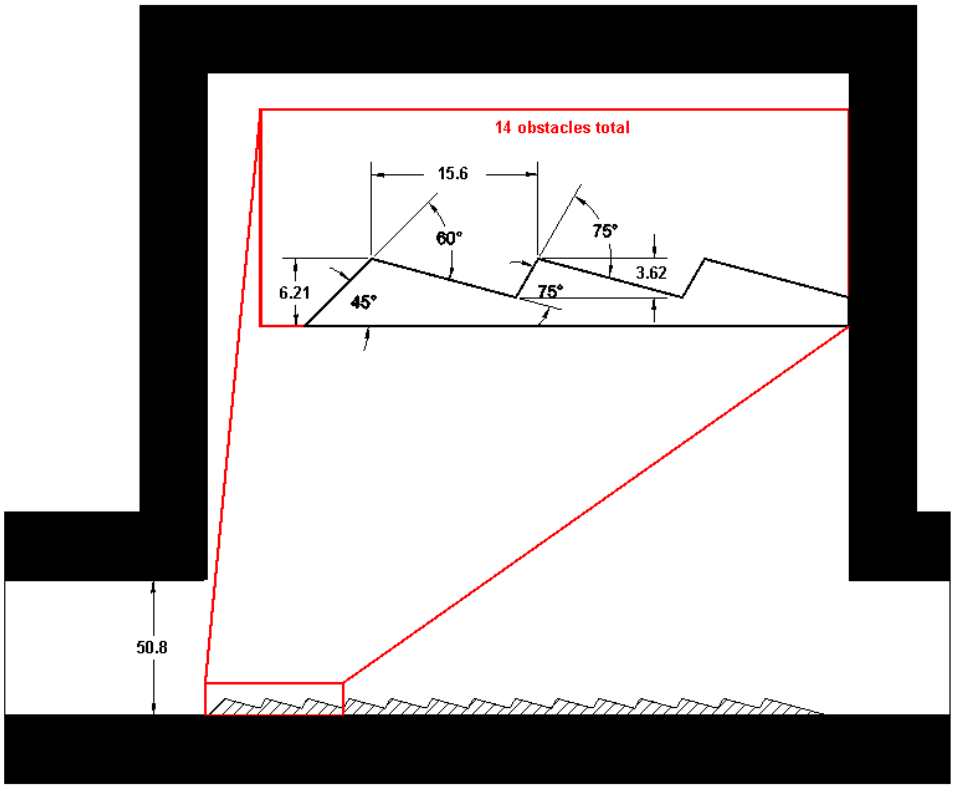

Case M3

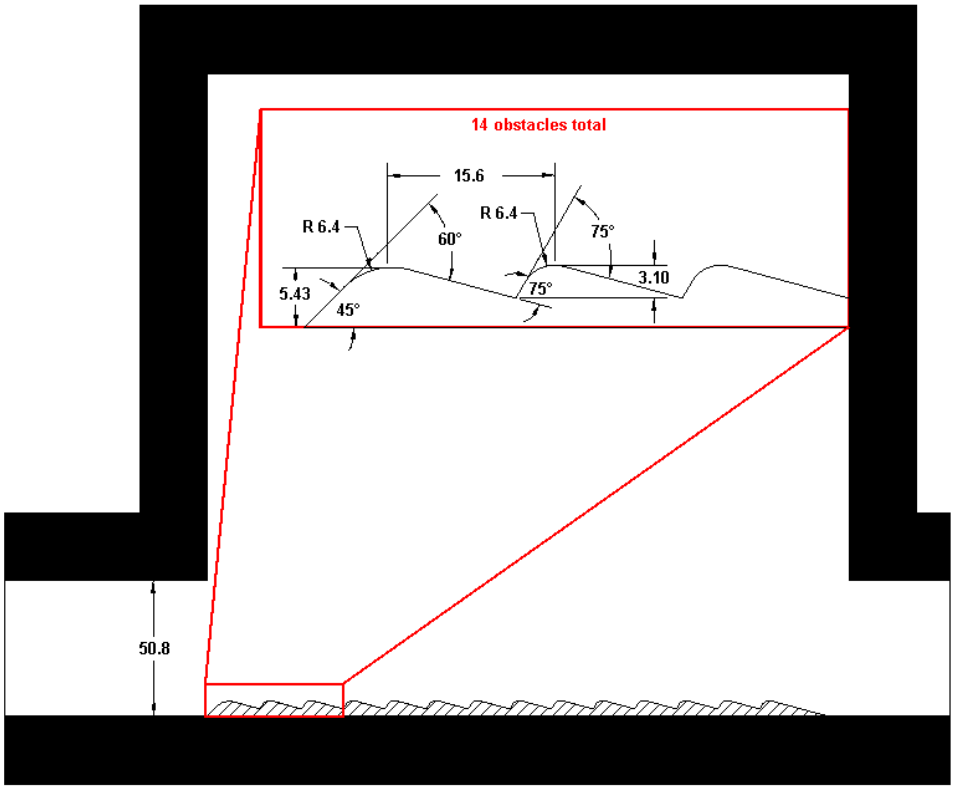

Case M4

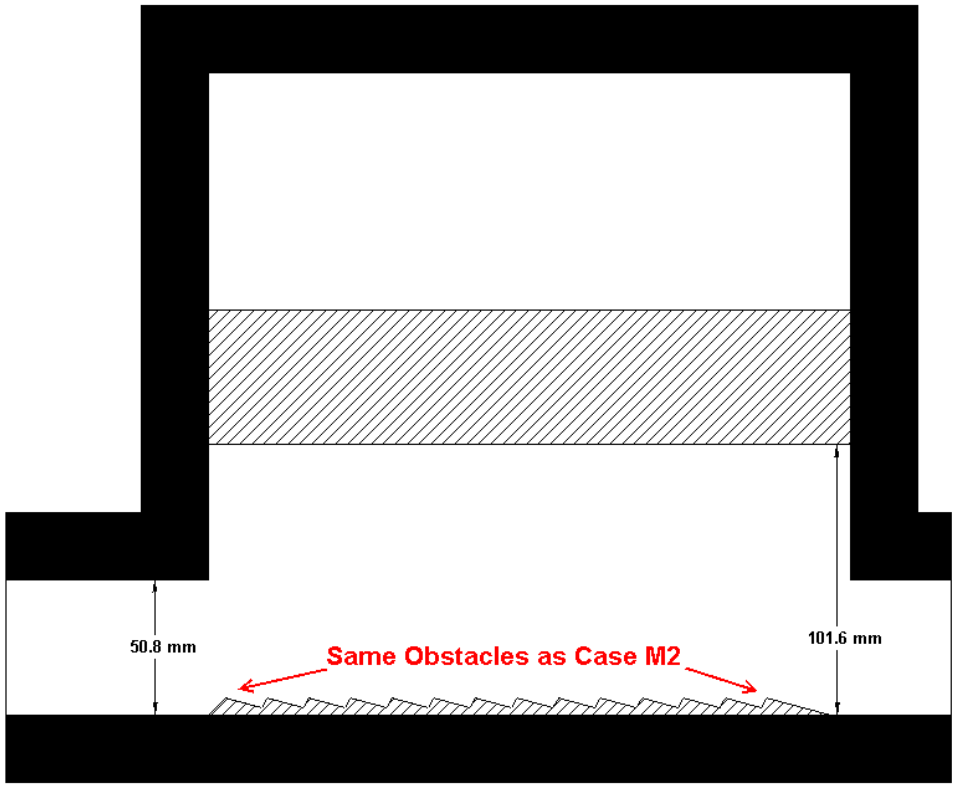

Case M5

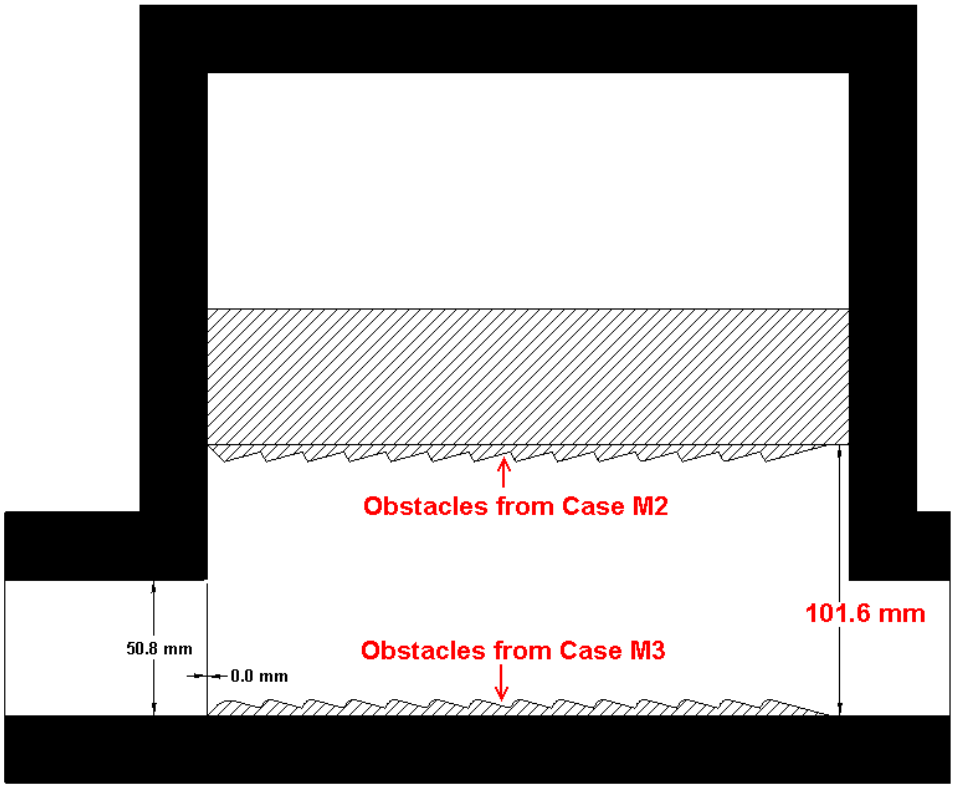

Case M6

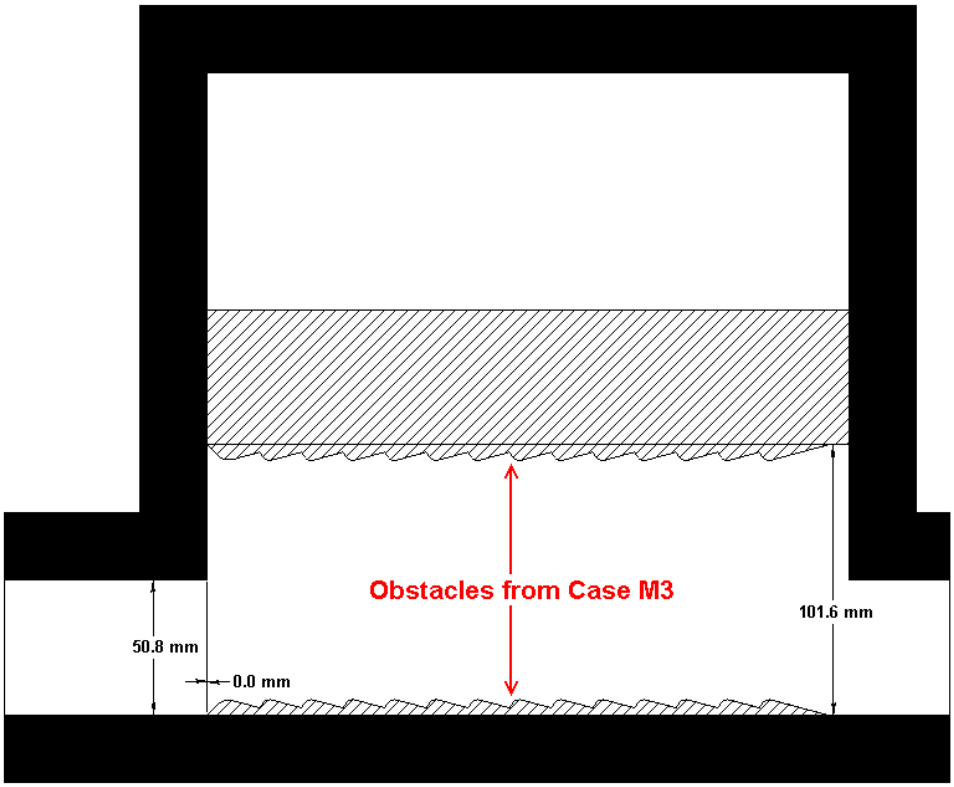

Case M7

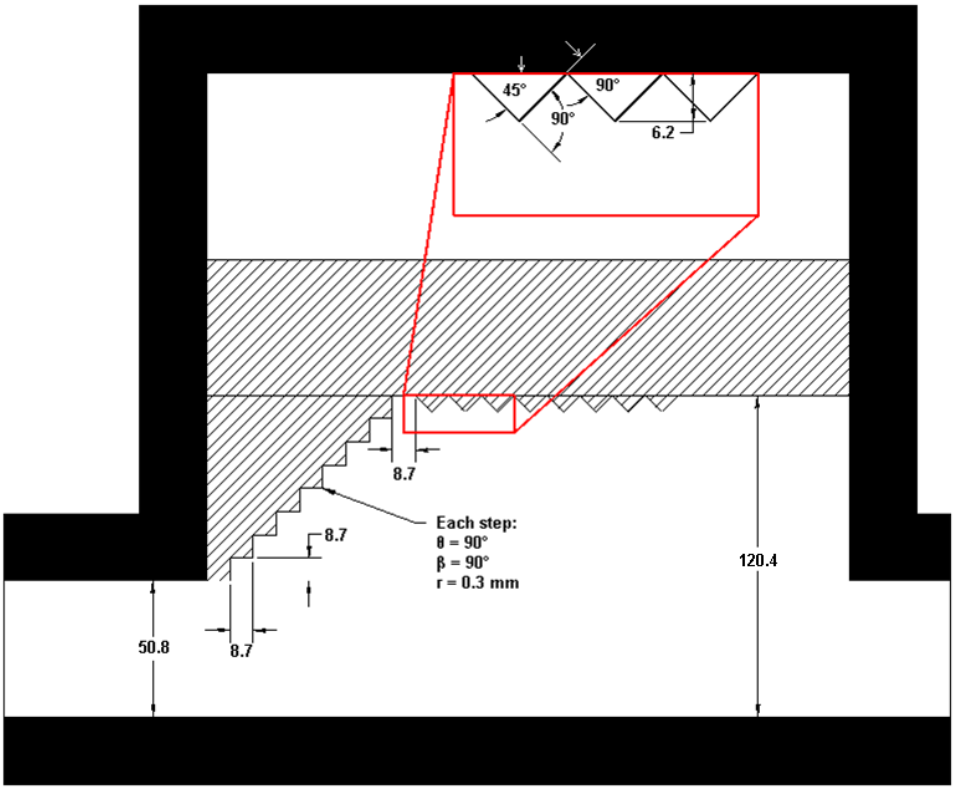

Case M8

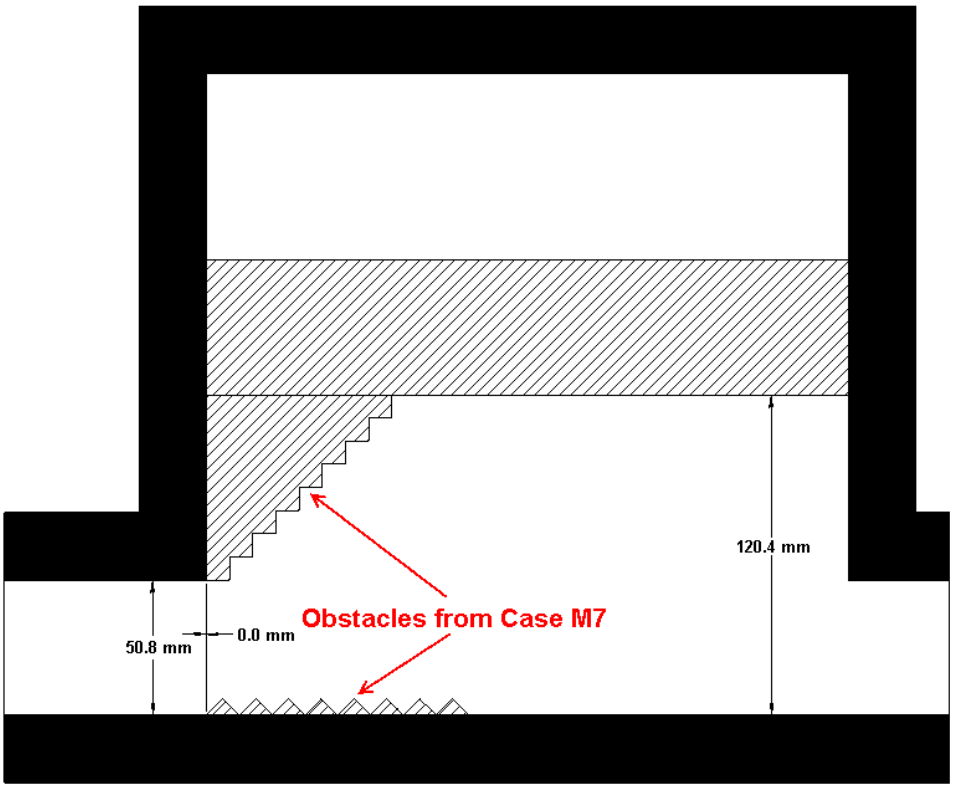

Case M9

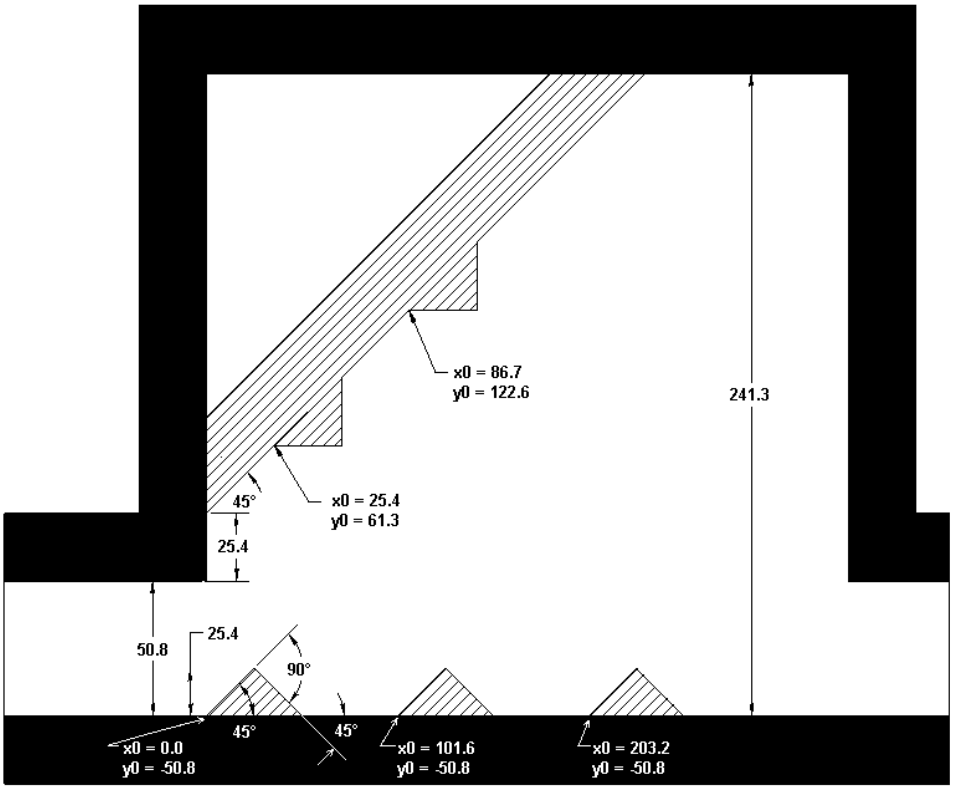

Case M10

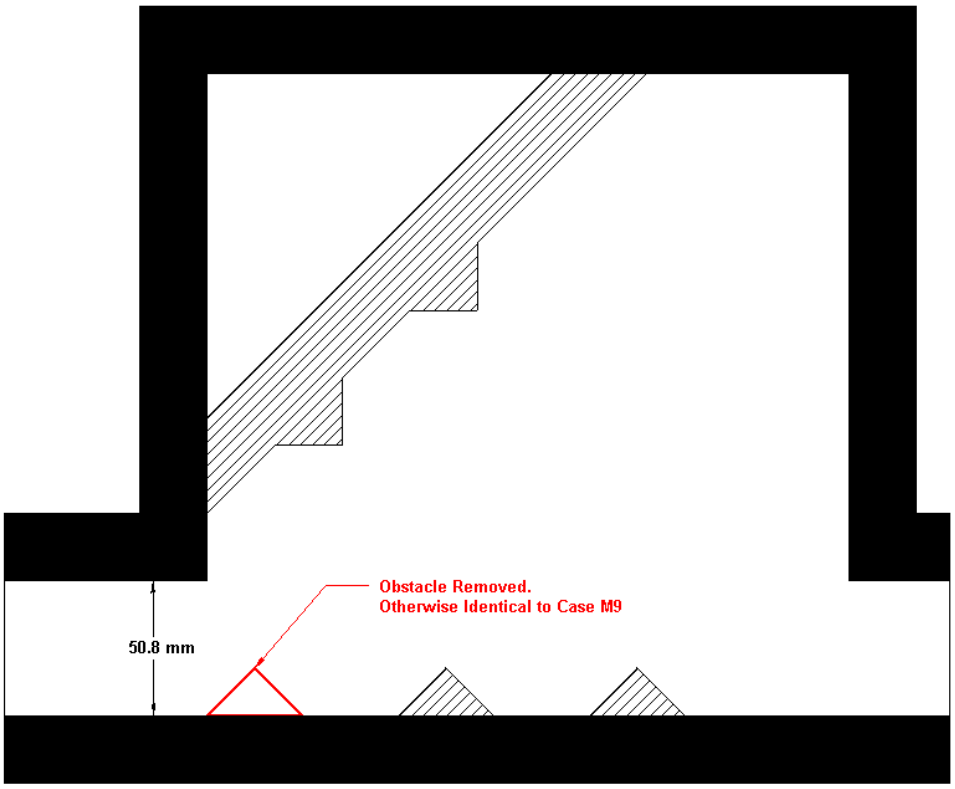

Case M11

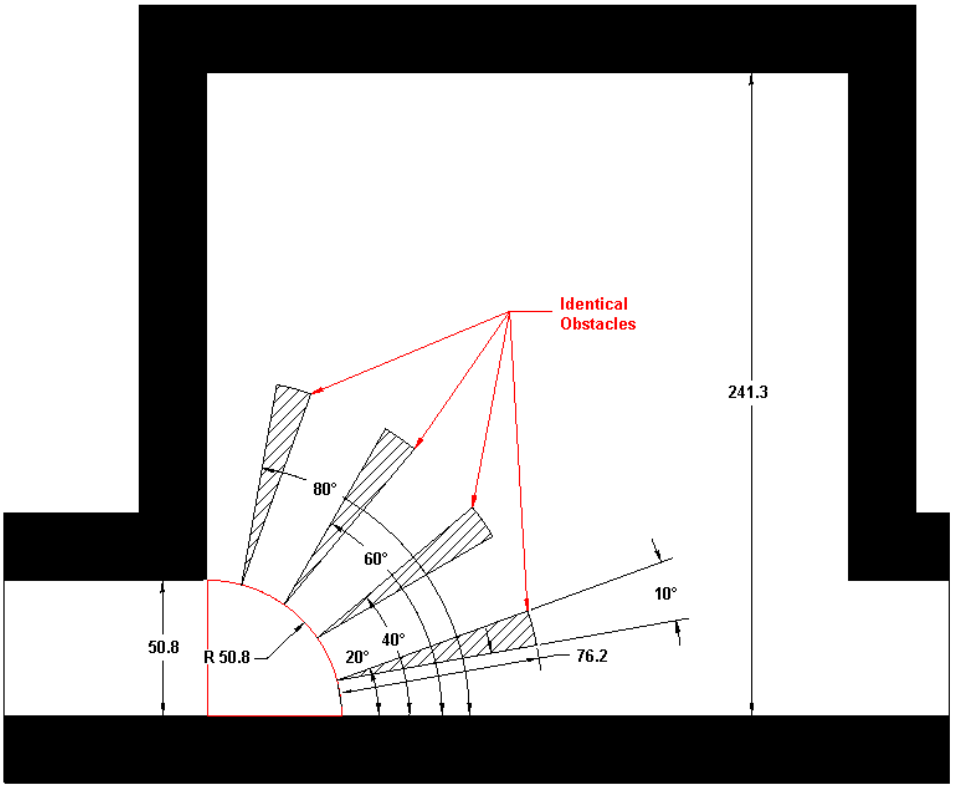

XI. Appendix C –Video Stills

D-Series Cases

Case D1: Straight Channel (θ = 0, r = ∞)

Run 1 Run 2 Run 3 Run 4

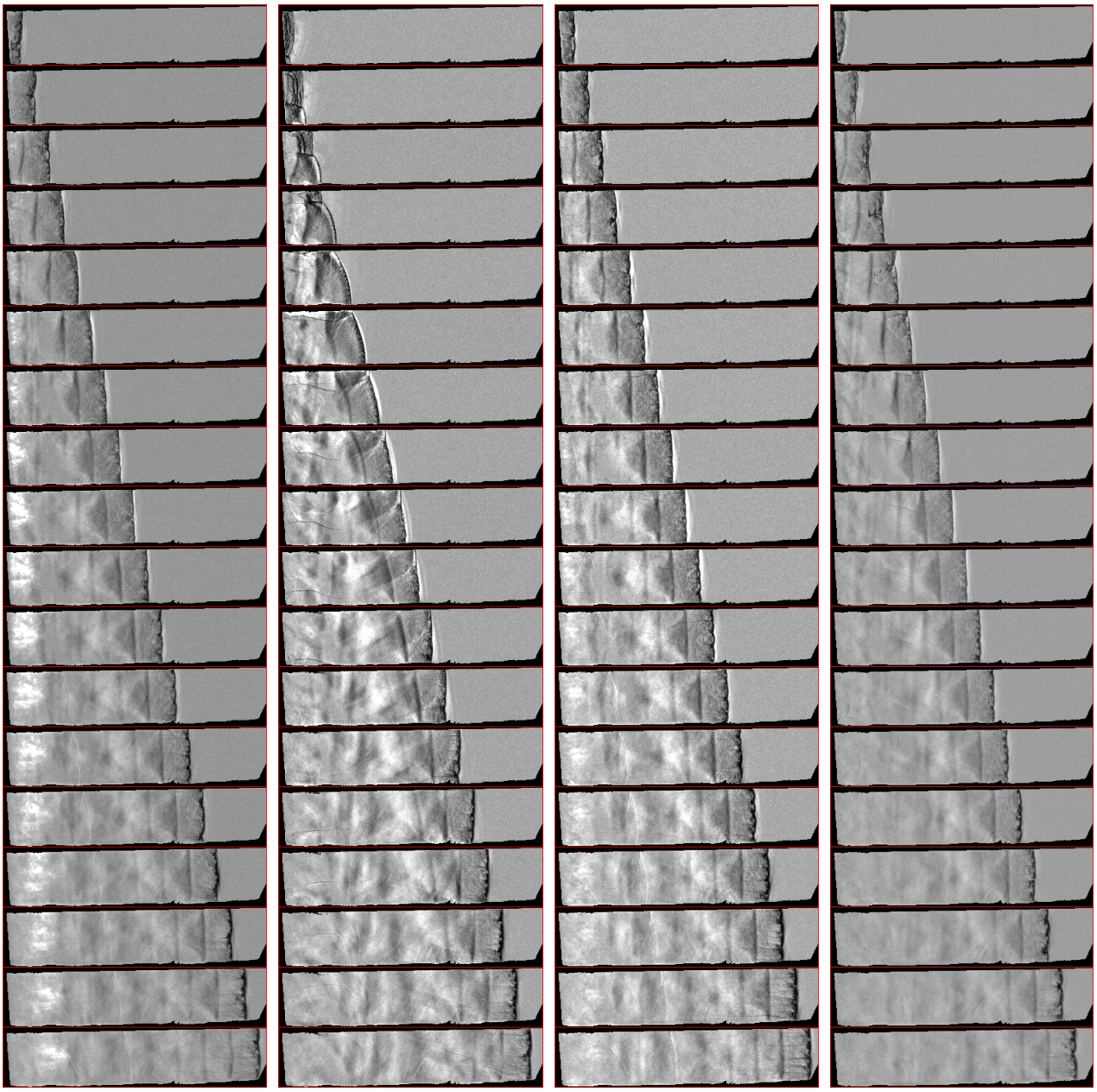

Case D2: θ = 90°, r = 2.0 mm

Run 1 Run 2 Run 3 Run 4

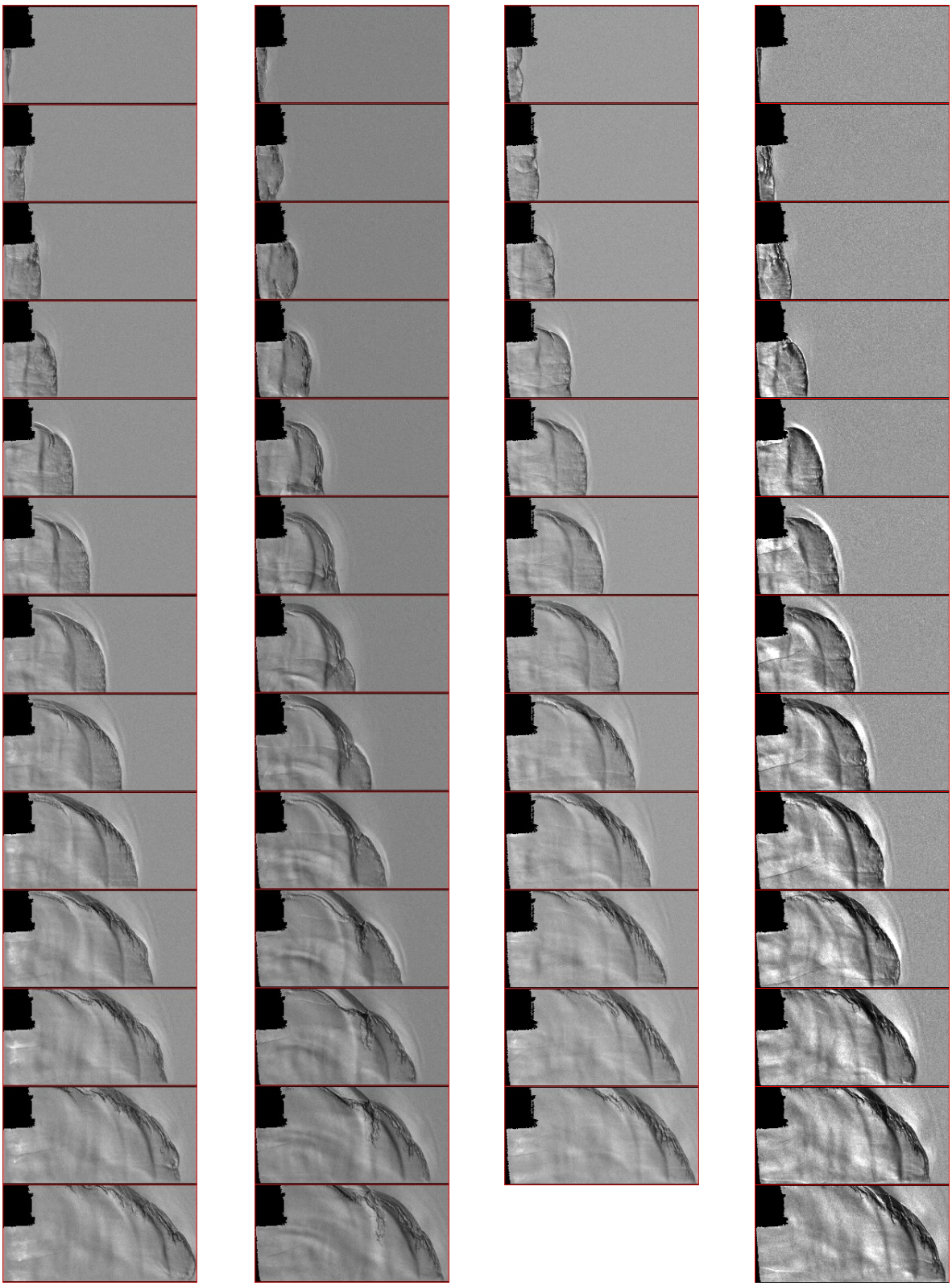

Case D2 (continued)

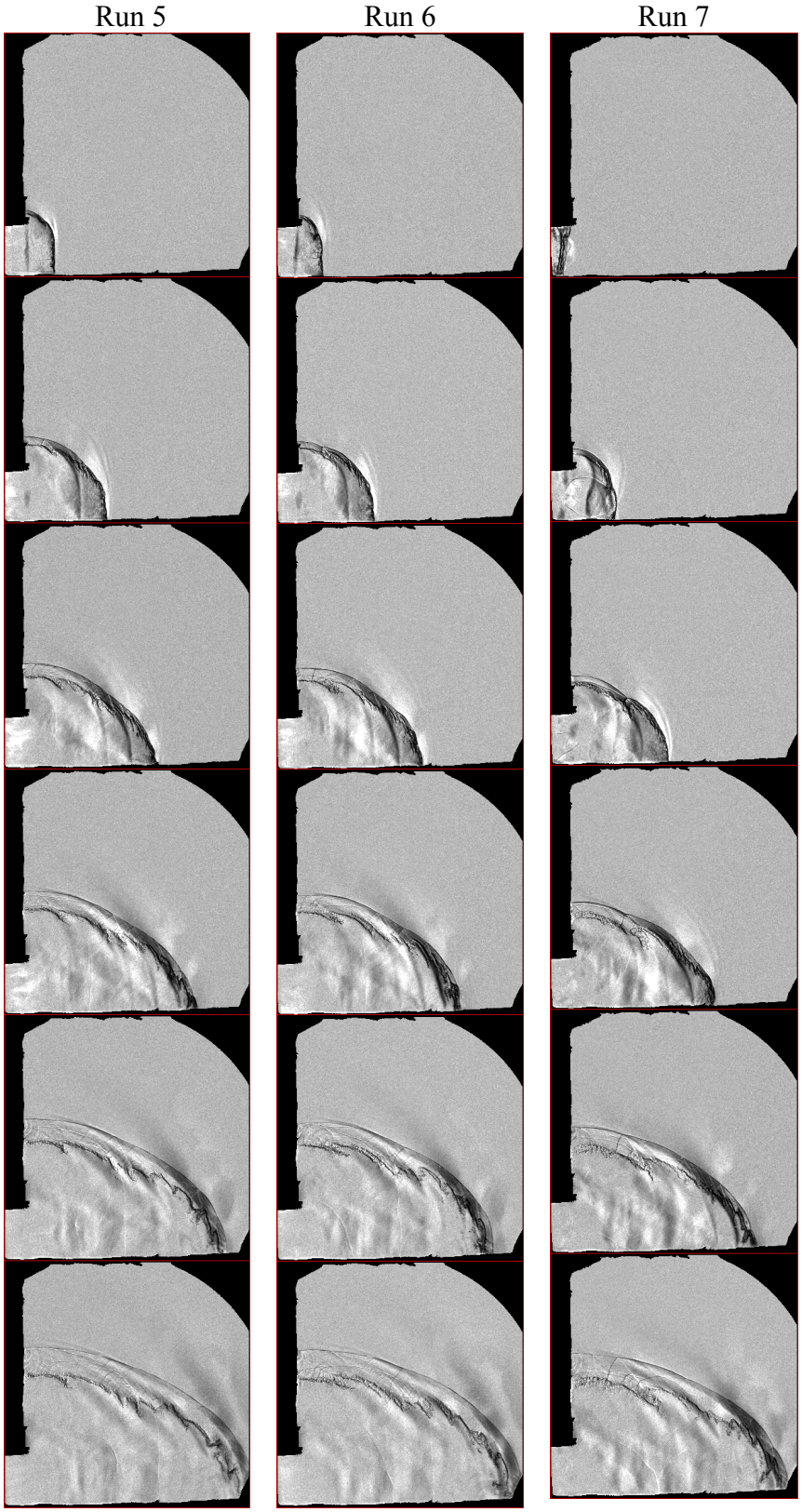

Case D3: θ = 15° r = 2.0 mm

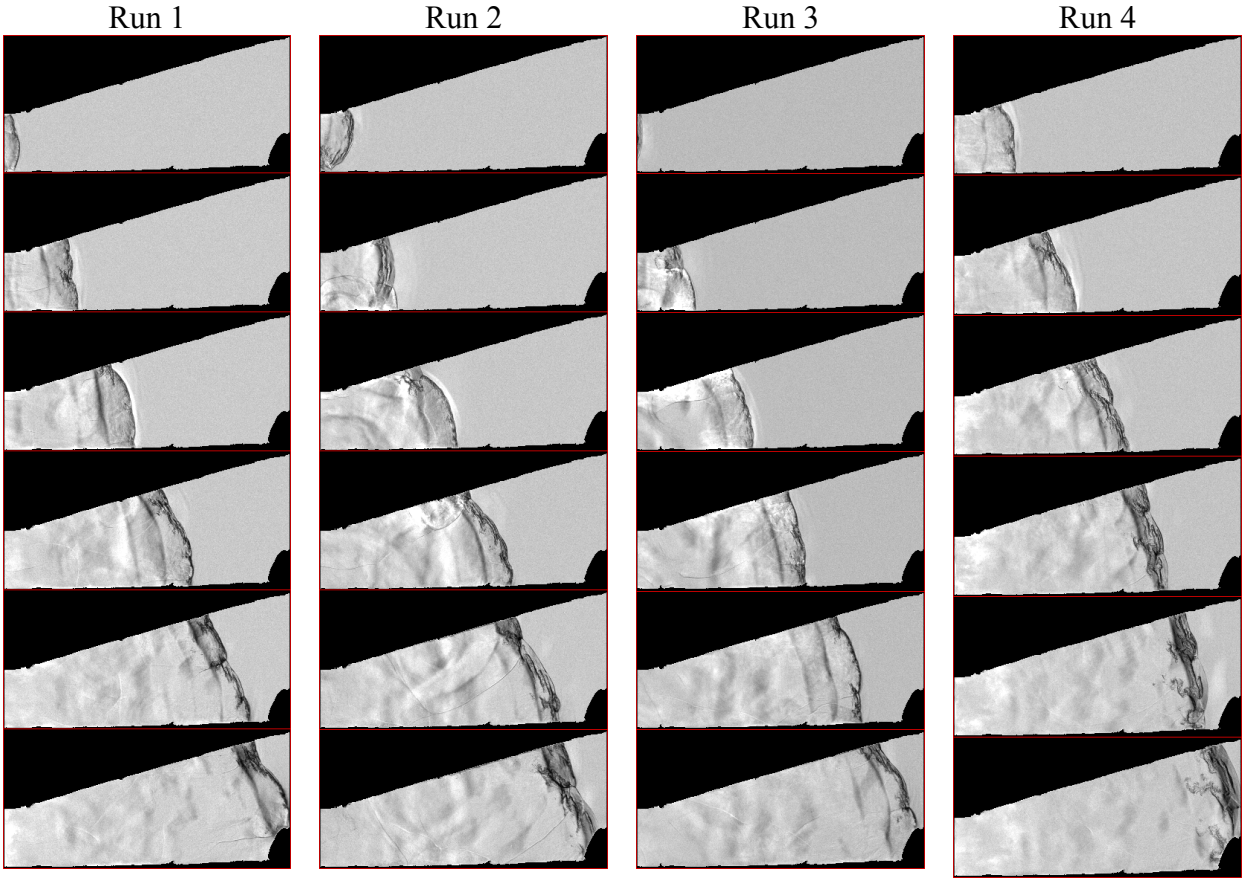

Case D3 (continued)

Run 5

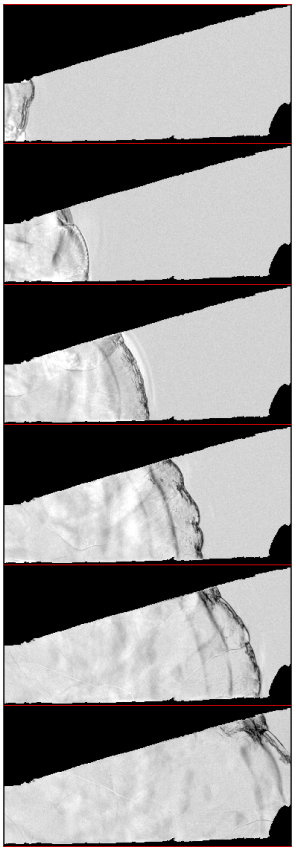

Run 6

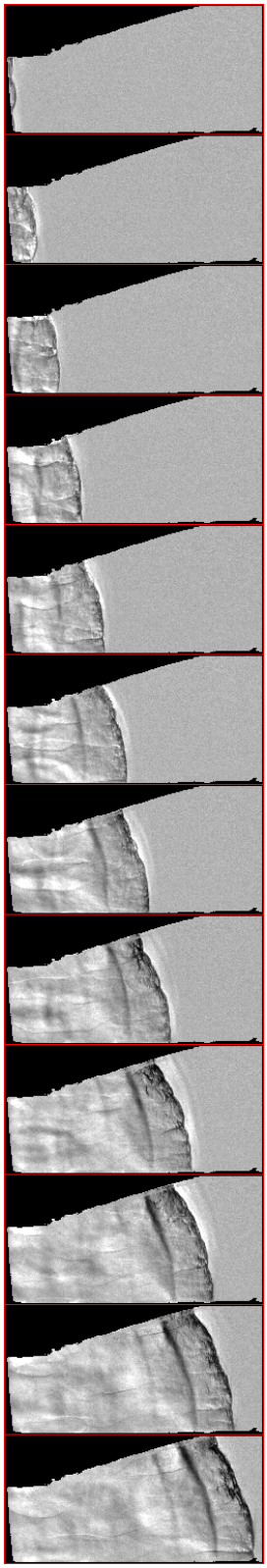

Run 7

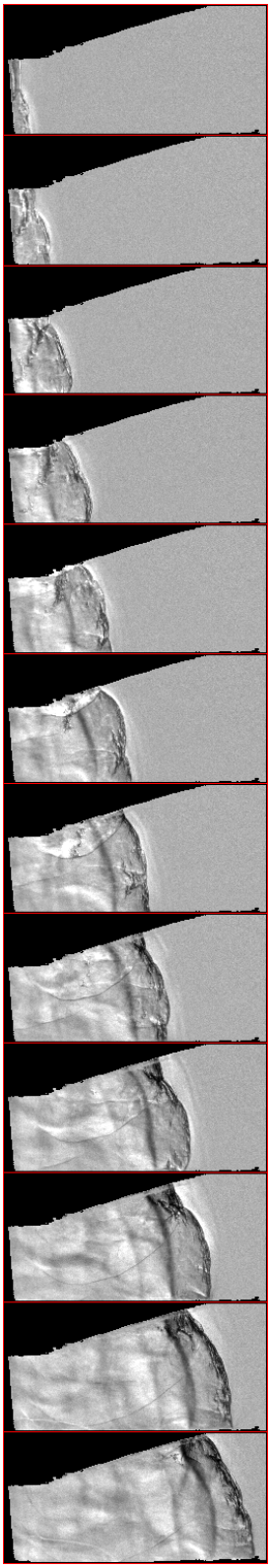

Run 8

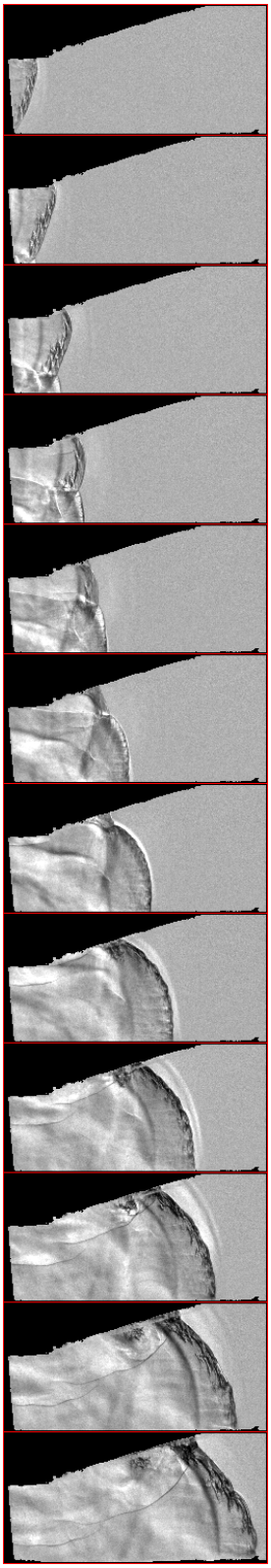

Case D3 (continued)

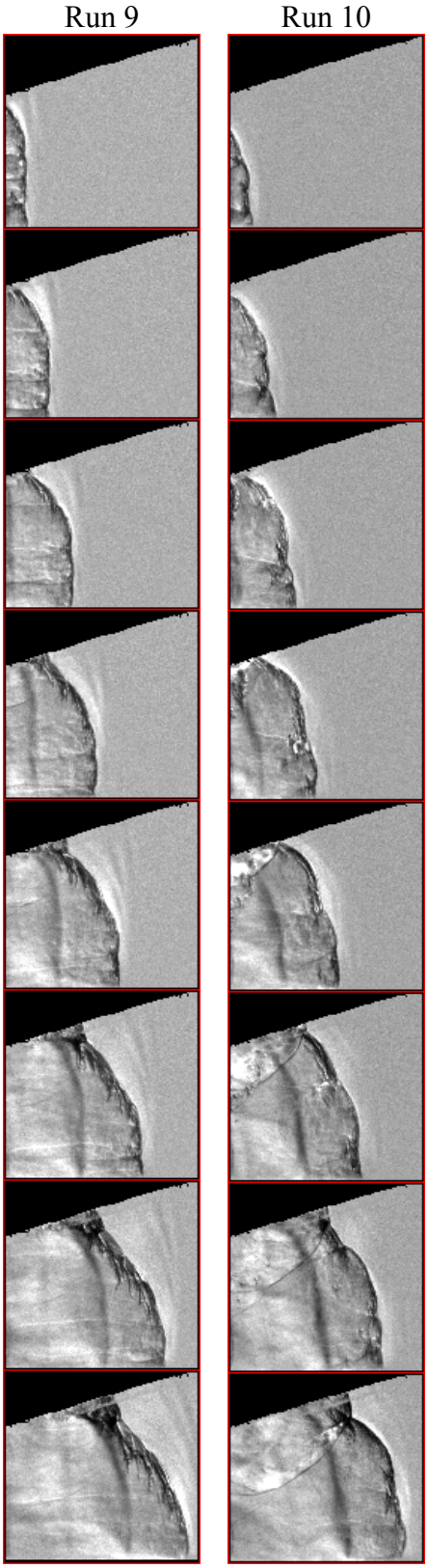

Case D4: θ = 90°, r = 25.4 mm

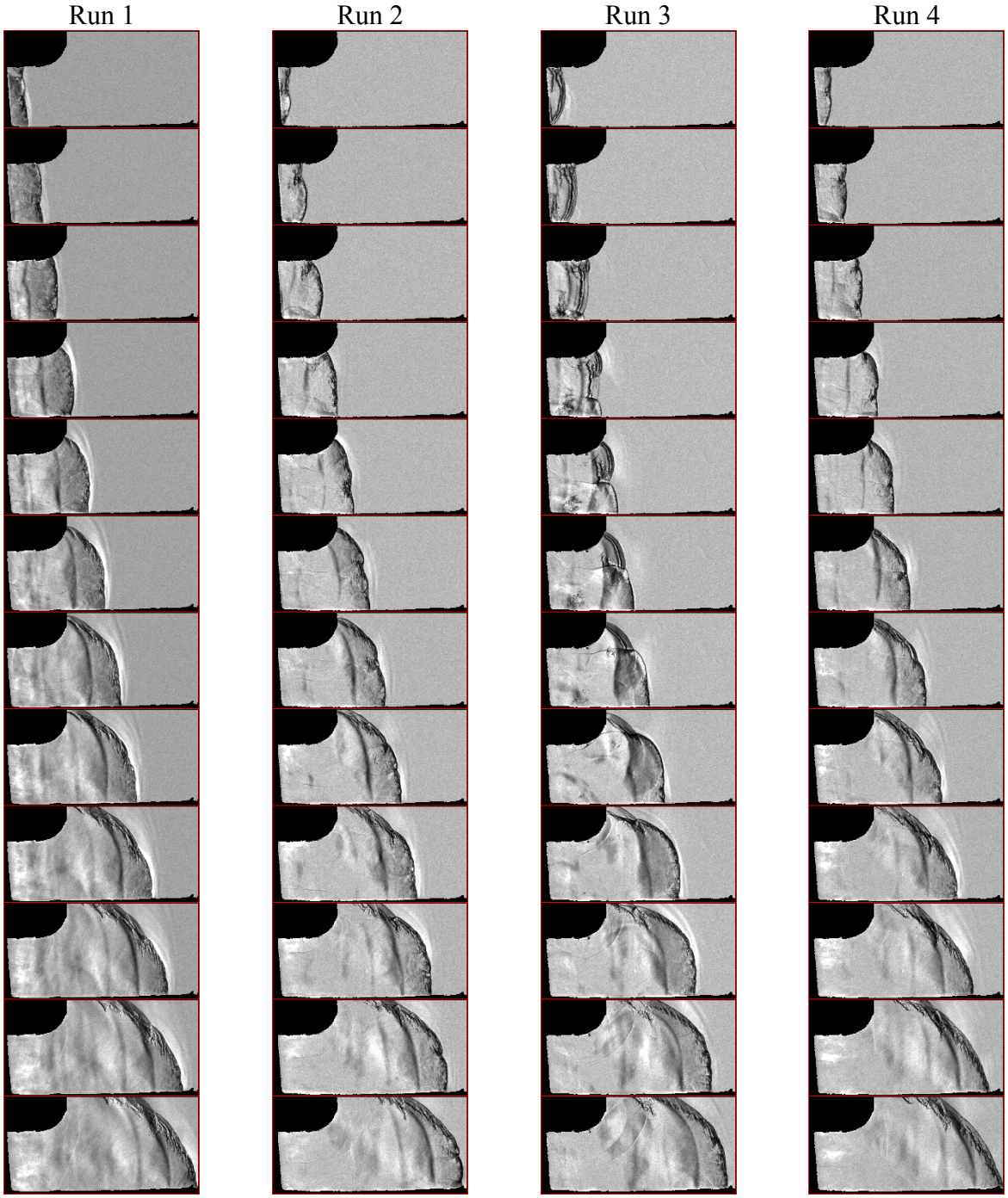

Case D4 (continued)

Run 5

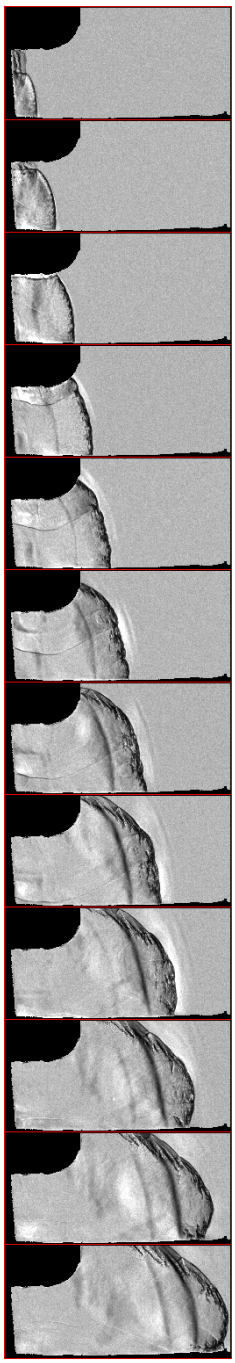

Run 6

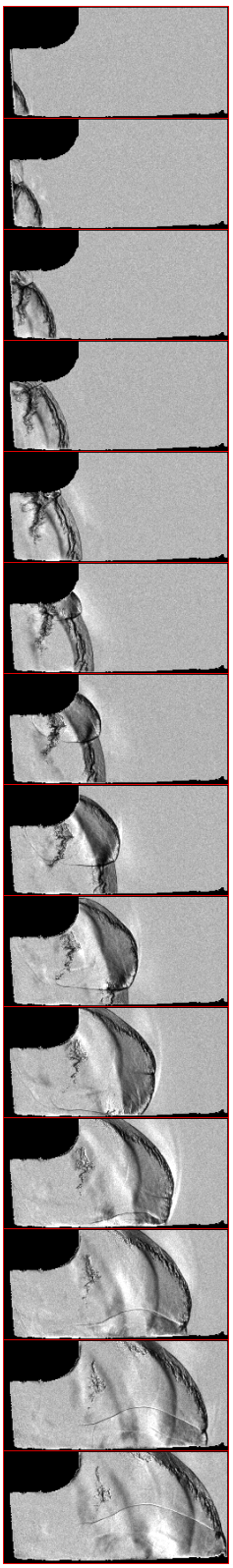

Run 7

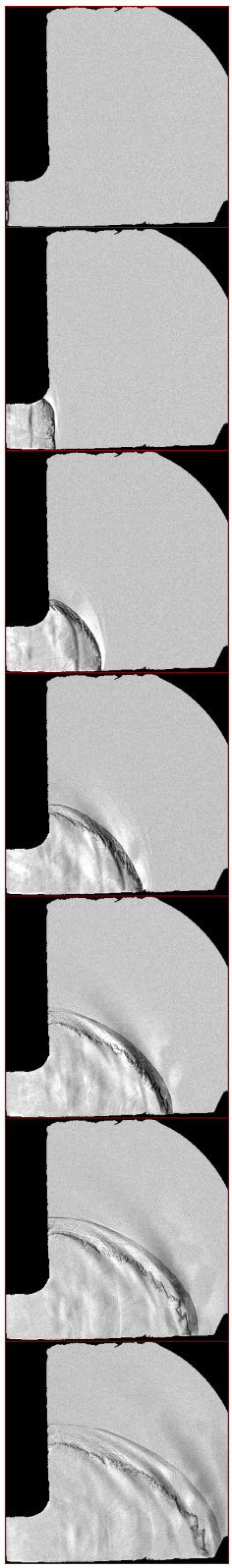

Run 8

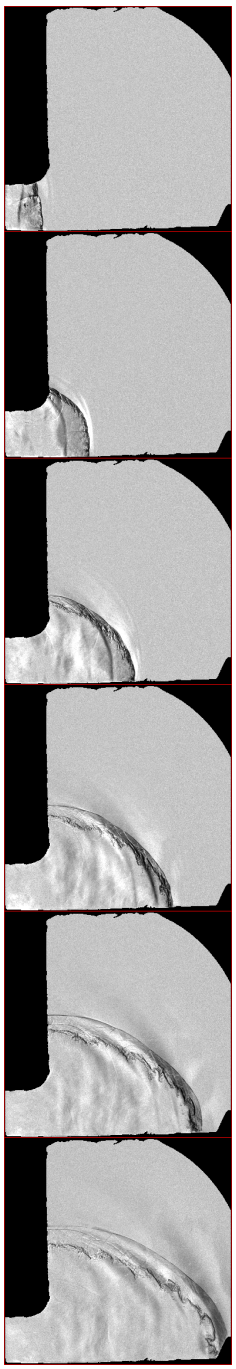

Case D4 (continued)

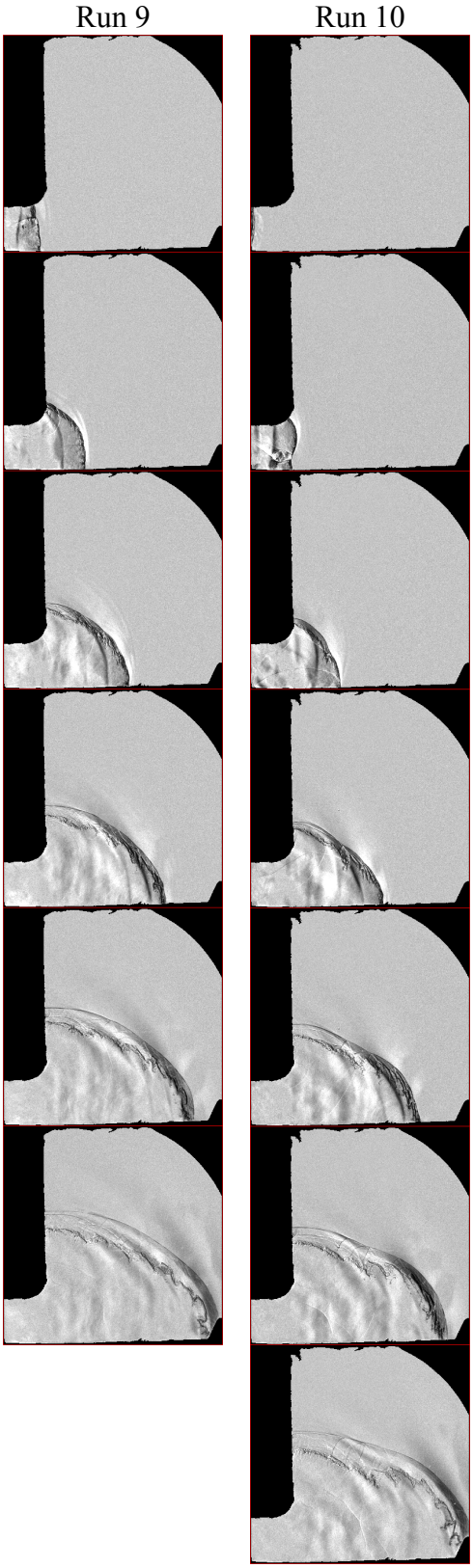

XII. R-Series Cases

Case R1: $\beta = 45°$, $x_0 = 162.2$ mm, $y_0 = -50.2$ mm

Run 1 Run 2 Run 3 Run 4

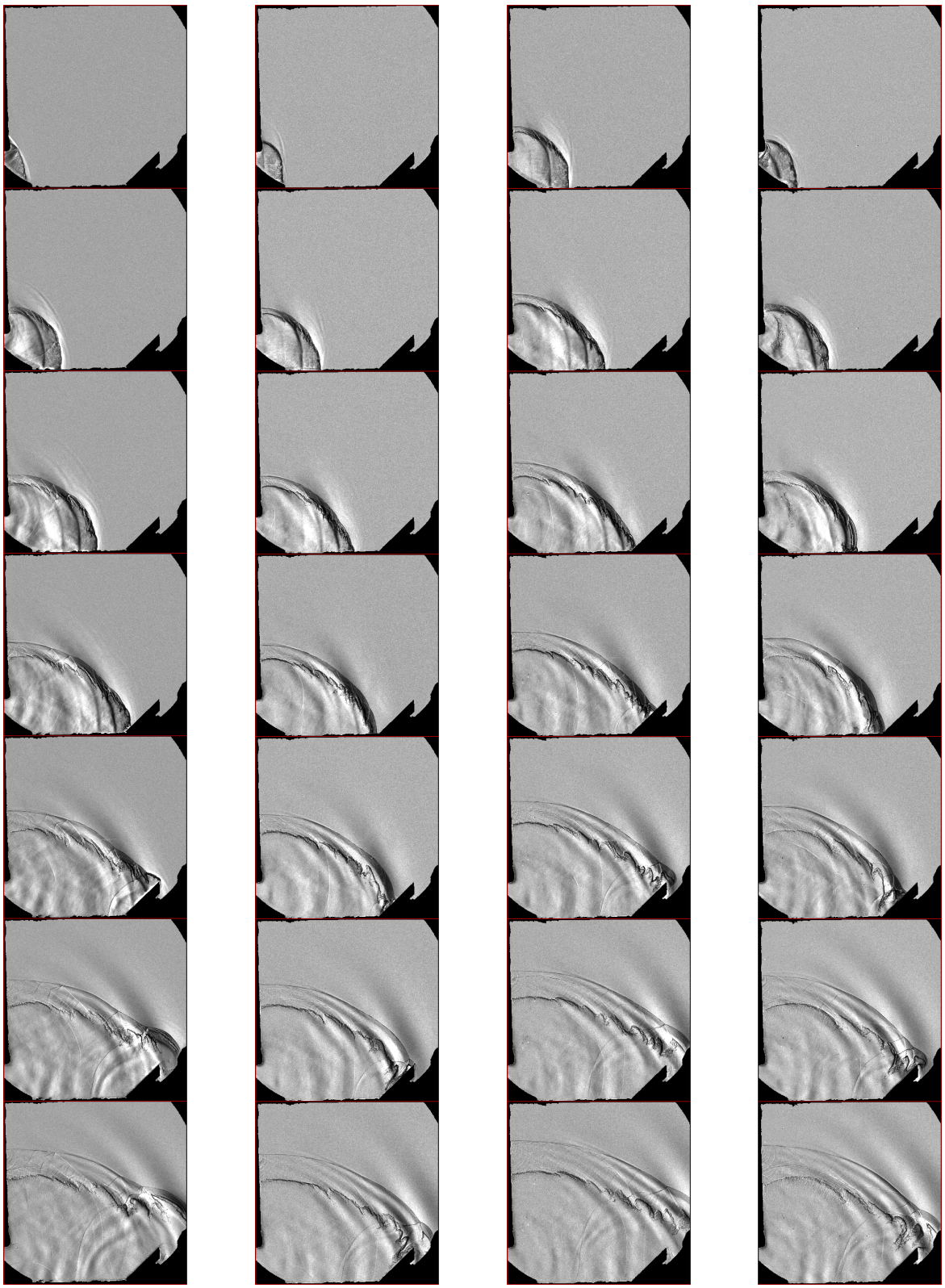

Case R1 (continued)

Run 5

Run 6

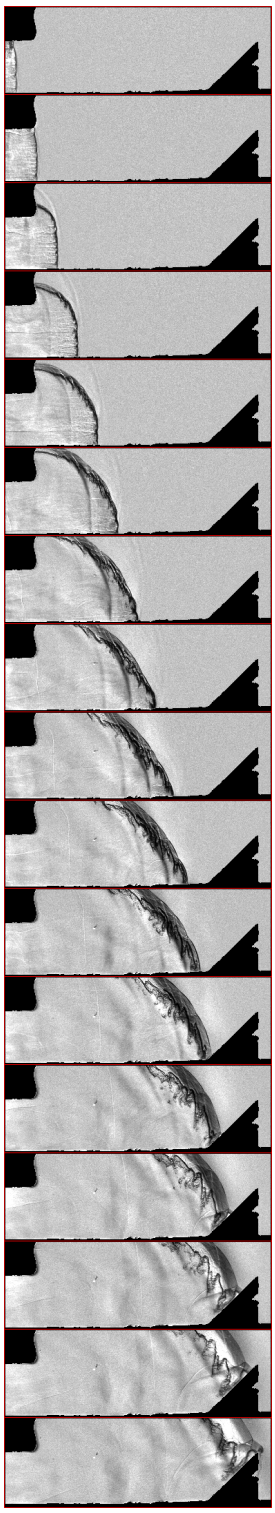

Run 7

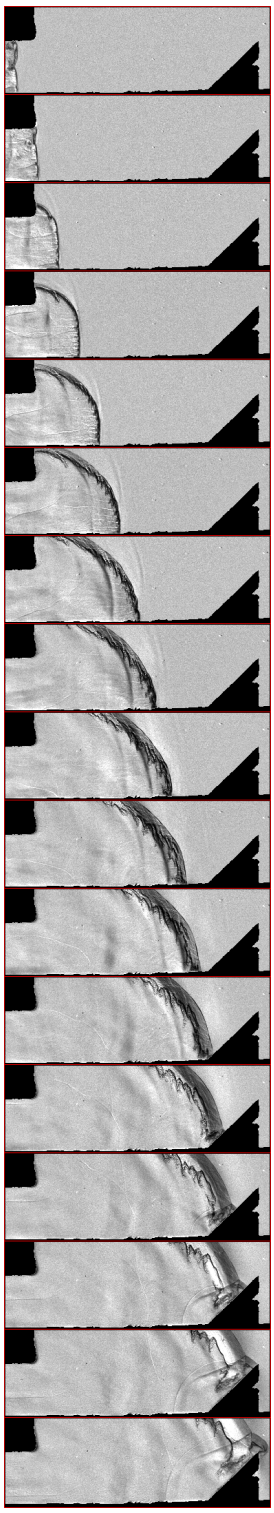

Run 8

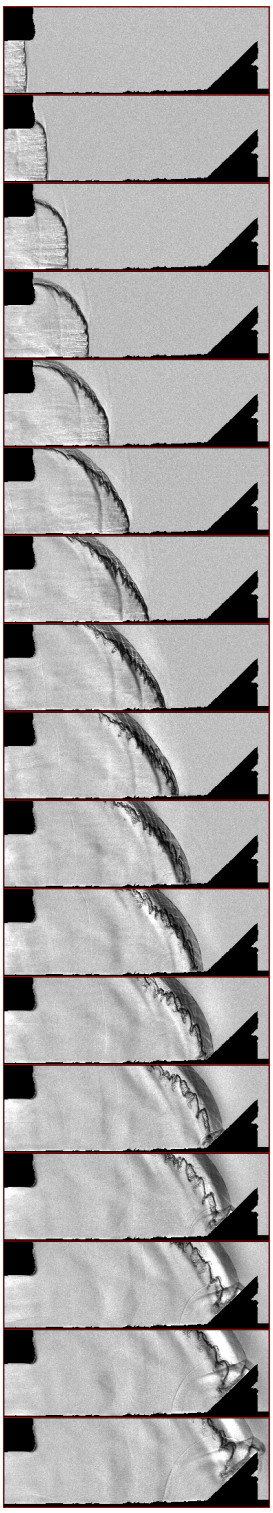

Case R1 (continued)

Run 9

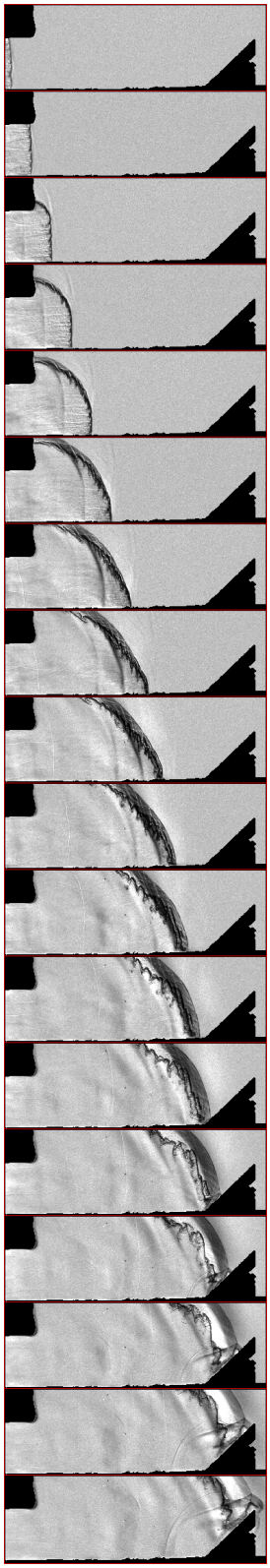

Run 10

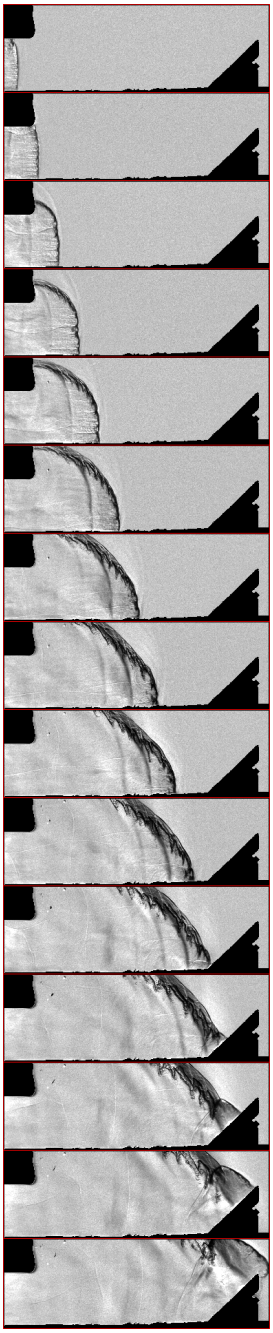

Case R2: β = 45°, x_0 = 84.7 mm, y_0 = -50.8 mm

Run 1 Run 2 Run 3 Run 4

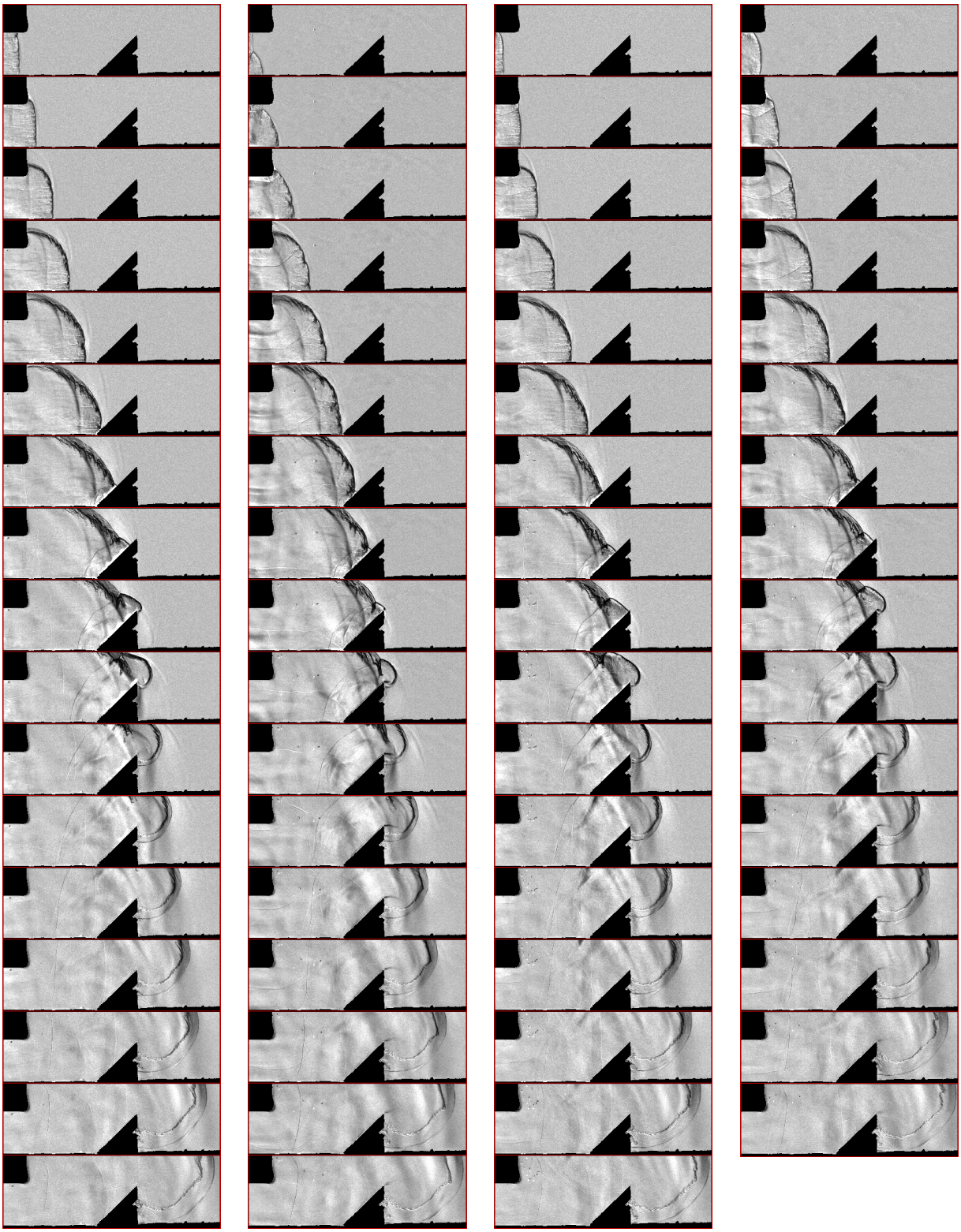

Case R2 (continued)

Run 5

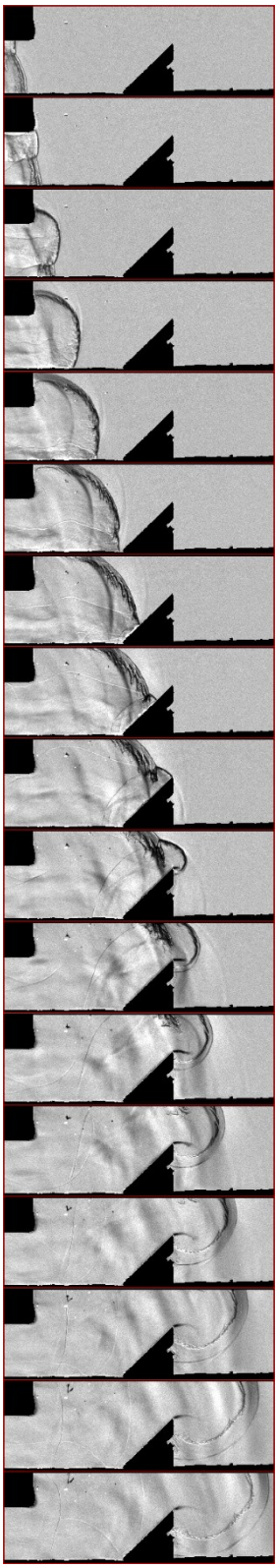

Run 6

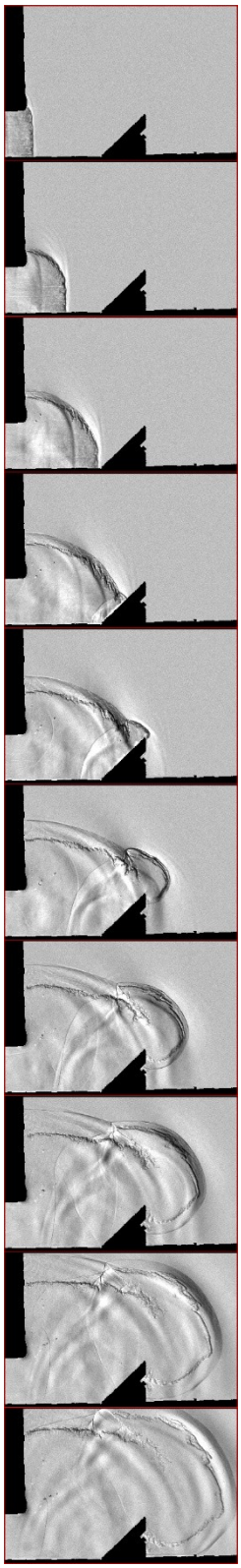

Run 7

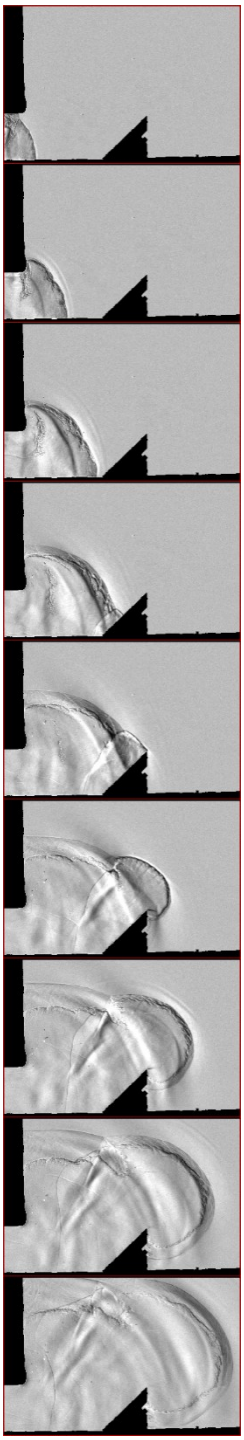

Run 8

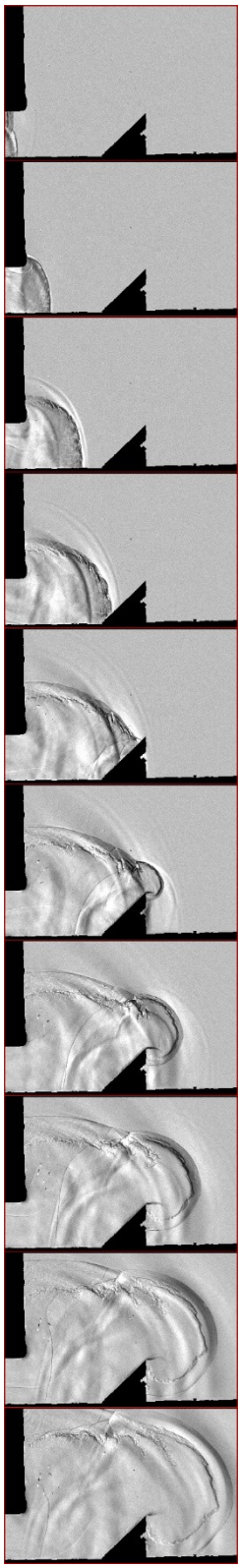

Case R2 (continued)

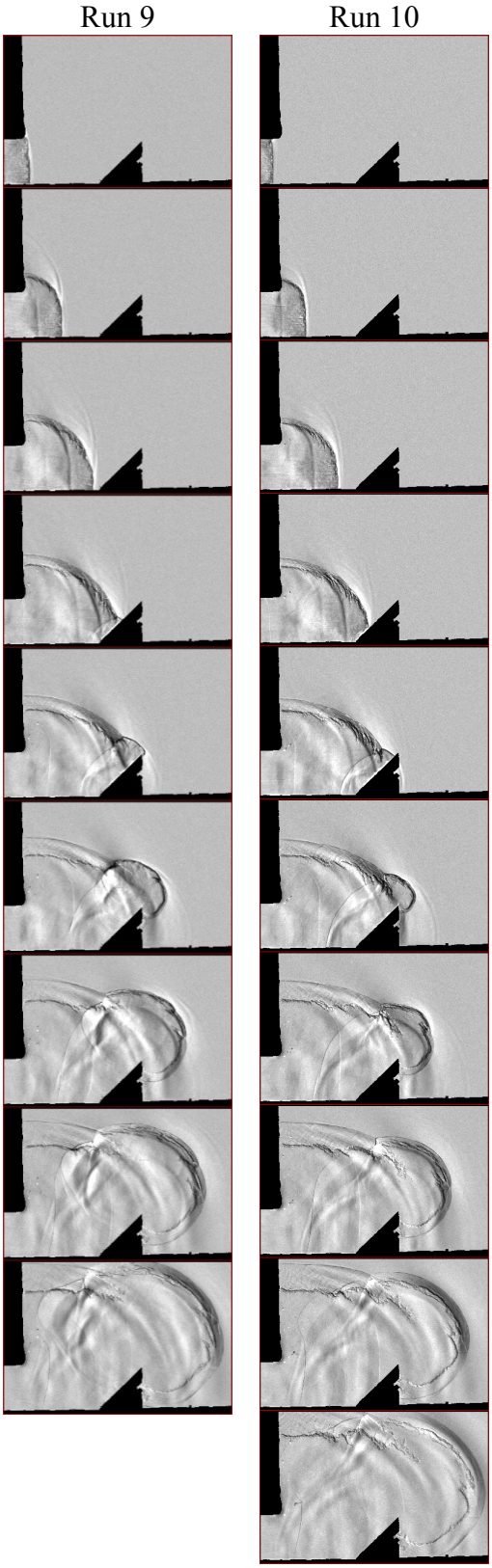

Case R3: $\beta = 30°$, $x_0 = 80.1$ mm, $y_0 = -50.8$ mm

Run 1 Run 2 Run 3 Run 4

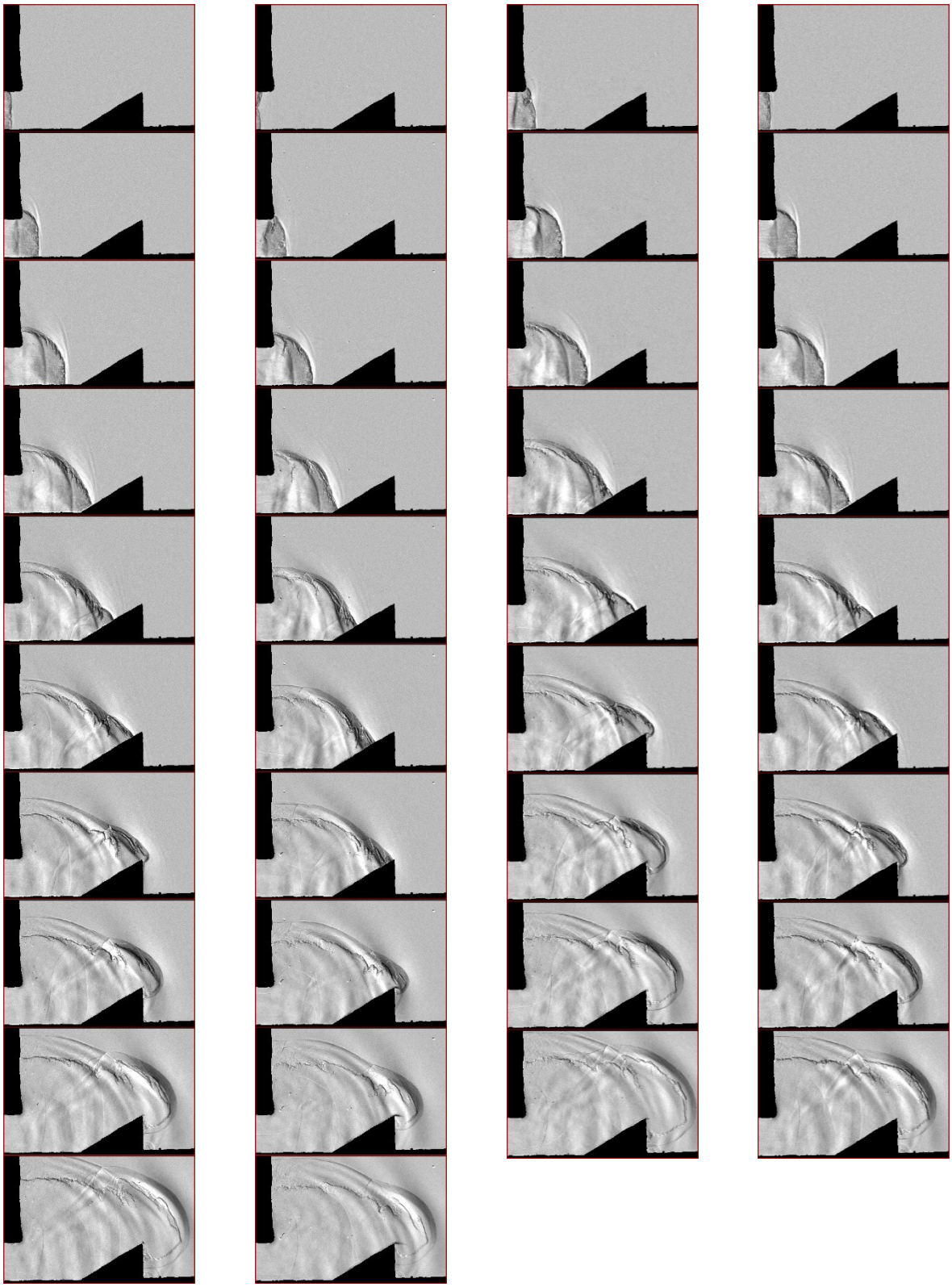

Case R3 (continued)

Run 5

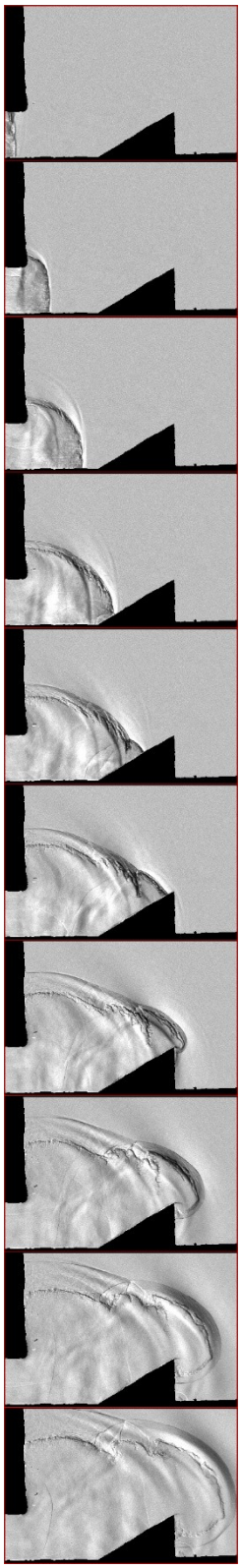

Run 6

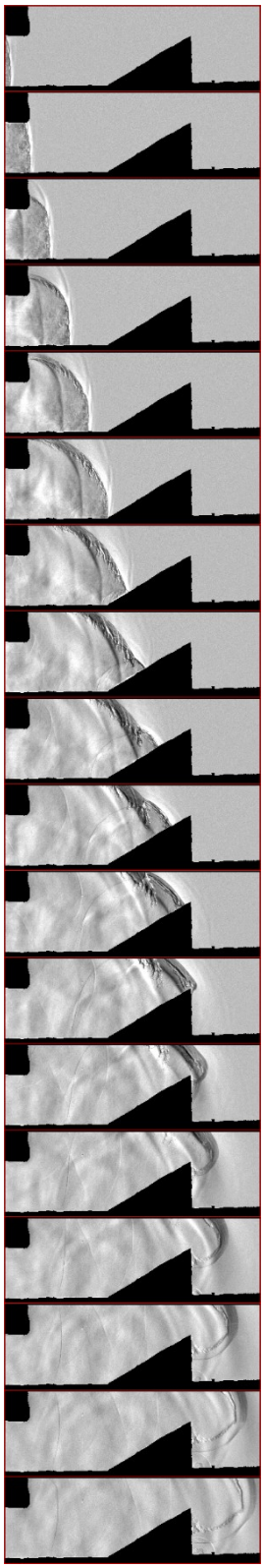

Run 7

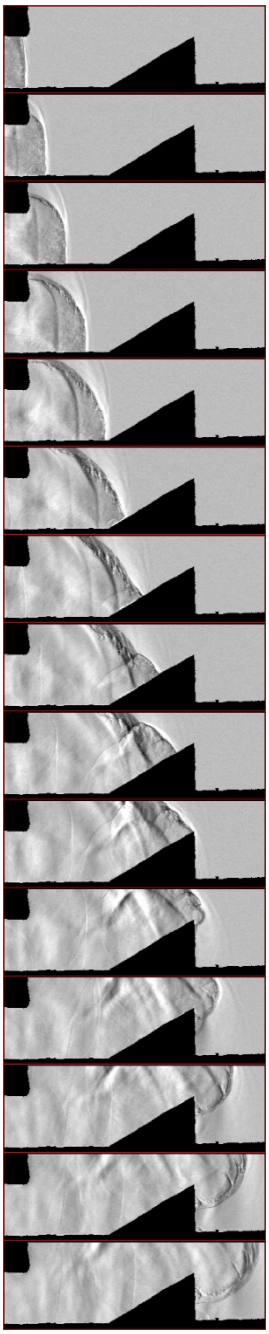

Run 8

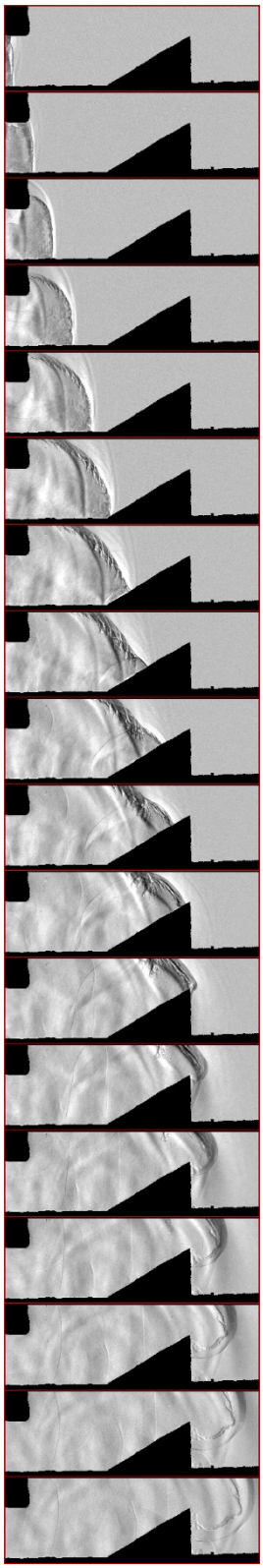

Case R3 (continued)

Run 9

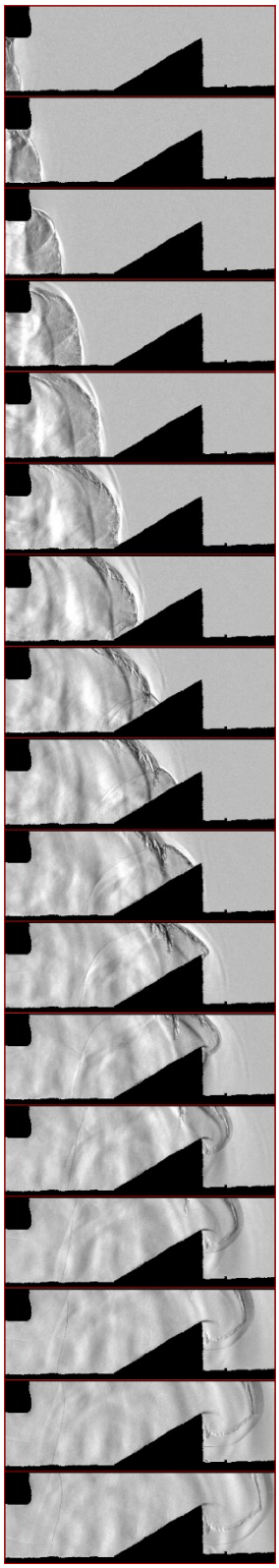

Run 10

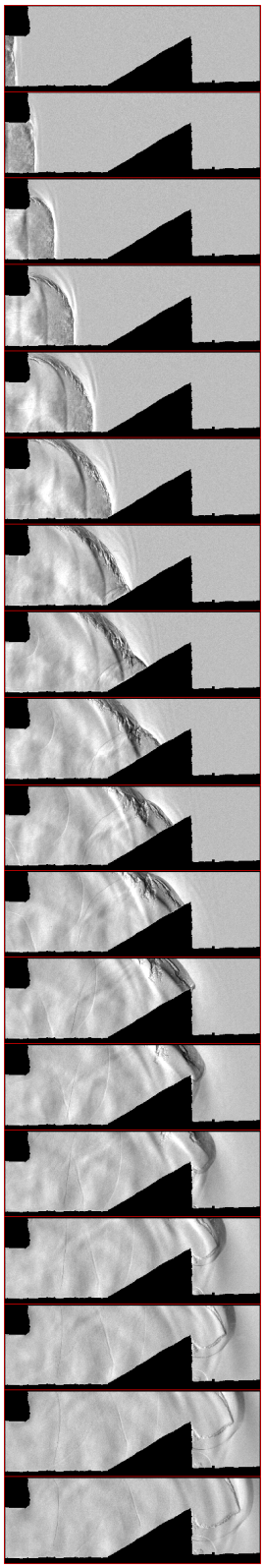

Case R4: $\beta = 15°$, $x_0 = 0.0$ mm, $y_0 = 50.8$ mm

Run 1 Run 2 Run 3 Run 4

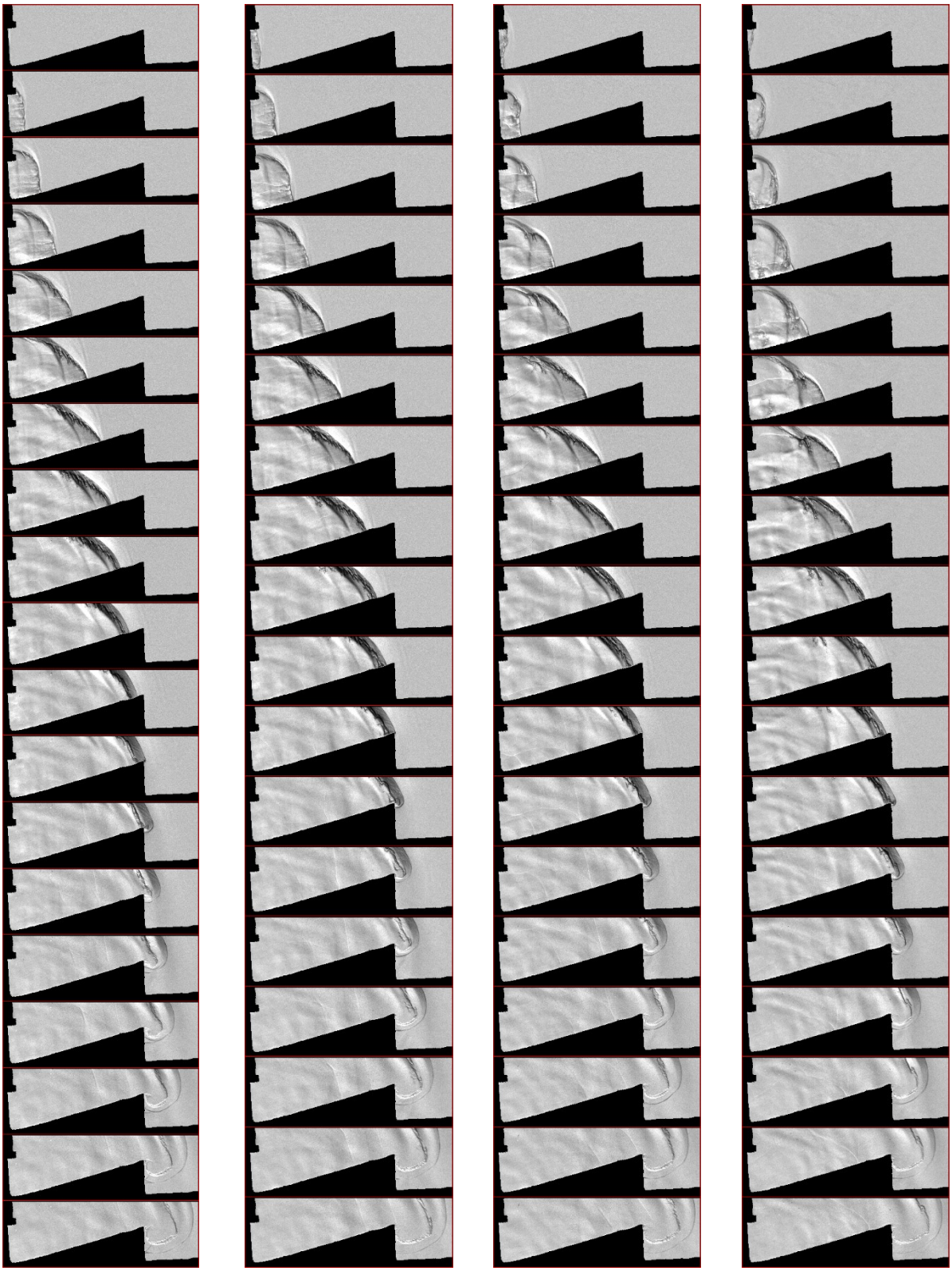

Case R4 (continued)

Run 5 Run 6

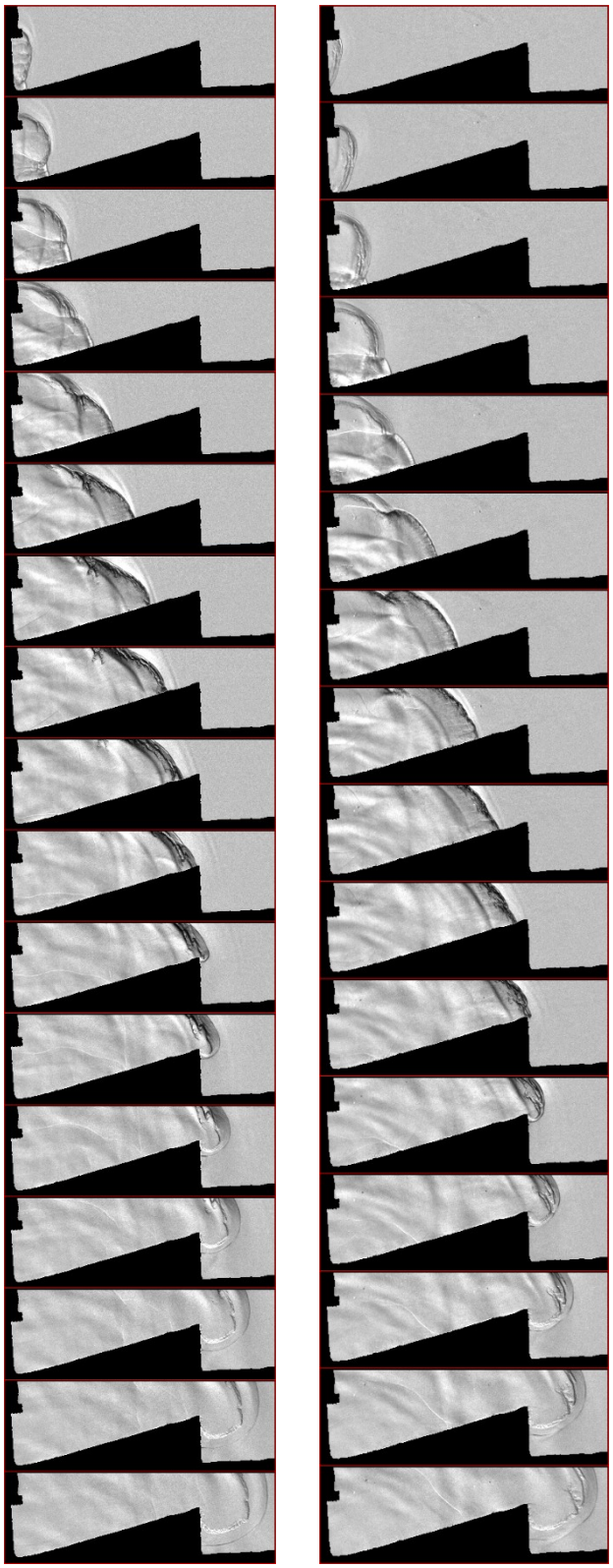

Case R5: $\beta = 30°$, $x_0 = 80.1$ mm, $y_0 = -50.8$ mm, $r = 25.4$mm

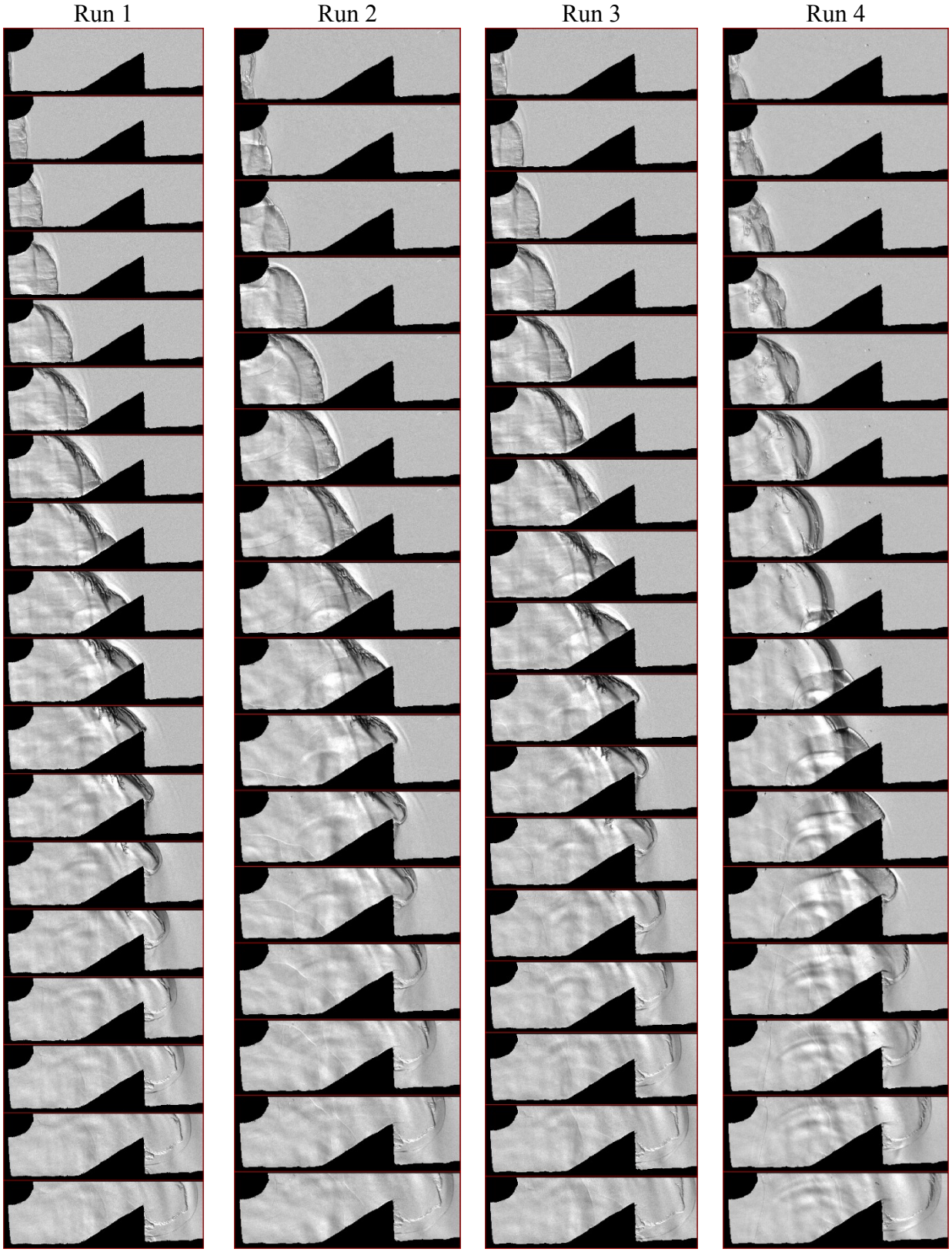

Case R5 (continued)

Run 5

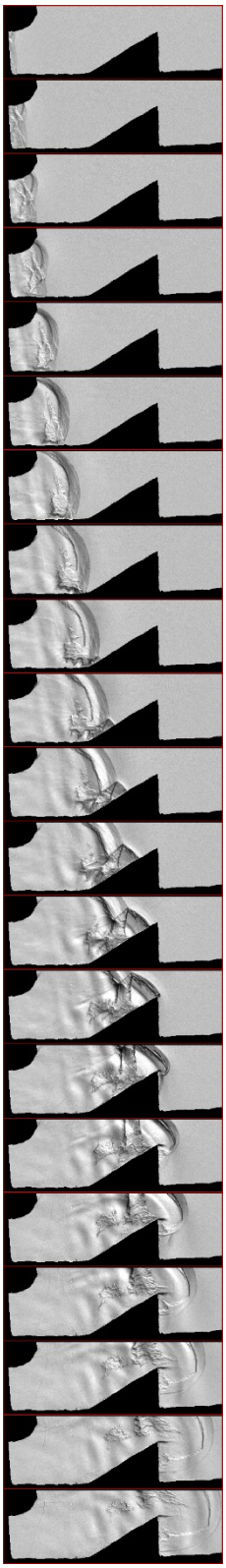

Run 6

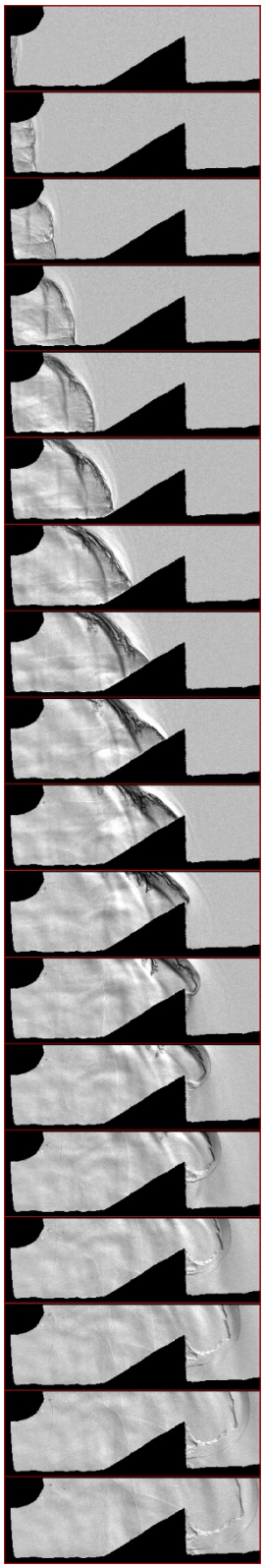

Case R6: β = -45° x0 = 0.0 mm, y0 = 50.8 mm

Run 1 Run 2 Run 3 Run 4

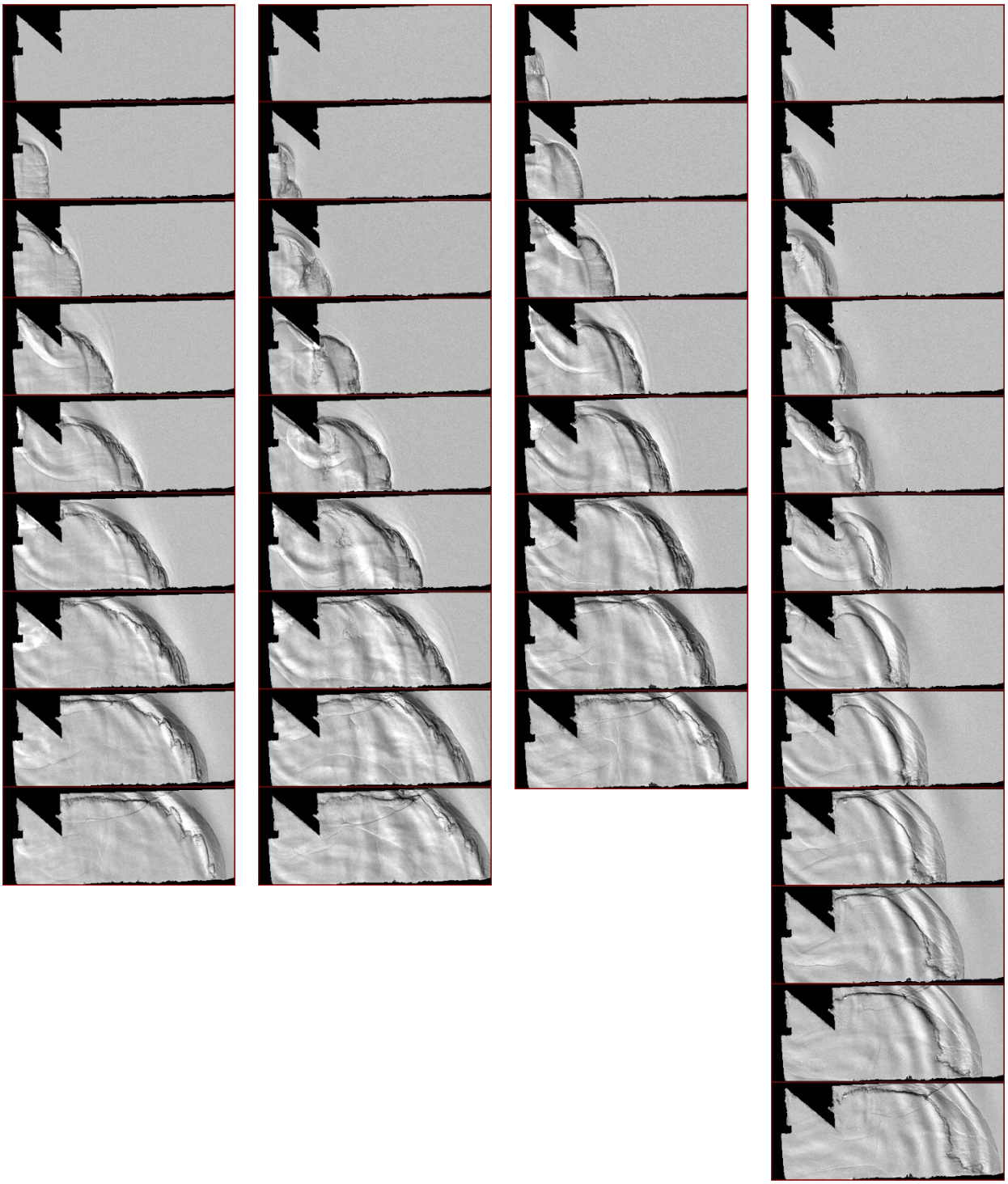

Case R6 (continued)

Run 5

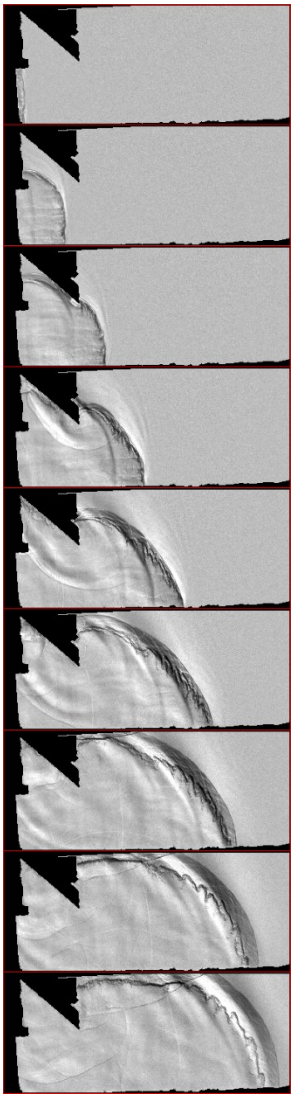

Run 6

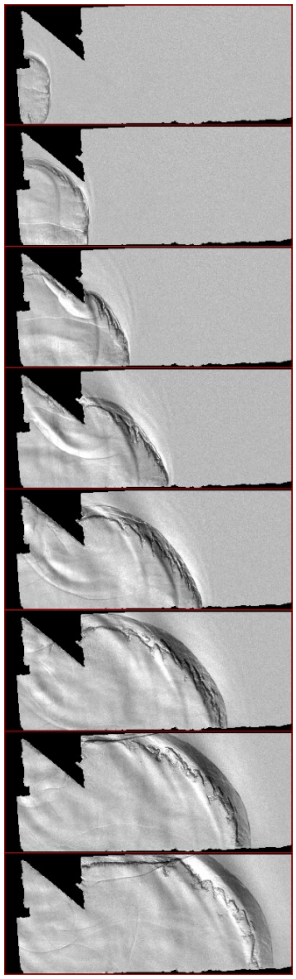

Run 7

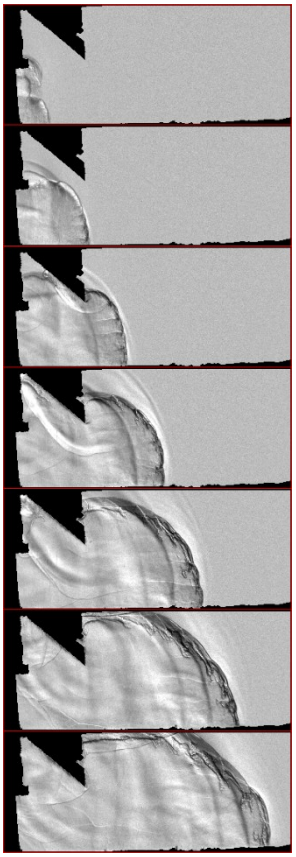

Run 8

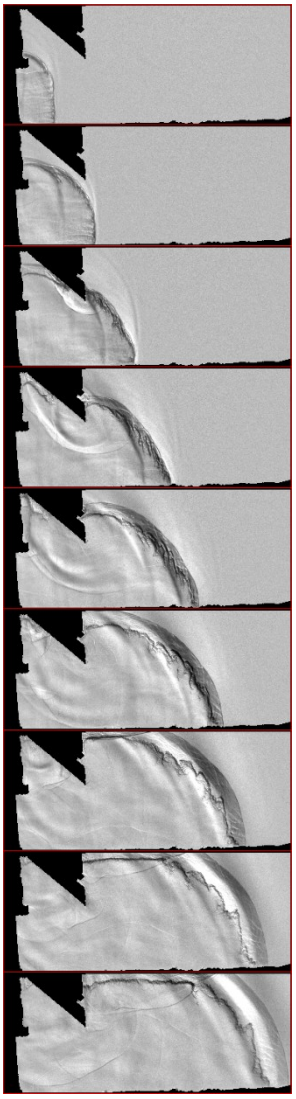

Case R6 (continued)

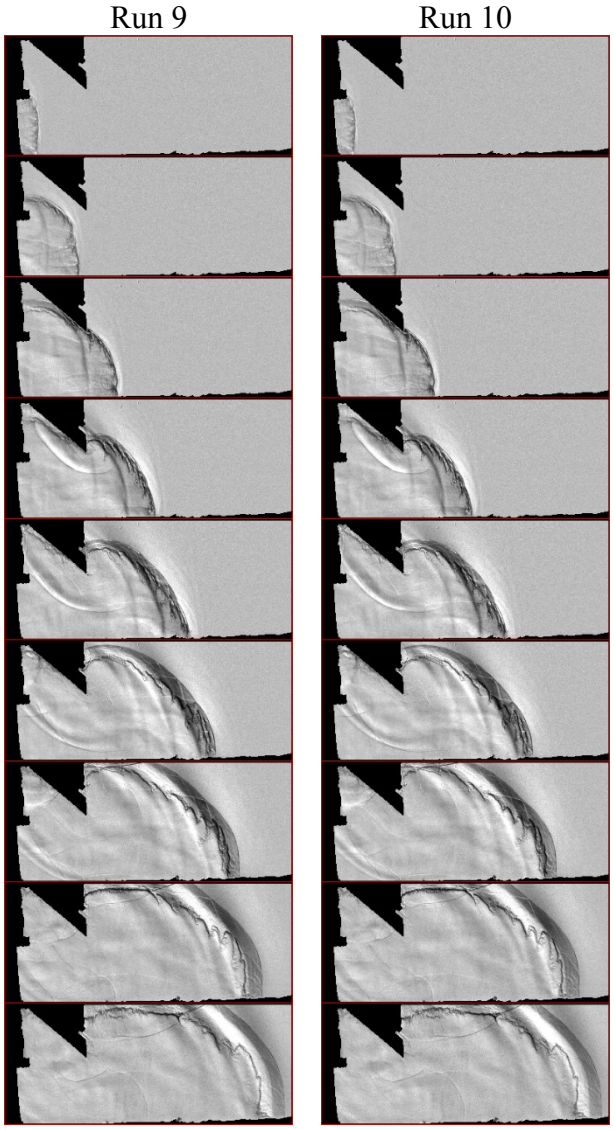

Case R7: β= -45°, x0 = 43.0 mm, y0 = 50.8 mm

Run 1 Run 2 Run 3 Run 4

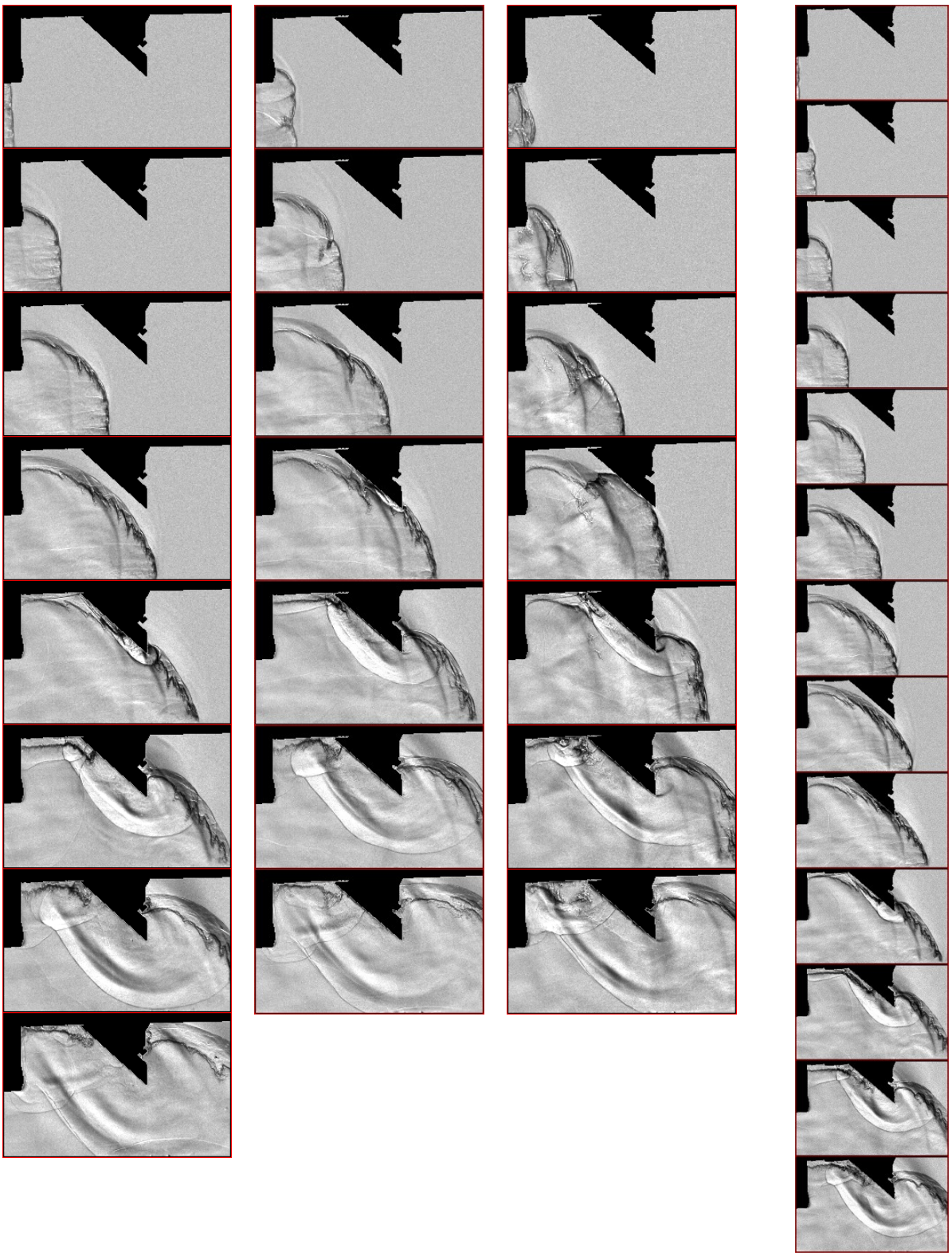

Case R7 (continued)

Run 5

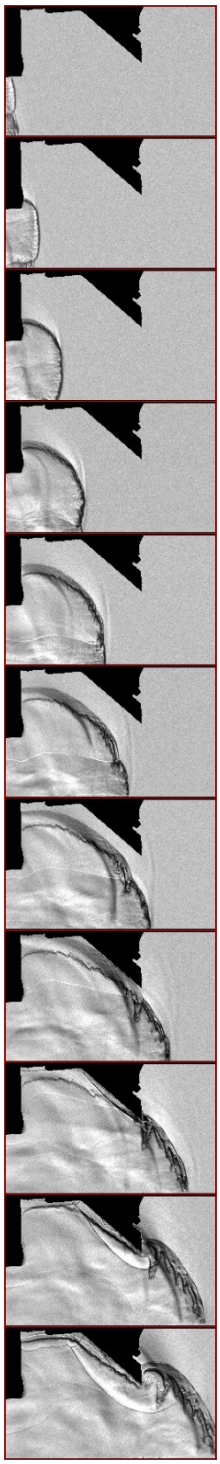

Run 6

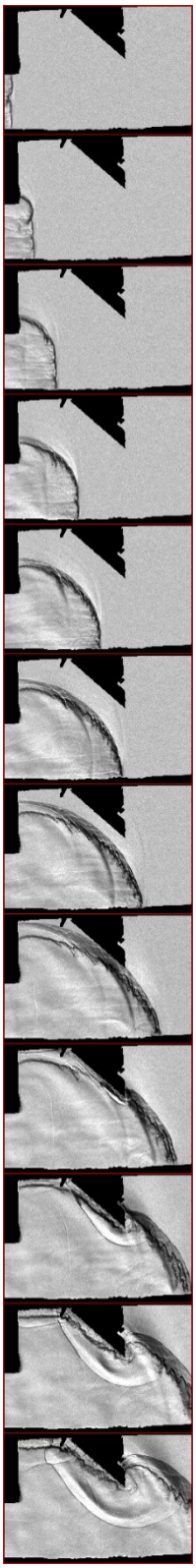

Run 7

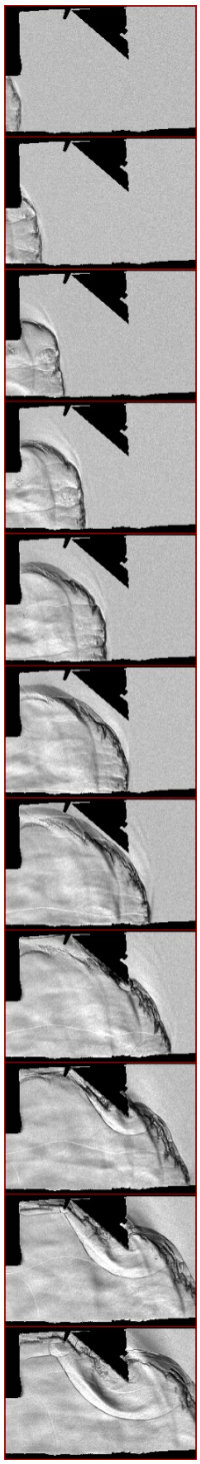

Run 8

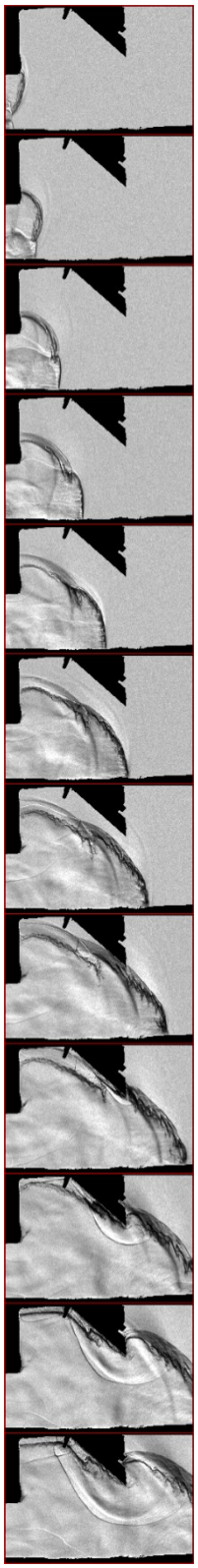

Case R8: β = -45°, x_0 = 169.3 mm, y0 = 50.8 mm

Run 1 Run 2 Run 3 Run 4

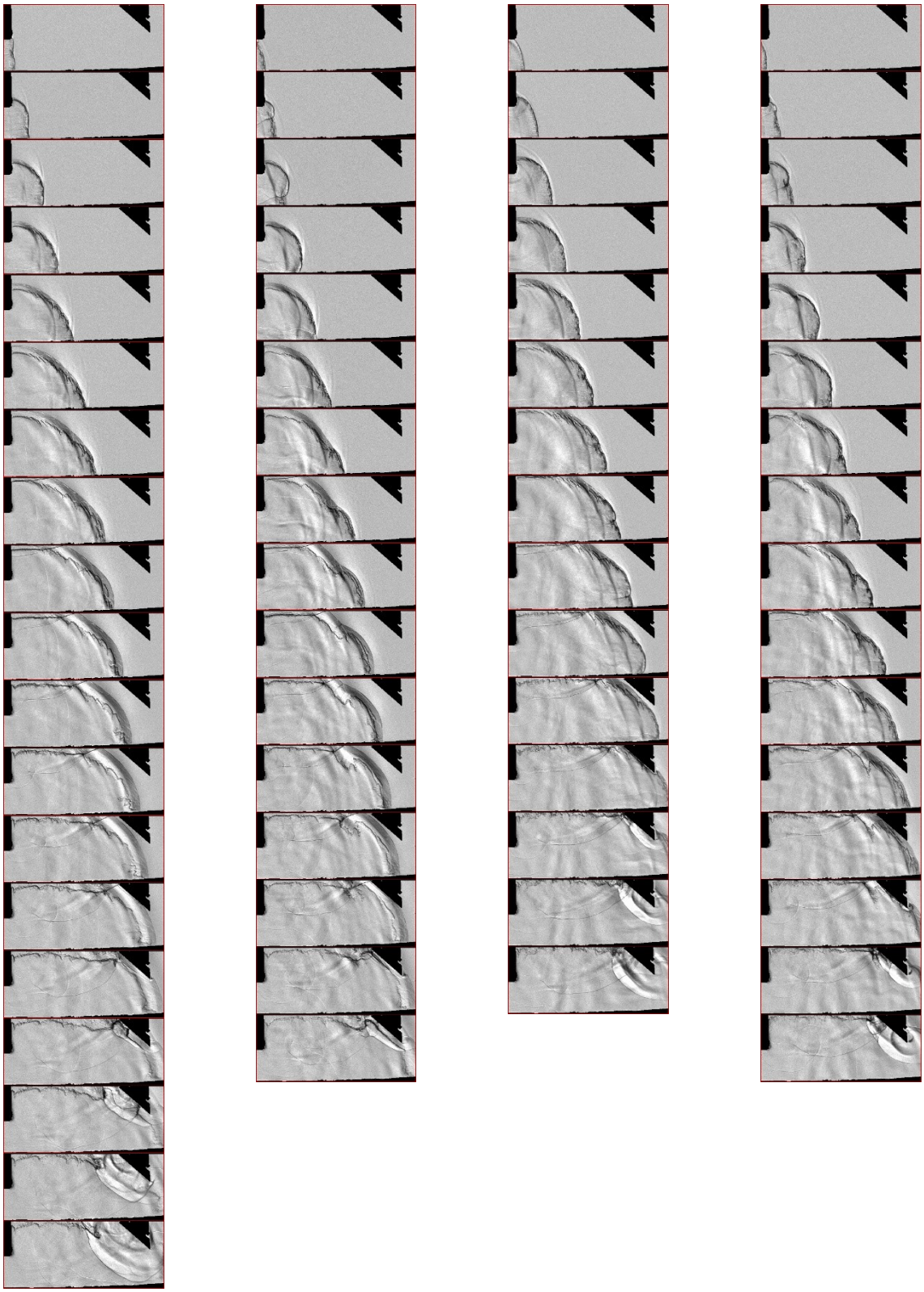

Case R8 (continued)

Run 5

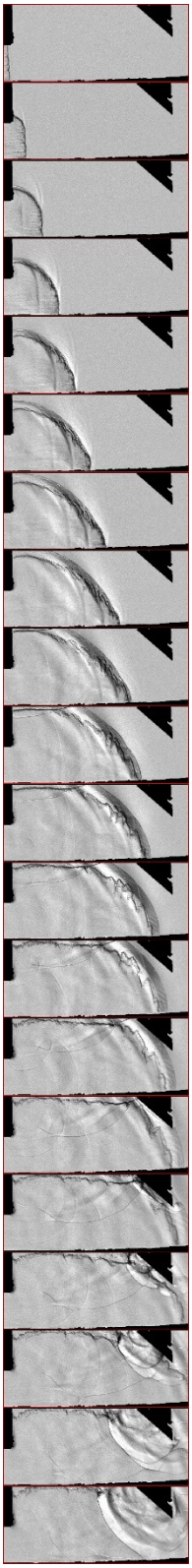

Run 6

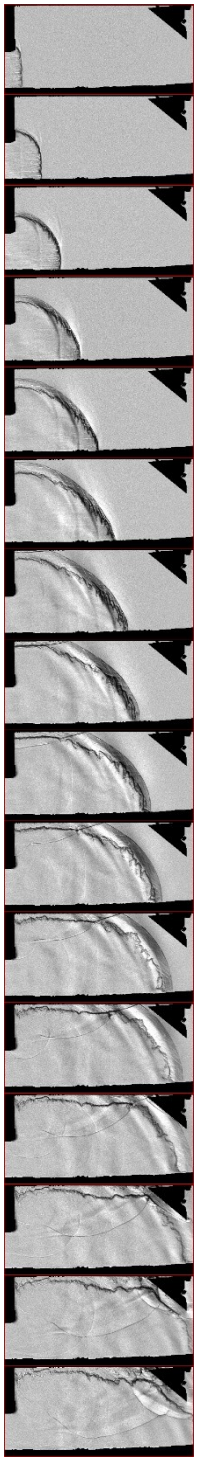

Run 7

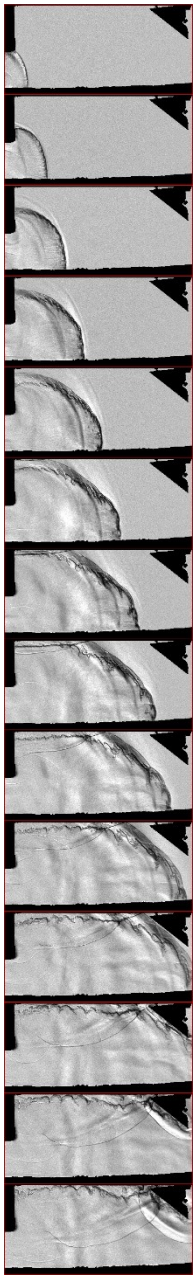

Run 8

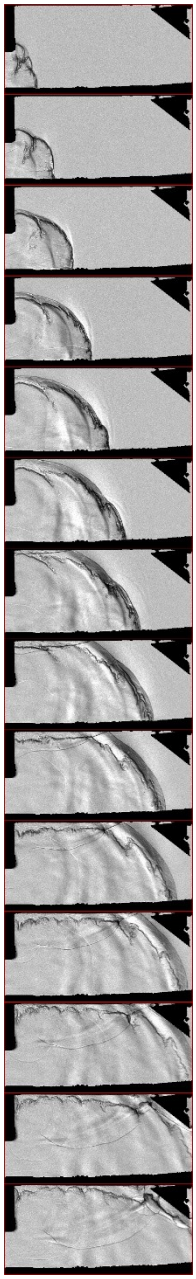

XIII. M-Series Cases

Case M1

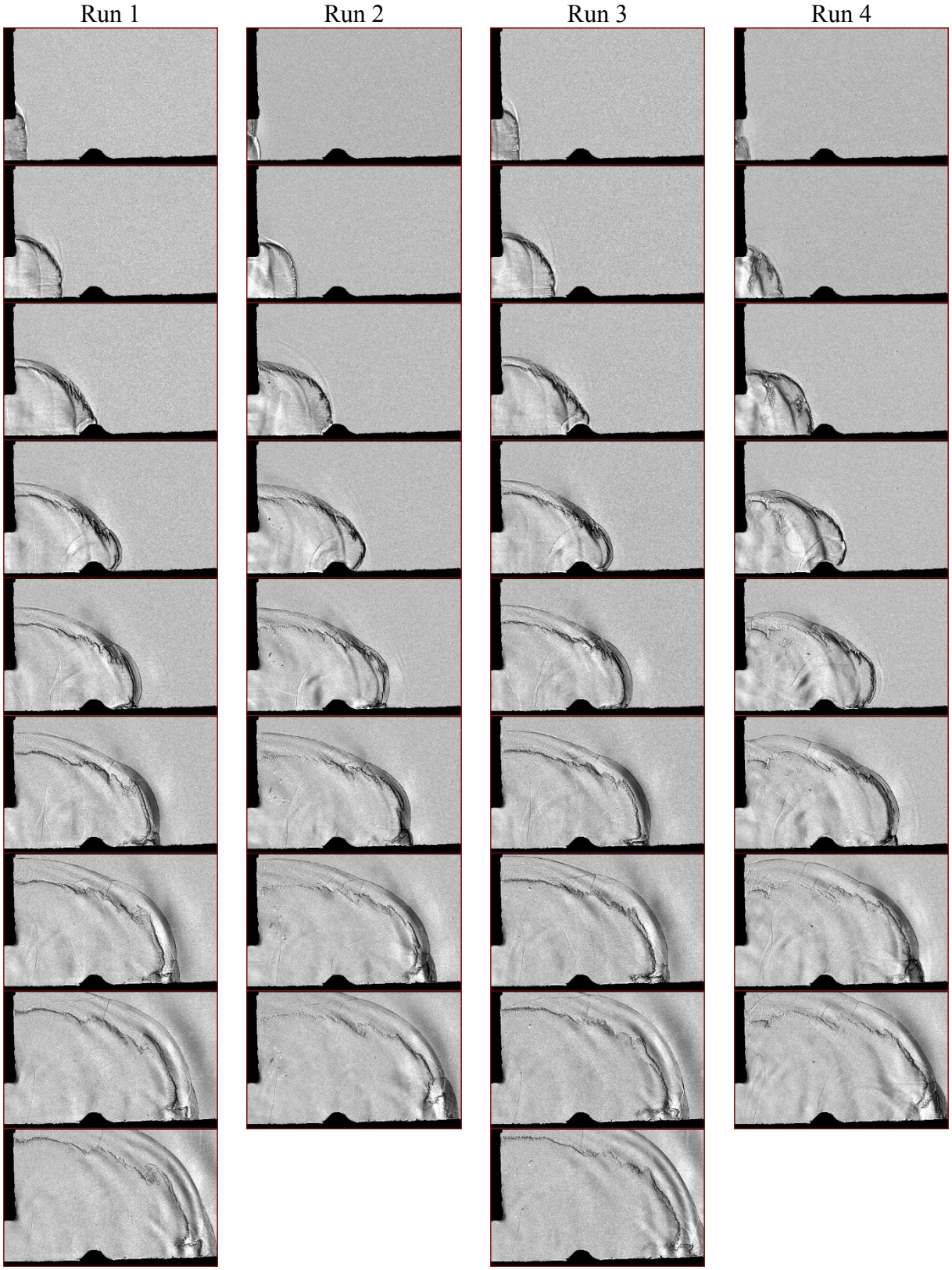

Case M2

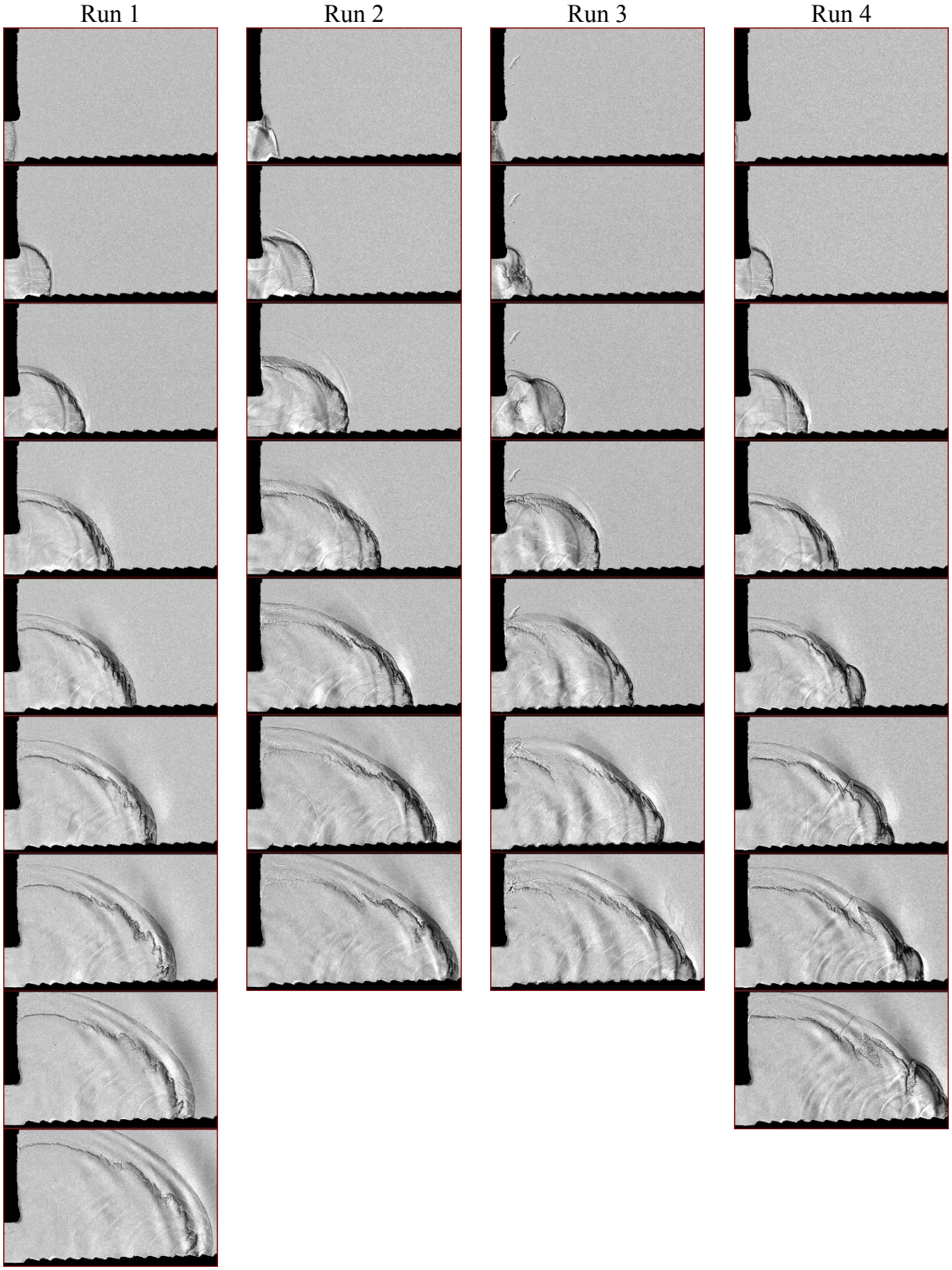

Case M2 (continued)

Run 5

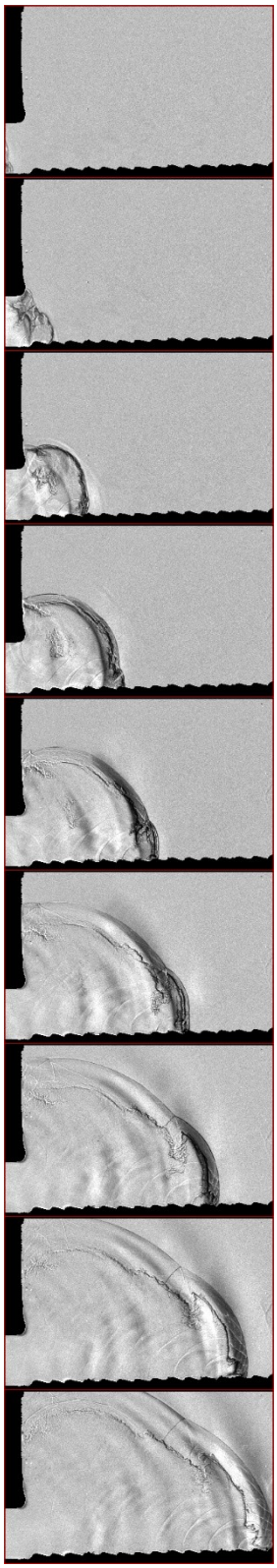

Run 6

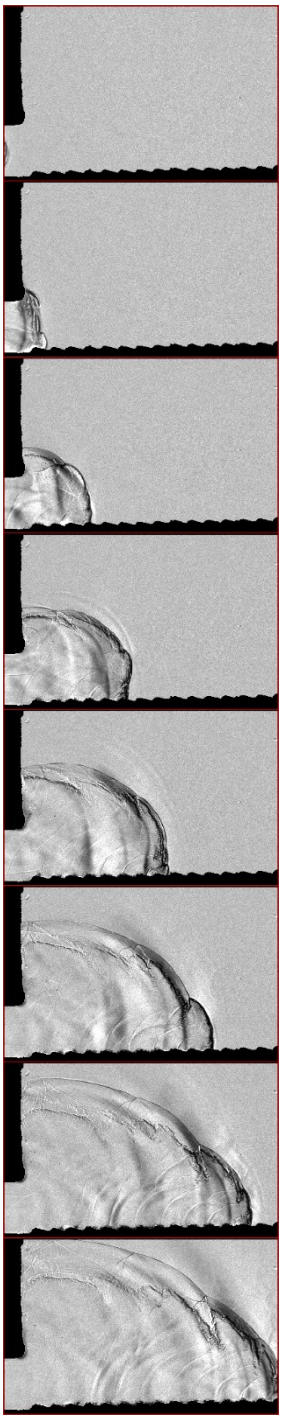

Run 7

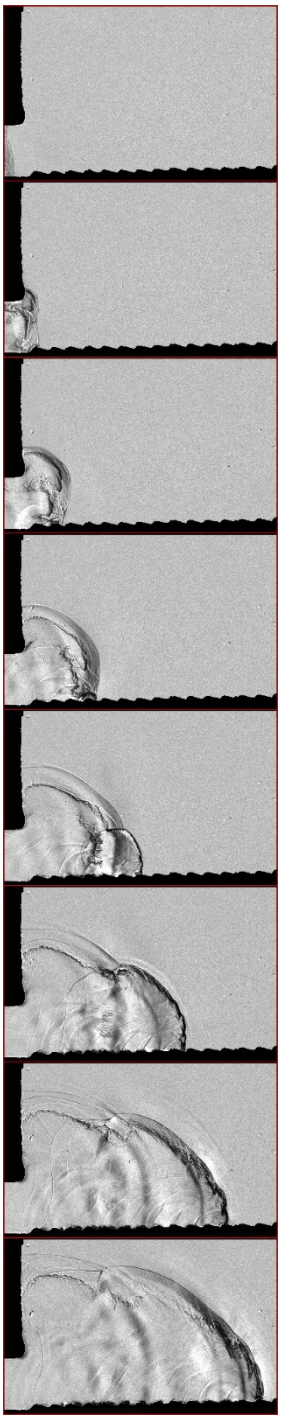

Run 8

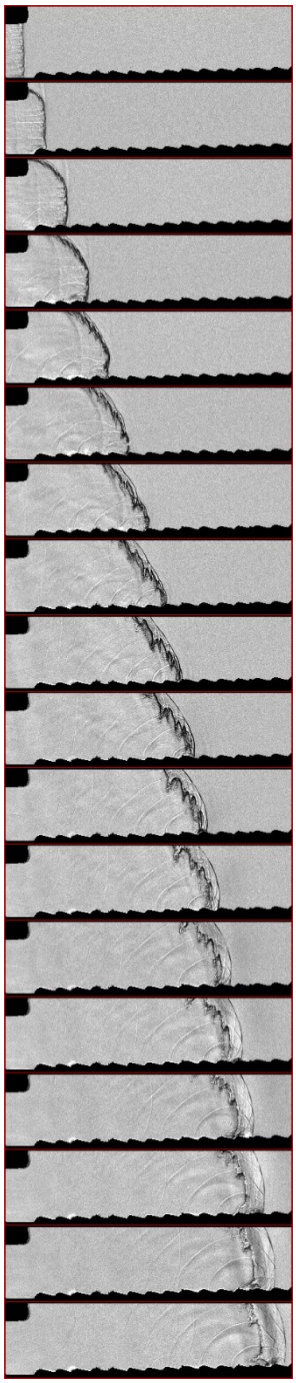

Case M2 (continued)

Run 9

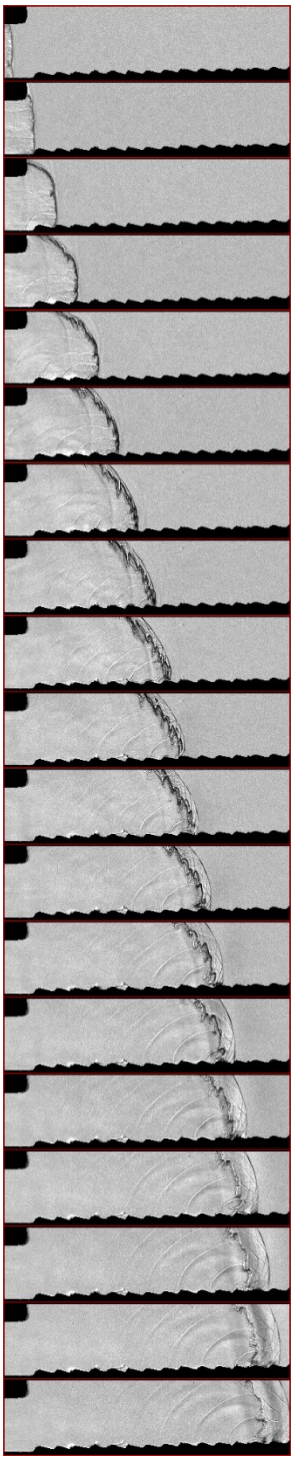

Run 10

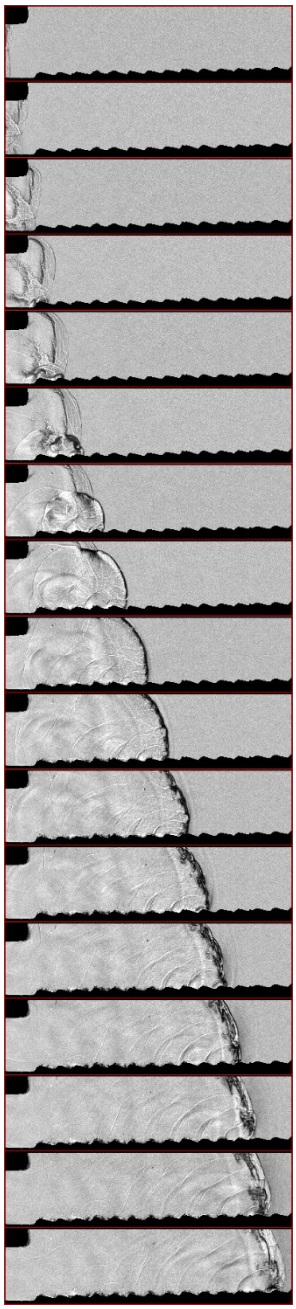

Run 11

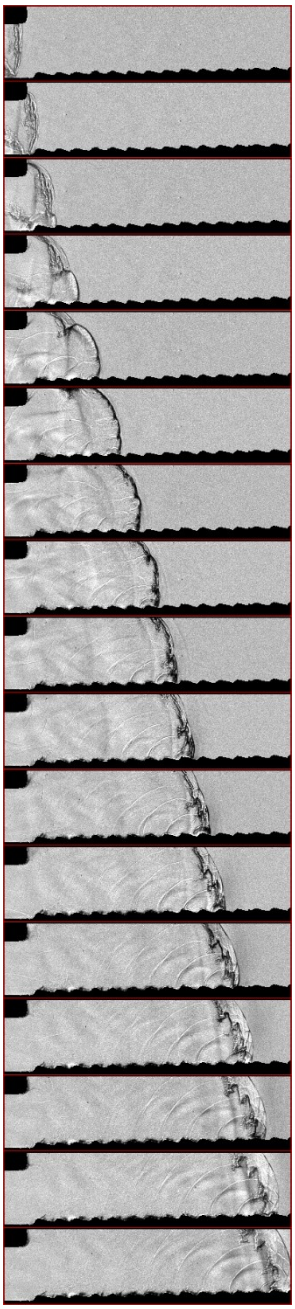

Run 12

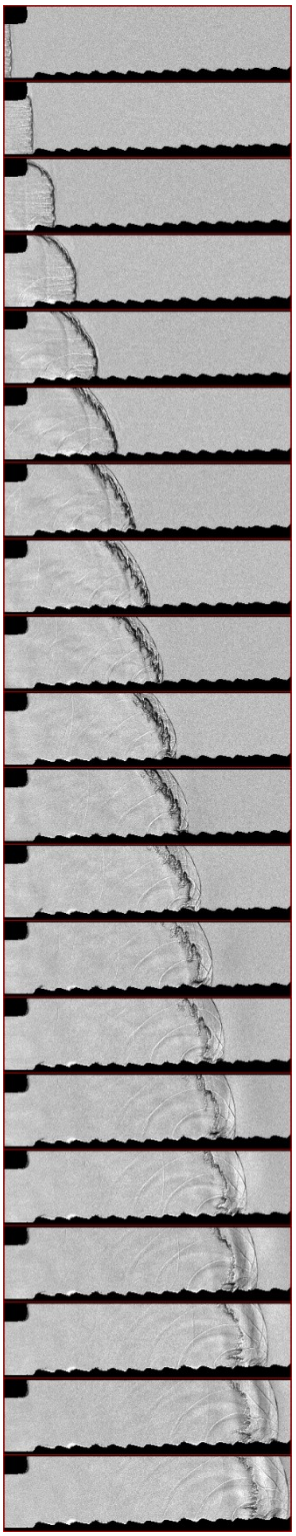

Case M2 (continued)

Run 13

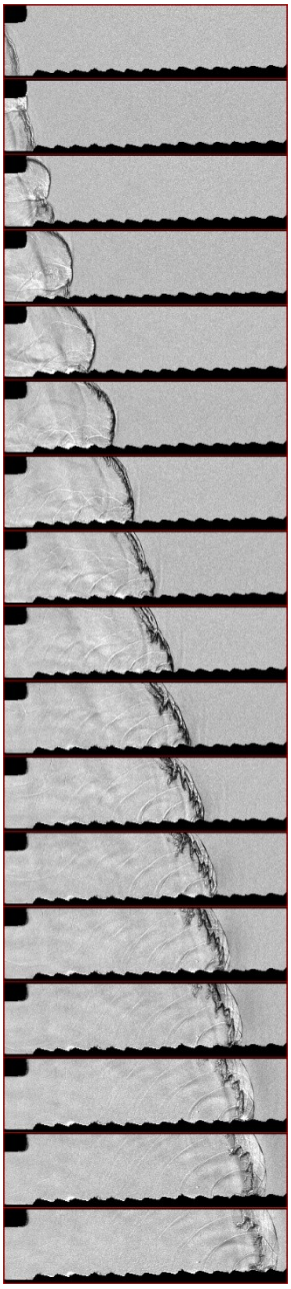

Run 14

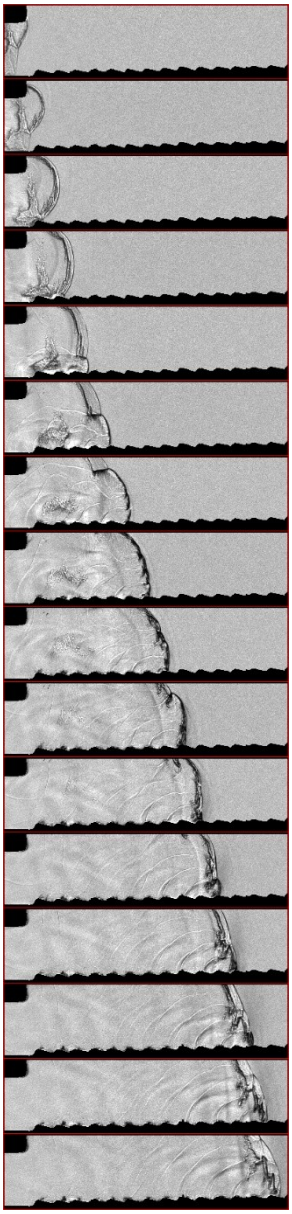

Run 15

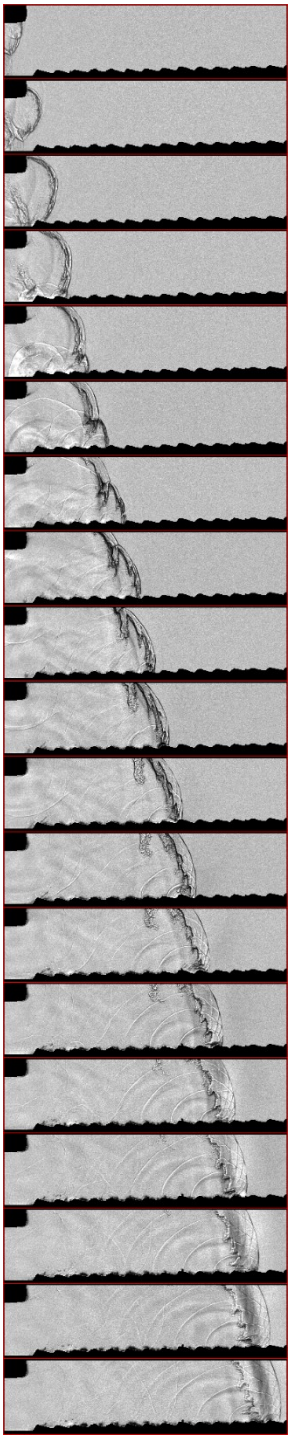

Run 16

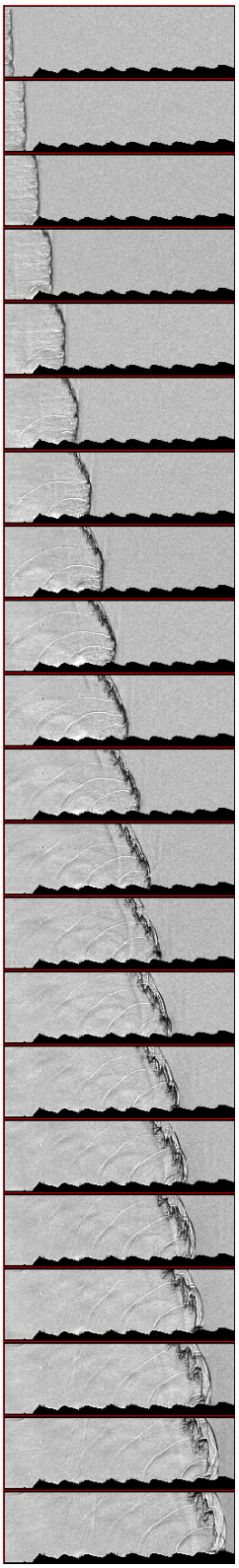

Case M2 (continued)

Run 17

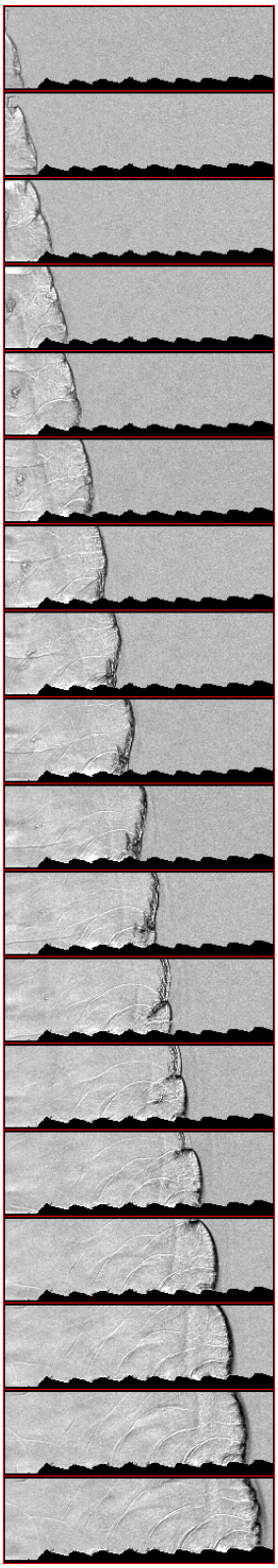

Run 18

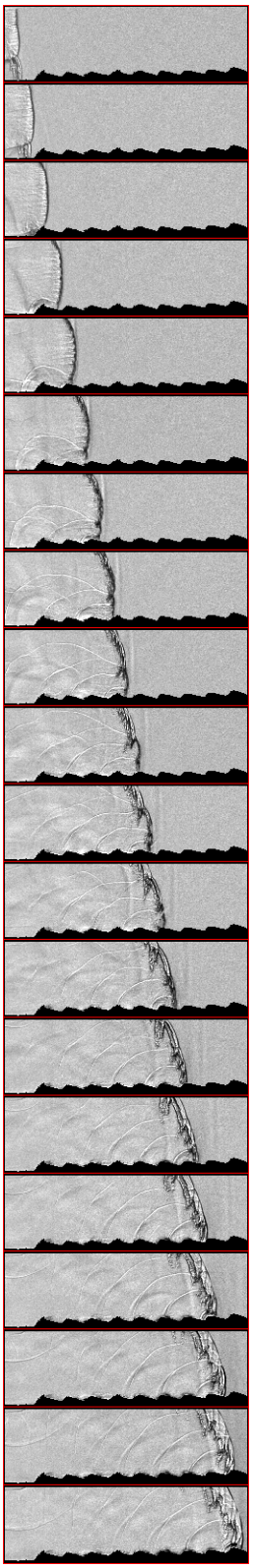

Run 19

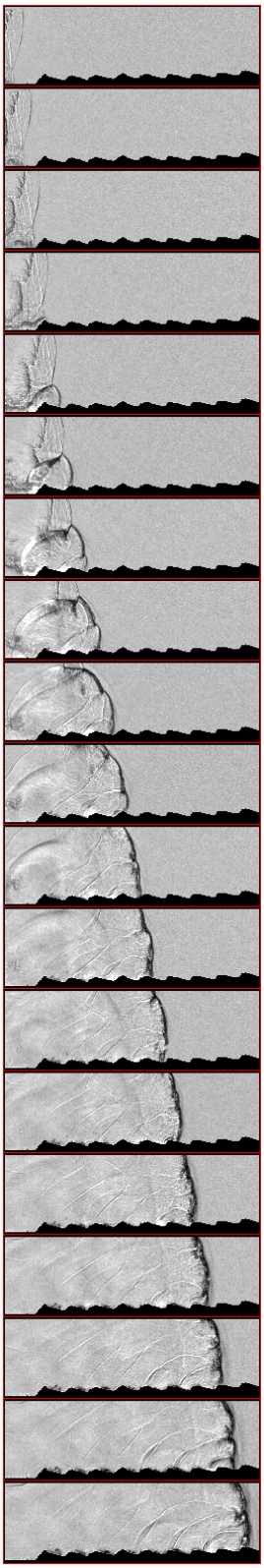

Run 20

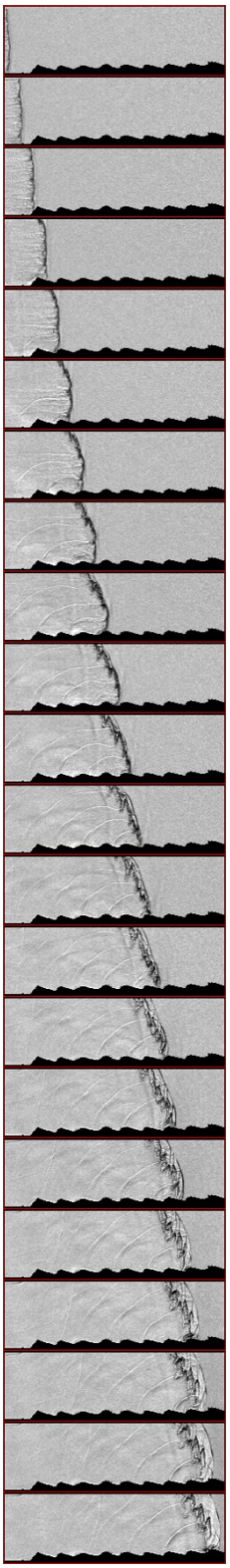

Case M2 (continued)

Run 21

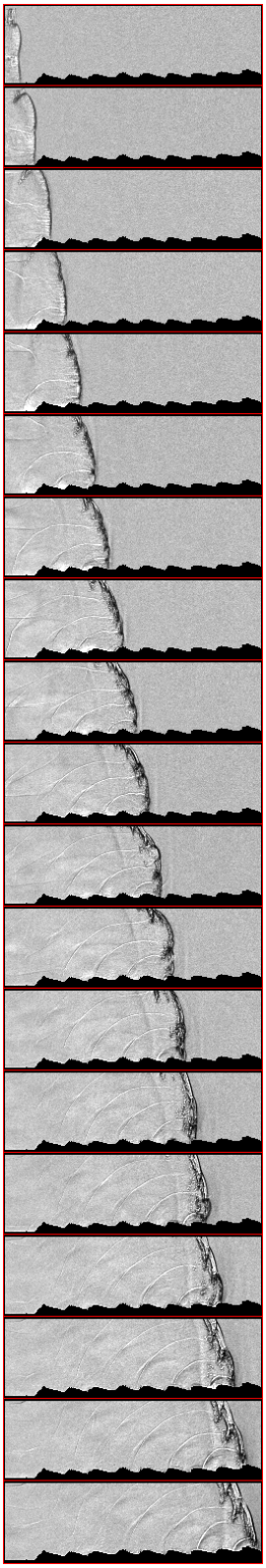

Run 22

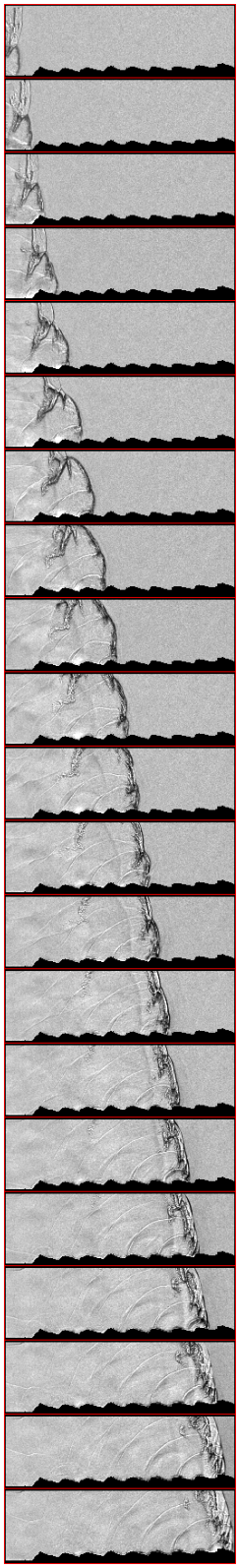

Case M3

Run 1

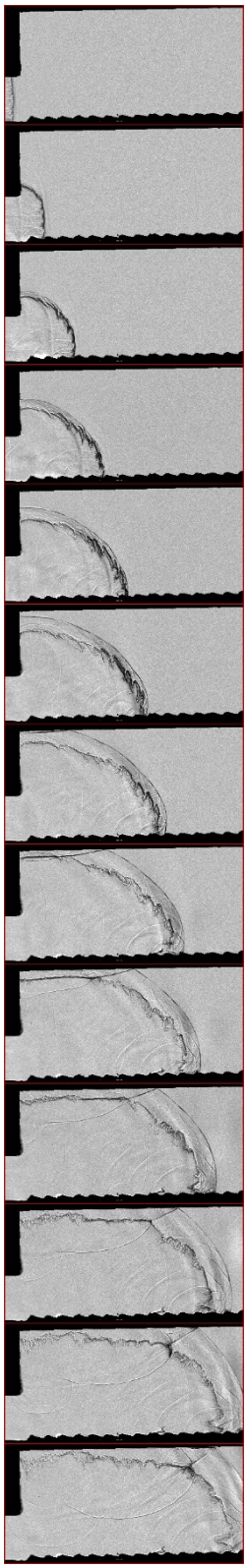

Run 2

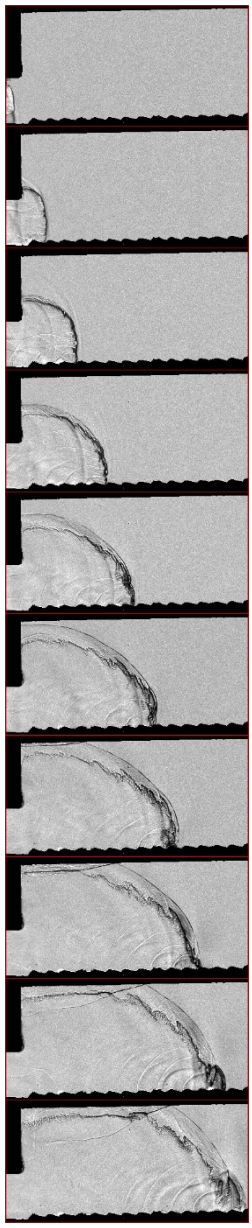

Run 3

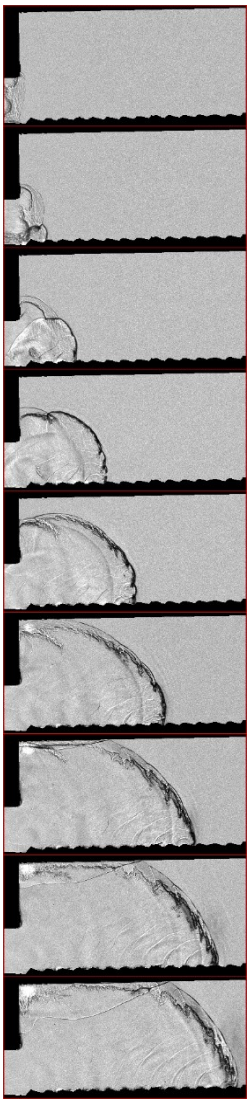

Run 4

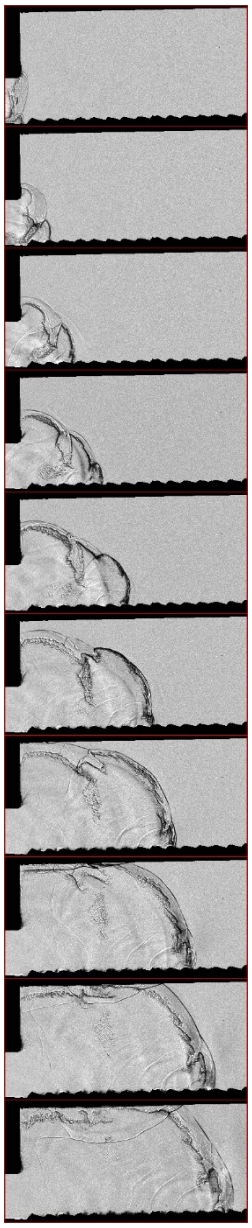

Case M3 (continued)

Run 5 Run 6 Run 7

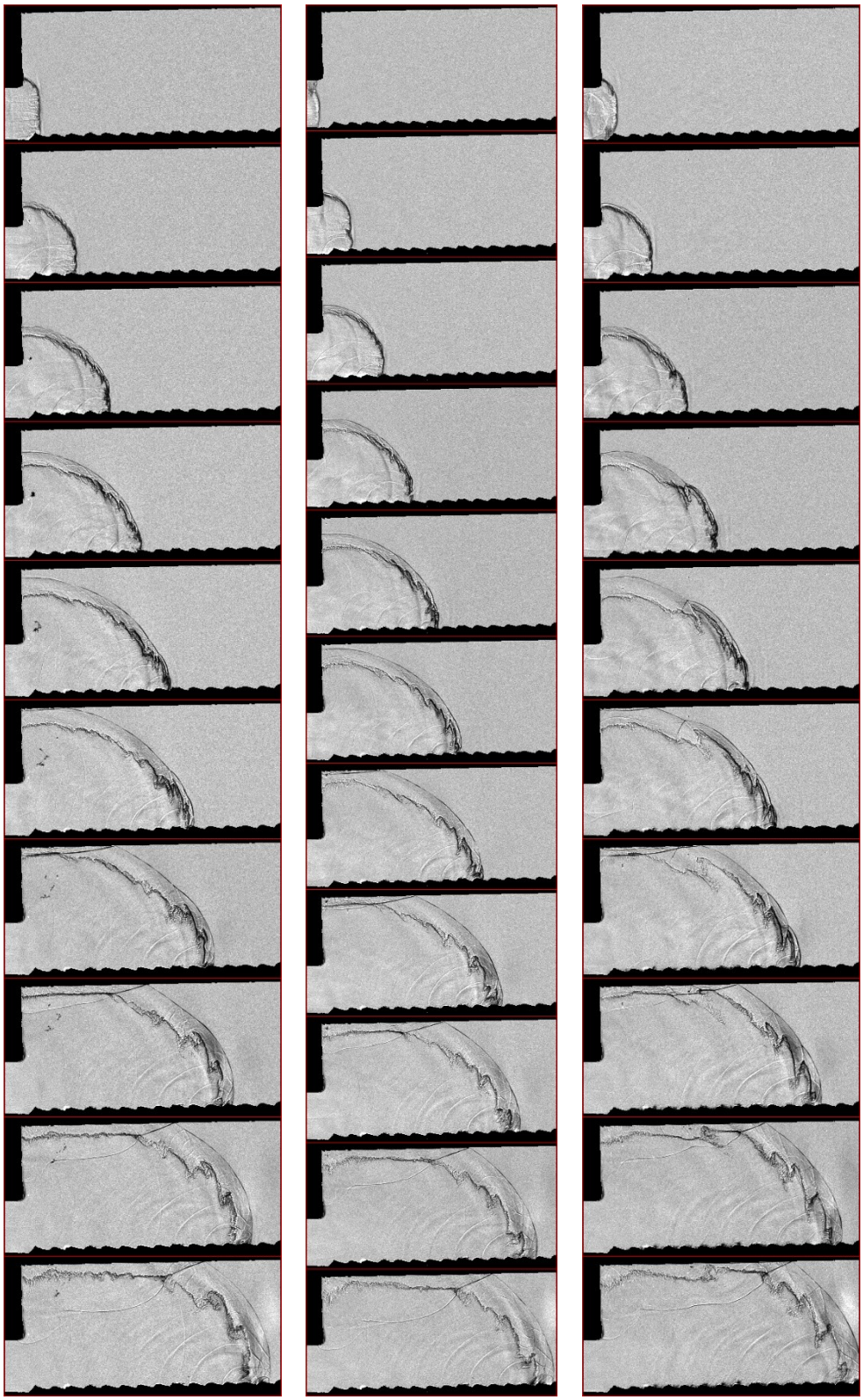

Case M4

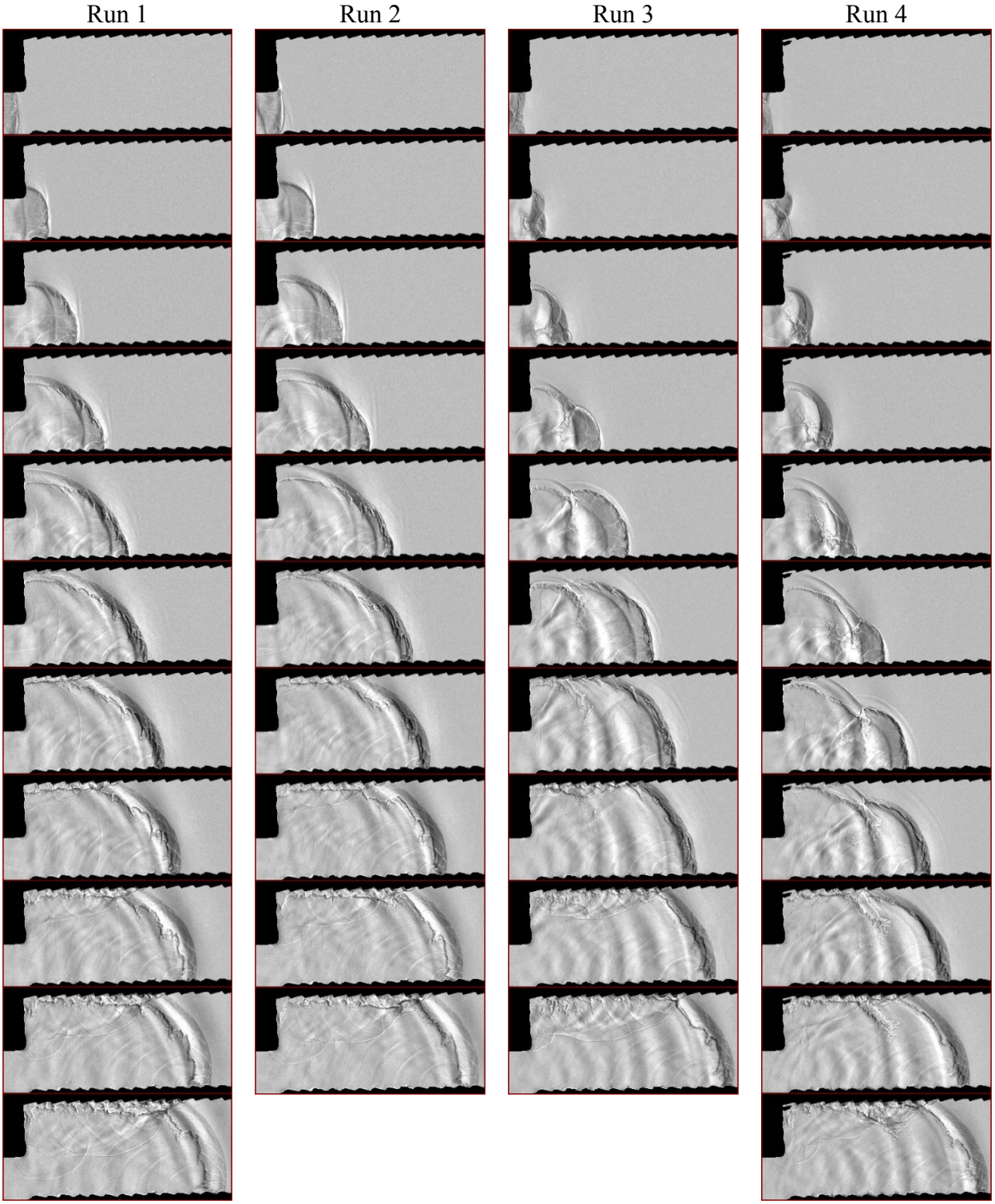

Case M4 (continued)

Run 5

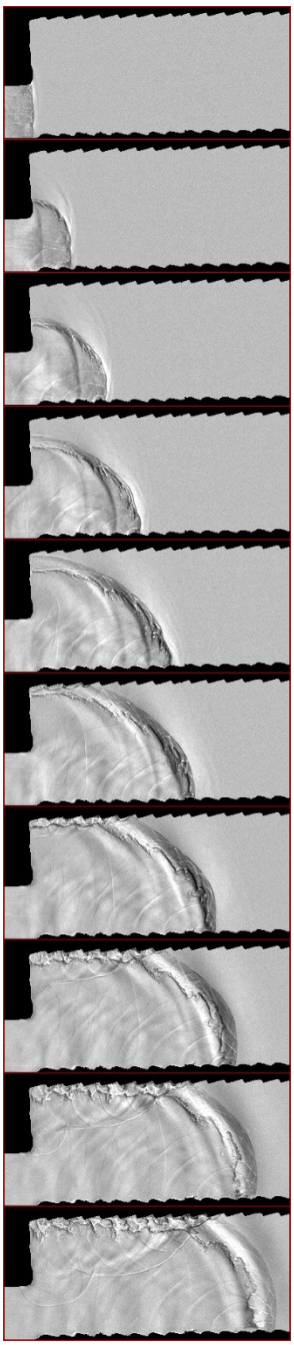

Run 6

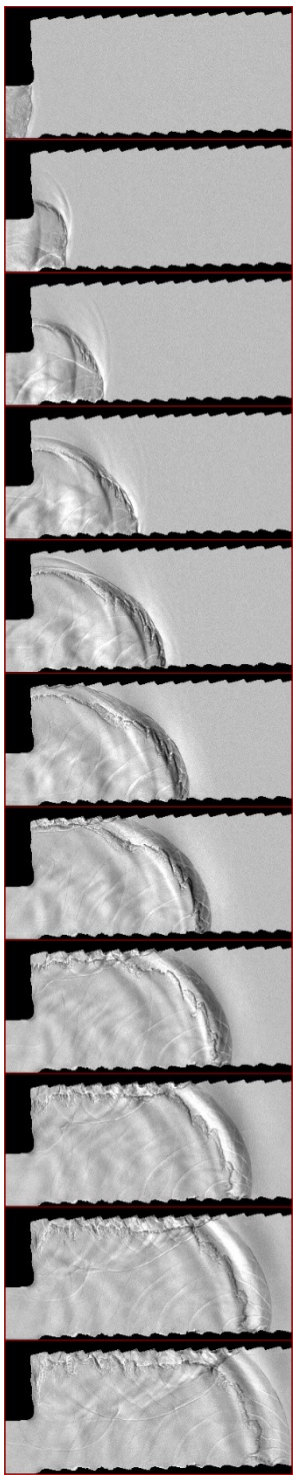

Run 7

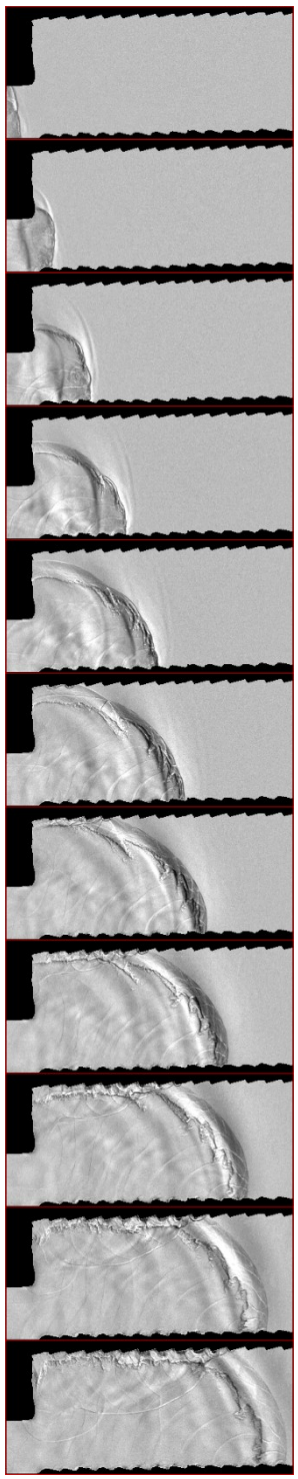

Run 8

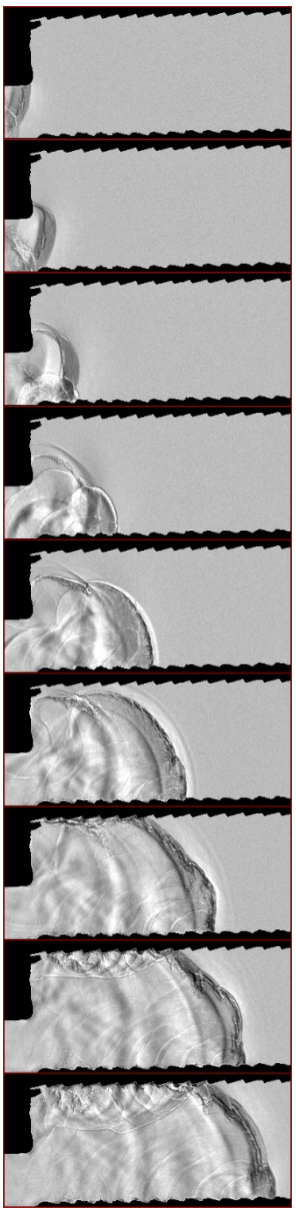

Case M5

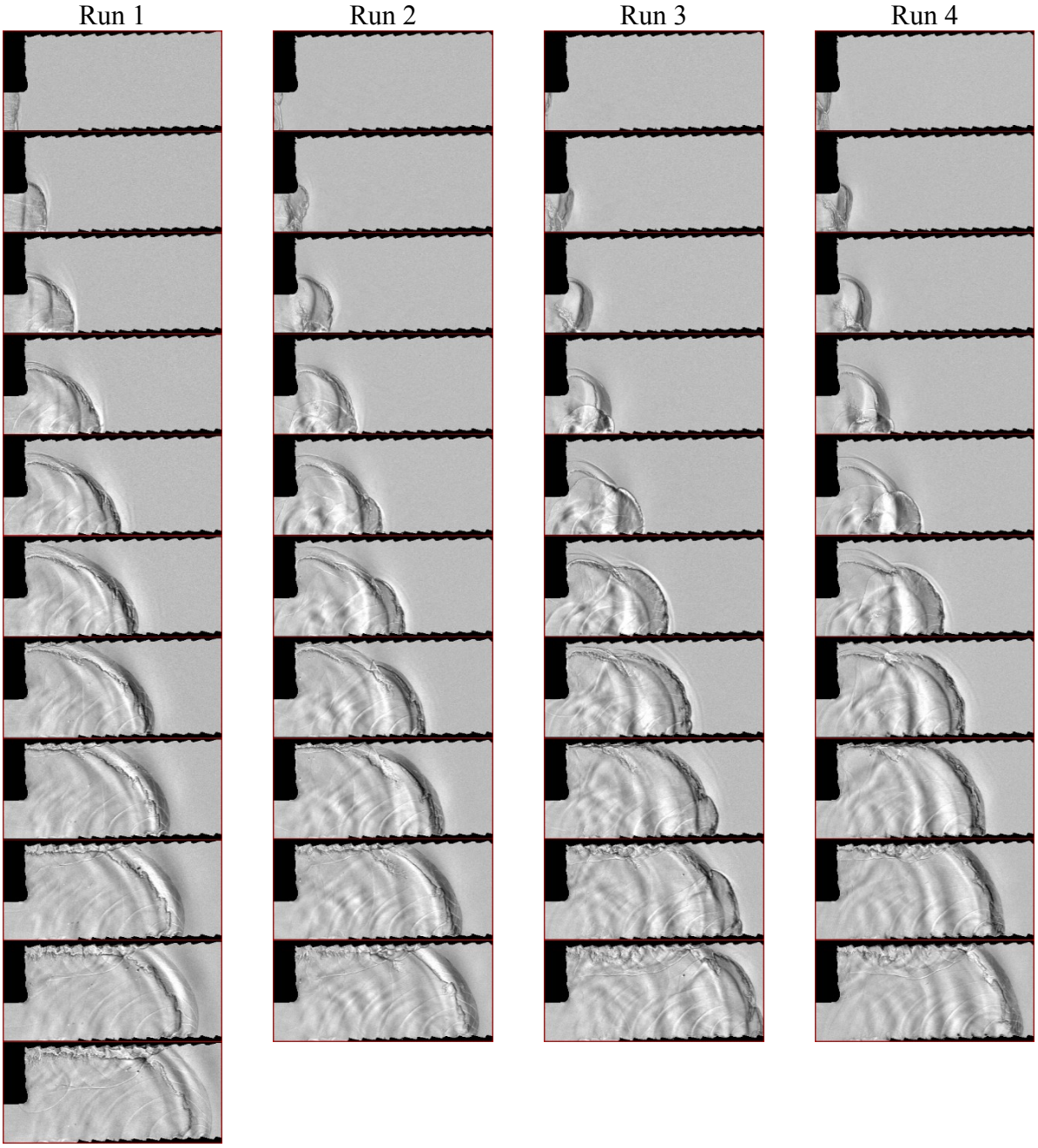

Case M5 (continued)

Run 5

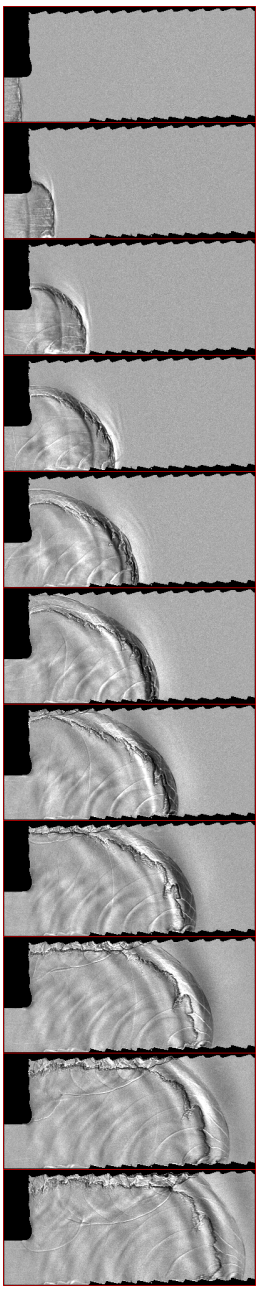

Run 6

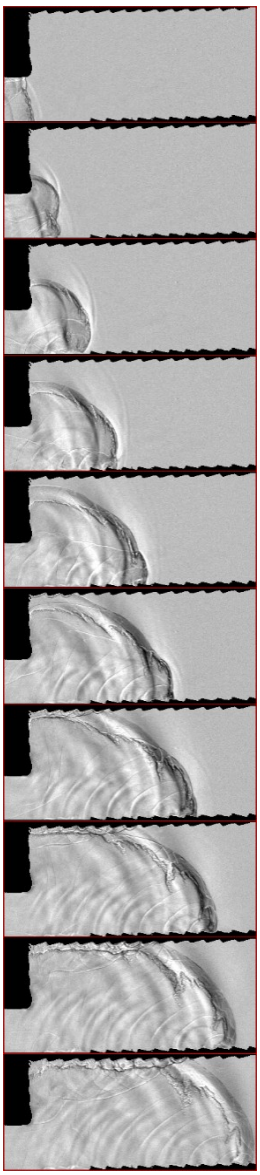

Run 7

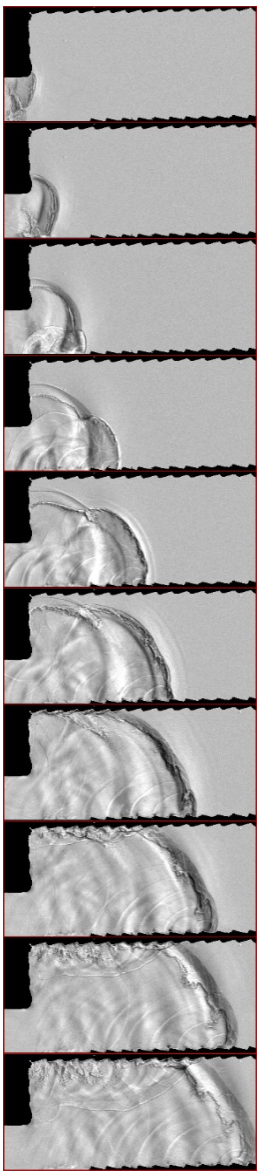

Run 8

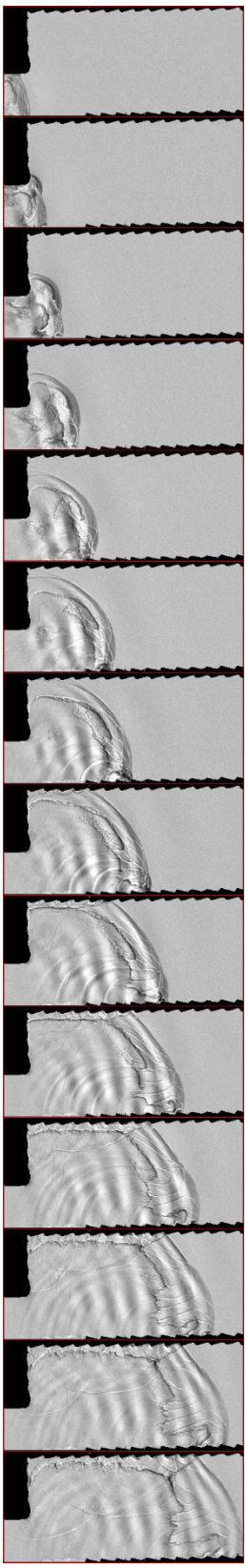

Case M5 (continued)

Run 9

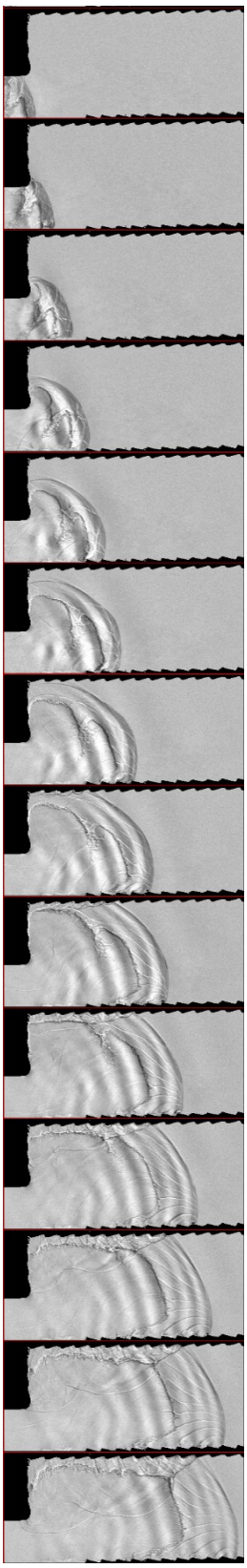

Run 10

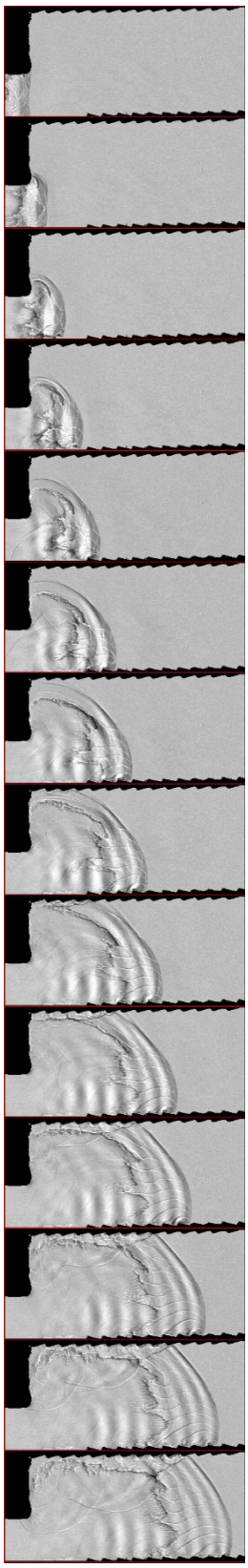

Run 11

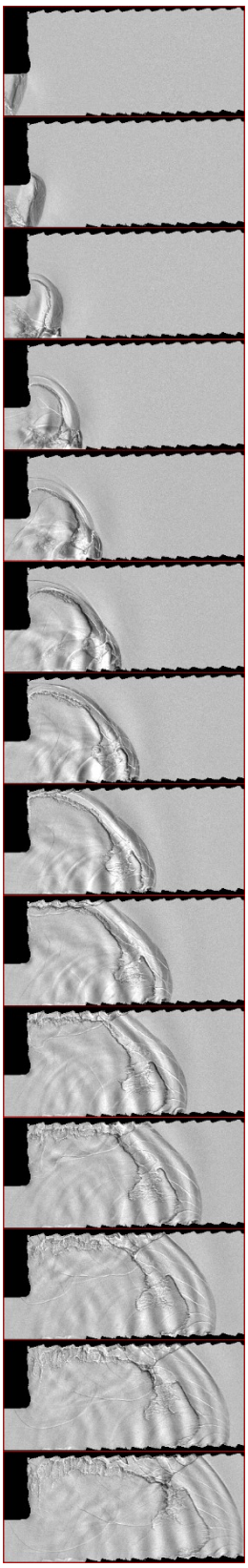

Run 12

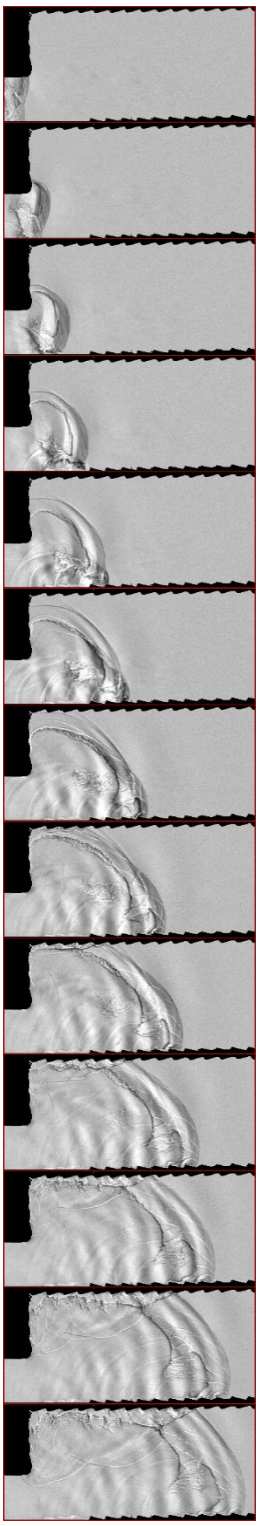

Case M5 (continued)

Run 13

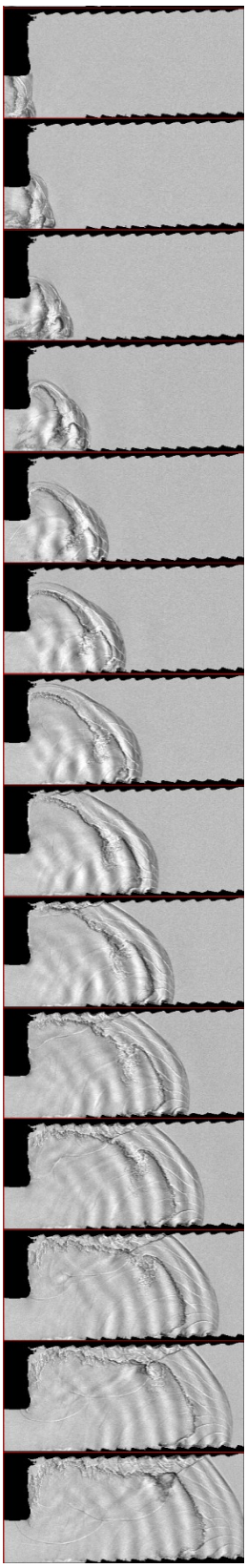

Run 14

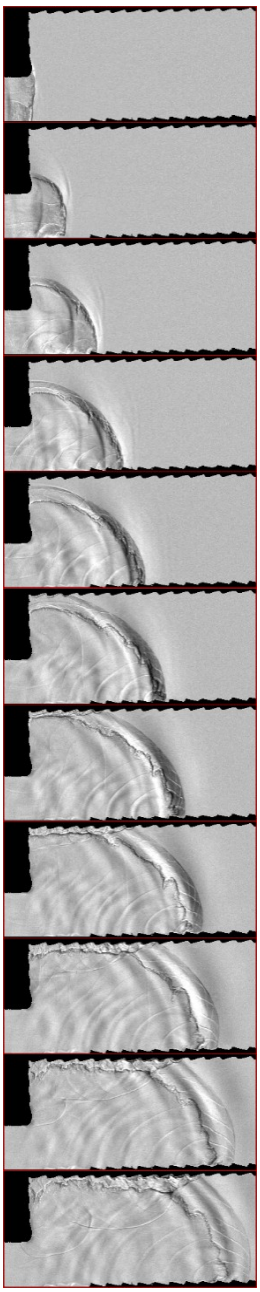

Run 15

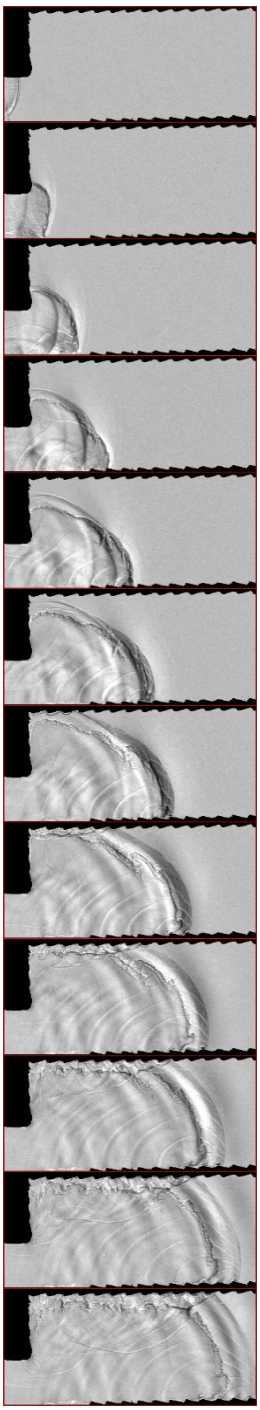

Run 16

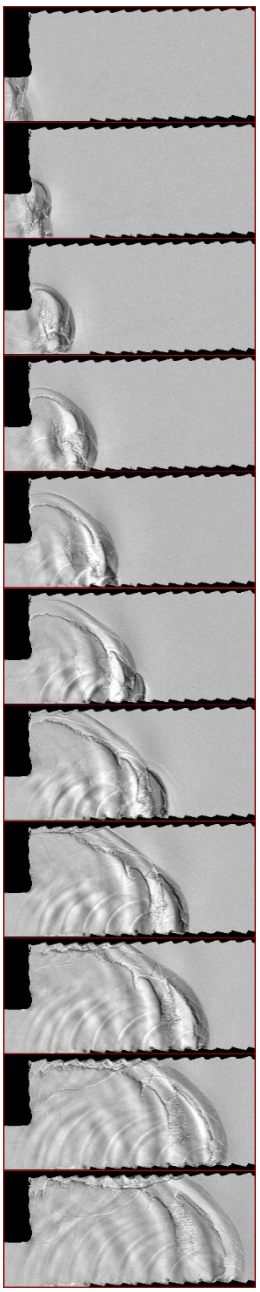

Case M6

Run 1 Run 2 Run 3 Run 4

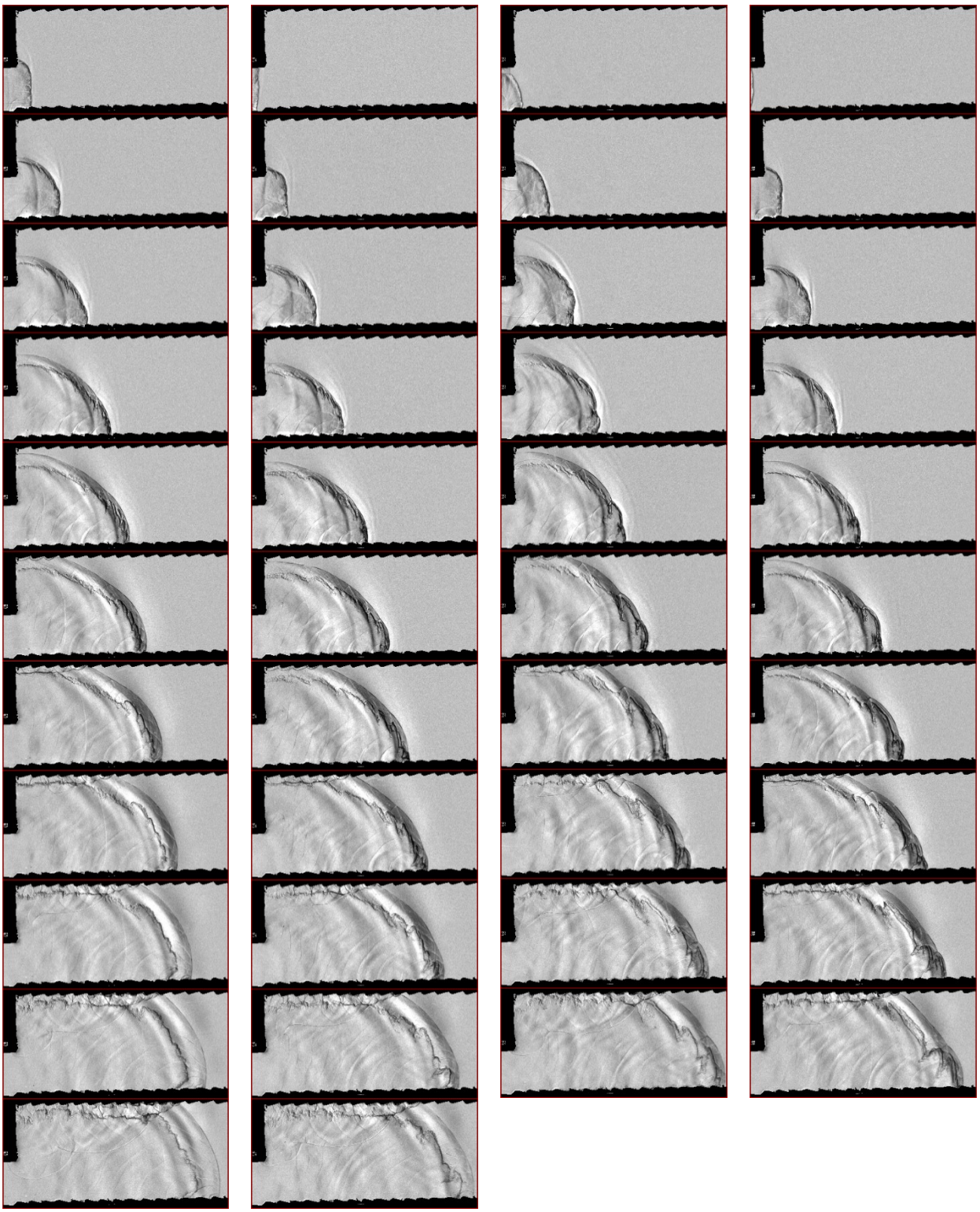

Case M6 (continued)

Run 5 Run 6 Run 7

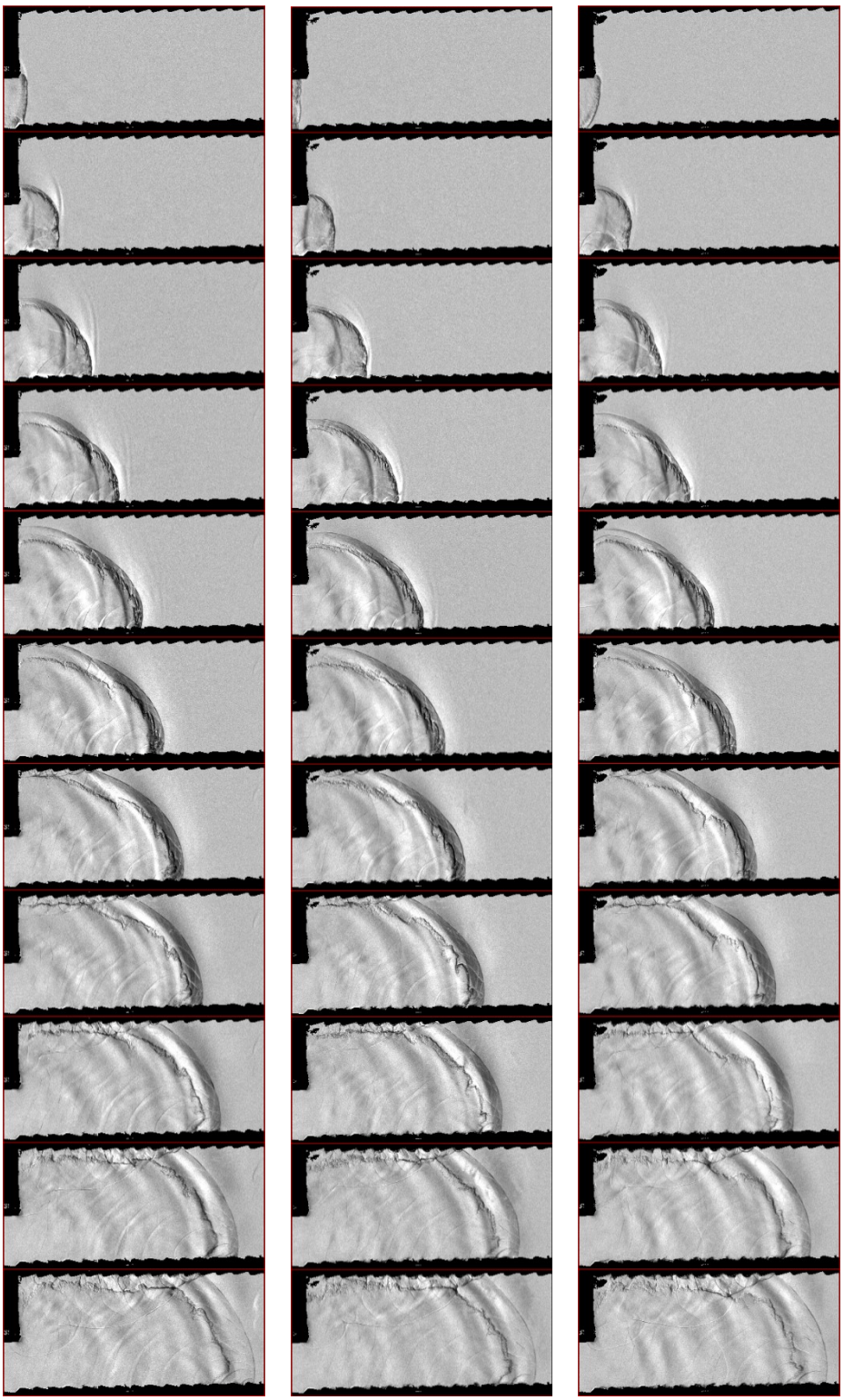

Case M7

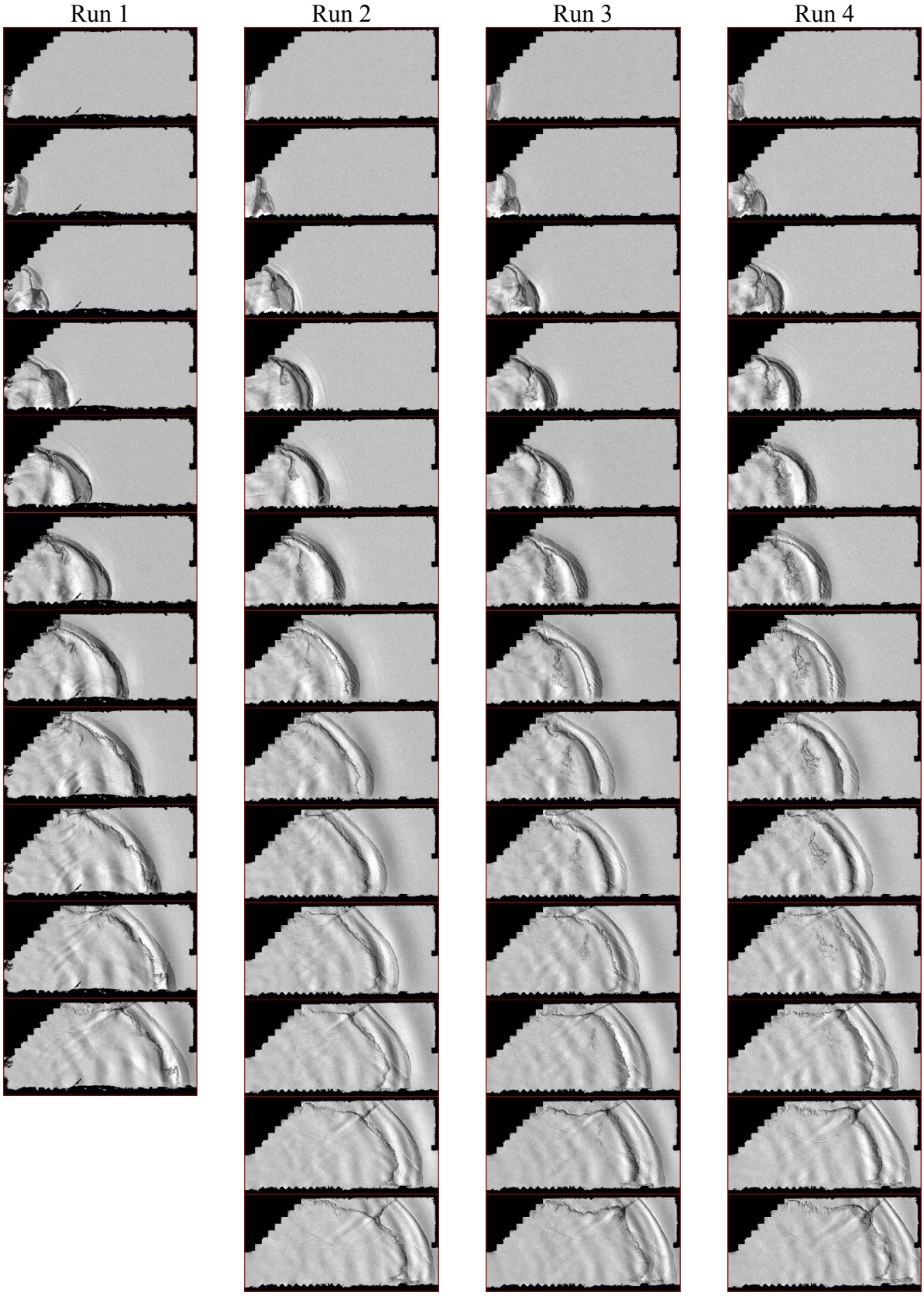

Case M7 (continued)

Run 5

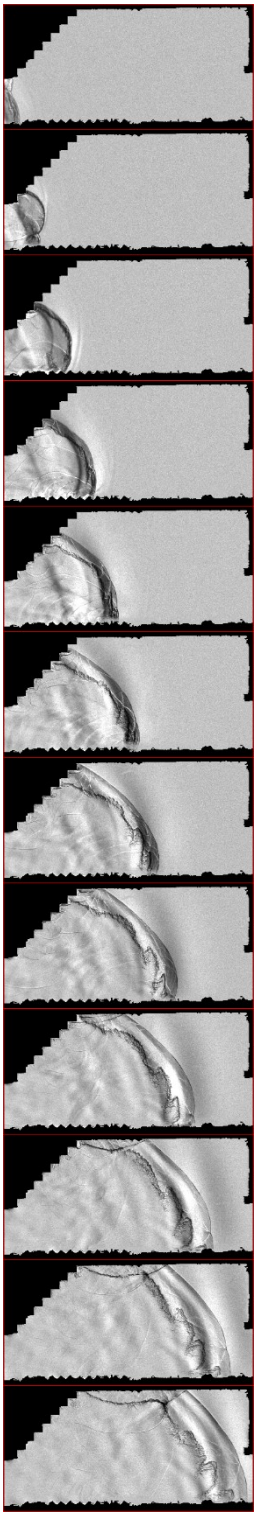

Run 6

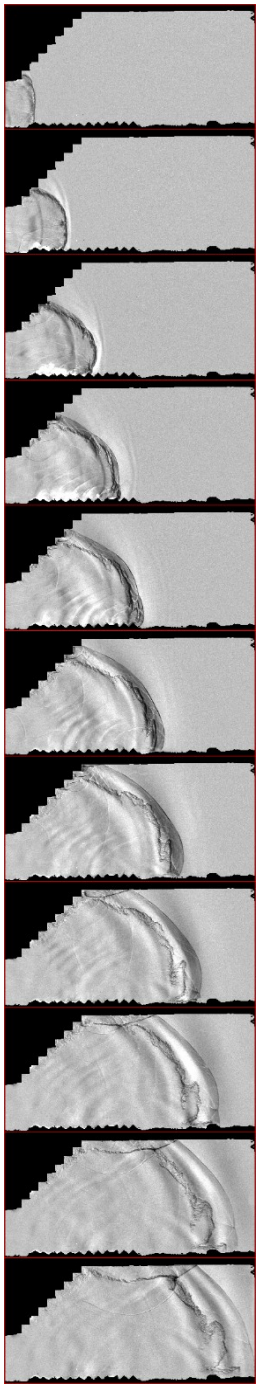

Run 7

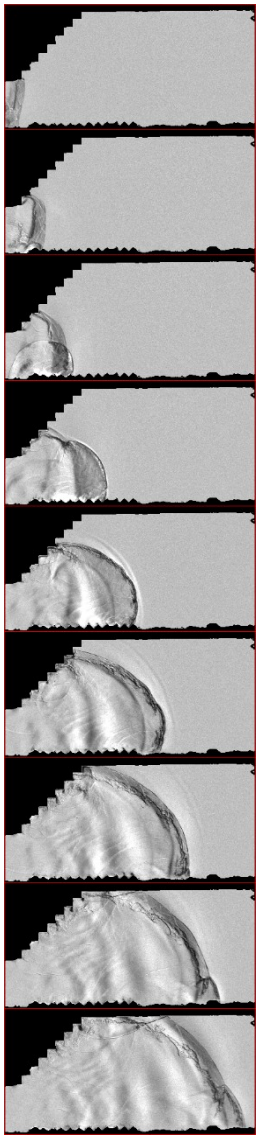

Run 8

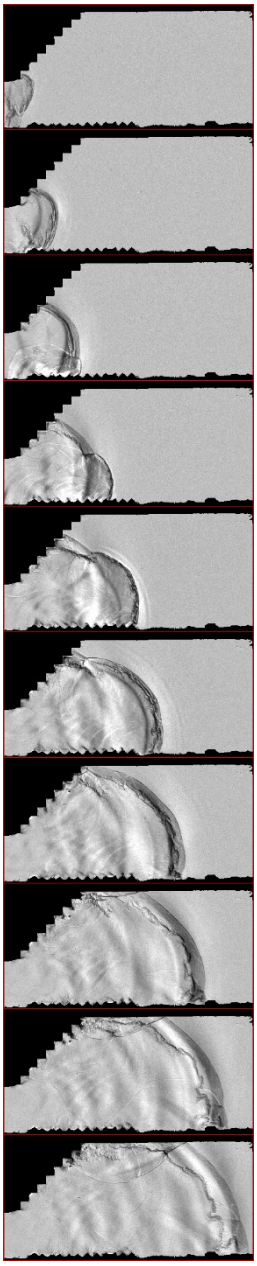

Case M7 (continued)

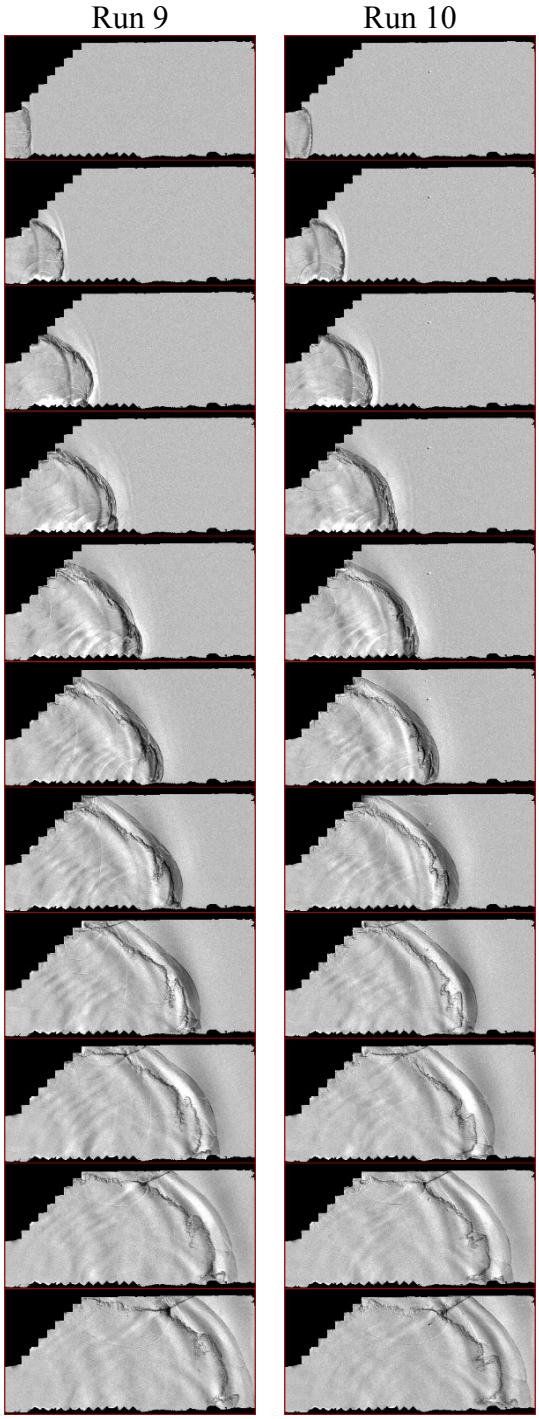

Case M8

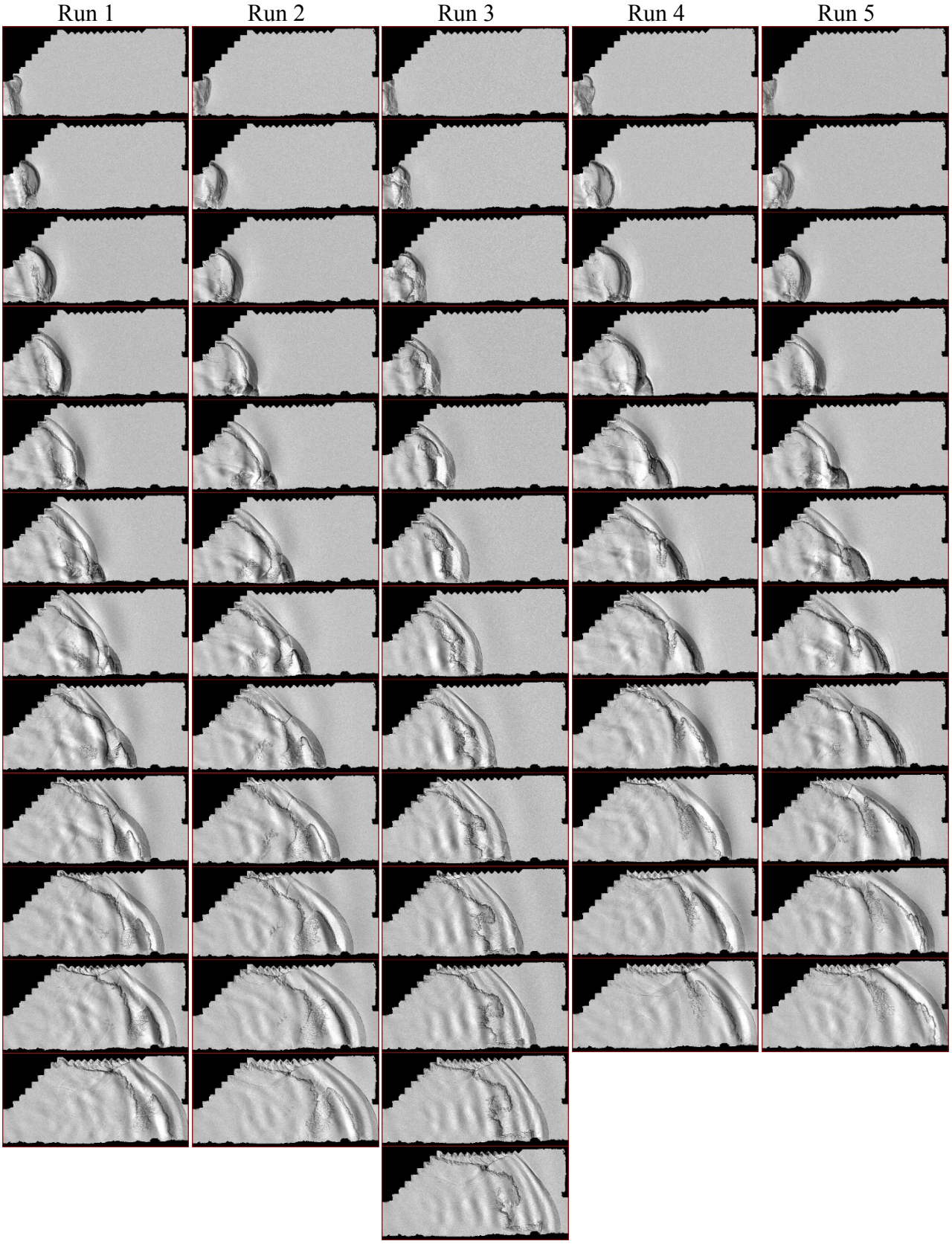

Case M9

Run 1 Run 2

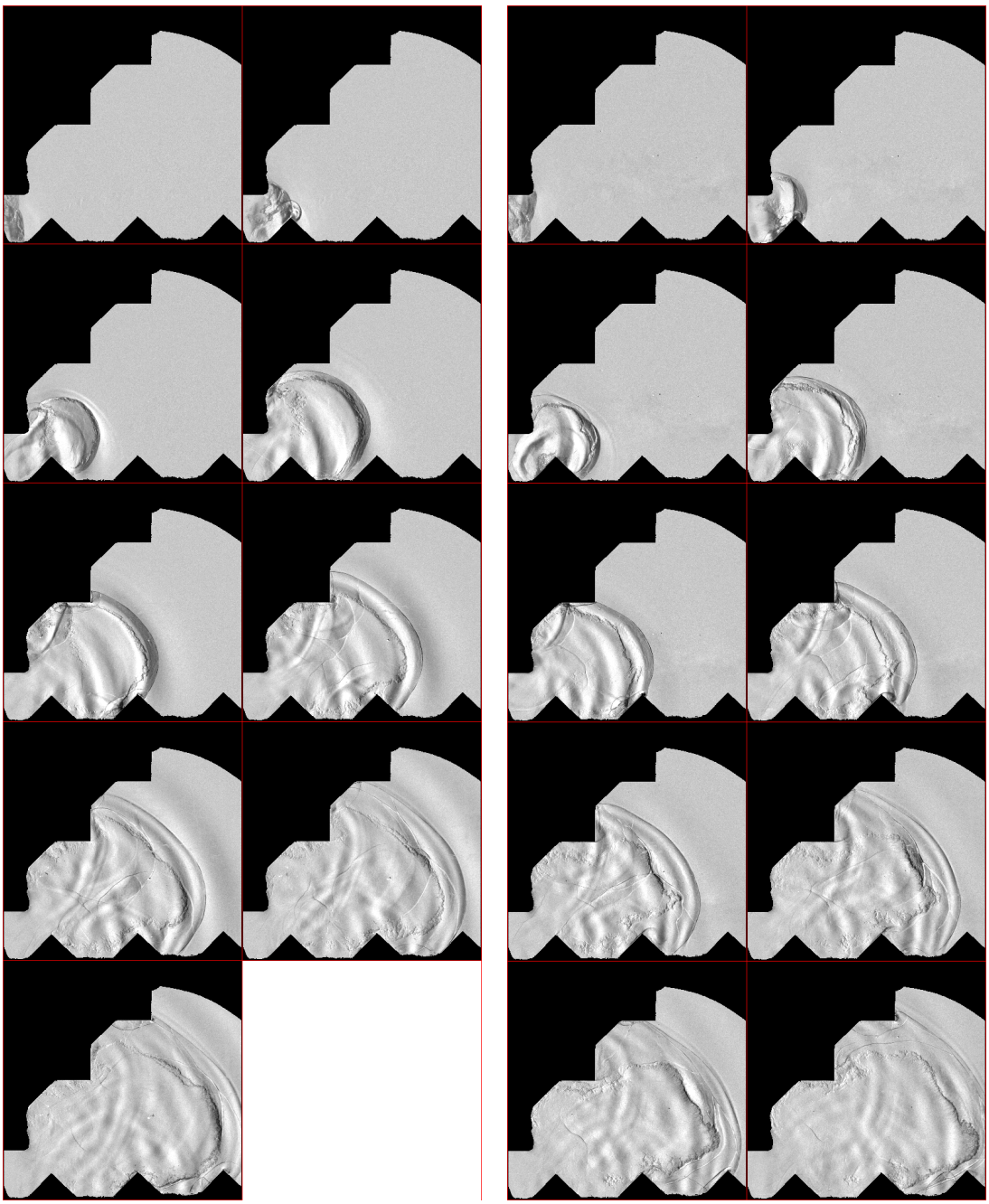

Case M9 (continued)

Run 3

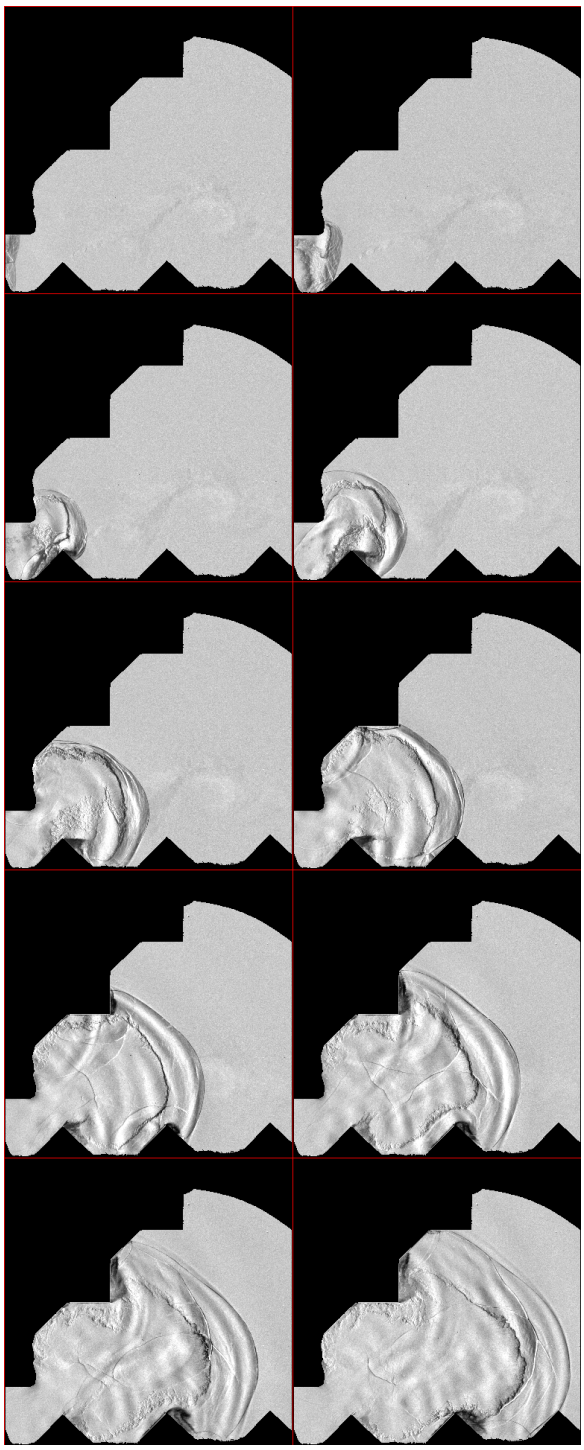

Run 4

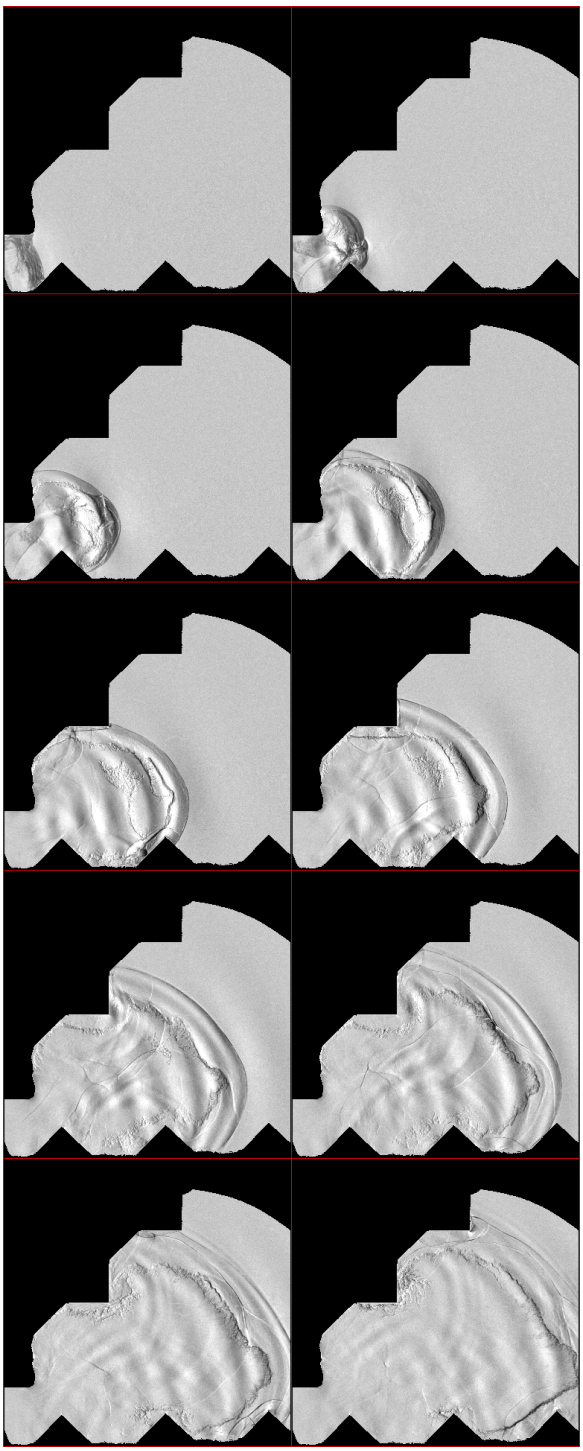

Case M9 (continued)

Run 5

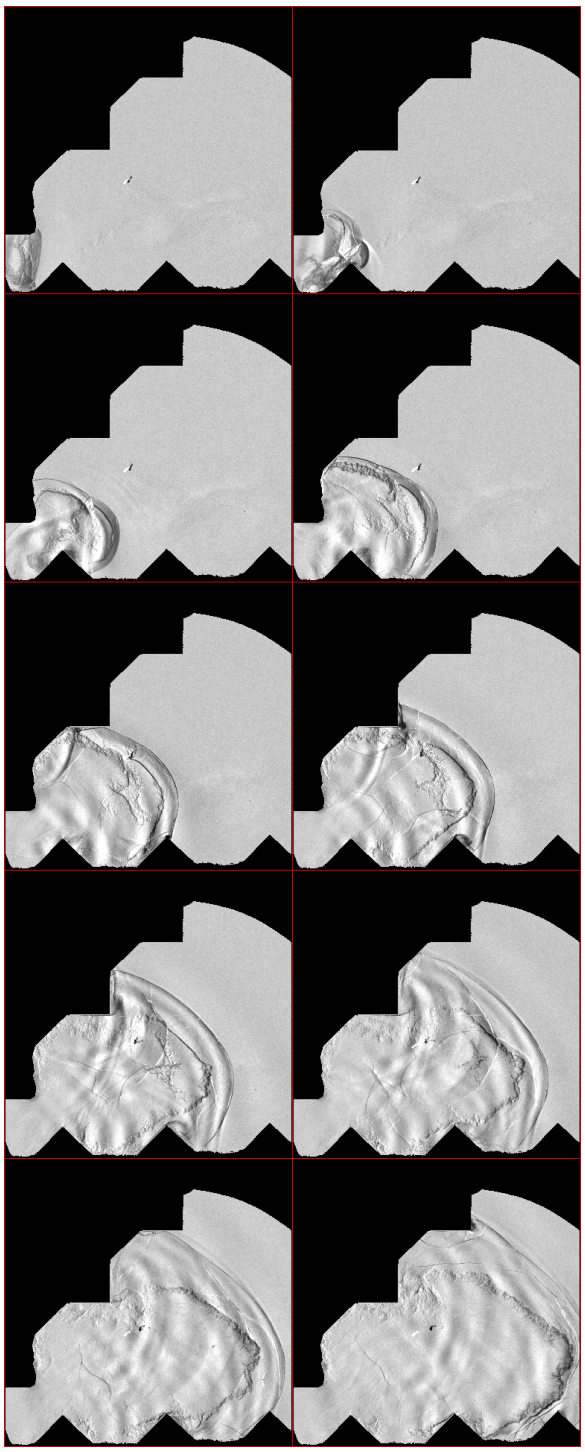

Run 6

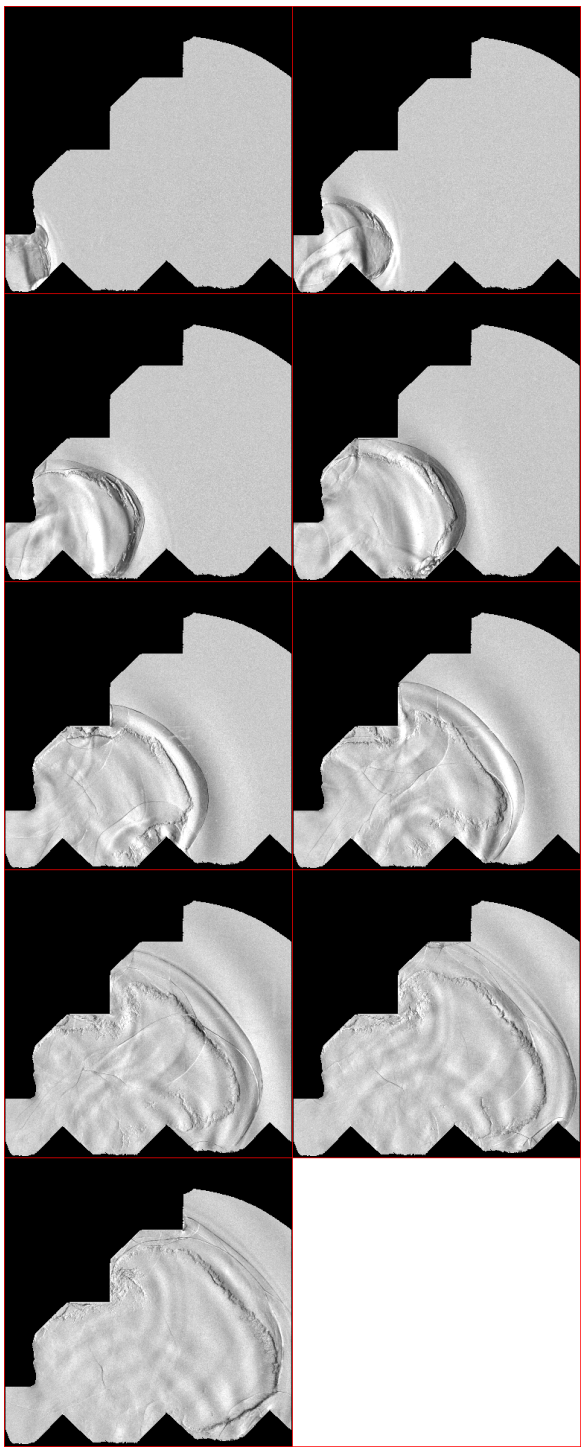

Case M9 (continued)

Run 7

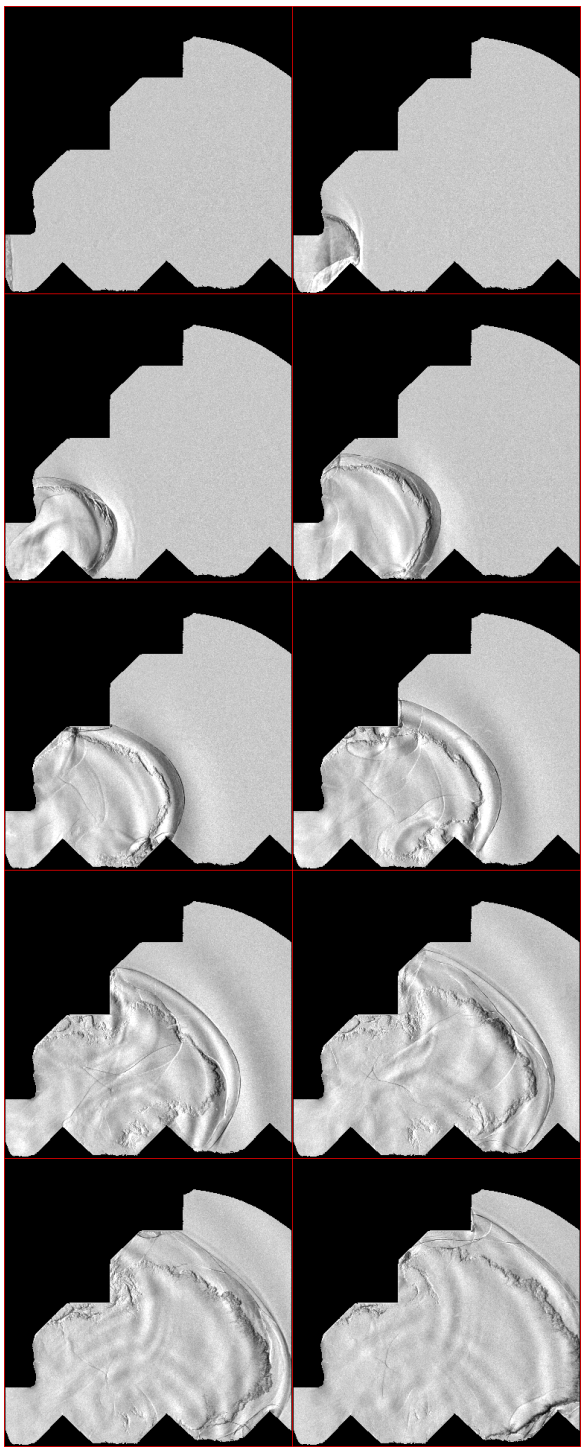

Run 8

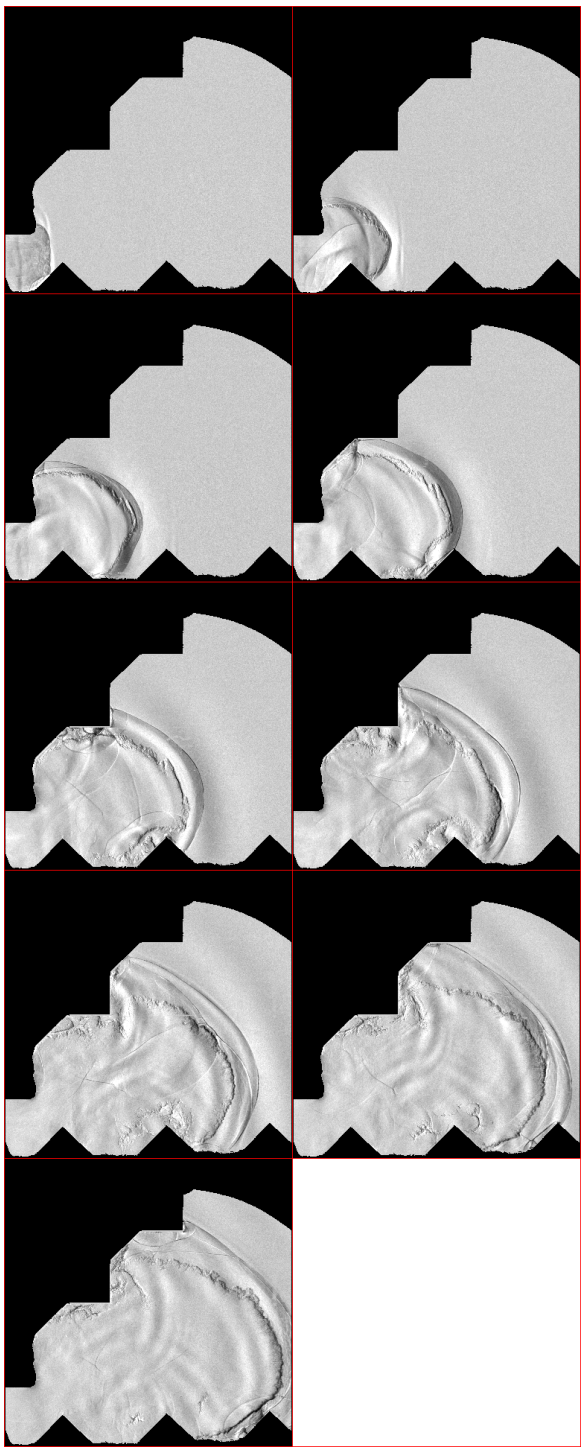

Case M9 (continued)

Run 9

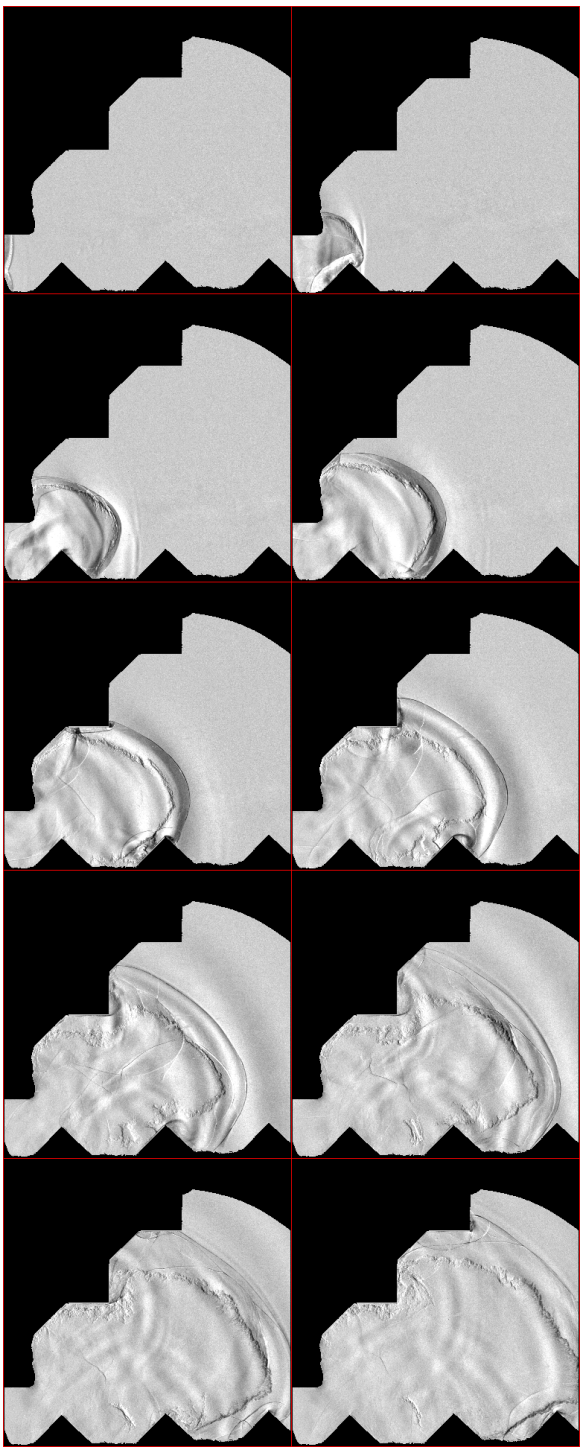

Case M10

Run 1

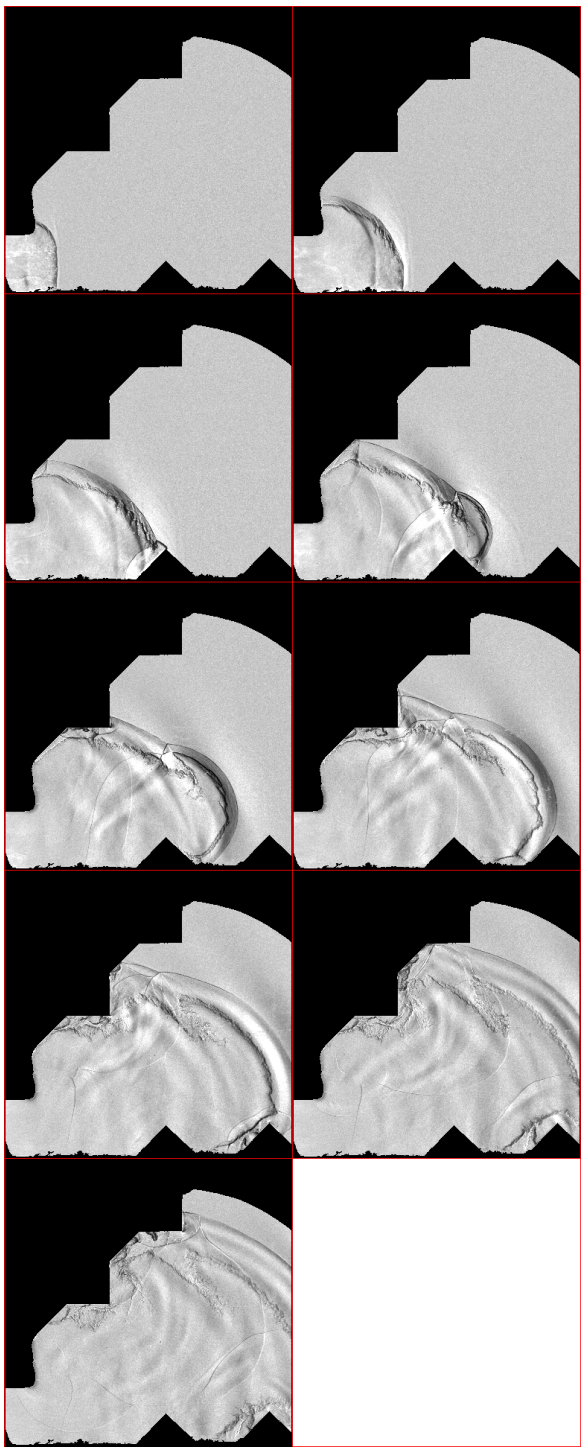

Run 2

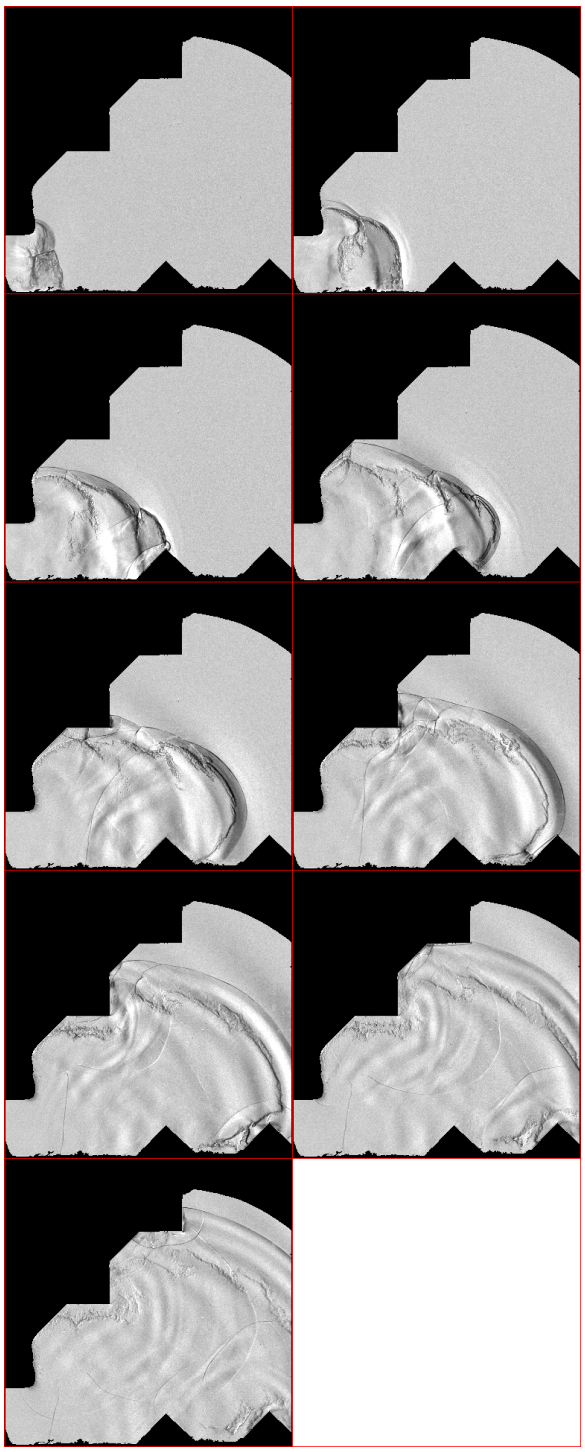

Case M10 (continued)

Run 3

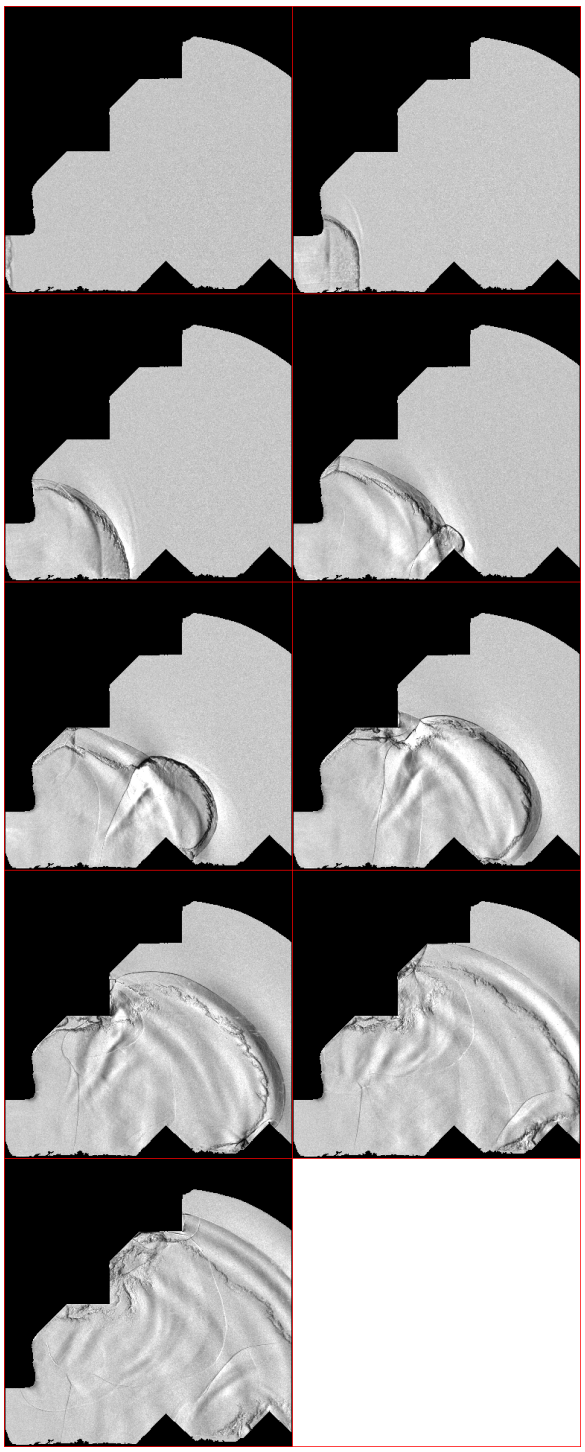

Run 4

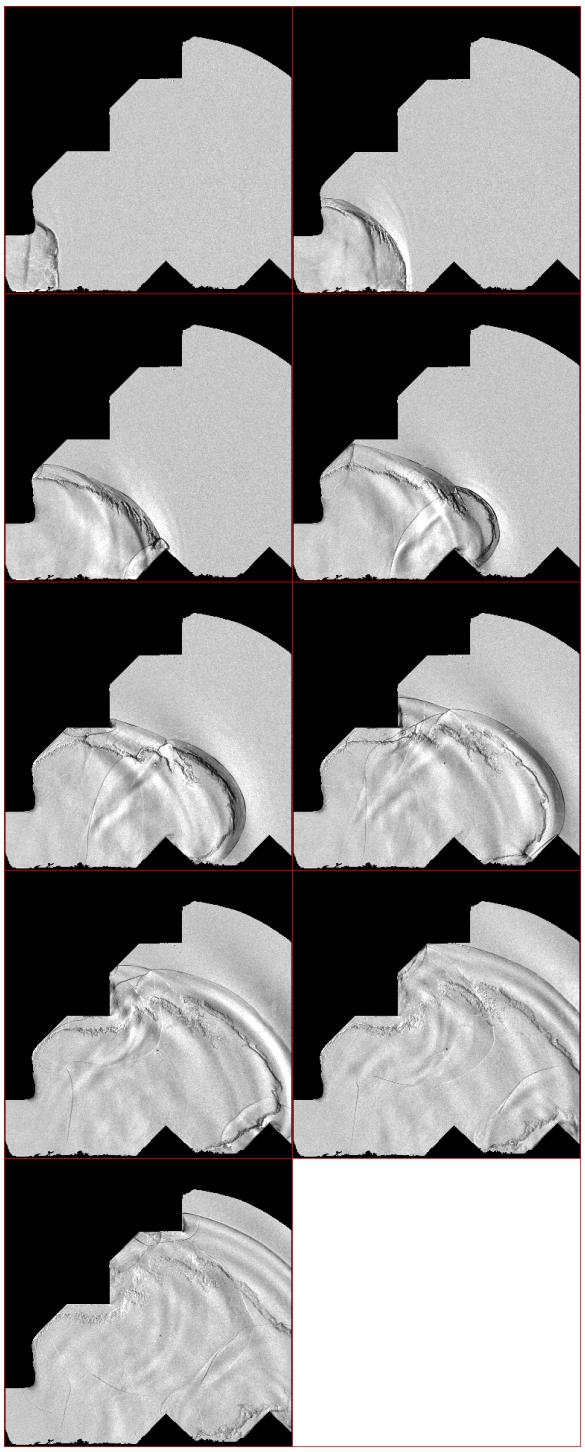

Case M10 (continued)

Run 5

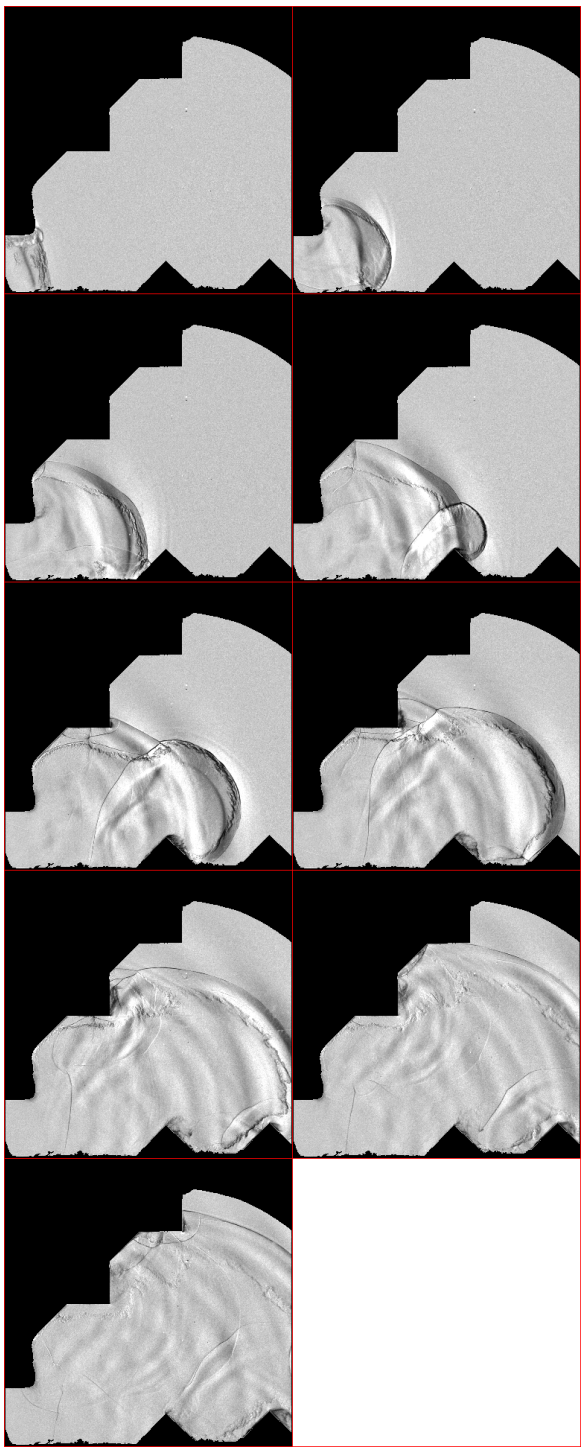

Case M11

Run 1

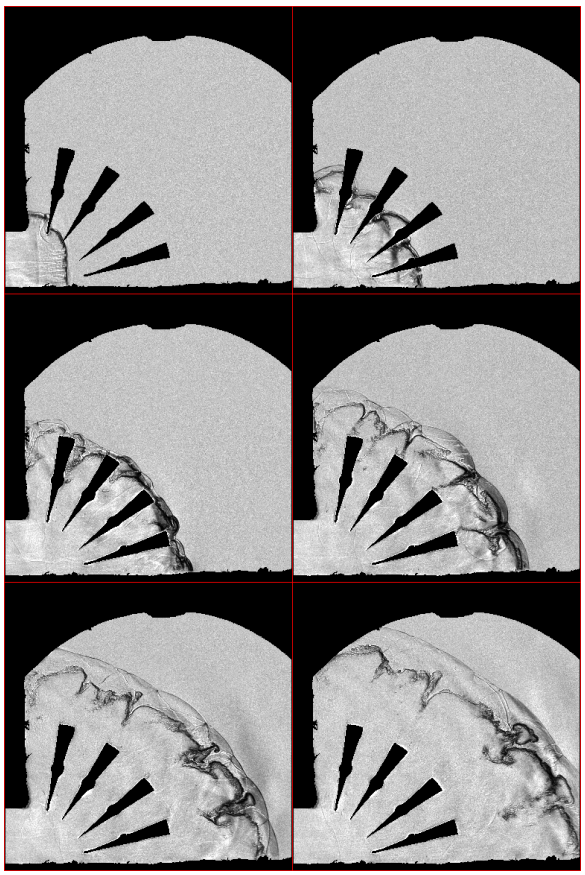

Run 2

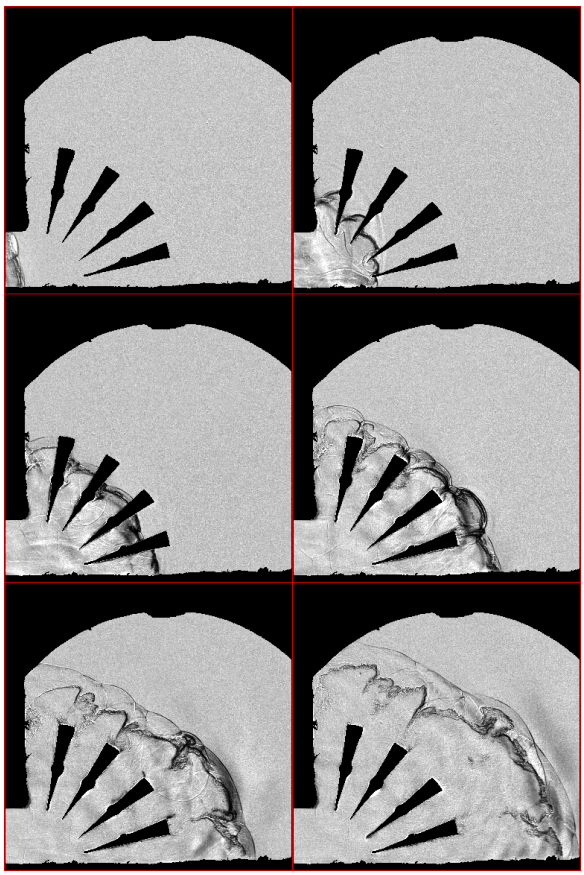

Case M11 (continued)

Run 3

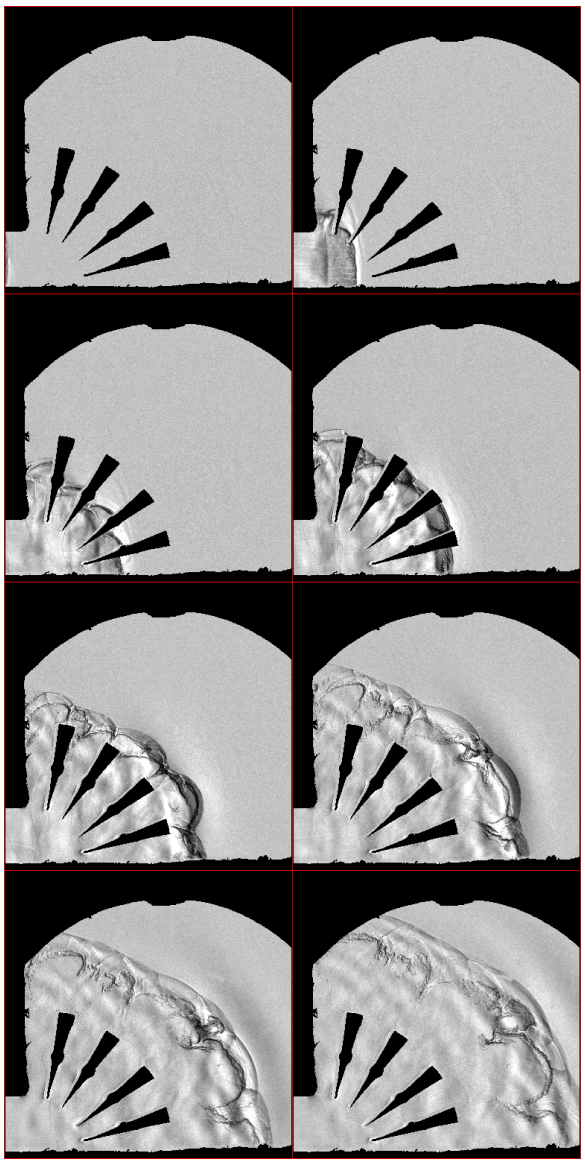

Run 4

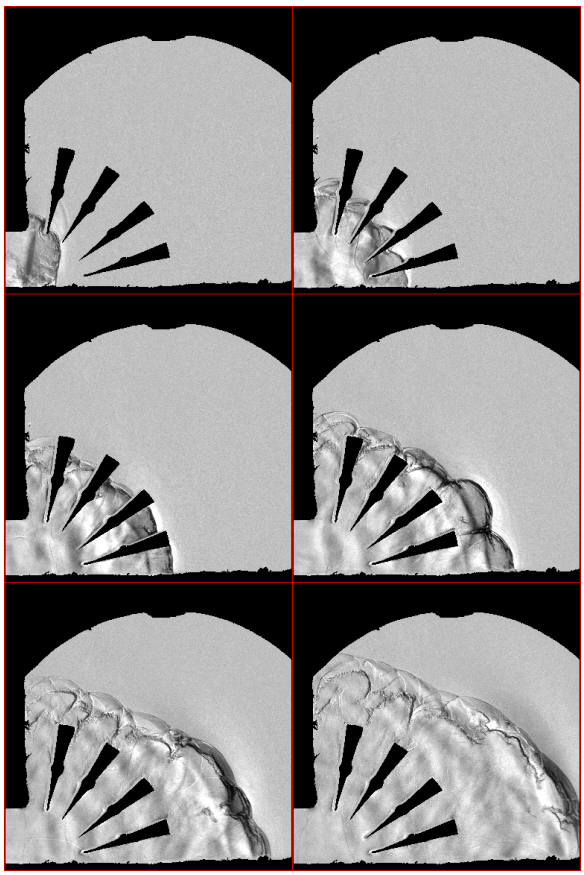

Case M11 (continued)

Run 5

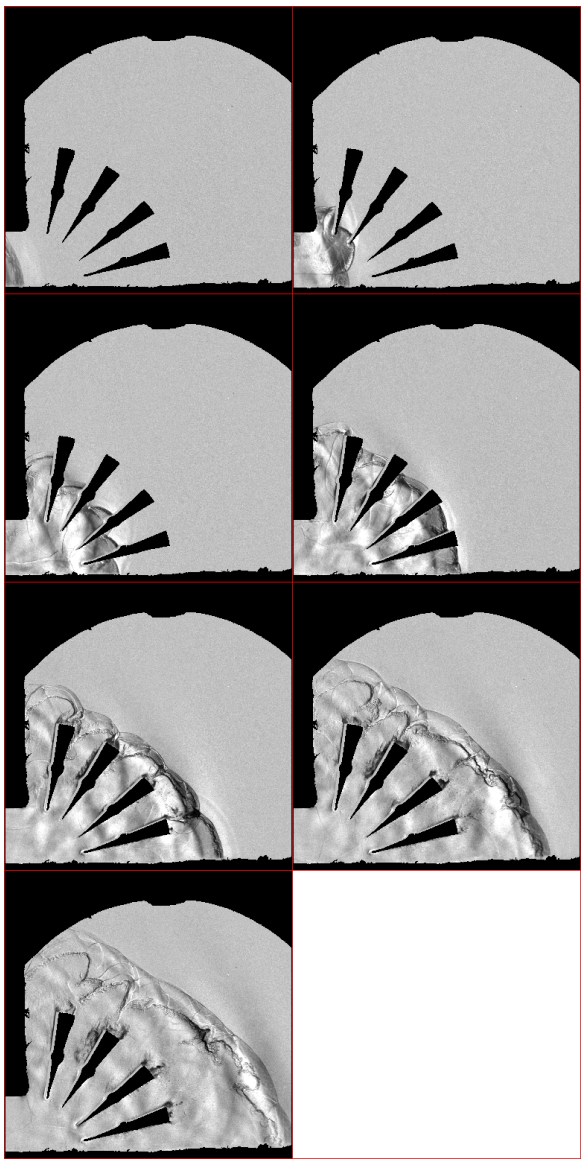

Run 6

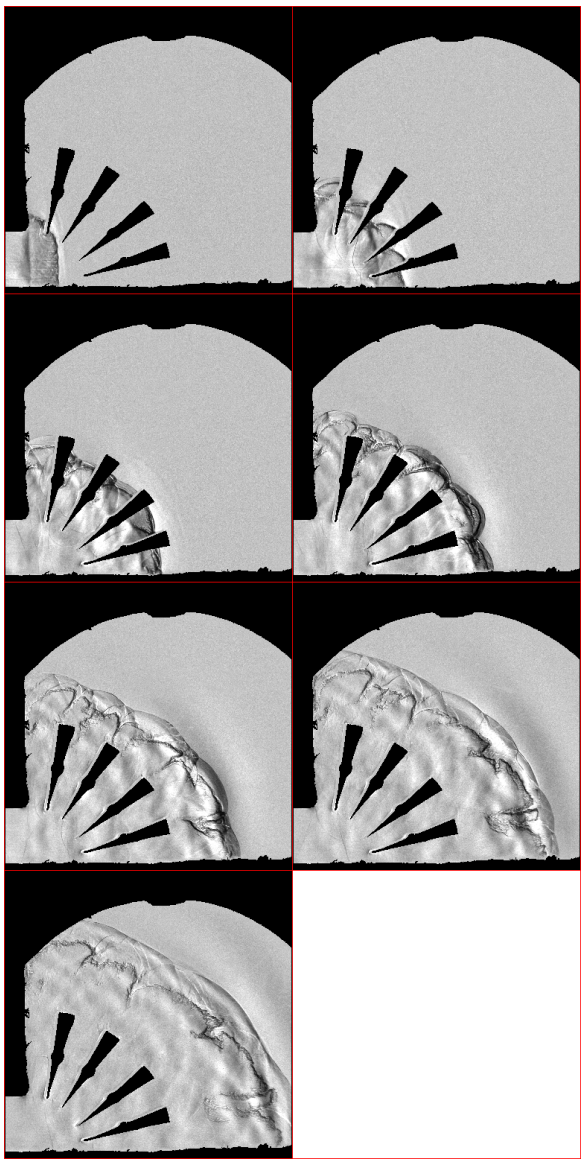

Case M11 (continued)

Run 7

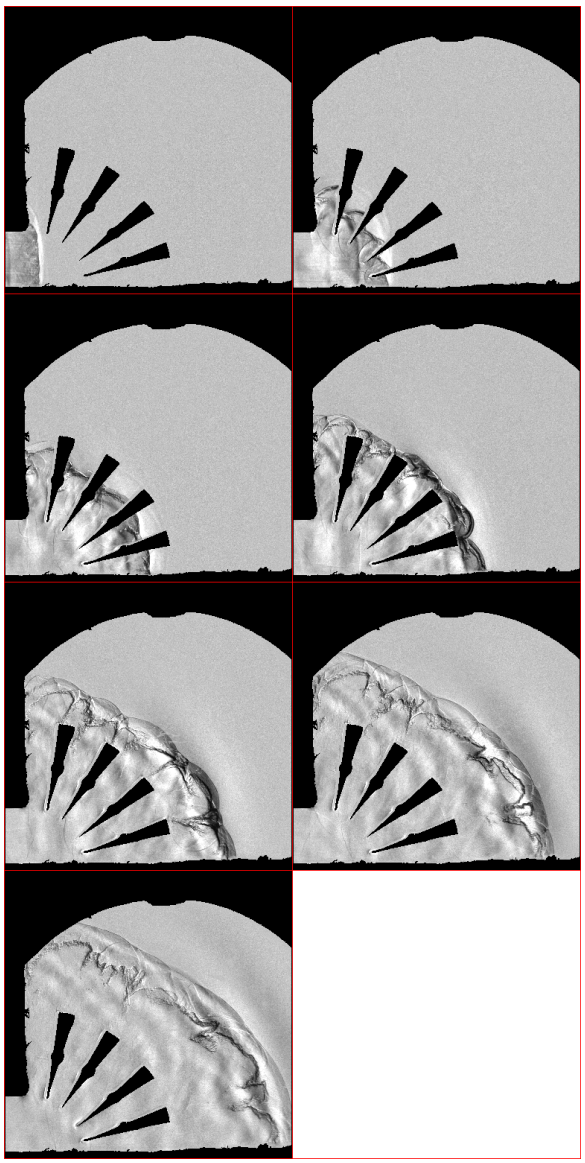

Run 8

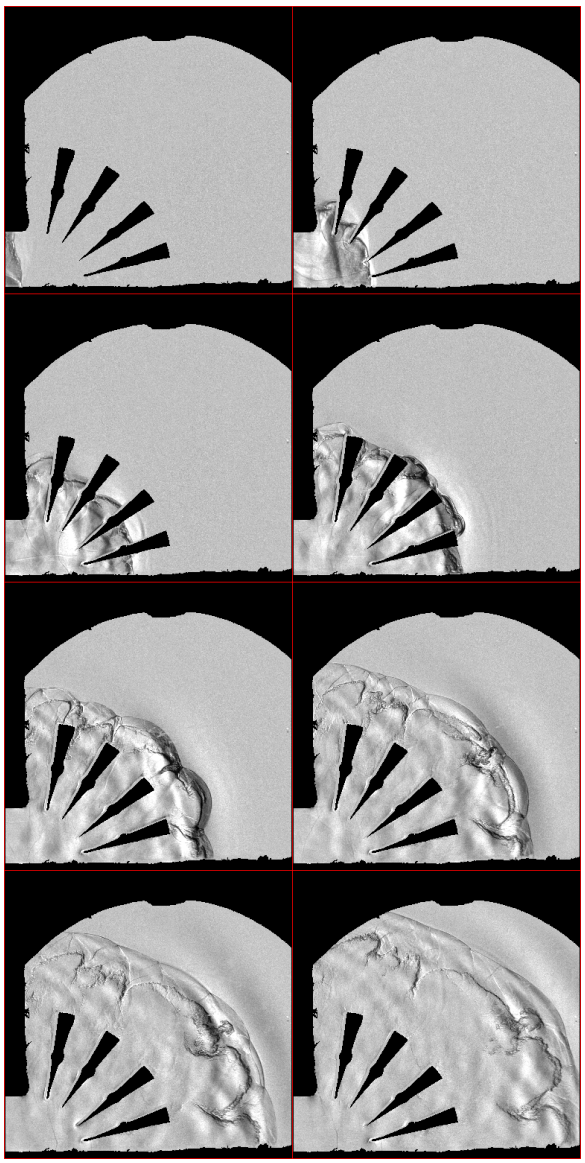

XIV. Appendix D: Source Code

Manual pixel selection and coordinate output: Markup2.m

```
function out = markup2(varargin)
% coords = markup2(frame)
% coords = markup2(Stack, frameNo)
% coords = markup2(Stack, frameNo, options)
%
%
% markup2 allows the user to inteactively select pixels from an image and returns
% the coordinates of the selected pixels as a Px2 matrix.
% Input: frame(numeric) - a matrix of pixel values.
%        Stack(ImStack) - an image stack
%        frameNo(scalar) - frame number
%        options(Param/Value pairs) - optional arguments
%          diff(logical) - In diff mode, the first frame of the
%                          stack is subtracted from the frame, and areas outside
%                          the region if interest are masked. Diff mode does
%                          not change single frame inputs.
%          cmap(string/nx3 numeric) - a colormap to use when displaying
%                                     intensity images. Does not change true
%                                     color images.
%
% Output: coords(Px2 double) - a list of coordinate pairs of the user selected
%                              pixels

%% Input checking and standardizing

%number of arguments
error(nargchk(1,6,nargin));

% frame
if nargin==1
   if ~isnumeric(varargin{1})
      error('invalid frame');
   end
   Stack = ImStack(varargin{1});
   frameNo = 1;
   diffMode = false;
   cMap = 'gray';
end

% Stack and frameNo
if nargin==2
   if ~isa(varargin{1},'ImStack')
      error('invalid ImStack');
```

```
    end
    Stack = varargin{1};

    if ~(isnumeric(varargin{2}) && isscalar(varargin{2}) &&
varargin{2}<=Stack.frameCount)
        error('invalid frame number');
    end
    frameNo = varargin{2};
    diffMode = false;
    cMap = 'gray';
end

% frame or Stack and frameNo with parameters
if nargin>2
    if isa(varargin{1},'ImStack') && isnumeric(varargin{2}) && isscalar(varargin{2})
        Stack = varargin{1};
        frameNo = varargin{2};
        diffMode = false;
        cMap = 'gray';
        argPtr = 3;

    elseif isnumeric(varargin{1});
        Stack = ImStack(varargin{1});
        frameNo = 1;
        diffMode = false;
        cMap = 'gray';
        argPtr = 2;

    else
        error('invalid argument');
    end

    % loop through param/value pairs
    for iArg = argPtr:2:nargin

        % switch on parameter name
        switch varargin{iArg}

            case 'diff' % set diff mode
                try
                    logical(varargin{iArg+1});
                catch ME
                    clear ME
                    error('invalid mode argument');
                end
```

```
            diffMode = logical(varargin{iArg+1});

        case 'cmap' %set colormap
            if ~chkCMap(varargin{iArg+1})
                error('invalid colormap');
            else
                cMap = varargin{iArg+1};
            end

            % reset map to default map: jet
            if strcmp(cMap,'default')
                cMap = 'jet';
            end

        case 'clip' %clip color scale
            assert(any(varargin{iArg+1} == [0 1 false true]),...
                'invalid mode argument');

        otherwise
            error('invalid parameter');
    end
  end
end

%% Apply optional differencing and color map

% differencing
if diffMode && frameNo>1
  frame = diff(Stack,frameNo);
else
  frame = Stack(frameNo);
end

% log scale and clip outliers
% frame = log10(frame-min(frame(:))+1);
[n,b] = hist(frame(:),unique(frame));
cLim = [b(find(n==2,1,'first')),b(find(n==2,1,'last'))];
% frame(frame<cLim(1)) = cLim(1);
% frame(frame>cLim(2)) = cLim(2);

% construct colormap and convert to RGB
if strcmp(Stack.colorFmt,'Monochrome');
  cLen = length(unique(frame));
  mn = min(frame(:));
  mx = max(frame(:));
  frame = round((cLen-1).*(frame-mn)./(mx-mn)+1);
```

```
    map = eval([cMap,'(',num2str(cLen),')']);
    frame = ind2rgb(frame,map);


    hmap = rgb2hsv(map);
    if mean(hmap(:,2))<0.3 %low saturation (nearly gray scale)
        selColor = [1,0,0]; %red
    elseif mean(hmap(:,3)) < 0.7 %low value (dark colormap)
        selColor = [1,1,1]; %white
    else
        selColor = [0,0,0]; %black
    end

else %true color image
    selColor = [1,0,0]; %red

end

%% Pre-Proc frame for display and create figure
[n,m] = size(Stack);

% shade outside the roi (a nice soothing blue)
frame = cat(3,frame(:,:,1),frame(:,:,2),frame(:,:,3)+frame(:,:,3).*~Stack.roi);
frame(frame>1) = 1;
cData = frame;

% create custom pointer
cd = NaN(16);
cd(8:9,:) = 1;
cd(:,8:9) = 1;
cd(8:9,6:11) = 2;
cd(6:11,8:9) = 2;
cd(7:10,7:10) = NaN;


% Initialize figure
hf = figure('Interruptible','off');
ss = get(0,'ScreenSize');
op = [-7,33,ss(3)+16,ss(4)-24];
set(hf,'OuterPosition',op,...
      'Pointer','custom',...
      'PointerShapeCData',cd,...
      'PointerShapeHotSpot',[8,8]);
hi = imshow(cData,map,'InitialMagnification','fit');
hz = zoom(gcf);
hp = pan(gcf);
```

```
axis on
title('Click to select first point then use num pad to select more');
xlabel('Press space to quit.');
pos = [.03,.03,.96,.96];
set(gca,'Position',pos,'TickDir','in');

%% Run user input loop
% Solicit first point
isDone = false;
set(hz,'Enable','on');
waitfor(hz.Enable,'off');
while ~isDone
   k = waitforbuttonpress();
   if k
      out = [];
      return
     % on a key input recycle
   else
      % on a mouse click toggle pan and zoom modes or select point
      if strcmp(hz.Enable,'on')
         waitfor(hz,'Enable','off');

      elseif strcmp(hp.Enable,'on')
         waitfor(hp,'Enable','off');

      else
         curPt = get(gca,'CurrentPoint');
         xLim = get(gca,'xLim');
         yLim = get(gca,'yLim');
         hWidth  = round(diff(xLim)/2);
         hHeight = round(diff(yLim)/2);
         isDone = true;
      end
   end
end %while

% get clicked point
j = round(min(max(curPt(1,1),1),m));
i = round(min(max(curPt(1,2),1),n));
points(1,:) = [i,j];
cData(i,j,:) = selColor;

% modify figure
set(hi,'cData',cData);

% add labels
```

```
title('Use numpad to add pixels to selection.');
xlabel('Press space to exit');

% define function to update selection
function update()
   points(end+1,:) = [i,j];
   cData(i,j,:) = selColor;
   set(hi,'cData',cData);
end

% define keypress fcn
function key_press(hf,event)
% runs on a key press in the figure should update cData and points on each
% key-press and exit on space

% interpret key
   switch event.Character
      case '1' %down-left
         j = round(max([1,j-1]));
         i = round(min([n,i+1]));
         update();

      case '2' %down
        % j = j
         i = round(min([n,i+1]));
         update();

      case '3' %down-right
         j = round(min([m,j+1]));
         i = round(min([n,i+1]));
         update();

      case '4' %left
         j = round(max([1,j-1]));
        % i = i
         update();

      case '5' % undo last
         %reset pixel
         cData(i,j,:) = frame(i,j,:);
         set(hi,'cData',cData);
         % remove last point on list
         points(end,:) = [];
         j = points(end,2);
         i = points(end,1);
```

```
        case '6' %right
            j = round(min([m,j+1]));
           % i = i
            update();

        case '7' %up-left
            j = round(max([1,j-1]));
            i = round(max([1,i-1]));
            update();

        case '8' %up
           % j = j
            i = round(max([1,i-1]));
            update();

        case '9' %up-right
            j = round(min([m,j+1]));
            i = round(max([1,i-1]));
            update();

        case ' ' %close the figure
            close(hf);

    end %switch

% recenter when current point gets close to edge
    i2 = i-0.5;
    j2 = j-0.5;
    m2 = m-0.5;
    n2 = n-0.5;

    if i2-yLim(1) < 10 && i2 > 10
        % recenter up
        yLim = [max([0.5          ,i2-hHeight]),...
                max([2*hHeight-0.5,i2+hHeight])];
        set(gca,'yLim',yLim)
    end

    if yLim(2)-i2 < 10 && i2 < n2-10
        % recenter down
        yLim = [min([n2-2*hHeight,i2-hHeight]),...
                min([i2+hHeight  ,n2        ])];
        set(gca,'yLim',yLim);
    end

    if j2-xLim(1) < 10 && j2 > 10
```

```
        % recenter left
        xLim = [max([0.5         ,j2-hWidth]),...
                max([2*hWidth-0.5,j2+hWidth])];
        set(gca,'xLim',xLim);
    end

    if xLim(2)-j2 < 10 && j2 < m2-10
        % recenter right
        xLim = [min([m2-2*hWidth,j2-hWidth]),...
                min([j2+hWidth  ,m2       ])];
        set(gca,'xLim',xLim);
    end
end %key_press


set(hf,'KeyPressFcn',@ key_press);
waitfor(hf);
% switch from ij to xy ordering (for easy plotting)
out = [points(:,2),points(:,1)];
end

%-----------------------------------------------------------------------
% Subfunctions
%-----------------------------------------------------------------------
function tf = chkCMap(arg)
% validate colormap by checking against the list of built in maps or checking
% for a nx3 numeric array

    if
any(strcmp(arg,{'jet','hsv','hot','cool','spring','summer','autumn','winter','gray','bone','copp
er','pink','lines','default','hilo'}));
        tf = true;
    elseif isempty(arg)
        tf = true;
    elseif isnumeric(arg) && size(arg,2)==3
        tf = true;
    else
        tf = false;
    end
end
```

Class for storing and manipulating image data: ImStack

```
classdef ImStack
% ImStack Create a multi-image stack object. ImStack tries to be more
% useful than the standard arrays when working with images and movies.
%
% Syntax:
% OBJ = ImStack()                 creates an empty image stack
% OBJ = ImStack(array)            creates a stack from an array
% OBJ = ImStack(fileName)         creates a stack from a file
% OBJ = ImStack(fileName,frames)    creates stack and loads only spec'd frames
%
% Input
%   array - a numeric array of two, three or four dimensions:
%           Height -by- Width
%           Height -by- Width -by- Frames
%           Heigth -by- Width -by- Colors -by- Frames
%   fileName - a string containing the name of the file to import. Partial
%              and full paths are also accepted as long as the file is on
%              the MATLAB search path.
%   frames - a numeric vector of frame numbers to load.
%
% Output
%   OBJ - an image stack with the following properties:
%         height      - image heigth in pixels
%         width       - image width in pixels
%         frameCount  - number of images in stack
%         class    - the data class of the images i.e. double, uint8, etc.
%         colorFmt    - either 'Monochrome' or 'RGB' depending on the format
%
%         and methods:
%         diff        - returns the difference between each image and the first
%                       one in the stack
%         length      - overloads the built-in function to retrun the number of
%                       frames
%         norm        - scales the images from 0 to 1 converting to double if
%                       necessary (useful for the imshow function)
%         read        - load images from file
%         size        - overloads the built-in function to return the frame size
%                       as [width, height, frameCount] for monochrome and
%                       [width, height,  3, frameCount] for RGB images.
%         convert_fmt - converts the imagesc back and forth between monochrome
%                       and RGB formats. R, G, and B channels are average when
%                       converting  to monochrome, but the original data is not lost.
%                       Runnning convert_fmt again restores the original images.
%                       Converting Monochrome to RGB duplicates the original
```

```
%                    imagesc in each color channel.
%                    This method is useful for false coloring, and uscaling.
%
% A note on indexing...
%
% Retriving properties and calling methods uses the standard syntax, but
% indexing an ImStack object returns the images themselves greatly reducing the
% complexity of code needed to access subsets of the stack. Indexing works as
% follows:
% Obj(scalar) - returns frame n
% Obj(vector) - returns the frames in the vector
% Obj(array)  - returns a subset of the 3D [width,height,frame] or 4D
%               [width, height, color, frame] stack.
%
% Chris Stevens
% Last Update: 11 Jul 2012

% PUBLIC PROPERTIES
   properties
      width
      height
      frameCount
      frameClass = 'double'
      colorFmt = 'Monochrome'
      roi
      medianFrame
      source
      bg
      times
      dt
   end

%% PRIVATE PROPERTIES
   properties(Access = 'private', Hidden)
      data
      dataFmt
      minVal
      maxVal
   end

%% PUBLIC METHODS
   methods (Access = 'public')


 %% ImStack (constructor)
      function This = ImStack(varargin)
```

```
%Use existence and type of argument to determine what to do
switch nargin
   case 0 % empty stack
      % Initialize properties
      This.frameClass = '';
      This.colorFmt = '';
      This.source = 'Workspace';

   case 1 % array or file
      argIn = varargin{1};
      if isnumeric(argIn)  % stack from array
         switch ndims(argIn)
            case 2 %single mono frame
               [This.height,...
                This.width] = size(argIn);
               This.frameCount = 1;
               This.frameClass = class(argIn);
               This.dataFmt = 'Monochrome';

            case 3 %single RGB frame or multiple mono frames
               if size(argIn(3)) == 3;
                  % can't tell from the argument so ask
                  button = questdlg('3 Mono frames or 1 RGB frame?',...
                     'Color Format:','Mono','RGB','Mono');
                  % use answer to set properties
                  switch button
                     case 'Mono'
                        [This.height,...
                         This.width,...
                         This.frameCount] = size(argIn);
                        This.dataFmt = 'Monochrome';
                     case 'RGB'
                        [This.height,...
                         This.width] = size(argIn);
                        This.frameCount = 1;
                        This.dataFmt = 'RGB';
                  end

               else
                  % must be monochrome
                  [This.height,...
                   This.width,...
                   This.frameCount] = size(argIn);
                  This.dataFmt = 'Monochrome';
               end
```

```
                case 4 %true color frames
                    [This.height,...
                     This.width,...
                     ~,...
                     This.frameCount] = size(argIn);
                    This.dataFmt = 'RGB';


                otherwise
                    error('Could not creat object, imvalid array dimension');
            end
            This.frameClass = class(argIn); % Use same class as input array
            This.source = 'Workspace';      % All arrays are sourced from the
workspace
            This.data = argIn;              % Copy input array to "data" property
        else
        % stack from file(s)
            assert(ischar(argIn) || iscellstr(argIn),'Invalid argument');

            if ischar(argIn)
                fileList = {argIn};
            else
                fileList = argIn;
            end

            % check for existence
            for iFile = 1:length(fileList);
                assert(exist(fileList{iFile},'file')==2,...
                      'File "%s" not found',...
                      fileList{iFile});
            end

            % read files
            This.source = fileList{1};
            This = read(This);
            for iFile = 2:length(fileList)
                This = This.append(fileList{iFile});
            end
            This.source = fileList;
        end

    % File name with a frame argument
    case 2
        assert(ischar(varargin{1}) && exist(varargin{1},'file') == 2,...
              'Bad file name or file not found');
        if isnumeric(varargin{2}) % single file and frame argument
```

```
                This.source = varargin{1};
                This = This.read(varargin{2});
            elseif ischar(varargin{2}) % two files
                fileList = varargin;
                This.source = fileList{1};
                This = read(This);
                for iFile = 2:length(fileList)
                    This = This.append(fileList{iFile});
                end
                This.source = fileList;
            else
                error('Invlaid argument');
            end

        % List of three or more file names
        otherwise
            for i = 1:nargin
                assert(ischar(varargin{i}) && exist(varargin{i},'file')== 2,...
                    'Invalid file name');
            end

            fileList = varargin;
            This.source = fileList{1};
            This = This.read();
            for iFile = 2:length(fileList)
                This = This.append(fileList{iFile});
            end
            This.source = fileList;
    end %switch

    %Set min and max properties
    This.minVal = min(This.data(:));
    This.maxVal = max(This.data(:));
    % calc the region of interest and median
    This.roi = mask(This);
    This.medianFrame = median(This.data);
    This.bg = This.get_frames(1);
end %ImStack

%-----------------------------------------------
% SIZE - Overload built-in SIZE to use properties
%-----------------------------------------------
function varargout = size(This)
    switch This.colorFmt
        case 'Monochrome'
            if nargout == 0
```

```
                varargout{1} = [This.height,This.width,This.frameCount];
            else
                varargout = {This.height,This.width,This.frameCount};
            end

        case 'RGB'
            if nargout == 0
                varargout{1} = [This.height,This.width,3,This.frameCount];
            else
                varargout = {This.height,This.width,3,This.frameCount};
            end

    end
end
%-----------------------------------------------
% LENGTH - Overload built ion length to return number of images in stack
%-----------------------------------------------
function l = length(This)
    l = This.frameCount;
end

%-----------------------------------------------
% END - Overload built-in END so modified indexing works
%-----------------------------------------------
function b = end(This,k,~)
    switch k
        case 1
            b = This.length;
        case 2
            b = This.width;
        case 3
            switch This.colorFmt
                case 'Monochrome'
                    b = This.length;
                case 'RGB'
                    b = 3;
            end
        case 4
            b = This.length;
    end
end %end

%-----------------------------------------------
% DIFF - returns the diffrence between the spec'd frame and the first frame
%-----------------------------------------------
function frame = diff(This,frameNo,reference)
```

```
        % use all frames if not set
        switch nargin
            case 1
                frameNo = 2:This.frameCount;
                reference = This.bg;
            case 2
                reference = This.bg;
        end

        % repeat subtracted frame to match size
        fn = This.get_frames(frameNo);
        if isscalar(frameNo)
            f1 = reference;
        else
            switch This.colorFmt
                case 'Monochrome'
                    f1 = repmat(reference,[1,1,numel(frameNo)]);
                case 'RGB'
                    f1 = repmat(reference,[1,1,1,numel(frameNo)]);
            end
        end

        % subtraction works differently on uints and floats
        switch This.frameClass
            %floating point subtraction
            case {'double','single'}
                frame = fn-f1;

            % uint subtraction scales to fit within range
            case {'uint8','uint16','uint32','uint64'}
                ceil = intmax(This.frameClass);
                rawFrame = (fn/2+ceil/2-f1/2);
                floored = rawFrame-min(rawFrame(:));
                scale = double(ceil)/double(max(floored(:)));
                frame = scale*floored;
        end
    end

%-----------------------------------------------
% DIVIDE - Returns the specified frame divided by the first frame.
%-----------------------------------------------
    function frame = divide(This,frameNo)
        This.frameClass = 'double';

        % return all frames if no frameNo given
        if nargin == 1
```

```
            frameNo = 2:This.frameCount;
        end

        if length(frameNo) == 1
            frame = This.get_frames(frameNo)./This.get_frames(1);
        else
            switch This.colorFmt
                case 'Monochrome'
                    repDims = [1,1,length(frameNo)];
                case 'RGB'
                    repDims = [1,1,1,length(frameNo)];
            end
            frame = This.get_frames(frameNo)./repmat(This.get_frames(1),repDims);
        end

        frame( isinf(frame) | isnan(frame)) = 0;
    end

%-----------------------------------------------
% NORM - returns a normalized (0 to 1), floating point version of
%        the spec'd frame.
%-----------------------------------------------
    function frame = norm(This,frameNo)

        if ~strcmp(This.frameClass,{'double','single'})
            This.frameClass = 'double';
        end

        % get frame(s) to norm
        This.frameClass = 'double';
        original = This.get_frames(frameNo);

        %scale intensities
        mx = double(This.maxVal);
        mn = double(This.minVal);
        frame = (original-mn)/(mx-mn);
    end

%-----------------------------------------------
% READ - import frames from file
%-----------------------------------------------
    function This = read(This,frames)
        % check that a file is associated with the object
        assert(~strcmp(This.source,'Workspace'),...
              '%s is not linked to a file. Cannot read frames',...
              inputname(1));
```

```
        % Get the file extension and the list of compatible file types
        fName = This.source;
        [~,~,ext] = fileparts(fName);
        stillExt = imformats;
        videoExt = {'avi','mpg','wmv','asf','asx'};

        % separate actions for video and stills
        switch ext(2:end);
           case videoExt
              % video files
              File = VideoReader(fName);
              if nargin == 1
                 This.data = read(File);
              else
                 This.data = read(File,frames);
              end
           case [stillExt(:).ext]
              % still image files
              This.data = imread(fName);
           otherwise
              error('Unsupported file type');
        end

        % set height, width, frameCount, and colorFmt properties
        if ndims(This.data) <= 3
           [This.height,...
            This.width,...
            This.frameCount] = size(This.data);
           This.dataFmt = 'Monochrome';
        else
           [This.height,...
            This.width,...
            ~,...
            This.frameCount] = size(This.data);
           This.dataFmt = 'RGB';
        end

        % update frameClass
        This.frameClass = class(This.data);
     end %read

%-----------------------------------------------
% APPEND - append frame(s) from other sources
%-----------------------------------------------
     function This = append(This,fileName)
```

```
% validate file name
assert(exist(fileName,'file')==2,'File not found');

% read file
oldData = This.data;
oldClass = class(oldData);
newData = imread(fileName);
newClass = class(newData);

% convert class if necessary
if ~isa(newData,oldClass)
   warning('ImStack:Append:rescaleOnAppend',...
      'bit depth mismatch, interpolating to highest bits/pixel');
   switch oldClass
      case 'double' % double/*
         newData = double(newData);
      case 'single'
         switch newClass
            case 'double' % single/double
               oldData = double(oldData);
            otherwise % single/uint*
               newData = single(oldData);
         end
      otherwise
         switch newClass
            case 'double' %uint*/double
               oldData = double(oldData);
            case 'single' %uint*/single
               oldData = single(oldData);
            otherwise %uint*/uint*
               oldBits = str2double(oldClass(5:end));
               newBits = str2double(newClass(5:end));
               if oldBits>newBits
                  newData = cast(newData,oldClass).*(2^oldbits-1)/(2^newBits-1);
               elseif oldBits<newBits
                  oldData = cast(oldData,newClass).*(2^newBits-1)/(2^oldBits-1);
               end
         end % switch newClass
   end % switch oldClass
end %if

%convert color format if needed
switch ndims(newData)
   case 2 %single grayscale frame'
      newFrameCount = 1;
      newFmt = 'Monochrome';
```

```
    case 3 %single RGB frame'
        if size(newData,3) == 3;

            % can't tell from the argument so ask
            button = questdlg('3 Mono frames or 1 RGB frame?',...
                'Color Format:','Mono','RGB','Mono');

            % use answer to set properties
            switch button
                case 'Mono'
                    newFrameCount = 3;
                    newFmt = 'Monochrome';
                case 'RGB'
                    newFrameCount = 1;
                    newFmt = 'RGB';
            end
        else % must be monochrome
            newFrameCount = size(newData,3);
            newFmt = 'Monochrome';
        end
    case 4 %multiple RGB frames'
        newFrameCount = size(newData,4);
        newFmt = 'RGB';
    otherwise
        error('Invalid image(s) in file');
end %switch

% default to RGB if formats disagree
if ~strcmp(newFmt,This.dataFmt)
    warning('ImStack:Append:colorMismatch',...
        'New color format does not match old format defaulting to RGB');
    if strcmp(newFmt,'Monochrome')
        newData = repmat(newData,[1,1,3,1]);
        newFmt = 'RGB';
    else
        oldData = repmat(oldData,[1,1,3,1]);
    end
end

%concatenate frames
if strcmp(newFmt,'RGB');
    This.data = cat(4,oldData,newData);
else
    This.data = cat(3,oldData,newData);
end
```

```
            % update propoerties
            This.frameClass = class(newData);
            This.dataFmt = newFmt;
            This.frameCount = This.frameCount+newFrameCount;
        end %fcn append

%-----------------------------------------------
% MAX - overload builtin max function
%-----------------------------------------------
        function mx = max(This)
            mx = cast(This.maxVal,This.frameClass);
        end

%-----------------------------------------------
% MIN - overload builtin max function
%-----------------------------------------------
        function mn = min(This)
            mn = cast(This.minVal,This.frameClass);
        end

%-----------------------------------------------
% CONVERT_FMT - switch between mono and RGB color formats
%-----------------------------------------------
        function This = convert_fmt(This)
            % change the type to the opposite
            switch This.colorFmt
                case 'Monochrome'
                    This.colorFmt = 'RGB';
                case 'RGB'
                    This.colorFmt = 'Monochrome';
            end
        end

%-----------------------------------------------
% CONVERT_TYPE - change the output class for functions and indexing
%-----------------------------------------------
    function This = convert_type(This,type)
        % Change the class of indexed output
        if ~strcmp(type,{'double','single','uint8','uint16','uint32','uint64'})
            error('Unsupported data class');
        end
        This.frameClass = type;
    end

%-----------------------------------------------
% SET_BG - sets the background image used in diff and div
```

```
%-----------------------------------------------
   function This = set_bg(This,bgFrames)
      % average selected frames to create a mean background
      This.bg = mean(This.data(:,:,:,bgFrames),4);

   end


   end %methods (public)

%------------- HIDDEN PUBLIC METHODS -------------
   methods (Access = 'public', Hidden)

%-----------------------------------------------
% SUBSREF - Overload normal subscripting to return frames for a scalar index
%-----------------------------------------------
       function b = subsref(This,s)
          % SUBSREF Implementing the following syntax:
          % obj()
          % obj(1)
          % obj([1, 2, 3])
          % obj.property
          % obj.method(args)

          switch s(1).type
             case '()'  % Array indexing
                b = This.get_frames(s(1).subs{1});
             case '.'

                % property access
                switch s(1).subs
                   % public
                   case 'height'
                      b = This.height;
                   case 'width'
                      b = This.width;
                   case 'frameCount'
                      b = This.frameCount;
                   case 'frameClass'
                      b = This.frameClass;
                   case 'colorFmt'
                      b = This.colorFmt;
                   case 'source'
                      b = This.source;
                   case 'roi'
                      b = This.roi;
```

```
case 'bg'
   b = This.bg;
% hidden
case 'data'
   if length(s) > 1
      b = This.data(s(2).subs{:});
   else
      b = This.data;
   end
case 'min'
   b = This.min();
case 'max'
   b = This.max();
case 'medianFrame'
   b = This.medianFrame;
case 'times'
   b = This.times;
case 'dt'
   b = This.dt;

% method access
case 'diff'
   if strcmp(s(2).subs{1},':')
      b = diff(This);
   else
      b = diff(This,s(2).subs{:});
   end
case 'divide'
   if strcmp(s(2).subs{:},':')
      b = divide(This);
   else
      b = divide(This,s(2).subs{:});
   end
case 'norm'
   if strcmp(s(2).subs{:},':')
      b = norm(This);
   else
      b = norm(This,s(2).subs{:});
   end
case 'read'
   b = read(This,s(2).subs{:});
case 'convert_fmt'
   b = convert_fmt(This);
case 'convert_type'
   b = convert_type(This,s(2).subs{:});
case 'append'
```

```
                    b = append(This,s(2).subs{:});
                case 'length'
                    b = length(This);
                case 'size'
                    b = size(This);
                case 'set_bg'
                    b = set_bg(This,s(2).subs{:});
                % throw controlled errors
                otherwise
                    if numel(s) == 1
                        error('Unknown property');
                    else
                        error('Unknown method)');
                    end
                end %switch s(2)
            otherwise
                error('Syntax error')
        end %switch s(1)
    end %subsref
end %methods (hidden)

% ---------------- PRIVATE METHODS ----------------
methods (Access = 'private')

%-----------------------------------------------
% GET_FRAMES - Returns frames with proper class, color format, and subscripting
%-----------------------------------------------
    function outFrames = get_frames(This,args)

        %convert color format if needed
        fmt = strcmp('RGB',{This.dataFmt,This.colorFmt});
        if fmt(1)==fmt(2)                   % same format
            outFrames = This.data;
        elseif fmt(2)                       % mono data/rgb frames
            temp = reshape(This.data,...
                [This.height,This.width,1,This.frameCount]);
            outFrames = repmat(temp,[1,1,3,1]);
        else                                % rgb data/mono frames
            outFrames = mean(This.data,3);
        end

        %convert class
        outFrames = cast(outFrames,This.frameClass);

        %sub sample full array
        rows = 1:This.height;
```

```
        cols = 1:This.width;
        switch This.colorFmt
            case 'RGB'
                colors = 1:3;
                isColor = true;
            case 'Monochrome'
                colors = [];
                isColor = false;
        end
        frames = 1:This.frameCount;
        switch length(args)
            case 1 % single full frame
                frames = args(1);
            case 2 % specified pixels only
                rows = args{1};
                cols = args{2};
            case 3 % pixels and frames
                rows = args{1};
                cols = args{2};
                frames = args{3};
            case 4 %fully spec'd true color
                rows = args{1};
                cols = args{2};
                colors = args{3};
                frames = args{4};
            otherwise
                error('Index exceeds dimensions')
        end
        if isColor
            outFrames = outFrames(rows,cols,colors,frames);
        else
            outFrames = outFrames(rows,cols,frames);
        end

    end %get_frames
  end %methods

end %classdef
```

Function to mask solid objects in images: roiMask

```
function roiMask = mask(This)
   % roiMask = mask(This)
   %
   %   mask returns a logical array which is true within the region of interest and
   %   false elsewhere. The roi is the light region of the first frame in Stack with
   %   the largest area.
   %
   %   Input: Stack - an image stack see the IMStack class for more info.
   %   Output: roiMask - a logical array the same size as the frames of Stack that
   %   is true within the roi and false elsewhere.

   im = This.get_frames(1);

   %Use intensity thresh to separate visible areas from black
   raw_roi = im > max(im(:)).*0.1;

   %remove undesired sections
   roiMask = true(size(raw_roi));
   s = regionprops(~raw_roi,'Area','PixelIdxList');
   area = cat(1,s.Area);
   pil = cat(1,s(area>200).PixelIdxList);
   roiMask(pil) = false;
end

function medFrame = median(data)
   m = (size(data,4)+1)*0.5;
   fs = sort(data,4); %sort frames

   if mod(m,1) % even frame count
      medFrame = (fs(:,:,:,m+0.5)+fs(:,:,:,m-0.5)).*0.5;
   else %even frame count
      medFrame = fs(:,:,:,m);
   end
end
```

Function to interpret binary video data: read_cine

```
function out = read_cine(varargin)
% out = read_cine(fileName)
% Reads a .cine file (Vision Research video format)
%
% Input:
%   fileName (string) - name of the cine file
%   range (2x1 numeric) - optional range of frames to read from file
%   option (string) - Optionally one of the three strings: 'ImStack', 'Array', or 'Struct'
%                     which specify the output format. ImStack is a class with
%                     some rudimentary analysis methods. Array is a 4D array of
%                     pixel intensities. Struct is a structure containing
%                     infromation from the cine file as well as pixel values.
%                     If not specified, read_cine returns a stuct
%
% Output:
%   out (varies) - The struct option returns with the following fields:
%       frameRate
%       exposure
%       frameCount
%       version
%       bitDepth
%       width
%       height
%       colorFormat
%               - The Array option is double class and 4D (height, width, color
%                frame)
% Type 'help ImStack' for information about the class

%% Validate arguments
error(nargchk(1,3,nargin));
fileName = varargin{1};
switch nargin
   case 3
      assert(any(numel(varargin{2}) == [0,2]) && isnumeric(varargin{2}),'Invalid range');
      range = varargin{2};
      assert(any(strcmpi(varargin{3},{'ImStack','Array','Struct'})),'Invalid option');
      outClass = lower(varargin{3});
   case 2 % name and range only
      assert(numel(varargin{2}) == 2 && isnumeric(varargin{2}),'Invalid range');
      outClass = 'imstack';
   case 1 % name only
      range = [];
      outClass = 'imstack';
end
```

```
%% Validate and open file
assert(exist(fileName,'file') == 2,'File not found'); % does it exist
global fid
fid = fopen(fileName,'r');
assert(fid ~= -1,'File unreadable'); % did it open
fileMarker = read(2,'CHAR');
assert(strcmp(fileMarker,'CI'),'File is not a cine file'); % is the marker correct

%% Read cine file header
headerSize = read('WORD');
compression = read('WORD');
version = read('WORD');
firstMovieImage = read('LONG');
totalImageCount = read('DWORD');
firstImageNo = read('LONG');
imageCount = read('DWORD');
offImageHeader = read('DWORD');
offSetup = read('DWORD');
offImageOffsets = read('DWORD');
triggerTime = read('TIME64');
fPos= ftell(fid);
assert(fPos == headerSize,'File read error: headerSize mismatch');

%% Read bit map info header
% check position and go to beginning of BITMAPINFOHEADER
if fPos ~= offImageHeader
   fseek(fid,offImageHeader,'bof');
end
biSize = read('DWORD');
biWidth = read('LONG');
biHeight = read('LONG');
biPlanes = read('WORD');
biBitCount = read('WORD');
biCompression = read('DWORD');
biSizeImage = read('DWORD');
biXPelsPerMeter = read('LONG');
biYPelsPerMeter = read('LONG');
biClrUser = read('LONG');
biClrImportant = read('DWORD');

%% Read setup structure
frameRate16 = read('WORD');
shutter16 = read('WORD');
postTrigger16 = read('WORD');
```

```
frameDelay16 = read('WORD');
aspectRatio = read('WORD');
contrast16 = read('WORD'); %unused
bright16 = read('WORD'); %unused
rotate16 = read('BYTE'); %unused
timeAnnotation = read('BYTE'); %unused
trigCine = read('BYTE'); %unused
trigFrame = read('BYTE');
shutterOn = read('BYTE'); %unused

% read description until 0x5343 ('ST')
descriptionOld = read(2,'CHAR');
while ~strcmp(descriptionOld(end-1:end),'ST')
   descriptionOld = [descriptionOld,read('CHAR')];
end
mark = descriptionOld(end-1:end);
descriptionOld = descriptionOld(1:end-2);
length_ = read('WORD');
binning = read('WORD');
sigOption = read('WORD');
binChannels = read('SHORT');
samplesPerImage = read('BYTE');
binName = cell(8,1);
for i = 1:8
   binName{i} = read(11,'STRING');
   read('BYTE');
end
anaOption = read('WORD');
anaChannels = read('SHORT');
res6 = read('BYTE');
anaBoard = read('BYTE');
chOption = read(8,'SHORT');
anaGain = read(8,'FLOAT');
anaUnit = cell(8,1);
for i = 1:8
   anaUnit{i} = read(5,'STRING');
   read('BYTE');
end
anaName = cell(8,1);
for i = 1:8
   anaName{i} = read(10,'STRING');
end
iFirstImage = read('LONG');
dwImageCount = read('DWORD');
nQFactor = read('SHORT');
wCineFileType = read('WORD'); %#ok<*NASGU>
```

```
szCinePath = cell(4,1);
for i = 1:4
   szCinePath{i} = read(65,'STRING');
end
bMainsFreq = read('WORD'); %unused
bTimeCode = read('BYTE'); %unused
bPriority = read('BYTE'); %unused
wLeapSecDY = read('WORD'); %unused
dDelayTC = read('DOUBLE'); %unused
dDelayPPS = read('DOUBLE'); %unused
genBits = read('WORD'); %unused
res1 = read('INT'); %ignore
res2 = read('INT'); %ignore
res3 = read('INT'); %ignore
imWidth = read('WORD');
imHeight = read('WORD');
edrShutter16 = read('WORD');
serial = read('UINT');
saturation = read('INT');
res5 = read('BYTE'); %ignore
autoExposure = read('UINT');
bFlipH = read('BOOL');
bFlipV = read('BOOL');
grid = read('UINT');
frameRate = read('UINT');
shutter = read('UINT');
edrShutter = read('UINT');
postTrigger = read('UINT');
frameDelay = read('UINT');
bEnableColor = read('BOOL');
cameraVersion = read('UINT');
firmwareVersion = read('UINT');
softwareVersion = read('UINT');
recordingTimeZone = read('INT'); %reads 18000 should be -5
cfa = read('UINT');
bright = read('INT')*10; % converted to sw scale
contrast = 10^(read('INT')/100); %converted to sw scale
gamma = 10^(read('INT')/100); % converted to sw scale
reserved1 = read('INT'); %ignore
autoExpLevel = read('UINT');
autoExpSpeed = read('UINT');
autoExpRect = read('RECT');
wbGain{i} = read(4,'WBGAIN');
rotate = read('INT');
wbView = read('WBGAIN');
realBPP = read('UINT');
```

```
conv8Min = read('UINT');
conv8Max = read('UINT');
filterCode = read('INT');
filterParam = read('INT');
uf = read('IMFILTER');
blackCalSVer = read('UINT');
whiteCalSVer = read('UINT');
grayCalSVer = read('UINT');
bStampTime = read('BOOL');
soundDest = read('UINT');
frpSteps = read('UINT');
frpImgNr = read(16,'INT');
frpRate = read(16,'UINT');
frpExp = read(16,'UINT');
mcCnt = read('INT');
mcPercent = read(64,'FLOAT');
ciCalib = read('UINT');
calibWidth = read('UINT');
calibHeight = read('UINT');
calibRate = read('UINT');
calibExp = read('UINT');
calibEDR = read('UINT');
calibTemp = read('UINT');
headSerial = read(4,'UINT');
rangeCode = read('UINT');
rangeSize = read('UINT');
decimation = read('UINT');
masterSerial = read('UINT');
sensor = read('UINT');
shutterNs = read('UINT');
edrShutterNs = read('UINT');
frameDelayNs = read('UINT');
imPosXAcq = read('UINT');
imPosYAcq = read('UINT');
imWidthAcq = read('UINT');
imHeightAcq = read('UINT');
description = read(4096,'STRING');

%% tagged info blocks
fseek(fid,offSetup+length_,'bof');
if (offSetup+length_)<offImageOffsets
    readMore = true;
    while readMore
        blockSize = read('DWORD');
        type = read('WORD');
        moreBlocks = read('WORD');
```

```
        switch type
            case 1002 %Time only block
                imTimes = read(imageCount,'TIME64');
            case 1003 %Exposure only block
                imExp = read(imageCount,'DWORD')./2^32;
            case 1005 % Binary signal block
                binSignal = read(blockSize{ctr}-8,'BTYE');
            case 1006 % Analog signal block
                anaSignal = read(blockSize{ctr}-8,'BYTE');
            otherwise
                error('Undefined block type');
        end
        readMore = moreBlocks;
    end
end

%% pointers to images
switch version
    case 0
        pImage = read(imageCount,'DWORD');
    case 1
        pImage = read(imageCount,'INT64');
end

%% images
% Initialize data structure
im = struct('annotationSize',{},...
            'annotation',{},...
            'imageSize',{},...
            'pixels',{});

% Calculate number of pixels and data format
if biBitCount > 16
    nPixels = 3*biWidth*biHeight;
    classStr = 'WORD';
elseif biBitCount > 8
    nPixels = biWidth*biHeight;
    classStr = 'WORD';
else
    nPixels = biWidth*biHeight;
    classStr = 'BYTE';
end

% Read frames
if isempty(range)
    range = [1,imageCount];
```

```
end

if range(1)<1
   range(1) = 1;
end

if range(2)>imageCount
   range(2) = imageCount;
end

nFrames = range(2)-range(1)+1;
if cfa == 0
   pixels = zeros(imHeight,imWidth,1,nFrames);
else
   pixels = zeros(imHeight,imWidth,3,nFrames);
end
for i = range(1):range(2)
   index = i-range(1)+1;
   im(index).annotationSize = read('DWORD');
   for j = 1:im(index).annotationSize-1*8
      im(index).annotation{j} = read('WORD');
   end
   im(index).imageSize = read('DWORD'); %size in bytes divide by two for DWORDS
   pixels(:,:,:,index) = flipud(reshape(read(nPixels,classStr),biWidth,biHeight)');
end

% Close the file
fclose(fid);
% Build output
switch outClass
   case 'imstack'
      out = ImStack(pixels);
      out.times = imTimes(:,6)-imTimes(1,6);
      out.dt = mean(diff(out.times));
      out.source = fileName;
   case 'array'
      out = pixels;
   case 'struct'
      out = struct('fileName',fileName,...
                   'frameCount',imageCount,...
                   'frameRate',frameRate,...
                   'exposure',shutterNs,...
                   'edr',edrShutterNs,...
                   'bitDepth',realBPP,...
                   'height',imHeight,...
                   'width',imWidth,...
```

```
                'frames',pixels,...
                'cameraSerial',serial,...
                'triggerTime',triggerTime,...
                'imageTime',imTimes,...
                'imageExp',imExp);
end
end %fcn

%% subfunctions
function out = read(varargin)
% read the file and return data of a certain type
error(nargchk(1,2,nargin));
global fid

if nargin == 1
   count = 1;
   type = varargin{1};
else
   count = varargin{1};
   type = varargin{2};
end

switch type
   case 'BYTE'
      out = fread(fid,count,'ubit8');
   case 'CHAR'
      out = fread(fid,count,'*char')';
   case 'WORD'
      out = fread(fid,count,'ubit16');
   case 'INT16'
      out = fread(fid,count,'*int16');
   case 'SHORT'
      out = fread(fid,count,'int16');
   case 'BOOL'
      out = logical(fread(fid,count,'ubit32'));
   case 'DWORD'
      out = fread(fid,count,'ubit32');
   case 'UINT'
      out = fread(fid,count,'*uint32');
   case 'LONG'
      out = fread(fid,count,'int32');
   case 'INT'
      out = fread(fid,count,'*int32');
   case 'INT64'
      out = fread(fid,count,'*int64');
   case 'FLOAT'
```

```
        out = fread(fid,count,'*single');
    case 'DOUBLE'
        out = fread(fid,count,'*double');
    case 'STRING'
        out = fread(fid,count,'*char');
    case 'TIME64'
        out = zeros(count,6);
        for i = 1:count
            fraction = fread(fid,1,'ubit32')/2^32;
            seconds = fread(fid,1,'ubit32');
            out(i,:) = datevec(seconds./(24*3600)+datenum('31 Dec 1969 18:00'));
            out(i,6) = out(i,6)+fraction;
        end

    case 'IMFILTER'
        out = struct('dim',[],'shifts',[],'bias',[],'coef',[]);
        for i = 1:count
            out(i).dim = fread(fid,1,'int32');
            out(i).shifts = fread(fid,1,'int32');
            out(i).bias = fread(fid,1,'int32');
            out(i).coef = fread(fid,25,'int32');
        end

    case 'WBGAIN'
        out = struct('r',[],'b',[]);
        for i = 1:count
            out(i).r = fread(fid,1,'single');
            out(i).b = fread(fid,1,'single');
        end
    case 'RECT'
        out = struct('r',[],'c',[],'h',[],'w',[]);
        for i = 1:count
            out(i).r = fread(fid,1,'int32');
            out(i).c = fread(fid,1,'int32');
            out(i).h = fread(fid,1,'int32');
            out(i).w = fread(fid,1,'int32');
        end
end
end
```

Function to calculate distance between two curves: cp_dist

```
function [dist,pos] = cp_dist(coords1,coords2,mode)
% dist = cp_dist(curve1,curve2,mode)
%
% cp_dist runs on one of three modes: 'closest', 'interp', or 'combined'
%
% In 'closest' mode, it returns a vector of the distance from curve1 to curve2
% using the closest point on curve2 to each point on curve1. The result is
% the same length as curve one.
%
% In 'interp' mode, attempts to align the meaurement better to the normal of the
% curves. Each curve is interpolated so that the number of data points is the
% average length of the two curves, then the distance is calculated point to point
%
% In 'combined' mode interpolates each curve as in 'interp' mode then uses the
% closest interpreted point to measure distance.
%
% In both cases, cp_dist returns dist and pos. Dist is a nx3 array
% [x-distance, y-distance, magnitude]. Pos is a 2xn array of the origins of the
% distance vectors.

switch mode
   case {1,'Closest','closest'}
   % Closest point
      n = length(coords1);
      dist = zeros(n,3);
      for iPt = 1:n
         d = sqrt((coords2(:,1)-coords1(iPt,1)).^2+(coords2(:,2)-coords1(iPt,2)).^2);
         [mag,ind] = min(d);

         dist(iPt,:) = [coords2(ind,1)-coords1(iPt,1),...
                        coords2(ind,2)-coords1(iPt,2),...
                        mag];
      end

      pos = coords1;

   case {2,'Interp','interp'}
   % Interpolated point-to-point
      n1 = length(coords1);
      n2 = length(coords2);
      nInt = max([n1,n2]);
      c1i = [interp1q((1:n1)',coords1(:,1),linspace(1,n1,nInt)'),...
            interp1q((1:n1)',coords1(:,2),linspace(1,n1,nInt)')];
```

```
        c2i = [interp1q((1:n2)',coords2(:,1),linspace(1,n2,nInt)'),...
              interp1q((1:n2)',coords2(:,2),linspace(1,n2,nInt)')];

        dist = [c2i(:,1)-c1i(:,1),...
                c2i(:,2)-c1i(:,2),...
                sqrt((c2i(:,1)-c1i(:,1)).^2+(c2i(:,2)-c1i(:,2)).^2)];

        pos = c1i;

    case {3,'Combined','combined'}
    % Interpolate points on each curve then use closest point for distance
        n1 = length(coords1);
        n2 = length(coords2);
        nInt = 2*max([n1,n2]);
        c1i = [interp1q((1:n1)',coords1(:,1),linspace(1,n1,nInt)'),...
              interp1q((1:n1)',coords1(:,2),linspace(1,n1,nInt)')];

        c2i = [interp1q((1:n2)',coords2(:,1),linspace(1,n2,nInt)'),...
              interp1q((1:n2)',coords2(:,2),linspace(1,n2,nInt)')];

        dist = zeros(nInt,3);
        for  iPt = 1:nInt
            d = sqrt((c2i(:,1)-c1i(iPt,1)).^2+(c2i(:,2)-c1i(iPt,2)).^2);
            [mag,ind] = min(d);
            dist(iPt,:) = [c2i(ind,1)-c1i(iPt,1),...
                           c2i(ind,2)-c1i(iPt,2),...
                           mag];
        end
        pos = {c1i,c2i};

    otherwise
        error('Invalid mode argument');

end
```

Function to calculate 2D polynomial fitting coefficients: polyfit2

```
function C = polyfit2(x,y,z, method)
% polyfit2 is for 2-D data fitting using least squares
%
% USAGE:   C = polyfit2(X,Y,Z, 'method')
%       where an output vector C contains the bi-linear or bi-cubic
%       coefficients of a least-squares polynomial in x and y, and
%       input matrices X, Y, Z are for a 2D function z=f(x,y).
%
% Here 'method' can be
%         'linear' - bilinear least squares fitting
%         'cubic'  - bicubic least squares fitting
%          n       - binomial of order n least squares fitting
%       Non-equally spaced (or even non-monotonic) X and Y are permitted.
%
%       For example, generate a coarse 2D curve and a least squares fitting
%       over finer mesh (meshdom with Matlab 3.5 BUT meshgrid with Matlab 4)
%               x = 0:10; y = 1:9;  [x y] = meshdom(x,y) ;
%                       z = sin(x.*y);
%               xi = 0:.25:10; yi=2:.5:8 ; [xi yi]=meshdom(xi,yi);
%               C  = polyfit2(x,y,z, 'cubic');
%               zi = polyval2(C, xi,yi, 'cubic');

%% Check arguments
error(nargchk(2,4,nargin,'struct'));

if size(x)~=size(z),
  error('X must have the same dimension as Z.');
end
if size(y)~=size(z),
  error('Y must have the same dimension as Z.');
end

if ~ischar(method)
    n = method;
    method = [num2str(n),'th order'];

    if n >= numel(x)
        error('Order must be less than number of data points');
    elseif numel(n) > 1
        error('Order must be a scalar');
    end
end

% Default to bilinear fit
```

```
if nargin<4
  method = 'linear';
end

%% Calculate coefficients
x = x(:);
y = y(:);
z = z(:);
len = length(z);
% Calculate A matrix
switch method
    case 'linear'
        A = [ ones(len,1), x, y, x.*y ] ;
    case 'cubic'
        A = [ ones(len,1), x, y, x.*y, x.^2, y.^2, (x.^2).*y, x.*(y.^2), x.^3, y.^3];
    otherwise % nth order binomial
        n = n+1;
        A = zeros(length(x),sum(1:n));

        ctr = 1;
        for nx = 0:n-1
            for ny = 0:n-1
                if nx+ny < n
                    A(:,ctr) = x.^nx .* y.^ny;
                    ctr = ctr+1;
                end
            end
        end
end

C = A \ z;
```

XV. Vita

Christopher A Stevens graduated from Kenton Ridge High School in Springfield, Ohio in June of 2002. He studied mechanical engineering at Rose-Hulman Institute of Technology in Terre Haute, Indiana where here graduated with a Bachelor of Science in May 2006. In September 2007, he entered the Air Force Institute of Technology Graduate School of Engineering and Management. He graduated in March of 2009 with a Master of Science in Aeronautical Engineering. He continued at AFIT pursuing a PhD in Aeronautical Engineering and graduated in March of 2014. He will continue in detonation research as a post-doctorate research engineer with Innovative Scientific Solutions Inc.

REPORT DOCUMENTATION PAGE		Form Approved OMB No. 0704–0188

The public reporting burden for this collection of information is estimated to average 1 hour per response, including the time for reviewing instructions, searching existing data sources, gathering and maintaining the data needed, and completing and reviewing the collection of information. Send comments regarding this burden estimate or any other aspect of this collection of information, including suggestions for reducing this burden to Department of Defense, Washington Headquarters Services, Directorate for Information Operations and Reports (0704–0188), 1215 Jefferson Davis Highway, Suite 1204, Arlington, VA 22202–4302. Respondents should be aware that notwithstanding any other provision of law, no person shall be subject to any penalty for failing to comply with a collection of information if it does not display a currently valid OMB control number. PLEASE DO NOT RETURN YOUR FORM TO THE ABOVE ADDRESS.

1. REPORT DATE (DD–MM–YYYY)	2. REPORT TYPE	3. DATES COVERED (From — To)
27-03-2014	Dissertation	27Mar2009-27Mar2014

4. TITLE AND SUBTITLE	5a. CONTRACT NUMBER
Development of a Detonation Diffuser	5b. GRANT NUMBER
	5c. PROGRAM ELEMENT NUMBER
6. AUTHOR(S) Stevens, Christopher A, CTR	5d. PROJECT NUMBER
	5e. TASK NUMBER
	5f. WORK UNIT NUMBER
7. PERFORMING ORGANIZATION NAME(S) AND ADDRESS(ES) Air Force Institute of Technology Graduate School of Engineering and Management (AFIT/EN) 2950 Hobson Way WPAFB OH 45433-7765	8. PERFORMING ORGANIZATION REPORT NUMBER AFIT-DS-ENY-14-M-05
9. SPONSORING / MONITORING AGENCY NAME(S) AND ADDRESS(ES) Intentionally Left Blank	10. SPONSOR/MONITOR'S ACRONYM(S)
	11. SPONSOR/MONITOR'S REPORT NUMBER(S)

12. DISTRIBUTION / AVAILABILITY STATEMENT
Distribution Statement A – Approved for public release; distribution is unlimited

13. SUPPLEMENTARY NOTES

14. ABSTRACT
This research includes an investigation of the mechanisms of diffraction and reinitiation that enable a detonation diffuser. It describes a set of geometric parameters necessary to design a diffuser for a given detonable mixture and initial channel height. Predetonators with channel height less than the critical height are ineffective because detonations in small channels decouple into separate shock and combustion fronts when the channel height increases. A detonation diffuser allows the channel height to increase by utilizing the decoupled shock wave to reinitiate detonation. In the diffuser, a detonation initially decouples into separate shock and combustion fronts, and then the decoupled shock front reflects from an oblique surface initiating a secondary detonation that survives the expansion. This research investigated the three regions of a detonation diffuser: the initial diffraction, the reflecting surface, and the second diffraction corner. Schlieren video of two-dimensional diffracting detonations recorded the position of the detonation, decoupled shock front and flame front. Observations of the decoupled shocks reflecting from surfaces showed that a 45° reflecting surface must be placed less than 80 mm downstream of the initial diffraction corner to initiate a secondary detonation in more than 91% of repeated trials. Observations of the interaction of diffracting detonations with multiple obstacles revealed that the best performance (smallest separation, and highest Mach number) occurred when the decoupled shock reflected from four separate obstacles at approximately the same time.

15. SUBJECT TERMS
Detonation Engine Diffraction Diffuser

16. SECURITY CLASSIFICATION OF:			17. LIMITATION OF ABSTRACT	18. NUMBER OF PAGES	19a. NAME OF RESPONSIBLE PERSON
a. REPORT U	b. ABSTRACT U	c. THIS PAGE U	UU	264	Dr. Paul I. King AFIT/ENY
					19b. TELEPHONE NUMBER (Include Area Code) (937) 255-3636 x4628 paul.king@afit.edu

Standard Form 298 (Rev. 8–98)
Prescribed by ANSI Std. Z39.18